BEILSTEIN JOURNAL OF NANOTECHNOLOGY

Functional nanostructures for electronics, spintronics and sensors

Edited by Anatolie S. Sidorenko

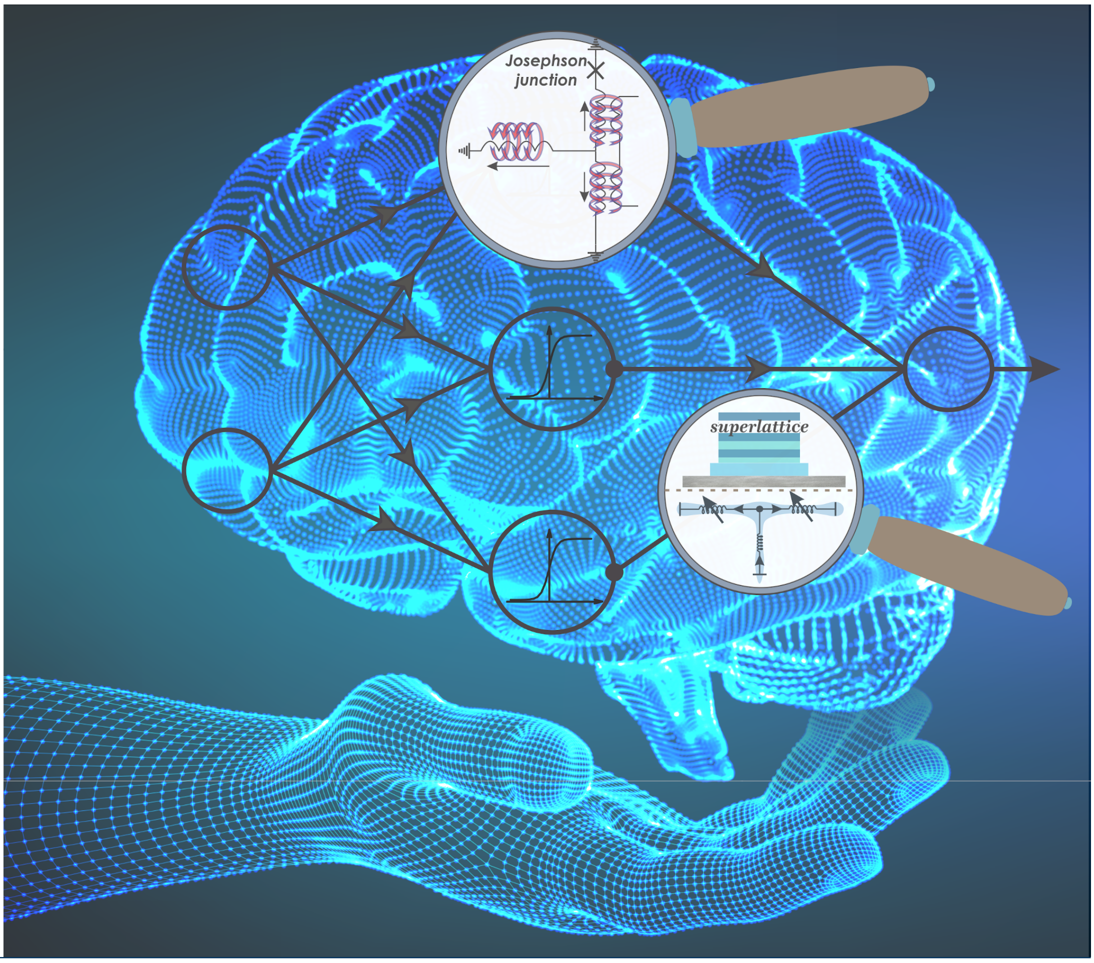

Imprint

Beilstein Journal of Nanotechnology
www.bjnano.org
ISSN 2190-4286
Email: journals-support@beilstein-institut.de

The *Beilstein Journal of Nanotechnology* is published by the Beilstein-Institut zur Förderung der Chemischen Wissenschaften.

Beilstein-Institut zur Förderung der
Chemischen Wissenschaften
Trakehner Straße 7–9
60487 Frankfurt am Main
Germany
www.beilstein-institut.de

The cover image is copyright (2020) Anatolie Sidorenko under the CC BY 4.0 license https://creativecommons.org/licenses/by/4.0/ and the hand vector is attributed to https://www.freepik.com/vectors/hand - www.freepik.com (created by user iuriimotov). This image depicts the development of the base elements for a possible design of a superconducting supercomputer with non-von Neumann architecture: an artificial network of neurons (Josephson junction) and synapses (superconducting layered kinetic inductivity) that "transforms" into a natural network of neurons and synapses (brain).

BEILSTEIN JOURNAL OF NANOTECHNOLOGY

Functional nanostructures for electronics, spintronics and sensors

Anatolie S. Sidorenko

Editorial

Address:
D. Ghitu Institute of Electronic Engineering and Nanotechnologies, Chisinau, Moldova and Orel State University, Orel, Russia

Email:
Anatolie S. Sidorenko - anatoli.sidorenko@kit.edu

Keywords:
functional nanostructures; nanoelectronics; post-Moore generation; sensors; spintronics; supercomputers

Beilstein J. Nanotechnol. **2020,** *11,* 1704–1706.
https://doi.org/10.3762/bjnano.11.152

Received: 20 July 2020
Accepted: 25 July 2020
Published: 10 November 2020

This article is part of the thematic issue "Functional nanostructures for electronics, spintronics and sensors".

Editor-in-Chief: T. Schimmel

Nanotechnology and functional nanostructures, exciting trends of the 21st century, are topics that have penetrated and influenced nearly all areas of human activity: from microelectronics to biology, from aerospace to medicine, from agriculture to novel materials engineering. One of the areas of nanoscience and nanotechnology that is developing especially rapidly is research on functional nanostructures for targeted applications. One of the most important and promising of these targeted applications are superconducting spintronic nanostructures for supercomputers of novel, “post-Moore” generation.

The exponential development of microelectronics and computers, based on traditional semiconductor chips, has followed the empirical Moore’s Law (formulated by one of the founders of Intel Corporation, Gordon Moore) for over four decades. Since 1965, Intel has designed chips that fit twice as many transistors into the same space of the chip every two years, following an exponential curve – this size shrinking of permanent transistors has made computers more powerful and compact. Nevertheless, in the last decade, a clear deviation has appeared – a slowing of Moore’s Law. Bob Colwell, the architect on the Pentium Pro, Pentium II, Pentium III and Pentium IV, described the stagnation of semiconductor technology as follows [1]:

“Officially Moore’s Law ends in 2020 at 7 nm, but nobody cares, because 11 nm isn’t any better than 14 nm, which was only marginally better than 22 nm … thermal dissipation issues thoroughly constraining the integration density, the multicore era effectively ends, leading to the “dark silicon” problem, i.e., only parts of available cores can be run simultaneously”.

Energy efficiency has now become a crucial parameter, limiting the advancement of supercomputers. The powerful, modern supercomputer, the Sunway Taihu Light [2], with a peak performance of 93 peta FLOPS (93×10^{15} floating point operations per second) has an energy consumption as high as 15.4 MW. This corresponds to a power plant capacity able to supply energy to a middle-sized city!

The low energy efficiency leads to high power consumption, and at the same time, limits the clock frequency of semiconductor computers to 4–5 GHz. This frequency limit occurs due to temperature limitations posed at the integration level and the switching rate of transistors.

It is important to realize that cryogenic cooling of semiconductor chips will not solve the problem [3]. The future of high-performance computing will most likely be associated with one of the alternative "post-Moore's" technologies where energy dissipation is drastically lower. It is expected that the most promising "post-Moore's" candidate to lead the technological way is superconductor digital technology (SDT) [4]. The switching energy of the SDT basic element is on the order of 10^{-19} J (including the power for cryogenic cooling of superconducting circuits), which demonstrates an energy efficiency of up to seven orders of magnitude as compared to the semiconductor analog [5]. The competitiveness of SDT illustrates a working prototype for a superconducting computer developed under the "Cryogenic computing complexity" IARPA program [6]. This is a 64-bit computing machine operating at a 10 GHz clock frequency with a throughput of 10^{13} bit-op/s and an energy efficiency of 10^{15} bit-op/J at a temperature of 4 K. A prospective investigation found that a superconductor computer could outperform its semiconductor competitor by two orders of magnitude in energy efficiency, demonstrating 250 GFLOPS/W [7]. The base elements of the superconductor computer are superconductor logic and memory circuits, where some of these prospective examples and the technological processes related to their fabrication are presented in this thematic issue.

In the last decade, very rapid development in a subfield of solid-state physics and engineering – superconducting spintronics based on functional nanostructures consisting of alternating layers of ferromagnetic and superconducting materials – has been observed. Due to the proximity effect of superconductor/ferromagnetic (S/F) layers and Andreev reflection of Cooper pairs at the S/F interface, a number of new phenomena were first theoretically predicted and then experimentally detected. Some examples include a nonuniform superconducting Fulde–Ferrell–Larkin–Ovchinnikov (FFLO) state, S/F π-junctions, oscillations of critical temperature and critical current in S/F hybrids on the thickness of the F-layer, multiperiodic re-entrant superconductivity, triplet pairing and triplet spin-valve and memory effects – just to name some of the new phenomena that have been detected in layered S/F hybrid nanostructures [8]. Moreover, the detected effects are very promising for technical applications directed towards enhancing the storage capacity of computer memory and the potential use as quantum computer building blocks.

Keeping in mind the trends with regard to "post-Moore's" electronics, this thematic issue aimed to cover theoretical, experimental and conceptual development towards superconducting supercomputer elements. Theoretical works on Josephson junctions as base elements for a superconducting computer were presented by Karabassov et al. [9] and Marychev et al. [10]. In the latter, the authors present a theoretical study of the current–phase relation of very promising SN-S-SN Josephson junctions, which could serve as energy efficient, high-performance superconducting electronics elements for fast computing.

This issue also contains progress towards various technological processes for fabrication and characterization of the base elements of a superconducting computer. For example, Arutyunov et al. [11] presented an advanced technology including lift-off electron-beam lithography followed by ultra-high-vacuum deposition of materials that was used for fabrication of nanostructured quasi-1D chains of Josephson junctions. This was followed by the work of Mohammed et al. [12] who presented a smart vacuum technology for the design of hetero-epitaxial S/F nanostructures. The elaborated and fabricated nanostructures can be utilized in superconducting memory and logic circuits as Josephson magnetic random access memory (MRAM) elements for a superconducting computer.

Other articles, more conceptual in nature, where the authors proposed, calculated, fabricated and investigated the novel base elements and electronic circuits for a superconducting computer include work by Bakurskiy et al. [13], where a tunable kinetic inductor is proposed as an artificial synapse for a superconducting neuronal network. This work combines the results of theoretical and experimental investigations of S/F superlattices. Such superlattices can be used as tunable kinetic inductivity synapses in artificial neural networks of a superconducting computer with non-von Neumann architecture. A further example by Novikov et al. [14] demonstrated the concept of "read-out" electronics for a superconducting computer where a low-noise cryogenic microwave amplifier as a read-out circuit of superconducting X-mon qubits is demonstrated.

Also, in addition to the progress towards theoretical and experimental developments of a superconducting computer, this thematic issues also includes several articles devoted to extra-sensitive detectors, their theoretical basis and technological process in terms of fabrication. For example, a novel phenomenon was presented in [15], which predicted the phenomena of superconductor–insulator quantum phase transitions in ultrathin capacitively coupled superconducting nanowires with quantum phase slips which may be used for interpretation of already existing experiments on meander-like nanowires and for the design of a novel set of superconducting sensors. Another very promising photon detector [16] was demonstrated for supersensitive detection in astrophysics and read-out tracts measuring signals generated by quantum circuits at a frequency of 6–9 GHz.

Summarizing the above-mentioned milestones, one can see that the main focus of this thematic issue is the new area of research: superconductor/ferromagnetic hybrid nanostructures and their applications for quantum electronics and spintronics. In addition to these highlighted works, there are also other interesting functional nanostructures, sensors and quantum detectors presented, to highlight the fascinating world of nanoelectronics.

The concept of this thematic issue emerged during the international SPINTECH conference "NANO-2019: Limits of Nanoscience and Nanotechnologies" and the summer school it followed, "S/F Hybrid Structures for Spintronics", that took place in September 2019 in Chisinau, Moldova. Presented by many of the participants of the conference and lecturers of the summer school, new ideas, technological approaches to design of functional nanostructures for superconducting spintronics, quantum electronics, sensors and novel base elements for superconducting supercomputers are the core of this thematic issue.

As the thematic issue editor, I would like to thank all highly experienced experts from 15 countries who presented novel, original results at the NANO-2019 conference and those who submitted valuable contributions to this issue. We believe that this thematic issue will attract the attention of scientists, technologists, and engineers and will be useful for a broad readership. The professional and permanent kind editorial support by the Production Team of the Beilstein Journals is greatly acknowledged. A.S. also thanks the SPINTECH project (G.A. Nr. 810144) and the Grant RSF Nr. 20-62-47009 "Physical and engineering basis of computers non-von Neumann architecture based on superconducting spintronics" for the support.

Anatolie Sidorenko

Chisinau, July 2020

ORCID® iDs

Anatolie S. Sidorenko - https://orcid.org/0000-0001-7433-4140

References

1. Colwell, R. The Chip Design Game at the End of Moore's Law, Hot Chips, August 2013. http://www.hotchips.org/wp-content/uploads/hc_archives/hc25/HC25.15-keynote1-Chipdesign-epub/HC25.26.190-Keynote1-ChipDesignGame-Colwell-DARPA.pdf (accessed July 29, 2020).
2. Sunway TaihuLight. http://www.top500.org/system/178764 (accessed July 29, 2020).
3. Mukhanov, O. A. *IEEE Trans. Appl. Supercond.* **2011,** *21,* 760–769. doi:10.1109/tasc.2010.2096792
4. Soloviev, I. I.; Klenov, N. V.; Bakurskiy, S. V.; Kupriyanov, M. Y.; Gudkov, A. L.; Sidorenko, A. S. *Beilstein J. Nanotechnol.* **2017,** *8,* 2689–2710. doi:10.3762/bjnano.8.269
5. Xu, Q.; Yamanashi, Y.; Ayala, C. L.; Takeuchi, N.; Ortlepp, T.; Yoshikawa, N. Design of an Extremely Energy-Efficient Hardware Algorithm Using Adiabatic Superconductor Logic. In *Proceedings of 15th International Superconductive Electronics Conference,* ISEC'2015, Nagoya, Japan, July 6–9, 2015; DS-P21. doi:10.1109/isec.2015.7383446
6. Cryogenic Computing Complexity (C3). https://www.iarpa.gov/index.php/research-programs/c3 (accessed July 29, 2020).
7. Holmes, D. S.; Kadin, A. M.; Johnson, M. W. *Computer* **2015,** *48,* 34–42. doi:10.1109/mc.2015.375
8. Sidorenko, A., Ed. *Fundamentals of Superconducting Nanoelectronics;* Springer: Berlin, Heidelberg, 2011. doi:10.1007/978-3-642-20158-5
9. Karabassov, T.; Guravova, A. V.; Kuzin, A. Y.; Kazakova, E. A.; Kawabata, S.; Lvov, B. G.; Vasenko, A. S. *Beilstein J. Nanotechnol.* **2020,** *11,* 252–262. doi:10.3762/bjnano.11.19
10. Marychev, P. M.; Vodolazov, D. Y. *Beilstein J. Nanotechnol.* **2020,** *11,* 858–865. doi:10.3762/bjnano.11.71
11. Arutyunov, K. Y.; Lehtinen, J. S. *Beilstein J. Nanotechnol.* **2020,** *11,* 417–420. doi:10.3762/bjnano.11.32
12. Mohammed, W. M.; Yanilkin, I. V.; Gumarov, A. I.; Kiiamov, A. G.; Yusupov, R. V.; Tagirov, L. R. *Beilstein J. Nanotechnol.* **2020,** *11,* 807–813. doi:10.3762/bjnano.11.65
13. Bakurskiy, S.; Kupriyanov, M.; Klenov, N. V.; Soloviev, I.; Schegolev, A.; Morari, R.; Khaydukov, Y.; Sidorenko, A. S. *Beilstein J. Nanotechnol.* **2020,** *11,* 1336–1345. doi:10.3762/bjnano.11.118
14. Novikov, I. L.; Ivanov, B. I.; Ponomarev, D. V.; Vostretsov, A. G. *Beilstein J. Nanotechnol.* **2020,** *11,* 1316–1320. doi:10.3762/bjnano.11.115
15. Latyshev, A.; Semenov, A. G.; Zaikin, A. D. *Beilstein J. Nanotechnol.* **2020,** *11,* 1402–1408. doi:10.3762/bjnano.11.124
16. Revin, L. S.; Pankratov, A. L.; Gordeeva, A. V.; Yablokov, A. A.; Rakut, I. V.; Zbrozhek, V. O.; Kuzmin, L. S. *Beilstein J. Nanotechnol.* **2020,** *11,* 960–965. doi:10.3762/bjnano.11.80

License and Terms

The definitive version of this article is the electronic one which can be found at:
https://doi.org/10.3762/bjnano.11.152

BEILSTEIN JOURNAL OF NANOTECHNOLOGY

Anomalous current–voltage characteristics of SFIFS Josephson junctions with weak ferromagnetic interlayers

Tairzhan Karabassov*[1], Anastasia V. Guravova[1], Aleksei Yu. Kuzin[2,3], Elena A. Kazakova[4], Shiro Kawabata[5], Boris G. Lvov[1] and Andrey S. Vasenko[1,6]

Full Research Paper

Open Access

Address:
[1]National Research University Higher School of Economics, 101000 Moscow, Russia, [2]Skolkovo Institute of Science and Technology, 121205 Moscow, Russia, [3]Department of Physics, Moscow State Pedagogical University, 119992 Moscow, Russia, [4]Sechenov First Moscow State Medical University, 119991 Moscow, Russia, [5]National Institute of Advanced Industrial Science and Technology,1-1-1 Umezono, Tsukuba, Ibaraki 305-8563, Japan and [6]I.E. Tamm Department of Theoretical Physics, P.N. Lebedev Physical Institute, Russian Academy of Sciences, 119991 Moscow, Russia

Email:
Tairzhan Karabassov* - iminovichtair@gmail.com

* Corresponding author

Keywords:
current–voltage characteristics; Josephson junctions; proximity effect, superconductivity; superconductor/ferromagnet hybrid nanostructures

Beilstein J. Nanotechnol. **2020,** *11,* 252–262.
doi:10.3762/bjnano.11.19

Received: 06 November 2019
Accepted: 14 January 2020
Published: 23 January 2020

This article is part of the thematic issue "Functional nanostructures for electronics, spintronics and sensors".

Guest Editor: A. S. Sidorenko

Abstract

We present a quantitative study of the current–voltage characteristics (CVC) of SFIFS Josephson junctions (S = bulk superconductor, F = metallic ferromagnet, I = insulating barrier) with weak ferromagnetic interlayers in the diffusive limit. The problem is solved in the framework of the nonlinear Usadel equations. We consider the case of a strong tunnel barrier such that the left SF and the right FS bilayers are decoupled. We calculate the density of states (DOS) in SF bilayers using a self-consistent numerical method. Then we obtain the CVC of corresponding SFIFS junctions, and discuss their properties for different set of parameters including the thicknesses of ferromagnetic layers, the exchange field, and the magnetic scattering time. We observe an anomalous nonmonotonic CVC in case of weak ferromagnetic interlayers, which we attribute to DOS energy dependencies in the case of small exchange fields in the F layers.

Introduction

It is well known that superconductivity and ferromagnetism are two competing antagonistic orders. In superconductors (S) electrons form Cooper pairs with opposite spins and momenta, while in ferromagnetic metals (F) electron spins tend to align in parallel. Nevertheless, it is possible to combine S and F layers in one hybrid structure, which leads to the observation of many striking phenomena. The reason is the superconducting proximity effect, i.e., the superconducting correlations leakage into a ferromagnetic metal due to Andreev reflection [1-7]. As a consequence, the real part of the pair wave function exhibits damped oscillatory behavior in a ferromagnetic metal. Hence, since the oscillations are spatially dependent, it is possible to realize a transition from "0" to "π" phase states in S/F/S structures upon changing the F layer thickness [1]. The proximity effect is characterized by the two length scales of decay and oscillations of the real part of the pair wave function in a ferromagnetic layer, ξ_{f1} and ξ_{f2}, correspondingly [1]. If we consider the exchange field h as the only important parameter of a ferromagnetic material, both lengths are equal to $\xi_h = \sqrt{D_f / h}$, where D_f is the diffusion constant in the ferromagnetic metal.

The existence of such phenomena enables the creation of so-called Josephson π junctions with a negative critical current [1,2]. Oscillations of the pair wave function in the F layer leads to several interesting phenomena in S/F/(S) systems, including nonmonotonic critical temperature dependence [8-12], Josephson critical current oscillations [13-41], and density of states (DOS) oscillations [42-45]. S/F hybrid structures have many promising applications in, e.g., single-flux quantum circuits [46,47], spintronic devices [48], memory elements [49-58] and spin-valves [59-65], magnetoelectronics [66-68], qubits [69], artificial neural networks [70], microrefrigerators [71,72], and low-temperature sensitive electron thermometers [73].

However, junctions with a ferromagnetic interlayer as well as other normal metal junctions (for example, SFNFS), proposed as elements of novel superconducting nanoelectronics, have limited applicability since such junctions have low resistance values [74,75]. This situation is resolved by addition of an insulating barrier (I) yielding a SFIFS layer sequence, which allows one to realize much larger values of the product $I_c R_n$, where I_c is the critical current of the junction and R_n its normal state resistance [36-38]. Recently, SIFS junctions attracted much attention and have been extensively studied both experimentally [32-41] and theoretically [23,45,76-80]. For instance, the current–voltage characteristics (CVC) of SIFS Josephson junctions with a strong insulating layer were studied in [45]. They exhibit interesting nonmonotonic behavior for weak ferromagnetic interlayers, i.e., small enough exchange fields. The reason for this behavior is the shape of the density of states in the F layer. At small exchange fields the decay length of superconducting correlations in the ferromagnetic material, ξ_h, is large enough, which leads to profound variations of the superconducting density of states in the F layer as a function of the energy and results in a corresponding CVC behavior. With an increase of the exchange field the ξ_h decreases, which suppresses the superconducting correlations in the F layer and makes the SIFS CVC similar to the I–V curve of the FIS junction.

In this paper we study the current–voltage characteristics of SFIFS Josephson junctions with two ferromagnetic interlayers. SFIFS structures were also proposed for various applications in memory elements [56-58], single-flux quantum circuits [47], and as injectors in superconductor–ferromagnetic transistors [81-84], which can be used as amplifiers for memory, digital, and RF applications. In this work we study the current–voltage characteristics of a SFIFS junction as shown below in Figure 1. We present a quantitative model of the quasiparticle current in SFIFS junctions for different sets of parameters characterizing the ferromagnetic interlayers. In case of weak ferromagnetic metals we find an anomalous nonmonotonic shape of the current–voltage characteristics at subgap voltages and compare the results with the CVC of SIFS junctions [45]. We ascribe this behavior to DOS energy dependencies in case of small exchange fields in the F layers. The shape is smeared if we include a finite magnetic scattering rate. The anomalous nonmonotonic shape of the current–voltage characteristics of SFIFS junctions with weak ferromagnetic layers looks similar to the fine structures of quasiparticle currents, recently obtained experimentally on similar systems [82-85].

The paper is organized as follows. In the first section ("Model") we formulate the theoretical model and basic equations and introduce the self-consistent numerical iterative method for calculating the density of states in S/F bilayers. In the next section ("Results and Discussion") we present and discuss the results for the density of states in S/F bilayers in case of subgap values of the exchange field and the current–voltage characteristics of SFIFS junctions. Finally we summarize the results in the last section ("Conclusion").

Model

In this section we present the theoretical model we use in our studies. The geometry of the considered system is depicted in Figure 1. It consists of two superconducting electrodes and a

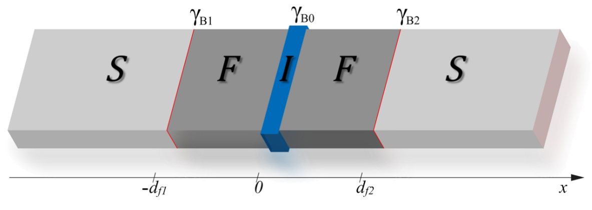

Figure 1: Schematic representation of the SFIFS hybrid structure (here S is a superconductor, F is a ferromagnetic metal and I is an insulating barrier). The thicknesses of the ferromagnetic interlayers are d_{f1} and d_{f2}, correspondingly. The transparency of the left S/F interface is characterized by the parameter γ_{B1}, while the transparency of the right F/S interface is characterized by the parameter γ_{B2}. Both parameters γ_{B1}, $\gamma_{B2} \ll 1$, which corresponds to transparent metallic interfaces. The insulating barrier between the left and right interfaces (I) is described by $\gamma_{B0} \gg 1$.

pair of ferromagnetic interlayers, with thicknesses $d_{\mathrm{f}1}$ and $d_{\mathrm{f}2}$. The system contains three interfaces: two S/F (superconductor/ferromagnet) boundaries and one tunnel F-I-F interface. Each of these interfaces is described by the dimensionless parameter $\gamma_{\mathrm{B}j} = R_{\mathrm{B}j}\sigma_n/\xi_n$ (j = 0, 1, 2), which is proportional to the resistance $R_{\mathrm{B}j}$ across the interface [86-88]. Here σ_n is the conductivity of the F layer and $\xi_n = \sqrt{D_{\mathrm{f}} / 2\pi T_{\mathrm{c}}}$ is the coherence length, where T_{c} is the critical temperature of the superconductor S (here and below we assume $\hbar = k_{\mathrm{B}} = 1$). In this paper we consider the diffusive limit, when the elastic scattering length ℓ is much smaller than the characteristic decay length of the real part of the pair wave function in the ferromagnet, $\xi_{\mathrm{f}1}$, which we introduce later in Equation 13 and Equation 14. We assume that the S/F interfaces are not magnetically active. We also neglect the nonequilibrium effects [89-91] and use the Matsubara Green's functions technique, which has been developed to describe many-body systems in equilibrium at finite temperature [92].

In our model the tunneling barrier is located between two F layers at $x = 0$ (Figure 1), whereas the other interfaces at $x = -d_{\mathrm{f}1}$ and $x = d_{\mathrm{f}2}$ are identical and transparent. This case corresponds to $\gamma_{\mathrm{B}1} = \gamma_{\mathrm{B}2} \ll 1$ and $\gamma_{\mathrm{B}0} \gg 1$. In case of a sufficiently strong tunnel barrier ($\gamma_{\mathrm{B}0} \gg 1$), the two S/F bilayers in the SFIFS junction are decoupled, i.e., the amplitudes of two-electron processes between left and right F layers are negligibly small. Hence, the quasiparticle current through the SFIFS junction, biased by the voltage eV, can be calculated by using the Werthamer formula [93],

$$I = \frac{1}{eR}\int_{-\infty}^{\infty} \mathrm{d}E\, N_{\mathrm{f}1}\left(E-eV\right)N_{\mathrm{f}2}\left(E\right)\left[f\left(E-eV\right)-f\left(E\right)\right], \quad (1)$$

where $N_{\mathrm{f}1,2}(E)$ are the densities of states (DOS) in the corresponding ferromagnetic layer at $x = 0$, $f(E)= [1 + e^{E/T}]^{-1}$ is the Fermi–Dirac distribution function, and $R = R_{\mathrm{B}0}$ is the resistance across the F-I-F interface. Both densities of states $N_{\mathrm{f}1,2}(E)$ are normalized to their values in the normal state.

In order to obtain the densities of states in ferromagnetic layers, $N_{\mathrm{f}1,2}(E)$, we use a self-consistent two-step iterative procedure, described below. As far as $\gamma_{\mathrm{B}0} \gg 1$, we can neglect the influence of the right F layer on the density of states in the left S/F bilayer and vice versa (see Figure 1). Thus we need to obtain the DOS at the outer border of each S/F bilayer. That can be done by solving the Usadel equations in the S/F bilayer system [94].

In the following, we use the θ-parameterizations of normal ($G = \cos\theta$) and anomalous ($F = \sin\theta$) Green's functions and write the Usadel equations in the F layers in the form [94,95],

$$\frac{D_{\mathrm{f}}}{2}\frac{\partial^2\theta_{\mathrm{f}\uparrow(\downarrow)}}{\partial x^2} = \left(\omega \pm ih + \frac{1}{\tau_z}\cos\theta_{f\uparrow(\downarrow)}\right)\sin\theta_{\mathrm{f}\uparrow(\downarrow)} + \frac{1}{\tau_x}\sin\left(\theta_{\mathrm{f}\uparrow}+\theta_{\mathrm{f}\downarrow}\right) \pm \frac{1}{\tau_{\mathrm{so}}}\sin\left(\theta_{\mathrm{f}\uparrow}-\theta_{\mathrm{f}\downarrow}\right), \quad (2)$$

where the positive and negative signs correspond to the spin-up (" ↑ ") and spin-down (" ↓ ") states, respectively. In terms of the electron fermionic operators $\psi_{\uparrow(\downarrow)}$ the spin-up state corresponds to the anomalous Green's function $F_{\uparrow} \sim \langle \psi_{\uparrow}\psi_{\downarrow} \rangle$, while spin-down state corresponds to $F_{\downarrow} \sim \langle \psi_{\downarrow}\psi_{\uparrow} \rangle$. The expressions $\omega = 2\pi T(n + 1/2)$ are the Matsubara frequencies, where $n = 0, \pm1, \pm2, \ldots$, and h is the exchange field in the ferromagnet. The scattering times are labeled here as τ_z, τ_x, and τ_{so}, where $\tau_{z(x)}$ corresponds to the magnetic scattering parallel (perpendicular) to the quantization axis, and τ_{so} is the spin–orbit scattering time [96-99].

Assuming a strong uniaxial anisotropy in ferromagnetic materials, in which case there is no coupling between spin-up and spin-down electron populations, we neglect τ_x ($\tau_x^{-1} \approx 0$). We also assume the ferromagnets to have a weak spin–orbit coupling and thus neglect the spin–orbit scattering time τ_{so}. After taking into account all the assumptions, the Usadel equations in the ferromagnetic layers for different spin states can be written as

$$\frac{D_{\mathrm{f}}}{2}\frac{\partial^2\theta_{\mathrm{f}\uparrow(\downarrow)}}{\partial x^2} = \left(\omega \pm ih + \frac{\cos\theta_{\mathrm{f}\uparrow(\downarrow)}}{\tau_{\mathrm{m}}}\right)\sin\theta_{\mathrm{f}\uparrow(\downarrow)}, \quad (3)$$

where $\tau_{\mathrm{m}} \equiv \tau_z$ is the magnetic scattering time. In the superconducting layer S the Usadel equation reads [94]

$$\frac{D_{\mathrm{s}}}{2}\frac{\partial^2\theta_{\mathrm{s}}}{\partial x^2} = \omega\sin\theta_{\mathrm{s}} - \Delta\left(c\right)\cos\theta_{\mathrm{s}}. \quad (4)$$

Here D_{s} is the diffusion coefficient in the S layer and $\Delta(x)$ is the pair potential in the superconductor. We note that $\Delta(x)$ vanishes in the F layer.

Equation 3 and Equation 4 must be supplemented with corresponding boundary conditions. At the S/F interfaces we apply the Kupriyanov–Lukichev boundary conditions. For example, at the left S/F interface they are written as [86],

$$\xi_n\gamma\left(\frac{\partial\theta_{\mathrm{f}}}{\partial x}\right)_{-d_{\mathrm{f}1}} = \xi_{\mathrm{s}}\left(\frac{\partial\theta_{\mathrm{s}}}{\partial x}\right)_{-d_{\mathrm{f}1}}, \quad (5)$$

$$\xi_n \gamma_{B1} \left(\frac{\partial \theta_f}{\partial x} \right)_{-d_{f1}} = \sin\left(\theta_s - \theta_f\right)_{-d_{f1}}. \qquad (6)$$

Similar equations can be written at the right S/F interface at $x = d_{f2}$. Here $\gamma = \xi_s \sigma_n / \xi_n \sigma_s$, where σ_s is the conductivity of the S layer and $\xi_s = \sqrt{D_s / 2\pi T_c}$ is the superconducting coherence length. The parameter γ defines the strength of the inverse proximity effect, i.e., the suppression of superconductivity in the adjacent S layer by the ferromagnetic layer F. We consider the parameter γ to be relatively small $\gamma \ll 1$, which corresponds to a rather weak suppression.

To calculate the density of states in the S/F bilayer we should set the boundary conditions at the outer boundary of the ferromagnet ($x = 0$),

$$\left(\frac{\partial \theta_f}{\partial x} \right)_0 = 0. \qquad (7)$$

To complete the boundary problem we also set a boundary condition at $x = \pm\infty$,

$$\theta_s\left(\pm\infty\right) = \arctan\left(\frac{\Delta}{\omega} \right), \qquad (8)$$

where the Green's functions acquire the well-known bulk BCS form. We notice that the density of states at $x = \pm\infty$ is given by standard BCS equation,

$$N_s\left(E\right) = \operatorname{Re}\left[\cos\theta_s\left(i\omega \to E + i0\right)\right] = \frac{|E|\Theta\left(|E| - \Delta\right)}{\sqrt{E^2 - \Delta^2}}, \qquad (9)$$

where $\Theta(x)$ is the Heaviside step function.

Finally the self-consistency equation for the superconducting order parameter takes the form,

$$\Delta\left(x\right)\ln\frac{T_c}{T} = \pi T \sum_{\omega>0} \left(\frac{2\Delta\left(x\right)}{\omega} - \sin\theta_{s\uparrow} - \sin\theta_{s\downarrow} \right) \qquad (10)$$

Equations Equation 3–Equation 8 and Equation 10 represent a closed set of equations that should be solved self-consistently.

The density of states $N_{f1,2}(E)$ normalized to the DOS in the normal state, can be written as

$$N_{fj}\left(E\right) = \frac{\left[N_{fj\uparrow}\left(E\right) + N_{fj\downarrow}\left(E\right)\right]}{2}, \quad j = 1,2, \qquad (11)$$

where $N_{fj\uparrow(\downarrow)}(E)$ are the spin-resolved densities of states written in terms of the spectral angle θ,

$$N_{fj\uparrow(\downarrow)}\left(E\right) = \operatorname{Re}\left[\cos\theta_{fj\uparrow(\downarrow)}\left(i\omega \to E + i0\right)\right], \quad j = 1,2. \quad (12)$$

To obtain $N_{f1,2}$, we use a self-consistent two-step iterative procedure [95,100-102]. In the first step we calculate the pair potential coordinate dependence $\Delta(x)$ using the self-consistency equation in the S layer (Equation 10). Then, by proceeding to the analytical continuation in Equation 3 and Equation 4 over the quasiparticle energy $i\omega \to E + i0$ and using the $\Delta(x)$ dependence obtained in the previous step, we find the Green's functions by repeating the iterations until convergency is reached.

The characteristic lengths of the decay and oscillations of the real part of the pair wave function in the ferromagnetic layer at the Fermi energy, $\xi_{f1,2}$, are given in our model by [45],

$$\frac{1}{\xi_{f1}} = \frac{1}{D_f}\sqrt{\sqrt{h^2 + \frac{1}{\tau_m^2}} + \frac{1}{\tau_m}}, \qquad (13)$$

$$\frac{1}{\xi_{f2}} = \frac{1}{D_f}\sqrt{\sqrt{h^2 + \frac{1}{\tau_m^2}} - \frac{1}{\tau_m}}. \qquad (14)$$

We see from these equations that with an increase of the magnetic scattering rate $\alpha_m = 1/\tau_m\Delta$ the length of decay ξ_{f1} decreases, while the length of oscillations ξ_{f2} increases. In the absence of magnetic scattering $\xi_{f1} = \xi_{f2} = \xi_h = \sqrt{D_f / h}$.

Results and Discussion

In this section we present the results of the DOS energy dependencies in SF bilayers at the free boundary of the F layer for $h \le \Delta$. The densities of states for $h \ge \Delta$ were thoroughly discussed in [45]. Then we calculate the corresponding CVC of the SFIFS junction using the Werthamer formula (Equation 1). In the case of $h \le \Delta$ we obtain an interesting nonmonotonic behavior of the quasiparticle current, presented in a subsection below ("Current–voltage characteristics of SFIFS junctions"). At large exchange fields the decay length ξ_{f2} of the real part of the pair wave function in the F layer becomes small (see Equation 13 and Equation 14), and the amplitude of DOS variations tends to zero. In this case the CVC of SFIFS junction tends to follow Ohm's law for $h \gg \Delta$. The ferromagnetic materials with small exchange fields can be fabricated as discussed in [103]. We also note that the DOS at the end of an SF bilayer in case of a domain wall in the ferromagnetic layer was studied in [104].

Density of states in SF bilayers for $h \leq \Delta$

Figure 2 and Figure 3 show the DOS energy dependencies for different values of $h \leq \Delta$ and for relatively thick F layers. In our calculations we fix the temperature at $T = 0.1T_c$, where T_c is the critical temperature of the superconductor S. In Figure 2 the characteristic "finger-like" shape of DOS is observed along with a minigap for $d_f = 2\xi_n$ (Figure 2a,c). At larger d_f and/or at larger h the minigap closes (Figure 2c and Figure 3a,c)]. In the absence of magnetic scattering ($\alpha_m = 1/\tau_m\Delta = 0$) we can roughly estimate the critical value h_c of the exchange field at which the minigap closes as [45]

$$h_c \sim E_{Th}, \quad E_{Th} = \frac{D_f}{d_f^2}, \tag{15}$$

where E_{Th} is the Thouless energy and d_f is the thickness of the F layer in the SF bilayer (d_{f1} or d_{f2} for the left or right SF bilayer, respectively, in Figure 1). Since we consider subgap values of h, the minigap closes at rather large values of d_f in the absence of magnetic scattering.

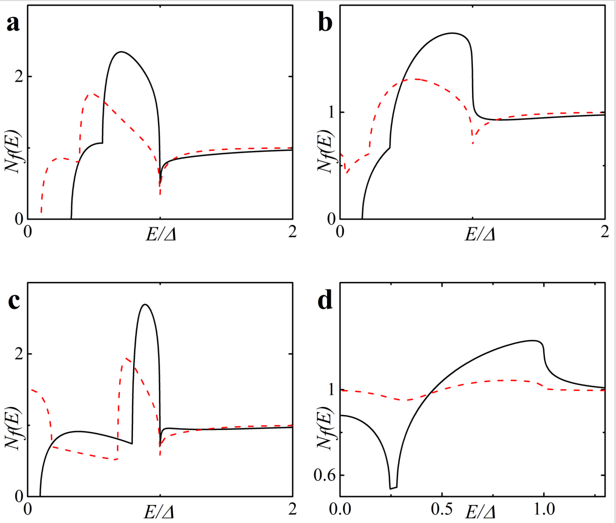

Figure 2: DOS $N_f(E)$ on the free boundary of the F layer in the FS bilayer obtained numerically for two cases: (a) in the absence of magnetic scattering, $\alpha_m = 1/\tau_m\Delta = 0$ (plots a and c) and in the case of finite magnetic scattering, i.e., plot b with $\alpha_m = 0.1$ and plot d with $\alpha_m = 0.5$. Parameters of the FS interface are $\gamma = \gamma_B = 0.01$, and $T = 0.1T_c$. Plots a, b: $h = 0.1\Delta$; plots c, d: $h = 0.3\Delta$. The black solid line corresponds to $d_f = 2\xi_n$, while the red dashed line corresponds to $d_f = 3\xi_n$.

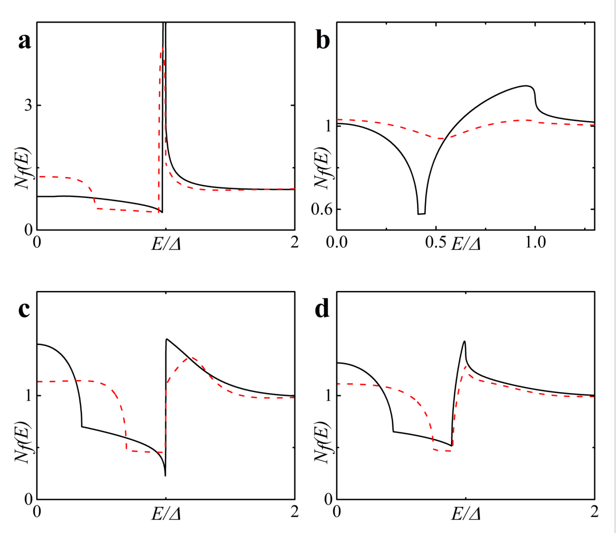

Figure 3: DOS $N_f(E)$ on the free boundary of the F layer in the FS bilayer obtained numerically in the absence of magnetic scattering, $\alpha_m = 1/\tau_m\Delta = 0$ (plots a and c) and in the case of finite magnetic scattering, i.e., plot b with $\alpha_m = 0.1$ and plot d with $\alpha_m = 0.5$. Plots a, b: $h = 0.5\Delta$; plots c, d: $h = 0.7\Delta$. The black solid line corresponds to $d_f = 2\xi_n$, while the red dashed line corresponds to $d_f = 3\xi_n$.

After the minigap closes the DOS at the Fermi energy $N_f(0)$ rapidly increases to values larger than unity with further increase of d_f and then it oscillates around unity while its absolute value exponentially approaches unity [45]. This is the well-known damped oscillatory behavior with the lengths of decay and oscillations given by Equation 13 and Equation 14, respectively. Figure 2b,d and Figure 3b,d show that stronger magnetic scattering leads to the minigap closing at smaller values of d_f. With the increase of $\alpha_m = 1/\tau_m\Delta$ the period of oscillations increases (ξ_{f2} in Equation 14 increases). At the same time the DOS variation amplitude becomes smaller and DOS features smear, since for larger α_m the dumped exponential decay of oscillations occurs faster (ξ_{f1} in Equation 13 decreases).

Finally, in Figure 4 we present plots for spin-resolved densities of states given by Equation 12 for both zero and finite magnetic scattering.

Current–voltage characteristics of SFIFS junctions

Using the densities of states $N_{f1,2}(E)$ obtained in the subsection above, we calculate a set of quasiparticle current curves using Equation 1 for various values of parameters describing properties of ferromagnetic material, which include the thicknesses of the F layers, d_{f1} and d_{f2}, the exchange field h, and the magnetic scattering rate α_m. In our calculations we fix the temperature at $T = 0.1T_c$, where T_c is the critical temperature of the superconducting lead.

Figure 5 shows the CVC of a symmetric SFIFS junction, where $d_{f1} = d_{f2} = d_f$ in the absence of magnetic scattering. For thin

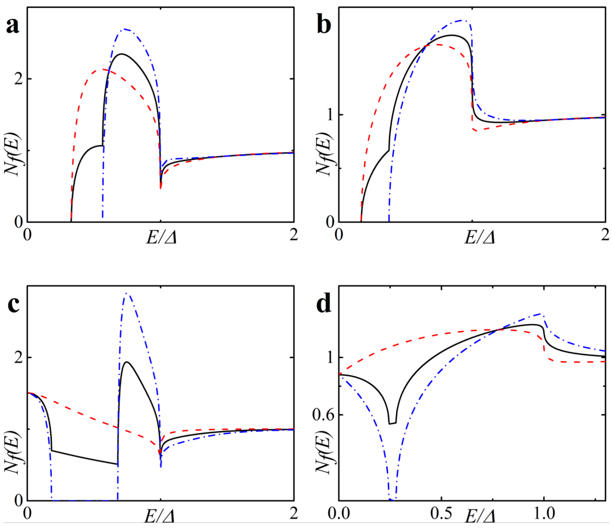

Figure 4: Spin-resolved DOS $N_{f\uparrow(\downarrow)}$ on the free boundary of the F layer in the FS bilayer obtained numerically in the absence of magnetic scattering, $\alpha_m = 0$ (plots a and c) and in the case of finite magnetic scattering, i.e., plot b with $\alpha_m = 0.1$ and plot d with $\alpha_m = 0.5$. Plots a, b: $h = 0.5\Delta$, $d_f = 2\xi_n$; plots c, d: $h = 0.3\Delta$, $d_f = 3\xi_n$ (c) and $d_f = 2\xi_n$ (d). The black solid line corresponds to $N_f(E)$, the red dashed line corresponds to $N_{f\uparrow}(E)$ and the blue dash-dotted line corresponds to $N_{f\downarrow}(E)$.

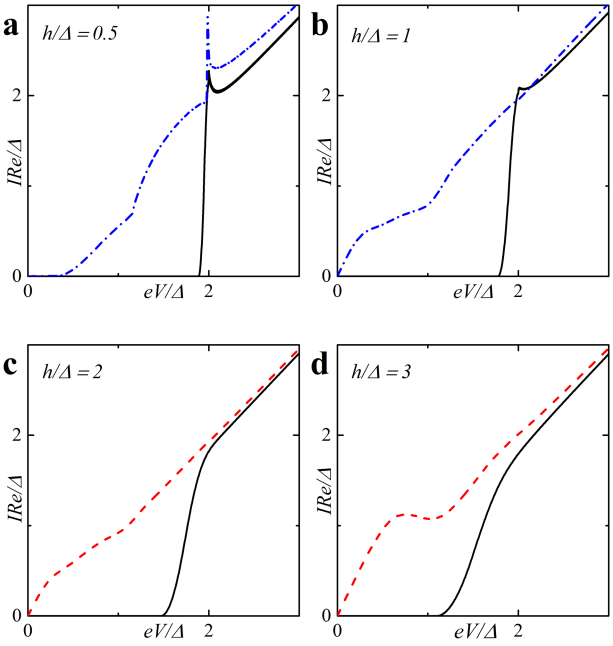

Figure 5: Current–voltage characteristics of the symmetric ($d_{f1} = d_{f2} = d_f$) SFIFS junction in the absence of magnetic scattering for different values of exchange field h. The temperature $T = 0.1T_c$. In each graph the curves were calculated for different values of F layer thickness d_f, $d_f = 0.5\xi_n$ (black solid line), $d_f = 1.0\xi_n$ (red dashed line), $d_f = 1.5\xi_n$ (blue dash-dotted line). The plots correspond to specific values of the exchange field h : plot (a) to $h = 0.5\Delta$, (b) to $h = 1.0\Delta$, (c) to $h = 2.0\Delta$ and (d) to $h = 3.0\Delta$.

enough ferromagnetic interlayers, $d_f/\xi_n = 0.5$, and a small enough value of the exchange field, $h = 0.5\Delta$, we observe CVC that resemble the I–V characteristic of a SNINS Josephson junction with a characteristic peak at $eV \approx 2\Delta$ (see Figure 5a, solid black line) [101]. With an increase of the exchange field h this peak becomes smeared (see Figure 5b–d, solid black line). Increasing d_f and/or h produces a set of I–V curves among which the red dashed line in Figure 5d is the most interesting because it exhibits a nonmonotonic behavior. The reason of this atypical nonmonotonic behavior will be explained later.

Figure 6 shows the current–voltage characteristics of SFIFS junctions at subgap values of the exchange field. We observe a nonmonotonic behavior for thick enough ferromagnetic layers at $h \leq \Delta$. Let us consider the CVC in Figure 6b, red dashed line. We can explain its behavior as well as any other nonmonotonic CVC behavior as the signature of the DOS energy dependence. The anomalous nonmonotonic $I(V)$ dependence arises from the shape features of the densities of states, see Figure 7. In symmetric SFIFS junctions, $N_{f1}(E) = N_{f2}(E) \equiv N_f(E)$ in Equation 1, which can be well approximated by taking $T = 0$ for small temperatures $T \ll T_c$. In this case the Fermi–Dirac distribution function $f(E)$ can be represented with the Heaviside step function $\Theta(-E)$ [and $f(E - eV)$ with $\Theta(eV - E)$]. As a result, the limits of integration in Equation 1 shrink to the interval $[0, eV]$.

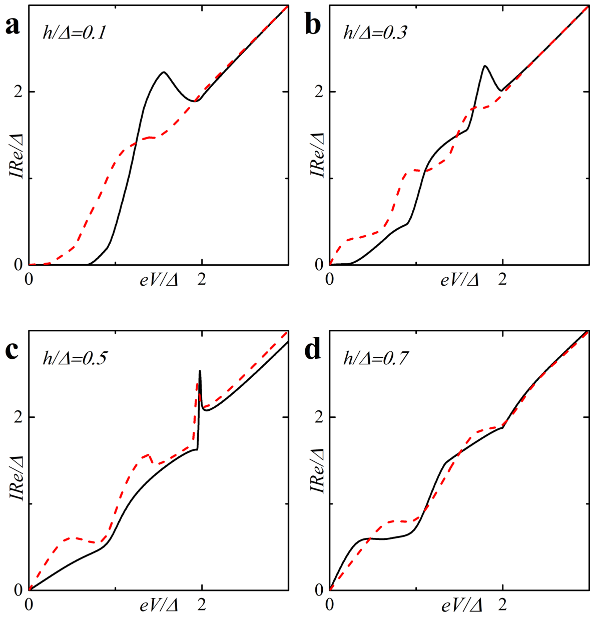

Figure 6: Current–voltage characteristics of a symmetric SFIFS junction for different values of the subgap exchange field h in the absence of magnetic scattering at a temperature $T = 0.1T_c$. In each graph the curves were calculated for different values of F layer thickness, d_f, $d_f = 2\xi_n$ (black solid line) and $d_f = 3\xi_n$ (red dashed line). The plots correspond to specific values of the subgap exchange field h: plot (a) to $h = 0.1\Delta$, (b) to $h = 0.3\Delta$, (c) to $h = 0.5\Delta$ and (d) to $h = 0.7\Delta$.

Hence, the current through the junction can be written as,

$$I = \frac{1}{eR}\int_{0}^{eV} \mathrm{d}E\, N_{\mathrm{f}}\left(E - eV\right) N_{\mathrm{f}}\left(E\right). \qquad (16)$$

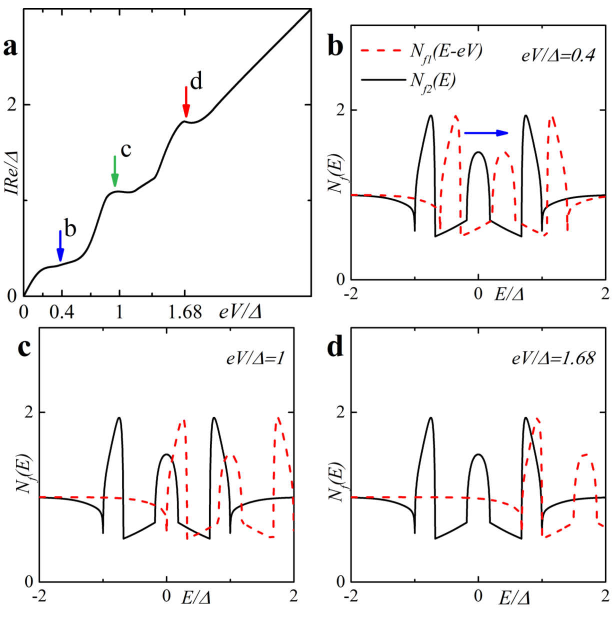

Figure 7: (a) CVC taken from Figure 6b, red dashed line, and visual explanation of the characteristic behavior of the quasiparticle current. (b–d) The DOS $N_f(E - eV)$ and $N_f(E)$ at particular values of eV revealing the origin of the current features in plot (a).

Using this expression, the origin of the nonmonotonic behavior of the CVC can be explained. At $eV = 0$ the upper limit of the integral in Equation 16 is zero and the current is zero. With the increase of the voltage, the current first increases linearly due to the broader region of integration as in Ohm's law. The first feature that is shown in Figure 7a is a significant change in the slope of the current. Figure 7b shows the relative positions of the densities of states $N_f(E - eV)$ and $N_f(E)$ in this case, where almost no peak overlap can be seen, resulting in relatively small values of the integral in Equation 16. As we proceed to larger values of eV, we reach the first local maximum of the CVC, which corresponds to a maximum overlap of the densities of states $N_f(E - eV)$ and $N_f(E)$ at $eV/\Delta \approx 1$ (see Figure 7c). The second maximum of the quasiparticle current occurs at $eV/\Delta \approx 1.68$, which corresponds to a perfect DOS peak overlap at $E/\Delta \approx 1$ Figure 7d). For large enough values of the voltage eV, a product of the DOS $N_f(E - eV)\, N_f(E) \approx 1$ and its integration does not produce any features. Thus, the CVC eventually coincides with Ohm's law in this case. In fact any shape of a SFIFS I–V curve can be explained and understood in this way. We note that in this paper we present the densities of states in SF bilayers only for subgap values of the exchange field. For $h \geq \Delta$ the DOS energy dependencies in SF bilayers can be found in [45].

Based on the properties of the density of states in FS bilayers we can see that even the tiny exchange field h can dramatically modify the current introducing anomalous nonmonotonic behavior in case of thick enough F layers (see Figure 5 and Figure 6). It is important to understand how the CVC of a SFIFS junction transforms as the exchange field h increases. In Figure 8 we demonstrate the plot of current–voltage characteristics calculated for a wide range of exchange field values h in the absence of magnetic scattering. From this plot it can be clearly seen that while for relatively small (subgap) values of the exchange field many interesting features appear in the structure of the current, at larger values of h these features are smeared and the CVC approaches Ohm's law. Figure 9 shows the current–voltage characteristics in the case of an asymmetric SFIFS junction, i.e., when $d_{f1} \neq d_{f2}$ in the scase of zero magnetic scattering.

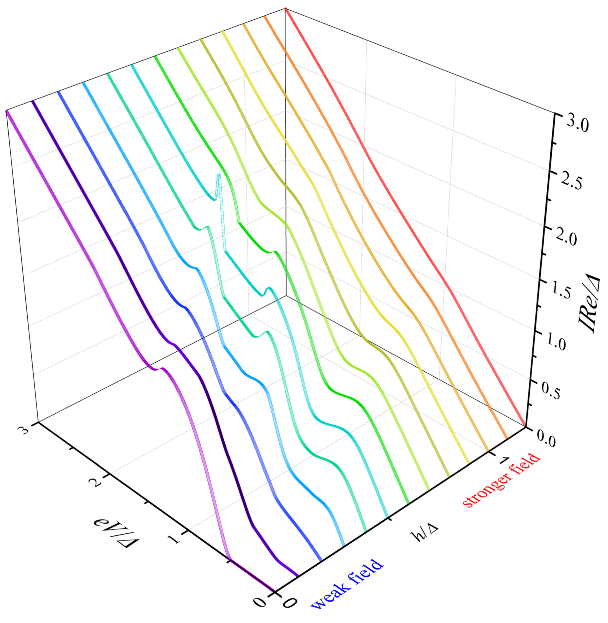

Figure 8: Current–voltage characteristics of a symmetric SFIFS junction in the absence of magnetic scattering for $d_f = 3\xi_n$. The temperature is $T = 0.1T_c$. The curves correspond to different values of h, from $h = 0$ to $h = 1.2\Delta$ with increments equal to 0.1Δ. The exchange field $h = 0$ corresponds to the case of a SNINS junction [101].

In this section we also present the current–voltage characteristics of a SFIFS junction calculated in the presence of magnetic scattering for different values of the subgap exchange field h. Figure 10 illustrates the CVC in case of a finite magnetic scattering rate $\alpha_m = 0.1$. We consider both symmetric and asymmetric SFIFS junctions. The insets show the CVC in case of zero magnetic scattering. For very small h nonzero magnetic scattering leads to smearing of characteristic features of the current as shown in Figure 10. At larger subgap values of the exchange field h we see a "triple kink" structure (Figure 10c). For large enough values of α_m the nonmonotonic behavior of the quasiparticle current will be smeared and the current approaches Ohm's law. This is due to the fact that increasing α_m the length of the superconducting correlations decay in the ferromagnetic layers decreases, see Equation 13, and the suppression of superconducting correlations in the F layers occurs faster.

We can compare these results with the I–V characteristics of SIFS Josephson junctions [45]. In this case at zero magnetic scattering we may also observe the nonmonotonic behavior, but with only one peak [see Ref. [45], Figure 6 (c)]. In case of finite magnetic scattering the CVC has a "double kink" structure [see Ref. [45], Figure 7 (a, c)]. In SFIFS junctions the overlap of subgap DOS structures $N_{f1}(E - eV)\, N_{f2}(E)$ in the integrand of the current equation, Equation 16, produce more complex behavior of the I–V characteristics.

We also notice that in recent experiments on SFIFS junctions as injectors of superconductor-ferromagnetic transistors some fine structures of the subgap quasiparticle current was observed [82-85], which looks similar to our theoretical results.

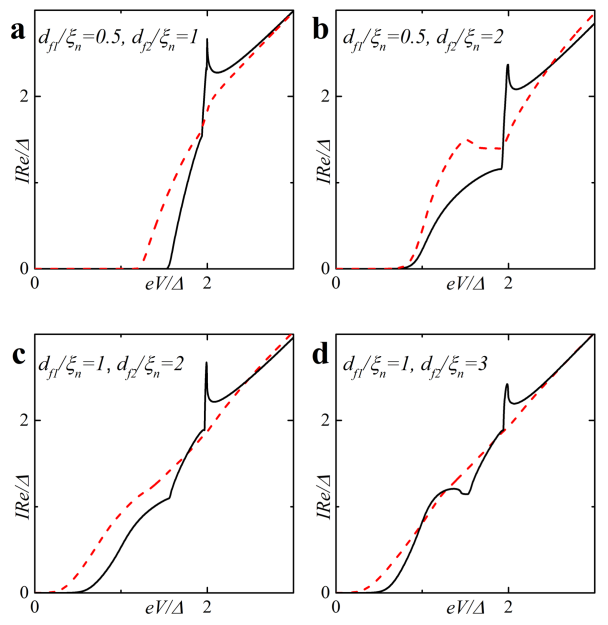

Figure 9: Current–voltage characteristics of an asymmetric ($d_{f1} \neq d_{f2}$) SFIFS junction for different values of F layer thicknesses d_{f1} and d_{f2} (indicated in the plot) in the absence of magnetic scattering. The temperature is $T = 0.1T_c$, $h = 0.5\Delta$ (black solid line) and $h = 1.0\Delta$ (red dashed line). The labels show the values of F layer thicknesses d_{f1} and d_{f2} for which the curves were calculated: plot (a) corresponds to $d_{f1} = 0.5\xi_n$ and $d_{f2} = 1.0\xi_n$, (b) to $d_{f1} = 0.5\xi_n$ and $d_{f2} = 2.0\xi_n$, (c) to $d_{f1} = 1.0\xi_n$ and $d_{f2}= 2.0\xi_n$ and (d) to $d_{f1} = 1.0\xi_n$ and $d_{f2} = 3.0\xi_n$.

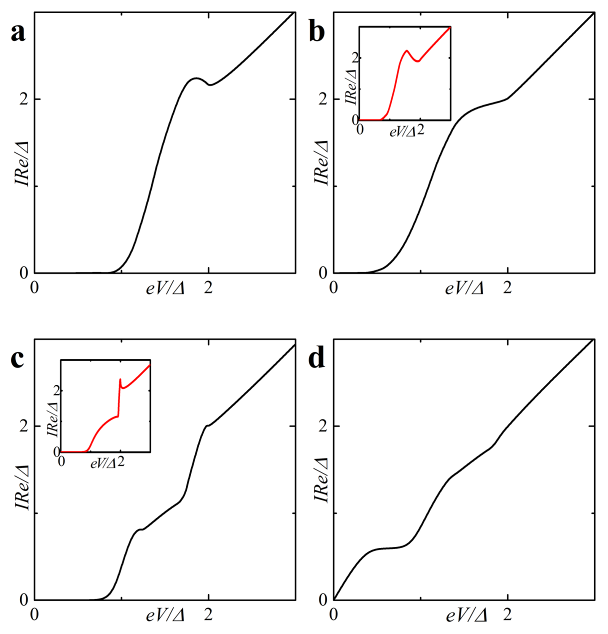

Figure 10: Current–voltage characteristics of a SFIFS junction in the presence of magnetic scattering ($\alpha_m = 0.1$). The temperature is $T = 0.1T_c$. In plot (a) the black solid line corresponds to $d_{f1} = 1\xi_n$, $d_{f2} = 2\xi_n$, in plots (b) and (d) to $d_{f1} = d_{f2} = 2\xi_n$, and finally in plot (c) the black line corresponds to $d_{f1} = 0.5\xi_n$, $d_{f2} = 2\xi_n$. Plots (a, b): $h = 0.1\Delta$; plot (c) and plot (d): $h = 0.5\Delta$ and $h = 0.7\Delta$, respectively. The insets show the CVC in case of zero magnetic scattering.

Conclusion

In this work we have presented the results of CVC calculations of a SFIFS junction for different set of parameters including the thicknesses of the ferromagnetic layers, d_{f1} and d_{f2}, the exchange field, and the magnetic scattering time $\alpha_m = 1/\tau_m\Delta$. We considered the case of a strong insulating barrier such that the left SF and the right FS bilayers are decoupled. In order to obtain the current–voltage characteristics we first calculated the densities of states on the free boundary of the F layer in each SF bilayer utilizing an iterative self-consistent approach. Using the numerically obtained DOS we have derived the quasiparticle current of a SFIFS junction in the case of symmetric ($d_{f1} = d_{f2}$) and asymmetric ($d_{f1} \neq d_{f2}$) structures. We have paid much attention to the case of a SFIFS junction with weak ferromagnetic interlayers with exchange fields $h \leq \Delta$. It was demonstrated that the CVC exhibits interesting and unusual features in this case, which can be ascribed to typical DOS behavior. We have provided a simple physical explanation for such anomalous CVC behavior. We have also illustrated how the CVC shape evolves as one increases the exchange field h. It should be emphasized that taking into account finite magnetic scattering leads to the smearing of characteristic features and, in particular cases, to a "triple kink" shape of the current.

Acknowledgements

The authors thank D. Beckmann for useful discussions. S.K. acknowledges the hospitality of the Quantum nanoelectronics laboratory of the Moscow Institute of Electronics and Mathematics in the National Research University Higher School of Economics during his stay in Moscow.

ORCID® iDs

Tairzhan Karabassov - https://orcid.org/0000-0001-7966-5221
Anastasia V. Guravova - https://orcid.org/0000-0002-1858-0483
Aleksei Yu. Kuzin - https://orcid.org/0000-0002-1147-9040
Elena A. Kazakova - https://orcid.org/0000-0002-9382-3799
Shiro Kawabata - https://orcid.org/0000-0003-2081-1110
Boris G. Lvov - https://orcid.org/0000-0001-6307-7724
Andrey S. Vasenko - https://orcid.org/0000-0002-2978-8650

Preprint

A non-peer-reviewed version of this article has been previously published as a preprint doi:10.3762/bxiv.2019.140.v1

References

1. Buzdin, A. I. *Rev. Mod. Phys.* **2005,** *77,* 935–976. doi:10.1103/revmodphys.77.935
2. Golubov, A. A.; Kupriyanov, M. Y.; Il'ichev, E. *Rev. Mod. Phys.* **2004,** *76,* 411–469. doi:10.1103/revmodphys.76.411
3. Bergeret, F. S.; Volkov, A. F.; Efetov, K. B. *Rev. Mod. Phys.* **2005,** *77,* 1321–1373. doi:10.1103/revmodphys.77.1321
4. Demler, E. A.; Arnold, G. B.; Beasley, M. R. *Phys. Rev. B* **1997,** *55,* 15174–15182. doi:10.1103/physrevb.55.15174
5. Ozaeta, A.; Vasenko, A. S.; Hekking, F. W. J.; Bergeret, F. S. *Phys. Rev. B* **2012,** *86,* 060509. doi:10.1103/physrevb.86.060509
6. Bergeret, F. S.; Tokatly, I. V. *Phys. Rev. Lett.* **2013,** *110,* 117003. doi:10.1103/physrevlett.110.117003
7. Bobkova, I. V.; Bobkov, A. M. *Phys. Rev. B* **2017,** *95,* 184518. doi:10.1103/physrevb.95.184518
8. Jiang, J. S.; Davidović, D.; Reich, D. H.; Chien, C. L. *Phys. Rev. Lett.* **1995,** *74,* 314–317. doi:10.1103/physrevlett.74.314
9. Izyumov, Y. A.; Proshin, Y. N.; Khusainov, M. G. *Phys.-Usp.* **2002,** *45,* 109–148. doi:10.1070/pu2002v045n02abeh001025
10. Fominov, Y. V.; Chtchelkatchev, N. M.; Golubov, A. A. *Phys. Rev. B* **2002,** *66,* 014507. doi:10.1103/physrevb.66.014507
11. Khaydukov, Y. N.; Vasenko, A. S.; Kravtsov, E. A.; Progliado, V. V.; Zhaketov, V. D.; Csik, A.; Nikitenko, Y. V.; Petrenko, A. V.; Keller, T.; Golubov, A. A.; Kupriyanov, M. Y.; Ustinov, V. V.; Aksenov, V. L.; Keimer, B. *Phys. Rev. B* **2018,** *97,* 144511. doi:10.1103/physrevb.97.144511
12. Karabassov, T.; Stolyarov, V. S.; Golubov, A. A.; Silkin, V. M.; Bayazitov, V. M.; Lvov, B. G.; Vasenko, A. S. *Phys. Rev. B* **2019,** *100,* 104502. doi:10.1103/physrevb.100.104502
13. Buzdin, A. I.; Bulaevskii, L. N.; Panyukov, S. V. *JETP Lett.* **1982,** *35,* 178.
14. Vdovichev, S. N.; Nozdrin, Y. N.; Pestov, E. E.; Yunin, P. A.; Samokhvalov, A. V. *JETP Lett.* **2016,** *104,* 329–333. doi:10.1134/s0021364016170148
15. Ryazanov, V. V.; Oboznov, V. A.; Rusanov, A. Y.; Veretennikov, A. V.; Golubov, A. A.; Aarts, J. *Phys. Rev. Lett.* **2001,** *86,* 2427–2430. doi:10.1103/physrevlett.86.2427
16. Ryazanov, V. V.; Oboznov, V. A.; Veretennikov, A. V.; Rusanov, A. Y. *Phys. Rev. B* **2001,** *65,* 020501. doi:10.1103/physrevb.65.020501
17. Blum, Y.; Tsukernik, A.; Karpovski, M.; Palevski, A. *Phys. Rev. Lett.* **2002,** *89,* 187004. doi:10.1103/physrevlett.89.187004
18. Sellier, H.; Baraduc, C.; Lefloch, F.; Calemczuk, R. *Phys. Rev. Lett.* **2004,** *92,* 257005. doi:10.1103/physrevlett.92.257005
19. Bauer, A.; Bentner, J.; Aprili, M.; Della Rocca, M. L.; Reinwald, M.; Wegscheider, W.; Strunk, C. *Phys. Rev. Lett.* **2004,** *92,* 217001. doi:10.1103/physrevlett.92.217001
20. Bell, C.; Loloee, R.; Burnell, G.; Blamire, M. G. *Phys. Rev. B* **2005,** *71,* 180501. doi:10.1103/physrevb.71.180501
21. Oboznov, V. A.; Bol'ginov, V. V.; Feofanov, A. K.; Ryazanov, V. V.; Buzdin, A. I. *Phys. Rev. Lett.* **2006,** *96,* 197003. doi:10.1103/physrevlett.96.197003
22. Shelukhin, V.; Tsukernik, A.; Karpovski, M.; Blum, Y.; Efetov, K. B.; Volkov, A. F.; Champel, T.; Eschrig, M.; Löfwander, T.; Schön, G.; Palevski, A. *Phys. Rev. B* **2006,** *73,* 174506. doi:10.1103/physrevb.73.174506
23. Vasenko, A. S.; Golubov, A. A.; Kupriyanov, M. Y.; Weides, M. *Phys. Rev. B* **2008,** *77,* 134507. doi:10.1103/physrevb.77.134507
24. Anwar, M. S.; Czeschka, F.; Hesselberth, M.; Porcu, M.; Aarts, J. *Phys. Rev. B* **2010,** *82,* 100501. doi:10.1103/physrevb.82.100501
25. Khaire, T. S.; Khasawneh, M. A.; Pratt, W. P.; Birge, N. O. *Phys. Rev. Lett.* **2010,** *104,* 137002. doi:10.1103/physrevlett.104.137002
26. Robinson, J. W. A.; Witt, J. D. S.; Blamire, M. G. *Science* **2010,** *329,* 59–61. doi:10.1126/science.1189246
27. Baker, T. E.; Richie-Halford, A.; Icreverzi, O. E.; Bill, A. *EPL* **2014,** *107,* 17001. doi:10.1209/0295-5075/107/17001
28. Alidoust, M.; Halterman, K. *Phys. Rev. B* **2014,** *89,* 195111. doi:10.1103/physrevb.89.195111
29. Loria, R.; Meneghini, C.; Torokhtii, K.; Tortora, L.; Pompeo, N.; Cirillo, C.; Attanasio, C.; Silva, E. *Phys. Rev. B* **2015,** *92,* 184106. doi:10.1103/physrevb.92.184106
30. Bakurskiy, S. V.; Filippov, V. I.; Ruzhickiy, V. I.; Klenov, N. V.; Soloviev, I. I.; Kupriyanov, M. Y.; Golubov, A. A. *Phys. Rev. B* **2017,** *95,* 094522. doi:10.1103/physrevb.95.094522
31. Yamashita, T.; Kawakami, A.; Terai, H. *Phys. Rev. Appl.* **2017,** *8,* 054028. doi:10.1103/physrevapplied.8.054028
32. Kontos, T.; Aprili, M.; Lesueur, J.; Genêt, F.; Stephanidis, B.; Boursier, R. *Phys. Rev. Lett.* **2002,** *89,* 137007. doi:10.1103/physrevlett.89.137007
33. Guichard, W.; Aprili, M.; Bourgeois, O.; Kontos, T.; Lesueur, J.; Gandit, P. *Phys. Rev. Lett.* **2003,** *90,* 167001. doi:10.1103/physrevlett.90.167001
34. Born, F.; Siegel, M.; Hollmann, E. K.; Braak, H.; Golubov, A. A.; Gusakova, D. Y.; Kupriyanov, M. Y. *Phys. Rev. B* **2006,** *74,* 140501. doi:10.1103/physrevb.74.140501
35. Pepe, G. P.; Latempa, R.; Parlato, L.; Ruotolo, A.; Ausanio, G.; Peluso, G.; Barone, A.; Golubov, A. A.; Fominov, Y. V.; Kupriyanov, M. Y. *Phys. Rev. B* **2006,** *73,* 054506. doi:10.1103/physrevb.73.054506
36. Weides, M.; Kemmler, M.; Goldobin, E.; Koelle, D.; Kleiner, R.; Kohlstedt, H.; Buzdin, A. *Appl. Phys. Lett.* **2006,** *89,* 122511. doi:10.1063/1.2356104
37. Weides, M.; Kemmler, M.; Kohlstedt, H.; Waser, R.; Koelle, D.; Kleiner, R.; Goldobin, E. *Phys. Rev. Lett.* **2006,** *97,* 247001. doi:10.1103/physrevlett.97.247001
38. Weides, M.; Schindler, C.; Kohlstedt, H. *J. Appl. Phys.* **2007,** *101,* 063902. doi:10.1063/1.2655487

39. Pfeiffer, J.; Kemmler, M.; Koelle, D.; Kleiner, R.; Goldobin, E.; Weides, M.; Feofanov, A. K.; Lisenfeld, J.; Ustinov, A. V. *Phys. Rev. B* **2008,** *77,* 214506. doi:10.1103/physrevb.77.214506
40. Bannykh, A. A.; Pfeiffer, J.; Stolyarov, V. S.; Batov, I. E.; Ryazanov, V. V.; Weides, M. *Phys. Rev. B* **2009,** *79,* 054501. doi:10.1103/physrevb.79.054501
41. Kemmler, M.; Weides, M.; Weiler, M.; Opel, M.; Goennenwein, S. T. B.; Vasenko, A. S.; Golubov, A. A.; Kohlstedt, H.; Koelle, D.; Kleiner, R.; Goldobin, E. *Phys. Rev. B* **2010,** *81,* 054522. doi:10.1103/physrevb.81.054522
42. Buzdin, A. *Phys. Rev. B* **2000,** *62,* 11377–11379. doi:10.1103/physrevb.62.11377
43. Kontos, T.; Aprili, M.; Lesueur, J.; Grison, X. *Phys. Rev. Lett.* **2001,** *86,* 304–307. doi:10.1103/physrevlett.86.304
44. Halterman, K.; Valls, O. T. *Phys. Rev. B* **2004,** *69,* 014517. doi:10.1103/physrevb.69.014517
45. Vasenko, A. S.; Kawabata, S.; Golubov, A. A.; Kupriyanov, M. Y.; Lacroix, C.; Bergeret, F. S.; Hekking, F. W. J. *Phys. Rev. B* **2011,** *84,* 024524. doi:10.1103/physrevb.84.024524
46. Hilgenkamp, H. *Supercond. Sci. Technol.* **2008,** *21,* 034011. doi:10.1088/0953-2048/21/3/034011
47. Shafranjuk, S.; Nevirkovets, I. P.; Mukhanov, O. A.; Ketterson, J. B. *Phys. Rev. Appl.* **2016,** *6,* 024018. doi:10.1103/physrevapplied.6.024018
48. Linder, J.; Robinson, J. W. A. *Nat. Phys.* **2015,** *11,* 307–315. doi:10.1038/nphys3242
49. Larkin, T. I.; Bolâginov, V. V.; Stolyarov, V. S.; Ryazanov, V. V.; Vernik, I. V.; Tolpygo, S. K.; Mukhanov, O. A. *Appl. Phys. Lett.* **2012,** *100,* 222601. doi:10.1063/1.4723576
50. Golovchanskiy, I. A.; Bol'ginov, V. V.; Stolyarov, V. S.; Abramov, N. N.; Ben Hamida, A.; Emelyanova, O. V.; Stolyarov, B. S.; Kupriyanov, M. Y.; Golubov, A. A.; Ryazanov, V. V. *Phys. Rev. B* **2016,** *94,* 214514. doi:10.1103/physrevb.94.214514
51. Bakurskiy, S. V.; Klenov, N. V.; Soloviev, I. I.; Kupriyanov, M. Y.; Golubov, A. A. *Appl. Phys. Lett.* **2016,** *108,* 042602. doi:10.1063/1.4940440
52. Soloviev, I. I.; Klenov, N. V.; Bakurskiy, S. V.; Kupriyanov, M. Y.; Gudkov, A. L.; Sidorenko, A. S. *Beilstein J. Nanotechnol.* **2017,** *8,* 2689–2710. doi:10.3762/bjnano.8.269
53. Caruso, R.; Massarotti, D.; Miano, A.; Bolginov, V. V.; Hamida, A. B.; Karelina, L. N.; Campagnano, G.; Vernik, I. V.; Tafuri, F.; Ryazanov, V. V.; Mukhanov, O. A.; Pepe, G. P. *IEEE Trans. Appl. Supercond.* **2018,** *28,* 1–6. doi:10.1109/tasc.2018.2836979
54. Nakatani, T.; Sasaki, T. T.; Li, S.; Sakuraba, Y.; Furubayashi, T.; Hono, K. *J. Appl. Phys.* **2018,** *124,* 223904. doi:10.1063/1.5063548
55. Bakurskiy, S. V.; Klenov, N. V.; Soloviev, I. I.; Pugach, N. G.; Kupriyanov, M. Y.; Golubov, A. A. *Appl. Phys. Lett.* **2018,** *113,* 082602. doi:10.1063/1.5045490
56. Nevirkovets, I. P.; Shafraniuk, S. E.; Mukhanov, O. A. *IEEE Trans. Appl. Supercond.* **2018,** *28,* 1–4. doi:10.1109/tasc.2018.2836938
57. Nevirkovets, I. P.; Mukhanov, O. A. *Phys. Rev. Appl.* **2018,** *10,* 034013. doi:10.1103/physrevapplied.10.034013
58. Shafraniuk, S. E.; Nevirkovets, I. P.; Mukhanov, O. A. *Phys. Rev. Appl.* **2019,** *11,* 064018. doi:10.1103/physrevapplied.11.064018
59. Tagirov, L. R. *Phys. Rev. Lett.* **1999,** *83,* 2058–2061. doi:10.1103/physrevlett.83.2058
60. Alidoust, M.; Halterman, K.; Valls, O. T. *Phys. Rev. B* **2015,** *92,* 014508. doi:10.1103/physrevb.92.014508
61. Halterman, K.; Alidoust, M. *Phys. Rev. B* **2016,** *94,* 064503. doi:10.1103/physrevb.94.064503
62. Halterman, K.; Alidoust, M. *Supercond. Sci. Technol.* **2016,** *29,* 055007. doi:10.1088/0953-2048/29/5/055007
63. Srivastava, A.; Olde Olthof, L. A. B.; Di Bernardo, A.; Komori, S.; Amado, M.; Palomares-Garcia, C.; Alidoust, M.; Halterman, K.; Blamire, M. G.; Robinson, J. W. A. *Phys. Rev. Appl.* **2017,** *8,* 044008. doi:10.1103/physrevapplied.8.044008
64. Halterman, K.; Alidoust, M. *Phys. Rev. B* **2018,** *98,* 134510. doi:10.1103/physrevb.98.134510
65. Alidoust, M.; Halterman, K. *Phys. Rev. B* **2018,** *97,* 064517. doi:10.1103/physrevb.97.064517
66. Baek, B.; Rippard, W. H.; Benz, S. P.; Russek, S. E.; Dresselhaus, P. D. *Nat. Commun.* **2014,** *5,* 3888. doi:10.1038/ncomms4888
67. Gingrich, E. C.; Niedzielski, B. M.; Glick, J. A.; Wang, Y.; Miller, D. L.; Loloee, R.; Pratt Jr, W. P.; Birge, N. O. *Nat. Phys.* **2016,** *12,* 564–567. doi:10.1038/nphys3681
68. Golovchanskiy, I. A.; Abramov, N. N.; Stolyarov, V. S.; Shchetinin, I. V.; Dzhumaev, P. S.; Averkin, A. S.; Kozlov, S. N.; Golubov, A. A.; Ryazanov, V. V.; Ustinov, A. V. *J. Appl. Phys.* **2018,** *123,* 173904. doi:10.1063/1.5025028
69. Feofanov, A. K.; Oboznov, V. A.; Bol'ginov, V. V.; Lisenfeld, J.; Poletto, S.; Ryazanov, V. V.; Rossolenko, A. N.; Khabipov, M.; Balashov, D.; Zorin, A. B.; Dmitriev, P. N.; Koshelets, V. P.; Ustinov, A. V. *Nat. Phys.* **2010,** *6,* 593–597. doi:10.1038/nphys1700
70. Soloviev, I. I.; Schegolev, A. E.; Klenov, N. V.; Bakurskiy, S. V.; Kupriyanov, M. Y.; Tereshonok, M. V.; Shadrin, A. V.; Stolyarov, V. S.; Golubov, A. A. *J. Appl. Phys.* **2018,** *124,* 152113. doi:10.1063/1.5042147
71. Ozaeta, A.; Vasenko, A. S.; Hekking, F. W. J.; Bergeret, F. S. *Phys. Rev. B* **2012,** *85,* 174518. doi:10.1103/physrevb.85.174518
72. Kawabata, S.; Ozaeta, A.; Vasenko, A. S.; Hekking, F. W. J.; Sebastián Bergeret, F. *Appl. Phys. Lett.* **2013,** *103,* 032602. doi:10.1063/1.4813599
73. Giazotto, F.; Solinas, P.; Braggio, A.; Bergeret, F. S. *Phys. Rev. Appl.* **2015,** *4,* 044016. doi:10.1103/physrevapplied.4.044016
74. Bell, C.; Burnell, G.; Leung, C. W.; Tarte, E. J.; Kang, D.-J.; Blamire, M. G. *Appl. Phys. Lett.* **2004,** *84,* 1153–1155. doi:10.1063/1.1646217
75. Tafuri, F., Ed. *Fundamentals and Frontiers of the Josephson Effect;* Springer Series in Materials Science; Springer International Publishing: Cham, Switzerland, 2019. doi:10.1007/978-3-030-20726-7
76. Buzdin, A. *Phys. Rev. Lett.* **2008,** *101,* 107005. doi:10.1103/physrevlett.101.107005
77. Pugach, N. G.; Goldobin, E.; Kleiner, R.; Koelle, D. *Phys. Rev. B* **2010,** *81,* 104513. doi:10.1103/physrevb.81.104513
78. Pugach, N. G.; Kupriyanov, M. Y.; Vedyayev, A. V.; Lacroix, C.; Goldobin, E.; Koelle, D.; Kleiner, R.; Sidorenko, A. S. *Phys. Rev. B* **2009,** *80,* 134516. doi:10.1103/physrevb.80.134516
79. Volkov, A. F.; Efetov, K. B. *Phys. Rev. Lett.* **2009,** *103,* 037003. doi:10.1103/physrevlett.103.037003
80. Mai, S.; Kandelaki, E.; Volkov, A. F.; Efetov, K. B. *Phys. Rev. B* **2011,** *84,* 144519. doi:10.1103/physrevb.84.144519
81. Nevirkovets, I. P.; Shafraniuk, S. E.; Chernyashevskyy, O.; Yohannes, D. T.; Mukhanov, O. A.; Ketterson, J. B. *IEEE Trans. Appl. Supercond.* **2016,** *26,* 1–7. doi:10.1109/tasc.2016.2624752

82. Nevirkovets, I. P.; Chernyashevskyy, O.; Prokopenko, G. V.; Mukhanov, O. A.; Ketterson, J. B. *IEEE Trans. Appl. Supercond.* **2014,** *24,* 1–6. doi:10.1109/tasc.2014.2318317
83. Nevirkovets, I. P.; Chernyashevskyy, O.; Prokopenko, G. V.; Mukhanov, O. A.; Ketterson, J. B. *IEEE Trans. Appl. Supercond.* **2015,** *25,* 1–5. doi:10.1109/tasc.2015.2390143
84. Nevirkovets, I. P.; Shafraniuk, S. E.; Chernyashevskyy, O.; Yohannes, D. T.; Mukhanov, O. A.; Ketterson, J. B. *IEEE Trans. Appl. Supercond.* **2017,** *27,* 1–4. doi:10.1109/tasc.2016.2637864
85. Vávra, O.; Soni, R.; Petraru, A.; Himmel, N.; Vávra, I.; Fabian, J.; Kohlstedt, H.; Strunk, C. *AIP Adv.* **2017,** *7,* 025008. doi:10.1063/1.4976822
86. Kuprianov, M. Y.; Lukichev, V. F. *JETP Lett.* **1988,** *67,* 1163.
87. Bezuglyi, E. V.; Vasenko, A. S.; Shumeiko, V. S.; Wendin, G. *Phys. Rev. B* **2005,** *72,* 014501. doi:10.1103/physrevb.72.014501
88. Bezuglyi, E. V.; Vasenko, A. S.; Bratus, E. N.; Shumeiko, V. S.; Wendin, G. *Phys. Rev. B* **2006,** *73,* 220506. doi:10.1103/physrevb.73.220506
89. Vasenko, A. S.; Hekking, F. W. J. *J. Low Temp. Phys.* **2009,** *154,* 221–232. doi:10.1007/s10909-009-9869-z
90. Arutyunov, K. Y.; Auraneva, H.-P.; Vasenko, A. S. *Phys. Rev. B* **2011,** *83,* 104509. doi:10.1103/physrevb.83.104509
91. Arutyunov, K. Y.; Chernyaev, S. A.; Karabassov, T.; Lvov, D. S.; Stolyarov, V. S.; Vasenko, A. S. *J. Phys.: Condens. Matter* **2018,** *30,* 343001. doi:10.1088/1361-648x/aad3ea
92. Belzig, W.; Wilhelm, F. K.; Bruder, C.; Schön, G.; Zaikin, A. D. *Superlattices Microstruct.* **1999,** *25,* 1251–1288. doi:10.1006/spmi.1999.0710
93. Werthamer, N. R. *Phys. Rev.* **1966,** *147,* 255–263. doi:10.1103/physrev.147.255
94. Usadel, K. D. *Phys. Rev. Lett.* **1970,** *25,* 507–509. doi:10.1103/physrevlett.25.507
95. Gusakova, D. Y.; Golubov, A. A.; Kupriyanov, M. Y.; Buzdin, A. *JETP Lett.* **2006,** *83,* 327–331. doi:10.1134/s0021364006080066
96. Abrikosov, A. A.; Gor'kov, L. P. *JETP Lett.* **1961,** *12,* 337.
97. Fauré, M.; Buzdin, A. I.; Golubov, A. A.; Kupriyanov, M. Y. *Phys. Rev. B* **2006,** *73,* 064505. doi:10.1103/physrevb.73.064505
98. Bergeret, F. S.; Volkov, A. F.; Efetov, K. B. *Phys. Rev. B* **2007,** *75,* 184510. doi:10.1103/physrevb.75.184510
99. Ivanov, D. A.; Fominov, Y. V.; Skvortsov, M. A.; Ostrovsky, P. M. *Phys. Rev. B* **2009,** *80,* 134501. doi:10.1103/physrevb.80.134501
100. Golubov, A. A.; Kupriyanov, M. Y.; Fominov, Y. V. *JETP Lett.* **2002,** *75,* 190–194. doi:10.1134/1.1475721
101. Golubov, A. A.; Kupriyanov, M. Y. *J. Low Temp. Phys.* **1988,** *70,* 83–130. doi:10.1007/bf00683247
102. Golubov, A. A.; Houwman, E. P.; Gijsbertsen, J. G.; Krasnov, V. M.; Flokstra, J.; Rogalla, H.; Kupriyanov, M. Y. *Phys. Rev. B* **1995,** *51,* 1073–1089. doi:10.1103/physrevb.51.1073
103. Vasenko, A. S.; Kawabata, S.; Ozaeta, A.; Golubov, A. A.; Stolyarov, V. S.; Bergeret, F. S.; Hekking, F. W. J. *J. Magn. Magn. Mater.* **2015,** *383,* 175–179. doi:10.1016/j.jmmm.2014.11.009
104. Bobkova, I. V.; Bobkov, A. M. *JETP Lett.* **2019,** *109,* 57–62. doi:10.1134/s0021364019010016

License and Terms

The definitive version of this article is the electronic one which can be found at:
doi:10.3762/bjnano.11.19

BEILSTEIN JOURNAL OF NANOTECHNOLOGY

High dynamic resistance elements based on a Josephson junction array

Konstantin Yu. Arutyunov*[1,2] and Janne S. Lehtinen[3,4]

Full Research Paper

Open Access

Address:
[1]National Research University Higher School of Economics, 101000, Moscow, Russia, [2]P.L. Kapitza Institute for Physical Problems RAS, Moscow, 119334, Russia, [3]VTT Technical Research Centre of Finland Ltd., 02150 Espoo, Finland and [4]Department of Physics, University of Jyvaskyla, PB 35, FI-40014 Jyvaskyla, Finland

Email:
Konstantin Yu. Arutyunov* - karutyunov@hse.ru

* Corresponding author

Keywords:
dynamic resistance; Josephson junction array; nanoelectronics; quantum phase slip; superconductivity; Ti nanowires

Beilstein J. Nanotechnol. **2020,** *11,* 417–420.
doi:10.3762/bjnano.11.32

Received: 08 November 2019
Accepted: 18 February 2020
Published: 03 March 2020

This article is part of the thematic issue "Functional nanostructures for electronics, spintronics and sensors".

Guest Editor: A. S. Sidorenko

Abstract

A chain of superconductor–insulator–superconductor junctions based on Al–AlO_x–Al nanostructures and fabricated using conventional lift-off lithography techniques was measured at ultra-low temperatures. At zero magnetic field, the low current bias dynamic resistance can reach values of $\approx 10^{11}$ Ω. It was demonstrated that the system can provide a decent quality current biasing circuit, enabling the observation of Coulomb blockade and Bloch oscillations in ultra-narrow Ti nanowires associated with the quantum phase-slip effect.

Introduction

The field of modern nanoelectronics is facing stagnation with respect to further miniaturization, deviating from Moore's law [1]. Typically, two main reason are quoted: severe heat dissipation per unit volume (surface), and various quantum phenomena that drive the operation of ultra-small devices and make them different from devices in the conventional (classical) regime. The radical solution to the first problem is to build the critical elements using superconductors. The basics of this approach were developed in the late 1980s, resulting in rapid single flux quantum (RSFQ) logic [2]. Since that time the concept has continued to develop. However, the corresponding systems so far have not developed into mass market commercial products, being limited solely to particular "cost-no-object" applications. Currently, the field of superconducting electronics is developing much faster mainly due to the understanding that (even taking into consideration the necessity of refrigeration) the energy consumption of next generation supercomputers can be as low as ≈10 MW, which is compared to values of ≈100 MW for conventional semiconductor complementary metal–oxide-semiconductor (CMOS) technology. In addition to heat dissipation, another issue is the speed of processing. It has been shown that the operational frequency of superconducting logic can be at least 100 times higher than for CMOS-based devices. It is universally accepted that the limiting factor for the speed of operation of various superconducting devices is the high-frequency impedance, e.g., originating from kinetic inductance. The effect should be taken into consideration for various cryoelectronic applications.

In addition to RSFQ computers which exploit classical 2-bit logic, during the last decades, there has been an increasing interest in quantum computing utilizing nonclassical approaches. There have been multiple suggestions regarding how to build quantum logic elements, such as quantum bits (qbits), including superconducting systems based on the Josephson effect. It has been shown that physics behind a Josephson junction (JJ) is dual to a quantum phase-slip junction (QPSJ) [3], whereby the corresponding QPSJ-based qbit operation has also been demonstrated [4]. At the same time, the quantum dynamics of a JJ (or a QPSJ) is strongly determined by the environment [5,6]. In particular, the utilization of devices based on quantum fluctuations of the macroscopic phase, φ, requires stabilization of the quantum conjugated quantity – charge q. The most straightforward approach is to use high-Ohmic on-chip current-biasing elements [7-10]. However, it was later understood that resistive dissipative elements inevitably act as a source of Johnson noise, leading to degradation of system performance [11].

Here we present an experimental study of a quasi-1D chain of JJs. A sufficient high-frequency impedance was demonstrated to study the QPS phenomena without the undesired impact of Johnson noise typically associated with dissipative elements [12]. The I–V dependence studied in [12] demonstrated clear and expected characteristics at low current, $I \rightarrow 0$: the so-called "Bloch nose" (back-bending of I–V), while at finite current values, the corresponding singularities were not so pronounced. The purpose of this paper is to provide an in-depth analysis of the I–V dependence of the same JJ chains used in the current-biasing elements in [12].

Experimental

Conventional lift-off electron-beam lithography followed by ultrahigh vacuum deposition of materials was used for the fabrication of the nanostructures. Hybrid QPSJ samples were made of Ti, Al and aluminum oxide [12]. The high-impedance JJs studied in this paper, similar to those from [12], were fabricated from superconducting thin film Al oxidized in situ to form tunnel barriers. Each sample consisted of 25 pairs of JJs connected in parallel where the area of each superconductor–insulator–superconductor (SIS) contact was about 100 × 100 nm (Figure 1). The samples were analyzed by scanning electron microscopy (SEM) (Figure 1) and atomic force microscopy (AFM).

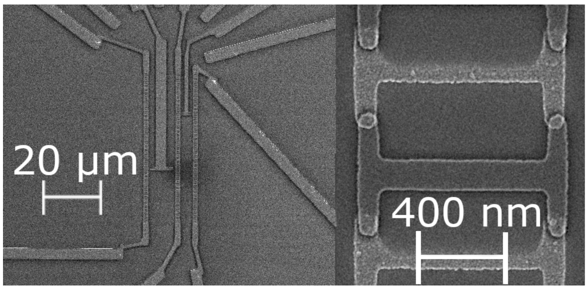

Figure 1: SEM images of the test sample fabricated from superconducting thin film aluminum oxidized in situ to form tunnel barriers. Left panel: overview of the structure. Right panel: details of the JJ element.

Transport measurements were made inside a ^{3}He^{4}He dilution refrigerator at temperatures below 400 mK, corresponding to the superconducting transition of Ti QPSJs [10,12]. All input/output lines were carefully filtered [13] to reduce the impact of the noisy electromagnetic environment. When necessary, a small magnetic field, up to 0.05 T, was applied using small superconducting coils wound directly on the sample holder cap.

Results and Discussion

The ultimate goal of this work is to study the quantum dynamics of the QPSJ, a system dual to JJ [3], including the observation of Coulomb blockade and Bloch oscillations [14]. Given that the macroscopic phase, φ, and the charge, q, are quantum conjugated values, $[\hat{\varphi},\hat{q}] = ih$, in order to enable the high rate of phase fluctuations, one should define the charge. The phase–charge duality in conventional JJ systems is well established [15-17]. Hence, to enable the phase fluctuation regime, the electric current, I, through a QPSJ, which is just the time derivative of charge, $I = \mathrm{d}q/\mathrm{d}t$, should be stabilized. The focus of this manuscript is to study the transport properties of JJ chains to be used as current-biasing elements of a QPSJ. Note that here the finite electric current is maintained by correlated Cooper pair tunneling at a voltage bias V across the QPSJ exceeding the particular Coulomb blockade threshold, V_C [14]. The tunneling happens at the Bloch oscillation rate, f_B. The synchronization of this "internal" periodic process with the external drive, f_RF, should result in quantized singularities (Bloch steps) at current values $I(n) = n(2e)f_\mathrm{RF}$, where $2e$ is the charge of the Cooper pair and n = 1,2,3... are integers. Furthermore, the study of QPSJ I–V characteristics demonstrating Coulomb blockade at zero current, $I = 0$, and voltages of $V < V_\mathrm{C}$ requires only the high-Ohmic environment with resistance R_env exceeding the quantum value $R_\mathrm{env} > R_\mathrm{Q} = h/e^2 \approx 26$ kΩ. While at finite current values, $I > 0$, one needs current stabilization at high frequency f_RF, which further requires high values of the high-frequency impedance, $Z_\mathrm{env}(f_\mathrm{RF})$. The observation of a pronounced

Coulomb blockade has been observed in JJs using both a high-resistive dissipative environment [7,8] and nonlinear Josephson elements with high dynamic resistance and/or kinetic inductance [6,18]. However, extended attempts to observe Bloch oscillation phenomena at finite currents in JJs provided rather modest results [7,8,19]. The recent progress in understanding the QPS phenomena [20] in ultra-narrow superconducting channels has revived interest in this topic, resulting in the observation of a decent Coulomb blockade [9,10], while quite blurred Bloch steps at finite current values have been detected so far [10]. Later it was understood that the straightforward approach of using a high-Ohmic dissipative environment, $R_{\mathrm{env}} > R_{\mathrm{Q}}$, is far from optimal, as it introduces Johnson noise, washing out the desired current singularities [11]. Various JJ-based systems were suggested which take advantage of the high kinetic inductance of superconducting quantum interference devices (SQUIDs) [21,22] ($L_{\mathrm{k}} = \cos^{-1}(\Phi/\Phi_0)$ at a degeneracy point when $\Phi/\Phi_0 \rightarrow \pi/2$, where Φ is the magnetic flux through the SQUID area and Φ_0 is the magnetic flux quantum, $\Phi_0 = h/2e = 2 \times 10^{-15}$ Wb). Hence the SQUID-based approach requires application of a finite magnetic field. Given that the electromagnetic horizon of our QPSJ is of the order of ≈100 µm [23-25], the corresponding high-impedance current biasing circuit should be of appropriate (small) dimensions. Thus the area of the SQUID is small, and hence a magnetic field corresponding to $\Phi/\Phi_0 \rightarrow \pi/2$ can easily reach the ≈10 mT range. At such a magnetic field, two undesirable effects might happen both with the biasing superconducting leads and with the QPSJ. Namely, the formation of Abrikosov vortices and a noticeable suppression of the energy gap. Consequently, in our approach, we opted for a non-dissipative (superconducting) high-impedance environment under zero magnetic field.

Our quasi-one-dimensional arrays of SIS junctions contain loops forming SQUIDs (Figure 1). The Josephson current is very small (Figure 2a), $I_{\mathrm{c}} < 10$ pA, and application of the magnetic field only monotonically suppresses the superconducting gap. The corresponding *I–V* dependence can be understood as a tunnel characteristic of multiple SIS junctions connected in series. The *I–V* characteristics (Figure 2a) with a gap of ≈10 mV corresponds well with 25 SIS junctions connected in series, each being a Al–AlO$_x$–Al junction with a gap of about 400 µV. The charging energy, $E_{\mathrm{c}} = \mathrm{e}^2/2\mathrm{C}$, of each SIS contact (considering it to be a plate capacitor with dielectric constant $\varepsilon \approx 10$, area 100 × 100 nm and distance between plates ≈2 nm) is about two orders of magnitude higher than the Josephson energy, $E_{\mathrm{J}} = I_{\mathrm{c}}/2\mathrm{e}$. As $E_{\mathrm{J}} << E_{\mathrm{c}}$ the physics of the system is dominated solely by charging phenomena. At zero magnetic field and small current bias, the dynamic resistance $R_{\mathrm{dyn}} \equiv \mathrm{d}V/\mathrm{d}I$ of the JJ chain can reach $\approx 10^{11}$ Ω (Figure 2b), while at a higher bias, R_{dyn} ($I >> 0$) approaches 100 kΩ.

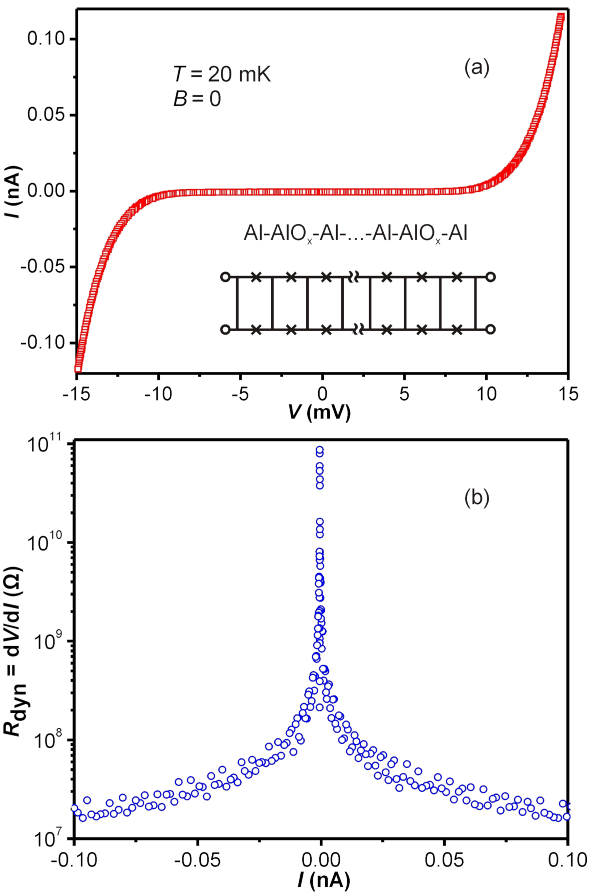

Figure 2: (a) Experimental *I–V* characteristics of 50 pairs of Al–AlO$_x$ junctions connected in series. Inset shows a schematic of the structure. (b) Dynamic resistance $R_{\mathrm{dyn}} \equiv \mathrm{d}V/\mathrm{d}I$ obtained by numeric differentiation of the *I–V* dependence.

The SIS junction chain has been used to current bias narrow Ti nanowires [12], with cross sections demonstrating various phenomena attributed to the QPS effect [10,26-33]. The observation of Coulomb blockade and Bloch steps [12] confirms the usefulness of the suggested concept, that is, the utilization of SIS junction chains.

Summarizing, we can conclude that chains of series-connected tunnel SIS junctions can provide high dynamic resistance at low current, which is necessary to stabilize the charge of a quantum circuit and hence enable the high level of phase fluctuations. The absence of dissipation makes such elements very useful for experimental studies of mesoscopic scale objects at ultralow temperature applications, where even a very small amount of Johnson noise may overheat electrons above the phonon bath. However, the non-linearity of a SIS junction *I–V* characteristic makes them less useful at finite current biases, which dramatically reduces the dynamic resistance. A promising solution might be the utilization of superconducting circuits with a high level of kinetic inductance capable to provide a sufficient impedance at high frequencies.

Funding

The article was prepared within the framework of the Academic Fund Program at the National Research University Higher School of Economics (HSE) in 2019–2020 (grant No. 19-01-050) and by the Russian Academic Excellence Project «5-100».

ORCID® iDs

Konstantin Yu. Arutyunov - https://orcid.org/0000-0001-9373-5185
Janne S. Lehtinen - https://orcid.org/0000-0002-5334-016X

Preprint

A non-peer-reviewed version of this article has been previously published as a preprint doi:10.3762/bxiv.2019.142.v1

References

1. Moore, G. *Electronics* **1965,** *38,* 1–4.
2. Likharev, K. K.; Semenov, V. K. *IEEE Trans. Appl. Supercond.* **1991,** *1,* 3–28. doi:10.1109/77.80745
3. Mooij, J. E.; Nazarov, Y. V. *Nat. Phys.* **2006,** *2,* 169–172. doi:10.1038/nphys234
4. Astafiev, O. V.; Ioffe, L. B.; Kafanov, S.; Pashkin, Y. A.; Arutyunov, K. Y.; Shahar, D.; Cohen, O.; Tsai, J. S. *Nature* **2012,** *484,* 355–358. doi:10.1038/nature10930
5. Schön, G.; Zaikin, A. D. *Phys. Rep.* **1990,** *198,* 237–412. doi:10.1016/0370-1573(90)90156-v
6. Watanabe, M.; Haviland, D. B. *Phys. Rev. Lett.* **2001,** *86,* 5120–5123. doi:10.1103/physrevlett.86.5120
7. Kuzmin, L. S.; Haviland, D. S. *Phys. Rev. Lett.* **1991,** *67,* 2890–2893. doi:10.1103/physrevlett.67.2890
8. Kuzmin, L. S.; Haviland, D. B. *Phys. Scr.* **1992,** *T42,* 171–176. doi:10.1088/0031-8949/1992/t42/029
9. Hongisto, T. T.; Zorin, A. B. *Phys. Rev. Lett.* **2012,** *108,* 097001. doi:10.1103/physrevlett.108.097001
10. Lehtinen, J. S.; Zakharov, K.; Arutyunov, K. Y. *Phys. Rev. Lett.* **2012,** *109,* 187001. doi:10.1103/physrevlett.109.187001
11. Webster, C. H.; Fenton, J. C.; Hongisto, T. T.; Giblin, S. P.; Zorin, A. B.; Warburton, P. A. *Phys. Rev. B* **2013,** *87,* 144510. doi:10.1103/physrevb.87.144510
12. Wang, Z. M.; Lehtinen, J. S.; Arutyunov, K. Y. *Appl. Phys. Lett.* **2019,** *114,* 242601. doi:10.1063/1.5092271
13. Zavyalov, V. V.; Chernyaev, S. A.; Shein, K. V.; Shukaleva, A. G.; Arutyunov, K. Y. *J. Phys.: Conf. Ser.* **2018,** *969,* 012086. doi:10.1088/1742-6596/969/1/012086
14. Averin, D. V.; Zorin, A. B.; Likharev, K. K. *Sov. Phys. - JETP* **1985,** *61,* 407–412.
15. Zaikin, A. D.; Panyukov, S. V. *Phys. Lett. A* **1987,** *120,* 306–311. doi:10.1016/0375-9601(87)90677-3
16. Averin, D. V.; Odintsov, A. A. *Phys. Lett. A* **1989,** *140,* 251–257. doi:10.1016/0375-9601(89)90934-1
17. Zaikin, A. D. *J. Low Temp. Phys.* **1990,** *80,* 223–235. doi:10.1007/bf00683632
18. Watanabe, M.; Haviland, D. B. *Phys. Rev. B* **2003,** *67,* 094505. doi:10.1103/physrevb.67.094505
19. Andersson, K. Coulomb blockade of Cooper pair tunneling in one dimensional Josephson junction arrays. Ph.D. Thesis, Department of Physics, Royal Institute of Technology, Stockholm, 2002.
20. Arutyunov, K. Y.; Golubev, D. S.; Zaikin, A. D. *Phys. Rep.* **2008,** *464,* 1–70. doi:10.1016/j.physrep.2008.04.009
21. Bell, M. T.; Sadovskyy, I. A.; Ioffe, L. B.; Kitaev, A. Y.; Gershenson, M. E. *Phys. Rev. Lett.* **2012,** *109,* 137003. doi:10.1103/physrevlett.109.137003
22. Masluk, N. A.; Pop, I. M.; Kamal, A.; Minev, Z. K.; Devoret, M. H. *Phys. Rev. Lett.* **2012,** *109,* 137002. doi:10.1103/physrevlett.109.137002
23. Ingold, G.-L.; Nazarov, Yu. V. Charge Tunneling Rates in Ultrasmall Junctions. In *Single Charge Tunneling;* Grabert, H.; Devoret, M. H., Eds.; NATO ASI Series (Series B: Physics), Vol. 294; Springer US: Boston, MA, U.S.A., 1992; pp 21–107. doi:10.1007/978-1-4757-2166-9_2
24. Wahlgren, P.; Delsing, P.; Haviland, D. B. *Phys. Rev. B* **1995,** *52,* R2293–R2296. doi:10.1103/physrevb.52.r2293
25. Wahlgren, P.; Delsing, P.; Claeson, T.; Haviland, D. B. *Phys. Rev. B* **1998,** *57,* 2375–2381. doi:10.1103/physrevb.57.2375
26. Lehtinen, J. S.; Sajavaara, T.; Arutyunov, K. Y.; Presnjakov, M. Y.; Vasiliev, A. L. *Phys. Rev. B* **2012,** *85,* 094508. doi:10.1103/physrevb.85.094508
27. Arutyunov, K. Y.; Hongisto, T. T.; Lehtinen, J. S.; Leino, L. I.; Vasiliev, A. L. *Sci. Rep.* **2012,** *2,* 293. doi:10.1038/srep00293
28. Lehtinen, J. S.; Arutyunov, K. Y. *Supercond. Sci. Technol.* **2012,** *25,* 124007. doi:10.1088/0953-2048/25/12/124007
29. Arutyunov, K. Y.; Lehtinen, J. S.; Rantala, T. *J. Supercond. Novel Magn.* **2016,** *29,* 569–572. doi:10.1007/s10948-015-3298-9
30. Arutyunov, K. Y.; Lehtinen, J. S. *Nanoscale Res. Lett.* **2016,** *11,* 364. doi:10.1186/s11671-016-1582-7
31. Arutyunov, K. Y.; Lehtinen, J. S. *Phys. C (Amsterdam, Neth.)* **2017,** *533,* 158–160. doi:10.1016/j.physc.2016.02.010
32. Arutyunov, K. Y.; Lehtinen, J. S.; Radkevich, A. A.; Semenov, A. G.; Zaikin, A. D. *J. Magn. Magn. Mater.* **2018,** *459,* 356–358. doi:10.1016/j.jmmm.2017.08.026
33. Elo, T.; Lähteenmäki, P.; Golubev, D.; Savin, A.; Arutyunov, K.; Hakonen, P. *J. Low Temp. Phys.* **2017,** *189,* 204–216. doi:10.1007/s10909-017-1802-2

License and Terms

The definitive version of this article is the electronic one which can be found at:
doi:10.3762/bjnano.11.32

BEILSTEIN JOURNAL OF NANOTECHNOLOGY

Epitaxial growth and superconducting properties of thin-film PdFe/VN and VN/PdFe bilayers on MgO(001) substrates

Wael M. Mohammed[1], Igor V. Yanilkin[1], Amir I. Gumarov[1], Airat G. Kiiamov[1],
Roman V. Yusupov*[1] and Lenar R. Tagirov[1,2]

Full Research Paper

Open Access

Address:
[1]Kazan Federal University, Kremlyovskaya str. 18, 420008 Kazan, Russia and [2]E. K. Zavoisky Physical-Technical Institute, FRC Kazan Scientific Centre of RAS, 420029 Kazan, Russia

Email:
Roman V. Yusupov* - Roman.Yusupov@kpfu.ru

* Corresponding author

Keywords:
epitaxial growth; epitaxial superconductor–ferromagnet heterostructure; palladium–iron alloy (PdFe); vanadium nitride (VN); superconducting spintronics

Beilstein J. Nanotechnol. **2020,** *11,* 807–813.
doi:10.3762/bjnano.11.65

Received: 29 February 2020
Accepted: 30 April 2020
Published: 15 May 2020

This article is part of the thematic issue "Functional nanostructures for electronics, spintronics and sensors".

Guest Editor: A. S. Sidorenko

Abstract

Single-layer vanadium nitride (VN) and bilayer $Pd_{0.96}Fe_{0.04}$/VN and VN/$Pd_{0.92}Fe_{0.08}$ thin-film heterostructures for possible spintronics applications were synthesized on (001)-oriented single-crystalline magnesium oxide (MgO) substrates utilizing a four-chamber ultrahigh vacuum deposition and analysis system. The VN layers were reactively magnetron sputtered from a metallic vanadium target in Ar/N_2 plasma, while the $Pd_{1-x}Fe_x$ layers were deposited by co-evaporation of metallic Pd and Fe pellets from calibrated effusion cells in a molecular beam epitaxy chamber. The VN stoichiometry and $Pd_{1-x}Fe_x$ composition were controlled by X-ray photoelectron spectroscopy. In situ low-energy electron diffraction and ex situ X-ray diffraction show that the 30 nm thick single-layer VN as well as the double-layer VN(30 nm)/$Pd_{0.92}Fe_{0.08}$(12 nm) and $Pd_{0.96}Fe_{0.04}$(20 nm)/VN(30 nm) structures have grown cube-on-cube epitaxially. Electric resistance measurements demonstrate a metallic-type temperature dependence for the VN film with a small residual resistivity of 9 μΩ·cm at 10 K, indicating high purity and structural quality of the film. The transition to the superconducting state was observed at 7.7 K for the VN film, at 7.2 K for the $Pd_{0.96}Fe_{0.04}$/VN structure and at 6.1 K for the VN/$Pd_{0.92}Fe_{0.08}$ structure with the critical temperature decreasing due to the proximity effect. Contrary to expectations, all transitions were very sharp with the width ranging from 25 mK for the VN film to 50 mK for the VN/$Pd_{0.92}Fe_{0.08}$ structure. We propose epitaxial single-crystalline thin films of VN and heteroepitaxial $Pd_{1-x}Fe_x$/VN and VN/$Pd_{1-x}Fe_x$ ($x \leq 0.08$) structures grown on MgO(001) as the materials of a choice for the improvement of superconducting magnetic random access memory characteristics.

Introduction

Since its invention, rapid single-flux quantum (RSFQ) logic [1,2] based on superconducting digital electronics has been seriously considered as an alternative to semiconductor electronics for supercomputing applications [3-5]. Merging it with magnetism [6-8] has given a birth to superconducting spintronics [9,10]. The latter concept was implemented in the US Cryogenic Computing Complexity (C3) Program [11-13] with the goal "to demonstrate a small-scale computer based on superconducting logic and cryogenic memory that is energy-efficient, scalable and able to solve interesting problems", opening prospects of reaching 100 PFLOPS/s with about 200 kW of electric power consumption including the cryogenic cooling. Niobium-based Josephson junction technology is currently implied to be used for the logics fabrication, however, hybrid Josephson junctions incorporating magnetic components are also considered for the mainframe computation components [9,14-19], and cache and main memories [8,20-25]. It is argued that the use of magnetic Josephson junctions in single-flux quantum electronics significantly reduces the number of junctions and interconnects in the circuits [26] and also has other important advantages such as wide operation margins and low bit-error rate [27]. The magnetic material has to be magnetically soft, tunable and weak in the sense of small spin-polarization of the conduction band [10,28]. The latter provides a large superconducting coherence length and hence bypasses a necessity to deposit flat, nanometer-thick continuous layers expected for strong elemental ferromagnets. A combination of niobium as a superconductor with a $Pd_{1-x}Fe_x$ alloy as a soft and weak ferromagnet was considered as material of choice for superconducting magnetic random access memories (MRAM) [8,29,30]. However, no further developments towards a prototype using a $Pd_{1-x}Fe_x$ alloy have been demonstrated. There are indications of non-homogeneous, nanoclustered magnetism in $Pd_{0.99}Fe_{0.01}$ films grown on niobium [31], which may cause a shortening of the spin-memory length [32] and a reduction of the Josephson critical current.

In general, the metallic Nb lattice (body-centered cubic with a_{Nb} = 329.4 pm) poorly matches that of the palladium-rich $Pd_{1-x}Fe_x$ alloys (face-centered cubic with a_0 = 389 pm). Therefore, a good crystallinity of the layer stack can hardly be expected. In the resulting polycrystalline films, crystallite boundaries and crystal lattice imperfections can lead to the segregation of iron impurities and to nanoclustering of the alloy. Following the development of a way to grow single-crystalline, magnetically homogeneous epitaxial $Pd_{1-x}Fe_x$ films on MgO(001) single-crystalline substrates [33], we propose fully epitaxial $Pd_{1-x}Fe_x$/VN and VN/$Pd_{1-x}Fe_x$ ($x \leq 0.08$) building blocks as an alternative choice for superconducting MRAM materials, in which vanadium nitride (VN) serves as the superconductor. The magnetic anisotropies of a 20 nm thick $Pd_{0.96}Fe_{0.04}$ film of the first-generation epitaxial sample of VN/$Pd_{0.96}Fe_{0.04}$ on MgO(001) were studied by using a ferromagnetic resonance technique in [34].

Results and Discussion

Sample preparation

Single-crystalline MgO(001) (henceforth designated MgO) epi-polished substrates (CRYSTAL GmbH, Germany) with a size of 10 × 5 × 0.5 mm^3 were annealed at 800 °C for 5 min in the ultrahigh vacuum (UHV) molecular beam epitaxy (MBE) chamber with a residual pressure below 10^{-10} mbar (SPECS, Germany). Then, depending on the desired structure, either the $Pd_{1-x}Fe_x$ alloy layer or the VN layer was deposited. The $Pd_{1-x}Fe_x$ layers were grown by means of UHV MBE following a three-step procedure described in detail in [33]. Metallic Pd (99.95% purity, EVOCHEM GmbH, Germany) and Fe (99.97% purity, ChemPur GmbH, Germany) were co-evaporated from the pre-calibrated high-temperature effusion cells to obtain the desired $Pd_{1-x}Fe_x$ composition.

Vanadium nitride layers were synthesized by using reactive DC magnetron sputtering (MS) in the UHV chamber with a base pressure of $p \leq 5 \times 10^{-10}$ mbar (BESTEC, Germany). During this process, the substrate had a temperature of 500 °C. A mixture of high-purity (99.9999%) argon (Ar) from a gas chromatography purification system and high-purity (99.9999%) nitrogen (N_2) at a composition of Ar/N_2 = 60:40 was used as plasma gas for the reactive synthesis of VN. During the deposition process, the pressure of the Ar/N_2 gas mixture in the chamber was automatically kept at 6×10^{-3} mbar. A metallic vanadium disk of 99.95% purity (GIRMET Ltd, Russia) was used as a target. The magnetron power was 50 W, the distance between the target and the substrate was 20 cm, and the deposition rate was 0.2 nm/min.

To grow heterostructures, the samples on the molybdenum holder were moved without breaking vacuum via the UHV transfer line between the MBE and MS deposition chambers as well as the analysis chamber (SPECS, Germany).

To perform a comparative study allowing to see only the proximity effect of the ferromagnetic layer on the properties of the superconducting VN layer, the latter was deposited in one run for all studied samples. To do this, we mounted two 10 × 5 × 0.5 mm^3 MgO substrates close and parallel to each other on the sample holder and used a system of two orthogonal shutters in the MBE chamber. After depositing a 20 nm thick $Pd_{0.96}Fe_{0.04}$ layer onto one substrate (with the second being blocked by the shutter), the sample holder was moved to the magnetron chamber, and a 30 nm layer of VN was grown on both substrates. Then, the holder was moved back to the MBE chamber, and a 12 nm thick $Pd_{0.92}Fe_{0.08}$ layer was deposited to a half of both samples using the second shutter. The thicknesses of the $Pd_{1-x}Fe_x$ layers were adjusted to possess identical magnetic moments. In situ tests of crystallinity, VN stoichiometry and resulting composition of $Pd_{1-x}Fe_x$ were taken at each deposition step using low-energy electron diffraction (LEED) and X-ray photoelectron spectroscopy (XPS). Finally, all structures were capped with 10 nm layer of undoped Si by magnetron sputtering to prevent sample deterioration. Thus, a VN film and stacks of $Pd_{0.96}Fe_{0.04}$/VN and VN/$Pd_{0.92}Fe_{0.08}$ (the first component in a stack being directly deposited to MgO) have been obtained with the identical properties of the VN layer in each sample.

Crystallinity and epitaxial growth

The crystallinity and the epitaxial growth of the thin films were examined in situ by using LEED (SPECS, Germany). LEED images were taken of the pristine MgO(001) substrate after annealing (Figure 1a), after the deposition of VN(30 nm) on MgO (Figure 1b), after the deposition of $Pd_{0.92}Fe_{0.08}$ on VN (Figure 1c) and after the deposition of VN on $Pd_{0.96}Fe_{0.04}$ (Figure 1d). Figure 1b indicates that the individual VN thin film has grown cube-on-cube epitaxially (for an individual $Pd_{1-x}Fe_x$ film see the full crystallinity analysis in [33]). Figure 1c,d shows that the $Pd_{0.96}Fe_{0.04}$/VN and VN/$Pd_{0.92}Fe_{0.08}$ heterostructures are pass-through epitaxial. This is, first of all, due to the good lattice match between MgO, VN and Pd: a_{MgO} = 421.2 pm, a_{VN} = 413.7 pm [35] and a_{Pd} = 389.1 pm. Thus, the lattice mismatch between MgO and VN is only about 1.7%, and between Pd and VN it is as small as 5.95%.

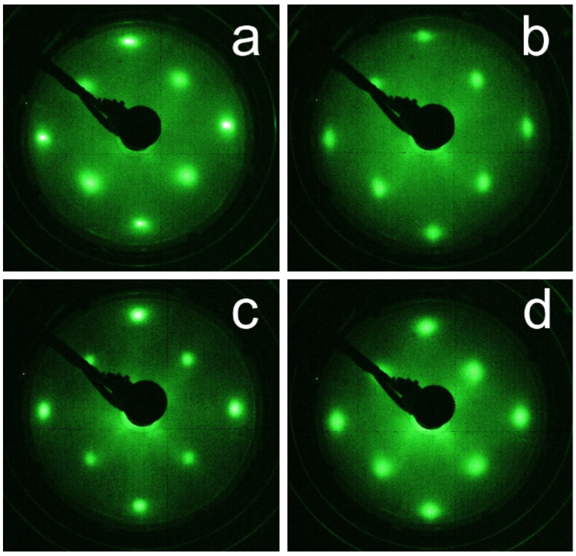

Figure 1: LEED patterns of (a) pristine MgO annealed at 800 °C, (b) the VN film, (c) the VN/$Pd_{0.92}Fe_{0.08}$ and (d) $Pd_{0.96}Fe_{0.04}$/VN structures on the MgO(001) substrate. All patterns were taken at an electron energy of 140 eV.

The in situ LEED analysis was corroborated with ex situ X-ray diffraction (XRD, BRUKER D8, Germany) measurements using Cu Kα (λ = 1.5418 Å) radiation in the Bragg–Brentano geometry with a scanning rate of 0.002°/s in the 2θ range from 17° to 82° and a step width of 0.0153°. Room-temperature XRD patterns of the pristine MgO(001) substrate, the VN thin film on MgO, $Pd_{0.96}Fe_{0.04}$ on MgO and the $Pd_{0.96}Fe_{0.04}$/VN heterostructure are shown in Figure 2. The θ–2θ scans clearly indicate the single-crystalline structure of the VN and $Pd_{0.96}Fe_{0.04}$ thin films and of the $Pd_{0.96}Fe_{0.04}$/VN heterostructures. The (002) reflex of the MgO substrate, the (002) reflex of the VN film (30 nm), and the (002) reflex of the $Pd_{0.96}Fe_{0.04}$ (20 nm) film can be easily identified.

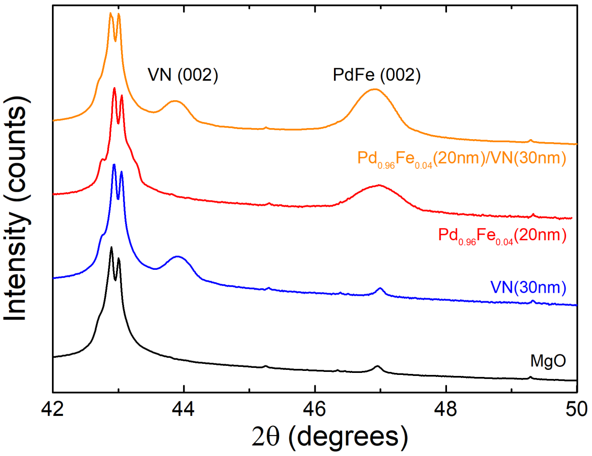

Figure 2: XRD patterns of pristine MgO substrate, VN, $Pd_{0.96}Fe_{0.04}$ (prepared in a separate deposition experiment) and $Pd_{0.96}Fe_{0.04}$/VN.

The significant peak broadening of the diffraction maxima of VN and $Pd_{0.96}Fe_{0.04}$ is primarily due to small coherent scattering range τ along the normal to the film plane (Scherrer broadening); XRD data with accounting for the instrument function [33] yields estimates of $\tau \approx 22.0$ nm for $Pd_{0.96}Fe_{0.04}$, $\tau \approx 12.6$ nm for $Pd_{0.92}Fe_{0.08}$ and $\tau \approx 30.4$ nm for VN, which agree quantitatively with the film thickness values $d(Pd_{0.96}Fe_{0.04}) \approx 21.5$ nm, $d(Pd_{0.92}Fe_{0.08}) \approx 12.5$ nm and $d(VN) \approx 29.8$ nm, respectively, measured ex situ with a BRUKER DektakXT stylus profiler by using the shadow mask method. Thus, LEED and XRD measurements confirm that the VN thin film and the $Pd_{0.96}Fe_{0.04}$/VN and VN/$Pd_{0.92}Fe_{0.08}$ heterostructures have grown cube-on-cube epitaxially and that all samples are single crystalline.

Stoichiometry and chemical composition

The stoichiometry and chemical composition of the VN and the $Pd_{1-x}Fe_x$ layers were analyzed in situ using XPS. The measurements were carried out in the UHV analysis chamber (base pressure $p < 3 \times 10^{-10}$ mbar) equipped with a Mg Kα X-ray source operated at 12.5 kV and 250 W, and a Phoibos-150 hemispherical energy analyzer (all from SPECS, Germany). Figure 3a,b shows the XPS spectra of the as-deposited VN/$Pd_{0.92}Fe_{0.08}$ thin film heterostructure. The binding energies of the Fe $2p_{1/2}$, Fe $2p_{3/2}$, and Pd $3d_{3/2}$ and Pd $3d_{5/2}$ states are 721.0, 707.7, and 340.2 and 335.0 eV, respectively, which agrees well with literature data [33,36].

Figure 3c,d shows the XPS spectra of the VN thin film on MgO. The binding energies of the V $2p_{1/2}$, V $2p_{3/2}$ and N 1s states are 521.1, 513.6 and 397.4 eV, respectively, which are very close to that given in the literature for crystalline VN [37,38]. The presence of a characteristic satellite at a binding energy of ca. 515 eV is a fingerprint of V in a nitride compound [37]. The chemical composition of the as-grown VN and $Pd_{1-x}Fe_x$ layers was analyzed with the CasaXPS software [39]. According to the XPS data, the stoichiometry of synthesized layers was Pd/Fe = 96:4, V/N = 52.5:47.5 and Pd/Fe = 92:8, respectively, with an accuracy of ±0.5%. Neither impurities nor surface contaminations were detected (compare with [40]). All recorded high-resolution XPS spectra of VN and $Pd_{1-x}Fe_x$ films were calibrated to the binding energies of crystalline VN at 513.6 eV and of metallic Pd at 335.0 eV [33,37], respectively.

Magnetic moment measurements shown in Figure 4 confirm the composition of $Pd_{0.96}Fe_{0.04}$ and $Pd_{0.92}Fe_{0.08}$ through the ferromagnetic transition temperature $T_C \approx 125$ K and $T_C \approx 240$ K, respectively [41].

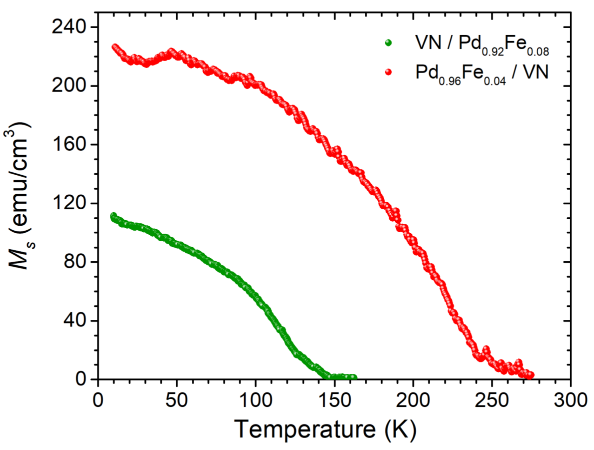

Figure 4: Saturation magnetization $M_s(T)$ as a function of the temperature of the $Pd_{0.96}Fe_{0.04}$/VN (green symbols) and VN/$Pd_{0.92}Fe_{0.08}$ (red symbols) heterostructures measured in a magnetic field of 200 Oe.

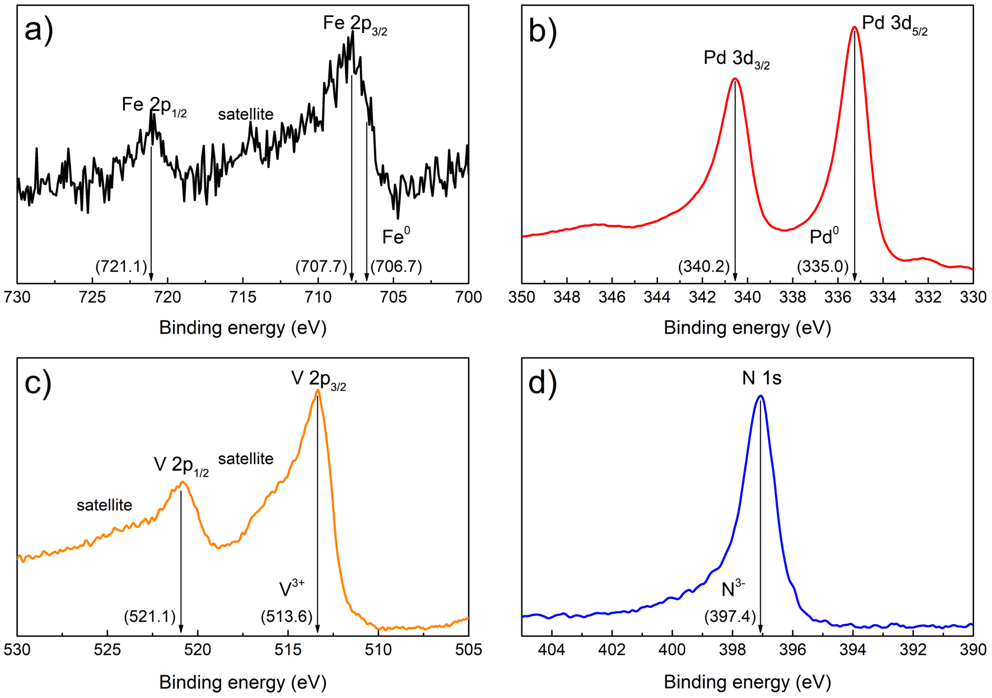

Figure 3: In situ XPS spectra of (a) Fe and (b) Pd of the VN/$Pd_{0.92}Fe_{0.08}$ sample, and of (c) V and (d) N of the VN film.

Temperature dependence of resistance and superconducting transition

A physical property measurement system (QUANTUM DESIGN PPMS-9, USA) was used for studying the temperature dependence of the electrical resistance of the VN thin films and $Pd_{0.96}Fe_{0.04}$/VN and VN/$Pd_{0.92}Fe_{0.08}$ heterostructures in the temperature range of 4.2–300 K. A four-probe resistance measurement scheme was used. Figure 5 shows the measurement results as a function of the temperature for the epitaxial VN film and the heteroepitaxial $Pd_{0.96}Fe_{0.04}$/VN and VN/$Pd_{0.92}Fe_{0.08}$ samples. Table 1 contains the data on the residual resistance ratio RRR (i.e., the ratio of room temperature resistance, R_{300K}, to the resistance at 10 K, R_{10K}), the superconducting transition temperature (mid-transition criterion) and the width of the superconducting transition (10–90% criterion) for the VN thin film and the heterostructures with $Pd_{1-x}Fe_x$.

Table 1: Electrical and superconducting properties of the VN film and the $Pd_{0.96}Fe_{0.04}$/VN and VN/$Pd_{0.92}Fe_{0.08}$ heteroepitaxial structures on MgO(001).

structure	RRR	T_c (K)	ΔT_c (mK)
VN(30 nm)	5.2	7.7	25
$Pd_{0.96}Fe_{0.04}$(20 nm)/VN(30 nm)	3.5	7.2	37
VN(30 nm)/$Pd_{0.92}Fe_{0.08}$(12 nm)	2.6	6.1	50

The temperature dependence of the resistance of the VN thin film is of metallic type and exhibits two temperature intervals, one above 250 K and another one in the range of 80–180 K, of quasi-linear temperature dependence with different temperature coefficients of resistivity (TCR), i.e., 9.7×10^{-3} Ω/K and 2.1×10^{-2} Ω/K, respectively, marked by red straight lines over the green line in Figure 5a. It is similar to the $R(T)$ behavior of VN/MgO(011) samples in [42], which was explained by a change in the electron/phonon scattering amplitude upon the structural phase transition from cubic to tetragonal at T_s = 250 K. Below 50 K the $R(T)$ dependence saturates approaching the residual resistance originating, in general, from impurities and imperfections. Further cooling results in the phase transition to the superconducting state as it is shown in Figure 5b. The RRR value of 5.2 and the room-temperature resistivity of 42.5 μΩ·cm for the 30 nm thick VN film are among the best values obtained to date [42-45], indicating the high purity and structural quality of our VN film.

The superconducting transition temperature T_c of the VN film is 7.7 K (see Table 1), which is well above the temperature of liquid helium, LHeT = 4.2 K. Figure 5b shows a very sharp resistive transition at T = 7.7 K with a small width of 25 mK, which is quite remarkable compared to an elemental niobium film of the same (30 nm) thickness deposited in the same chamber and under vacuum conditions (ΔT_c [Nb(30 nm)]) = 10–23 mK).

Combining the VN film into a heterostructure with a palladium-rich $Pd_{1-x}Fe_x$ alloy leads to a lowering of T_c because of the proximity effect [28]. This may shift the material operation temperature close to or even below the LHeT. With the iron content x in $Pd_{1-x}Fe_x$ alloy below 0.08 its magnetic properties meet all the requirements for the F-layer in superconducting spintronic S/F/S-type structures, i.e., it is a weak ferromagnet with a low coercive field [41]. It is important that magnetic properties of epitaxial $Pd_{1-x}Fe_x$ films are precisely controlled with the iron content x [41], and a perfect cube-on-cube epitaxy is realized with either the MgO(001) substrate or with the supercon-

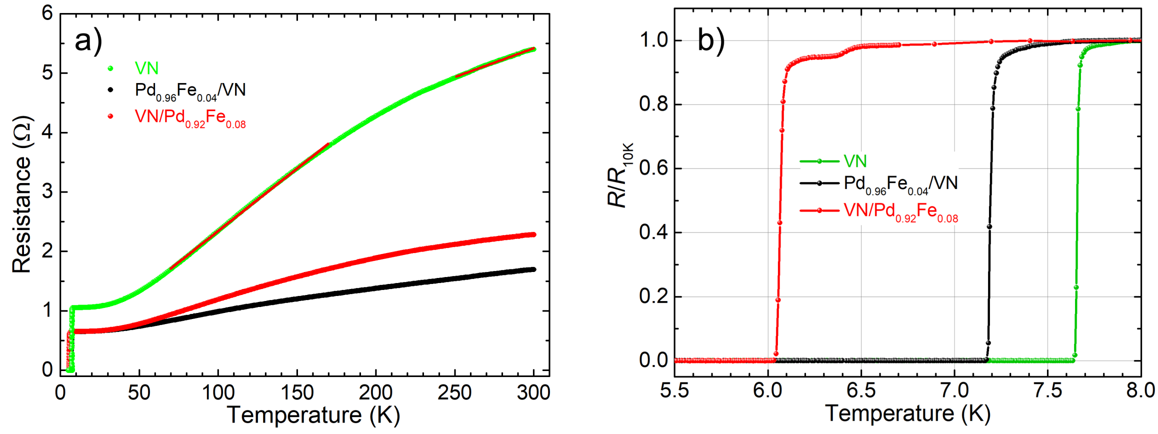

Figure 5: Temperature dependence of the electrical resistance of the VN film and the $Pd_{0.96}Fe_{0.04}$/VN and VN/$Pd_{0.92}Fe_{0.08}$ heterostructures: (a) full temperature range, (b) low-temperature region.

ducting VN layers in any sequence. Figure 5b shows that 12 nm thick layer of $Pd_{0.92}Fe_{0.08}$ alloy adjacent to the 30 nm VN film lowers T_c from 7.7 K to 6.1 K, which is well above the LHe*T*. Moreover, Figure 5b demonstrates that the transition stays sharp: the maximum ΔT_c increases only to 50 mK, and there is no tail towards lower temperatures. Also, there is a room to optimize the superconducting parameters of the VN film towards an increase in T_c by about 1 K [43,44]. In our opinion, the results hint at a possible use of heteroepitaxial combinations of nitrides as superconductors and palladium-rich $Pd_{1-x}Fe_x$ alloys as weak tunable ferromagnets to improve the operation characteristics of superconductor–ferromagnet–insulator heterojunctions for superconducting spintronics applications. For example, cubic superconducting MoN_x, which is a Josephson junction technology material [4,5,46], exhibits a good epitaxial match with $Pd_{1-x}Fe_x$ alloys, a_0(MoN) = 416.3 pm.

Conclusion

Fully epitaxial single-crystalline thin films of VN and heteroepitaxial structures of $Pd_{1-x}Fe_x$/VN and VN/$Pd_{1-x}Fe_x$ (x = 0.04, 0.08, respectively) were grown on single-crystalline MgO(001) substrates using a combination of UHV molecular beam epitaxy and magnetron sputtering. The obtained 30 nm thick VN films exhibit a sharp superconducting transition with T_c = 7.7 K and ΔT_c = 25 mK. The heteroepitaxial $Pd_{0.96}Fe_{0.04}$/VN and VN/$Pd_{0.92}Fe_{0.08}$ structures reveal a superconductor–ferromagnet proximity suppression of the transition temperature to T_c = 6.1 K. This is, however, well above the liquid helium temperature of 4.2 K and, therefore, suitable for superconducting spintronics. The superconducting transition stays sharp with a somewhat larger width of ΔT_c = 50 mK. Moreover, there is no resistive tail towards lower temperatures. These results, in our opinion, indicate that fully epitaxial $Pd_{1-x}Fe_x$/VN and VN/$Pd_{1-x}Fe_x$ thin film stacks can be considered as building blocks for superconducting spintronics elements.

Acknowledgements

The experimental work had been performed with the use of the equipment of the PCR Federal Center of Shared Facilities of Kazan Federal University.

Funding

This work was supported by the Russian Science Foundation (project no. 18-12-00459).

ORCID® iDs

Wael M. Mohammed - https://orcid.org/0000-0002-7829-1288
Igor V. Yanilkin - https://orcid.org/0000-0002-8879-8904
Amir I. Gumarov - https://orcid.org/0000-0002-7250-4377
Airat G. Kiiamov - https://orcid.org/0000-0001-5376-7000
Roman V. Yusupov - https://orcid.org/0000-0002-7516-2392
Lenar R. Tagirov - https://orcid.org/0000-0002-1549-7940

References

1. Mukhanov, O.; Semenov, V.; Likharev, K. *IEEE Trans. Magn.* **1987,** *23,* 759–762. doi:10.1109/tmag.1987.1064951
2. Likharev, K. K.; Semenov, V. K. *IEEE Trans. Appl. Supercond.* **1991,** *1,* 3–28. doi:10.1109/77.80745
3. Likharev, K. K. *Phys. C (Amsterdam, Neth.)* **2012,** *482,* 6–18. doi:10.1016/j.physc.2012.05.016
4. Tolpygo, S. K. *Low Temp. Phys.* **2016,** *42,* 361–379. doi:10.1063/1.4948618
5. Soloviev, I. I.; Klenov, N. V.; Bakurskiy, S. V.; Kupriyanov, M. Y.; Gudkov, A. L.; Sidorenko, A. S. *Beilstein J. Nanotechnol.* **2017,** *8,* 2689–2710. doi:10.3762/bjnano.8.269
6. Ryazanov, V. V. *Phys.-Usp.* **1999,** *42,* 825–827. doi:10.1070/pu1999v042n08abeh000600
7. Ustinov, A. V.; Kaplunenko, V. K. *J. Appl. Phys.* **2003,** *94,* 5405–5407. doi:10.1063/1.1604964
8. Larkin, T. I.; Bol'ginov, V. V.; Stolyarov, V. S.; Ryazanov, V. V.; Vernik, I. V.; Tolpygo, S. K.; Mukhanov, O. A. *Appl. Phys. Lett.* **2012,** *100,* 222601. doi:10.1063/1.4723576
9. Ryazanov, V. V.; Bol'ginov, V. V.; Sobanin, D. S.; Vernik, I. V.; Tolpygo, S. K.; Kadin, A. M.; Mukhanov, O. A. *Phys. Procedia* **2012,** *36,* 35–41. doi:10.1016/j.phpro.2012.06.126
10. Linder, J.; Robinson, J. W. A. *Nat. Phys.* **2015,** *11,* 307–315. doi:10.1038/nphys3242
11. Cryogenic Computing Complexity (C3) Program. https://www.iarpa.gov/index.php/research-programs/c3 (accessed Jan 15, 2020).
12. Manheimer, M. A. *IEEE Trans. Appl. Supercond.* **2015,** *25,* 1301704. doi:10.1109/tasc.2015.2399866
13. Holmes, D. S.; Ripple, A. L.; Manheimer, M. A. *IEEE Trans. Appl. Supercond.* **2013,** *23,* 1701610. doi:10.1109/tasc.2013.2244634
14. Ortlepp, T.; Ariando; Mielke, O.; Verwijs, C. J. M.; Foo, K. F. K.; Andreski, A.; Rogalla, H.; Uhlmann, F. H.; Hilgenkamp, H. *IEEE Trans. Appl. Supercond.* **2007,** *17,* 659–663. doi:10.1109/tasc.2007.898635
15. Khabipov, M. I.; Balashov, D. V.; Maibaum, F.; Zorin, A. B.; Oboznov, V. A.; Bolginov, V. V.; Rossolenko, A. N.; Ryazanov, V. V. *Supercond. Sci. Technol.* **2010,** *23,* 045032. doi:10.1088/0953-2048/23/4/045032
16. Feofanov, A. K.; Oboznov, V. A.; Bol'ginov, V. V.; Lisenfeld, J.; Poletto, S.; Ryazanov, V. V.; Rossolenko, A. N.; Khabipov, M.; Balashov, D.; Zorin, A. B.; Dmitriev, P. N.; Koshelets, V. P.; Ustinov, A. V. *Nat. Phys.* **2010,** *6,* 593–597. doi:10.1038/nphys1700
17. Nevirkovets, I. P.; Chernyashevskyy, O.; Prokopenko, G. V.; Mukhanov, O. A.; Ketterson, J. B. *IEEE Trans. Appl. Supercond.* **2014,** *24,* 1800506. doi:10.1109/tasc.2014.2318317
18. Yamanashi, Y.; Nakaishi, S.; Sugiyama, A.; Takeuchi, N.; Yoshikawa, N. *Supercond. Sci. Technol.* **2018,** *31,* 105003. doi:10.1088/1361-6668/aad78d
19. Yamanashi, Y.; Nakaishi, S.; Yoshikawa, N. *IEEE Trans. Appl. Supercond.* **2019,** *29,* 1301805. doi:10.1109/tasc.2019.2904700

20. Bakurskiy, S. V.; Klenov, N. V.; Soloviev, I. I.; Bol'ginov, V. V.; Ryazanov, V. V.; Vernik, I. V.; Mukhanov, O. A.; Kupriyanov, M. Y.; Golubov, A. A. *Appl. Phys. Lett.* **2013,** *102,* 192603. doi:10.1063/1.4805032
21. Baek, B.; Rippard, W. H.; Benz, S. P.; Russek, S. E.; Dresselhaus, P. D. *Nat. Commun.* **2014,** *5,* 3888. doi:10.1038/ncomms4888
22. Gingrich, E. C.; Niedzielski, B. M.; Glick, J. A.; Wang, Y.; Miller, D. L.; Loloee, R.; Pratt, W. P., Jr.; Birge, N. O. *Nat. Phys.* **2016,** *12,* 564–567. doi:10.1038/nphys3681
23. Nevirkovets, I. P.; Shafraniuk, S. E.; Mukhanov, O. A. *IEEE Trans. Appl. Supercond.* **2018,** *28,* 1800904. doi:10.1109/tasc.2018.2836938
24. Dayton, I. M.; Sage, T.; Gingrich, E. C.; Loving, M. G.; Ambrose, T. F.; Siwak, N. P.; Keebaugh, S.; Kirby, C.; Miller, D. L.; Herr, A. Y.; Herr, Q. P.; Naaman, O. *IEEE Magn. Lett.* **2018,** *9,* 3301905. doi:10.1109/lmag.2018.2801820
25. Klenov, N.; Khaydukov, Y.; Bakurskiy, S.; Morari, R.; Soloviev, I.; Boian, V.; Keller, T.; Kupriyanov, M.; Sidorenko, A.; Keimer, B. *Beilstein J. Nanotechnol.* **2019,** *10,* 833–839. doi:10.3762/bjnano.10.83
26. Katam, N. K.; Mukhanov, O. A.; Pedram, M. *IEEE Trans. Appl. Supercond.* **2018,** *28,* 1300212. doi:10.1109/tasc.2018.2797262
27. Shafraniuk, S. E.; Nevirkovets, I. P.; Mukhanov, O. A. *Phys. Rev. Appl.* **2019,** *11,* 064018. doi:10.1103/physrevapplied.11.064018
28. Buzdin, A. I. *Rev. Mod. Phys.* **2005,** *77,* 935–976. doi:10.1103/revmodphys.77.935
29. Vernik, I. V.; Bol'ginov, V. V.; Bakurskiy, S. V.; Golubov, A. A.; Kupriyanov, M. Y.; Ryazanov, V. V.; Mukhanov, O. A. *IEEE Trans. Appl. Supercond.* **2013,** *23,* 1701208. doi:10.1109/tasc.2012.2233270
30. Niedzielski, B. M.; Diesch, S. G.; Gingrich, E. C.; Wang, Y.; Loloee, R.; Pratt, W. P.; Birge, N. O. *IEEE Trans. Appl. Supercond.* **2014,** *24,* 1800307. doi:10.1109/tasc.2014.2311442
31. Uspenskaya, L. S.; Rakhmanov, A. L.; Dorosinskii, L. A.; Bozhko, S. I.; Stolyarov, V. S.; Bolginov, V. V. *Mater. Res. Express* **2014,** *1,* 036104. doi:10.1088/2053-1591/1/3/036104
32. Arham, H. Z.; Khaire, T. S.; Loloee, R.; Pratt, W. P., Jr.; Birge, N. O. *Phys. Rev. B* **2009,** *80,* 174515. doi:10.1103/physrevb.80.174515
33. Esmaeili, A.; Yanilkin, I. V.; Gumarov, A. I.; Vakhitov, I. R.; Gabbasov, B. F.; Kiiamov, A. G.; Rogov, A. M.; Osin, Y. N.; Denisov, A. E.; Yusupov, R. V.; Tagirov, L. R. *Thin Solid Films* **2019,** *669,* 338–344. doi:10.1016/j.tsf.2018.11.015
34. Esmaeili, A.; Mohammed, W. M.; Yanilkin, I. V.; Gumarov, A. I.; Vakhitov, I. R.; Gabbasov, B. F.; Kiiamov, A. G.; Aliyev, M. N.; Yusupov, R. V.; Tagirov, L. R. *Magn. Reson. Solids* **2019,** *21,* 19407. doi:10.26907/mrsej-19407
35. Wang, L.-B.; Lou, Z.-S.; Bao, K.-Y.; Liu, W.-Q.; Zhou, Q.-F. *Chin. Phys. Lett.* **2017,** *34,* 028101. doi:10.1088/0256-307x/34/2/028101
36. Muftikian, R.; Nebesny, K.; Fernando, Q.; Korte, N. *Environ. Sci. Technol.* **1996,** *30,* 3593–3596. doi:10.1021/es960289d
37. Haasch, R. T.; Lee, T.-Y.; Gall, D.; Greene, J. E.; Petrov, I. *Surf. Sci. Spectra* **2000,** *7,* 221–232. doi:10.1116/1.1367598
38. Liao, M. Y.; Gotoh, Y.; Tsuji, H.; Ishikawa, J. *J. Vac. Sci. Technol., A* **2004,** *22,* 146. doi:10.1116/1.1631473
39. *CasaXPS,* Version 2.3.19; Casa Software Ltd., 2013.
40. Bondarchuk, O.; Morel, A.; Bélanger, D.; Goikolea, E.; Brousse, T.; Mysyk, R. *J. Power Sources* **2016,** *324,* 439–446. doi:10.1016/j.jpowsour.2016.05.093
41. Esmaeili, A.; Yanilkin, I. V.; Gumarov, A. I.; Vakhitov, I. R.; Gabbasov, B. F.; Tatarsky, D. A.; Yusupov, R. V.; Tagirov, L. R. *arXiv* **2019,** No. 1912.04852.
42. Mei, A. B.; Hellman, O.; Wireklint, N.; Schleputz, C. M.; Sangiovanni, D. G.; Alling, B.; Rockett, A.; Hultman, L.; Petrov, I.; Greene, J. E. *Phys. Rev. B* **2015,** *91,* 054101. doi:10.1103/physrevb.91.054101
43. Zhao, B. R.; Chen, L.; Luo, H. L.; Jack, M. D.; Mullin, D. P. *Phys. Rev. B* **1984,** *29,* 6198–6202. doi:10.1103/physrevb.29.6198
44. Zasadzinski, J.; Vaglio, R.; Rubino, G.; Gray, K. E.; Russo, M. *Phys. Rev. B* **1985,** *32,* 2929–2934. doi:10.1103/physrevb.32.2929
45. Liu, X.; Lu, H.; He, M.; Jin, K.; Yang, G.; Ni, H.; Zhao, K. *Mater. Lett.* **2014,** *123,* 38–40. doi:10.1016/j.matlet.2014.02.079
46. Fabrication Services – SEEQC. https://seeqc.com/innovation/fabrication-services/ (accessed April 29, 2020).

License and Terms

The definitive version of this article is the electronic one which can be found at:
doi:10.3762/bjnano.11.65

BEILSTEIN JOURNAL OF NANOTECHNOLOGY

A Josephson junction based on a highly disordered superconductor/low-resistivity normal metal bilayer

Pavel M. Marychev* and Denis Yu. Vodolazov

Full Research Paper

Address:
Institute for Physics of Microstructures, Russian Academy of Sciences, Nizhny Novgorod, 603950, Russia

Email:
Pavel M. Marychev* - marychevpm@ipmras.ru

* Corresponding author

Keywords:
normal metal–superconductor bilayer; Josephson junction; Joule heating

Beilstein J. Nanotechnol. **2020,** *11,* 858–865.
doi:10.3762/bjnano.11.71

Received: 20 March 2020
Accepted: 22 May 2020
Published: 02 June 2020

This article is part of the thematic issue "Functional nanostructures for electronics, spintronics and sensors".

Guest Editor: A. S. Sidorenko

Abstract

We calculate the current–phase relation (CPR) of a SN-S-SN Josephson junction based on a SN bilayer of variable thickness composed of a highly disordered superconductor (S) and a low-resistivity normal metal (N) with proximity-induced superconductivity. In such a junction, the N layer provides both a large concentration of phase in the weak link and good heat dissipation. We find that when the thickness of the S and the N layer and the length of the S constriction are about the superconducting coherence length the CPR is single-valued and can be close to a sinusoidal shape. The product I_cR_n can reach $\Delta(0)/2|e|$ (I_c is the critical current of the junction, R_n is its normal-state resistance, $\Delta(0)$ is the superconductor gap of a single S layer at zero temperature). Our calculations show, that the proper choice of the thickness of the N layer leads both to nonhysteretic current–voltage characteristics even at low temperatures and a relatively large product I_cR_n.

Introduction

Josephson junctions are of interest for applications such as voltage standards [1], SQUID magnetometers [2], particle detectors [3], and energy-efficient superconductor logic and memory circuits [4,5]. These applications need to have a large critical current I_c to achieve high noise immunity. Also many of these applications require to have a nonhysteretic current–voltage characteristic (IVC) and a large characteristic voltage $V_c = I_cR_n$, where R_n is the normal-state resistance of the junction.

Tunnel superconductor–insulator–superconductor (SIS) Josephson junctions are characterized by small critical current densities (significantly smaller than the depairing current density of superconducting electrodes) and a hysteretic IVC (the latter is related with the large capacitance of the insulator layer), which restricts their applicability. Elimination of hysteresis in SIS junctions requires an external resistor or a more complex circuitry. S-c-S Josephson junctions (where “c” is a geometric constriction) have a small capacitance of the weak link and a high critical current (about the magnitude of the depairing current of a superconductor), which allows one to obtain high noise immunity. But due to large critical current and bad heat dissipation their IVCs are hysteretic due to Joule heating ($\approx I_c V_c \approx I_c^2 R_n$) and the subsequent formation of a stable region with suppressed superconductivity (a so-called “hot spot”) at $I > I_c$ [6-9]. At temperatures near the critical temperature T_c the hysteresis is absent because of the low I_c and, therefore, small dissipation, but this leads to a small voltage V_c.

Therefore, eliminating the thermal hysteresis without sacrificing the voltage V_c is important, albeit a nontrivial problem. One solution is a normal metal shunt either on top of the junction [10] or at a distance from it [11,12]. The resistance and the position of the shunt play an important role and they can lead to a reduction of the junction characteristics because of the proximity effect or a very small shunt resistance. In [13,14], it was proposed to use a variable-thickness SN-N-SN bilayer in which the superconducting layer is partially (or entirely) etched by means of a focused ion beam. A sufficiently thick normal metal layer act as a good thermal bath, which yields a nonhysteretic current–voltage characteristic even at low temperatures. However, the increase of the thickness of the N layer leads to a significant decrease of R_n and, hence, to smaller values of V_c.

In our work, we calculate the current–phase relation and heating effects in SN-S-SN Josephson junctions of variable thickness based on a thin dirty superconductor with large normal-state resistivity, $\rho_S \geq 100$ μΩ·cm, and a thin normal metal layer with low resistivity, $\rho_N \geq 2$ μΩ·cm. In such a thin SN bilayer the superconducting current mainly flows in the N layer (due to proximity-induced superconductivity and $\rho_S/\rho_N \gg 1$), and the critical current of the SN bilayer may exceed the critical current of a single S layer if the thickness of the S and the N layers are about the superconducting coherence length [15]. Because of the large diffusion coefficient, $D_N \gg D_S$, the N layer provides both a large phase concentration in the constriction leading to a single-valued current–phase relation (CPR) and an effective thermal bath into which the heat from the junction area could be dissipated, resulting in nonhysteretic IVC even at relatively low temperatures. We also find that in comparison with a SN-N-SN junction, the critical current density could be similar to the depairing current density of the S layer, which makes it possible to obtain $I_c R_n \approx \Delta(0)/2|e|$.

Model

The model system consists of a SN bilayer strip with length L made of a superconducting film with thickness d_S and a normal metal film with thickness d_N. At the center of the bilayer there is a constriction with length a and thickness d_c where the N layer and, partially, the S layer are removed (Figure 1).

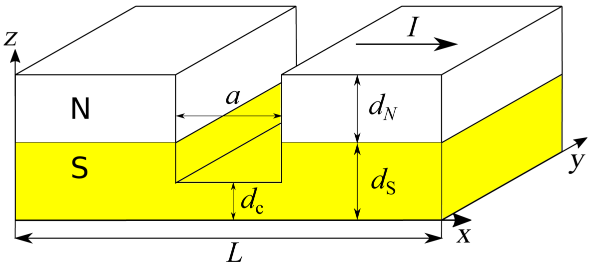

Figure 1: Sketch of a SN-S-SN Josephson junction based on a SN strip of variable thickness.

We assume that in our system the current flows in the x direction, and in the y direction the system is uniform. To find the current–phase relation of such a SN-S-SN Josephson junction at all temperatures below T_c we solve a 2D Usadel equation for quasiclassical normal g and anomalous f Green’s functions. With the angle parametrization $g = \cos\Theta$ and $f = \sin\Theta \exp(i\phi)$, the 2D Usadel equation in different layers can be written as

$$\begin{aligned}&\frac{\hbar D_S}{2}\left(\frac{\partial^2\Theta_S}{\partial x^2}+\frac{\partial^2\Theta_S}{\partial z^2}\right)\\&-\left(\hbar\omega_n+\hbar\frac{D_S}{2}q^2\cos\Theta_S\right)\sin\Theta_S\\&+\Delta\cos\Theta_S=0,\end{aligned} \tag{1}$$

$$\begin{aligned}&\frac{\hbar D_N}{2}\left(\frac{\partial^2\Theta_N}{\partial x^2}+\frac{\partial^2\Theta_N}{\partial z^2}\right)\\&-\left(\hbar\omega_n+\hbar\frac{D_N}{2}q^2\cos\Theta_N\right)\sin\Theta_N=0,\end{aligned} \tag{2}$$

where the subscripts S and N refer to the superconducting and the normal layer, respectively. Here $\hbar\omega_n = \pi k_B T(2n + 1)$ are the Matsubara frequencies (n is an integer number), $\mathbf{q} = \nabla\phi = (q_x, q_z)$ is the quantity that is proportional to the supervelocity $\mathbf{v}_s$, and ϕ is the phase of the superconducting order parameter. Δ is the magnitude of the order parameter, which should satisfy the self-consistency equation

$$\Delta\ln\left(\frac{T}{T_{c0}}\right)=2\pi k_B T\sum_{\omega_n>0}\left(\sin\Theta_S-\frac{\Delta}{\hbar\omega_n}\right), \tag{3}$$

where T_{c0} is the critical temperature of the single S layer. We assume that Δ is nonzero only in the S layer because of the absence of attractive phonon-mediated electron–electron coupling in the N layer. Equation 1 and Equation 2 are supplemented by the Kupriyanov–Lukichev boundary conditions [16] between the layers:

$$D_\mathrm{S}\frac{\mathrm{d}\Theta_\mathrm{S}}{\mathrm{d}z}\bigg|_{z=d_\mathrm{S}-0}=D_\mathrm{N}\frac{\mathrm{d}\Theta_\mathrm{N}}{\mathrm{d}z}\bigg|_{z=d_\mathrm{S}+0}. \tag{4}$$

In the model we assume a transparent interface between the N and the S layer, which leads to the continuity of Θ at the NS boundary. At the boundaries of the system with the vacuum we use $\mathrm{d}\Theta/\mathrm{d}n = 0$.

To find the phase distribution ϕ Equation 1–Equation 3 are supplemented by a 2D equation,

$$\operatorname{div}\mathbf{j}_\mathrm{s}=0. \tag{5}$$

Here, $\mathbf{j}_\mathrm{S}$ is the superconducting current density, which is determined by the following expression:

$$\mathbf{j}_\mathrm{s}=\frac{2\pi k_\mathrm{B}T}{e\rho}\mathbf{q}\sum_{\omega_n>0}\sin^2\Theta, \tag{6}$$

where ρ is the residual resistivity of the corresponding layer. At the SN-interface we use a boundary condition similar to Equation 4, and for the interfaces with the vacuum we use $\mathrm{d}\phi/\mathrm{d}n = 0$. At the system ends rigid boundary conditions are imposed:

$$\phi(0,z)=-\delta\phi/2,\ \ \phi(L,z)=\delta\phi/2, \tag{7}$$

where $\delta\phi$ is the fixed phase difference between the system ends. This is different from the phase drop near the junction, which we define as

$$\varphi=\delta\phi-kL, \tag{8}$$

where $k = q_x$ ($x = 0$) is far from the constriction (in a similar way φ is defined in [17,18]). The value of k is found from the self-consistings solution of Equation 1–Equation 3 and Equation 5.

In numerical calculations we use dimensionless units. The magnitude of the order parameter is normalized by $k_\mathrm{B}T_{c0} = \Delta(0)/1.76$, lengths are in units of $\xi_\mathrm{c}=\sqrt{\hbar D_\mathrm{S}/k_\mathrm{B}T_{c0}}\approx 1.33\xi(0)$, where $\xi(0)=\sqrt{\hbar D_\mathrm{S}/\Delta(0)}$ is the superconducting coherence length at $T = 0$, and the current is in units of the depairing current I_dep of the superconductor at $T = 0$.

To calculate the CPR we numerically solve Equation 1–Equation 3 and Equation 5 by using an iteration procedure with fixed $\delta\phi$. When self-consistency is achieved (we stop the calculations when the maximal relative change of Δ between consequent iterations is less than 10^{-4}) the Green's functions are used to calculate j_s and the supercurrent per unit of width, I_s:

$$I_\mathrm{s}=\int_0^{d_\mathrm{S}+d_\mathrm{N}} j_{\mathrm{s}x}(x=0)\,\mathrm{d}z. \tag{9}$$

We also compare the calculated CPR with the CPR of a 1D S'-S-S' system with a large ratio between the diffusion coefficients $D_\mathrm{S'}/D_\mathrm{S} \gg 1$ (the length of the superconductor S is equal to a). For these calculations we use a 1D Usadel equation.

Results

Current–phase relation of the SN-S-SN Josephson junction

The function $I_\mathrm{s}(q)$ in the SN bilayer may have one or two maxima depending on the value of d_S (see Figure 2) or of d_N (see Figure 3a in [15]). The maximum at small q is connected with the suppression of proximity-induced superconductivity in the N layer at $q > q_\mathrm{c1} \approx 1/\sqrt{D_\mathrm{N}}$ while the second maximum at $q = q_\mathrm{c2} \approx 1/\sqrt{D_\mathrm{S}} \gg q_\mathrm{c1}$ comes from the suppression of superconductivity in the S layer when $q > q_\mathrm{c2}$. The large difference between q_c1 and q_c2 leads to a larger phase concentration in the S constriction (see Figure 1) in comparison with the variable-thickness strip (or Dayem bridge) made of the same material and having the similar geometrical parameters. Because of that, for relatively thin S layers the CPR is single-valued (see Figure 3a), which is not easy to achieve in a Dayem bridge [19].

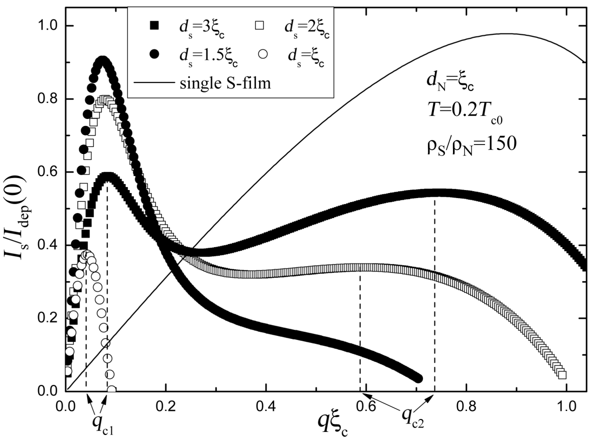

Figure 2: Dependence of the superconducting current I_s flowing along the SN bilayer on q for different d_S. The solid line shows the dependence of I_s on q for the single S strip. The dashed lines show the critical values of q. The current is normalized by the depairing current I_dep of the single S strip with thickness d_S at $T = 0$.

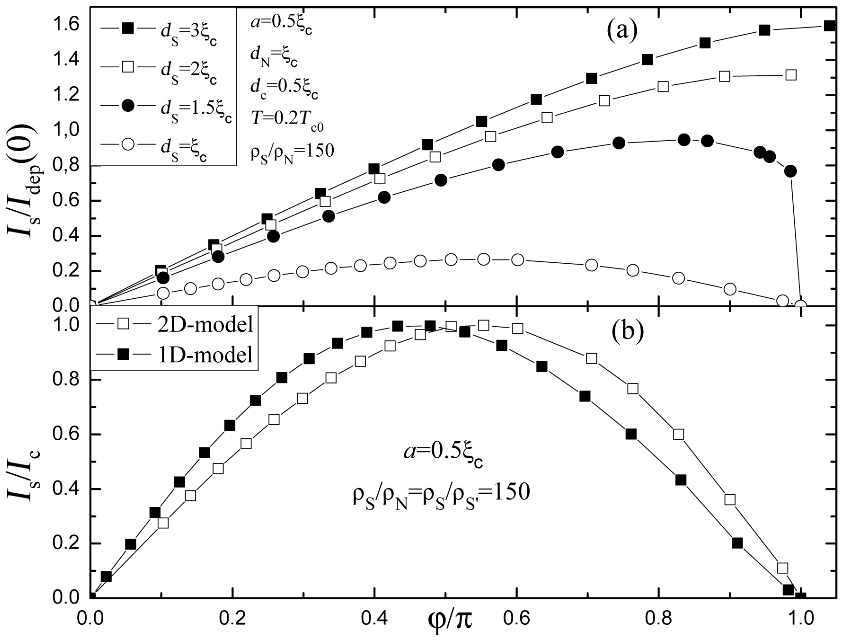

Figure 3: (a) Current–phase relation of a SN-S-SN Josephson junction at different d_S. The current is normalized by the depairing current I_{dep} of the single S strip with thickness d_c at $T = 0$. The junction parameters are shown in the figure. (b) Comparison of current–phase relations calculated on the basis of 1D and 2D models. For the 2D case the parameters are $d_S = d_N = \xi_c$, $d_c = 0.5\xi_c$, $T = 0.2T_{c0}$. For the 1D case the temperature $T = 0.6T_{c0}$ corresponds to $T = 0.6T_c$, where $T_c = 0.32T_{c0}$ is the critical temperature of the SN bilayer with the chosen parameters. The superconducting current is normalized by the critical current of the Josephson junction.

For relatively large d_S there is a noticeable contribution to the total supercurrent from the S layer, which means a smaller current (phase) concentration in the constriction like in a common Dayem bridge, and the CPR becomes multi-valued (see Figure 3a for $d_S = 2\xi_c$ and $3\xi_c$).

In some respect, the studied Josephson junction resembles Josephson junctions based on a S'-S-S' system composed of two superconductors S and S' having $D_{S'} \gg D_S$ and the same thicknesses $d_S = d_{S'}$ [17,20,21]. A Josephson junction based on this quasi 1D system has a single-valued CPR, which approaches a sinusoidal shape with increasing temperature. In Figure 3b we compare the CPRs calculated for 1D S'-S-S' and 2D SN-S-SN systems. Since in the 1D model there is no suppression of T_c through the N layer, we use in the calculations the ratio T/T_{c0}, which corresponds to the ratio T/T_c of the 2D SN structure. Visible differences between the calculated CPRs using different models could be related with a transversal inhomogeneity near the S constriction in the 2D case.

We have also studied the evolution of the CPR of the SN-S-SN Josephson junction when varying different parameters. In Figure 4a we demonstrate that with increase of the temperature the current–phase relation comes close to a sinusoidal shape. At $T = 0.3T_{c0}$ the amplitude of the first harmonic, sin ϕ, is $0.98I_c$ and the amplitude of the second harmonic, sin 2ϕ, is $-0.19I_c$). This is typical for S'-S-S' junctions [21] and is related to the increase of the temperature-dependent coherence length $\xi(T)$. The effect of different d_N is shown in Figure 4b. An increase in d_N leads to a slight shift of the maximum of $I_s(\varphi)$ to the left and a decrease of I_c. This can be explained by a lowering of T_c of the SN bilayer for thicker N layers. A lower I_c means smaller values of I_cR_n. However, as we discuss below, a large value of d_N provides better cooling of the S constriction and nonhysteretic IVCs.

An increase of the length of the weak link, a, leads to the shift of the maximum of $I_s(\varphi)$ to the right (see Figure 4c) as it is typical for common Josephson junctions with variable thickness. Interestingly, in contrast to common junctions, I_c increases in the SN-S-SN system. This can be explained by a lower value of the superconducting order parameter in SN banks in comparison with Δ in the S constriction at $I_s = 0$. With increasing a the superconducting order parameter in the constriction increases and I_c increases too.

Finally, Figure 4d illustrates that a decrease of the ratio ρ_S/ρ_N to a third of the initial value hardly changes the current–phase relation. Both the critical current and the shape of the CPR vary only little.

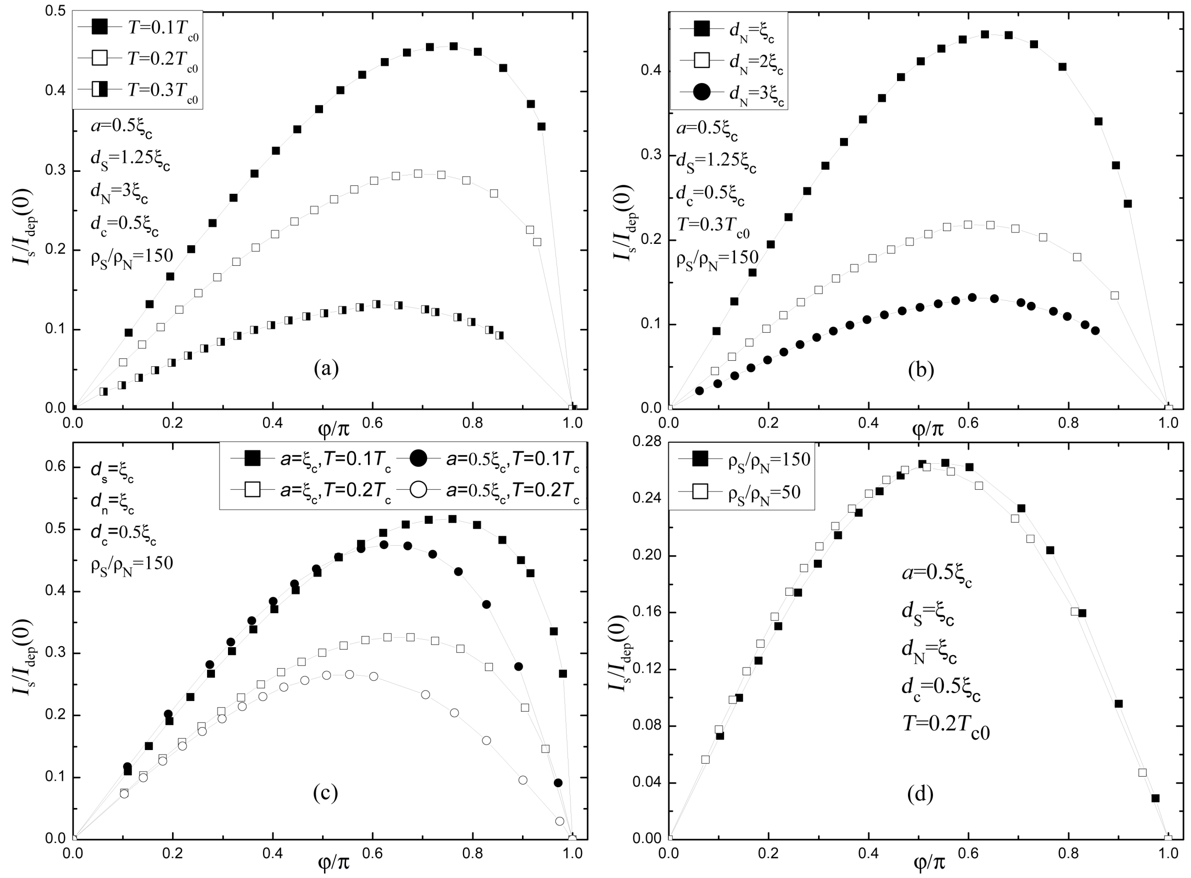

Figure 4: Variation of current–phase relation of SN-S-SN junction as a function of: (a) the temperature; (b) the thickness of the N layer d_N; (c) the length of the constriction, *a*; (d) the ratio between the resistivities. The current is normalized by the depairing current I_{dep} of the superconducting strip with thickness d_c at $T = 0$.

Effect of Joule heating in SN-S-SN junctions

The absence of hysteresis in the current–voltage characteristics is important for devices based on Josephson junctions. The hysteresis in Dayem bridge, variable-thickness, S'-S-S' or S-N-S junctions is mainly caused by the temperature rise in the weak-link region in the resistive state due to Joule heating and the formation of hot spots [7-9]. A relatively large gap Δ in superconducting banks plays an important role here because it prohibits heat dissipation from the S or the N link at low temperatures $k_BT < \Delta$ and it leads to hysteresis even for S-N-S junctions of variable thickness [22]. This problem could be resolved by adding heat sinks (voltage leads attached to the N link could play such a role [23]). However, this complicates the geometry of the junction. Local heat production is expected to be large in a SN-S-SN junction due to large critical current density, which is about the depairing current density of the superconductor. As we show below, the presence of a relatively thick N layer with large diffusion coefficient and small minigap in the electron spectra provides efficient cooling of the constriction.

To estimate the increase of temperature in the resistive state we use a two-temperature (2T) model [24,25] for the SN-S-SN junction. We suppose that electron temperature $T_e = T + \delta T_e$ and phonon temperature $T_p = T + \delta T_p$ are close to the substrate temperature, $\delta T_e, \delta T_p \ll T$ and do not vary along the thickness. In the N layer the proximity-induced gap (minigap) is small, and, due to the inverse proximity effect, the gap in the relatively thin S layer ($d_S \leq 1.5\xi_c$) is also suppressed in comparison with a single S layer, which permits heat diffusion from the N to the S layer in SN banks. In the S constriction being in the resistive state at $I > I_c$ the superconducting order parameter is also suppressed. It allows us to use normal-state heat conductivity both in the SN and the S region in the heat conductance equation for the calculation of δT_e. This is in contrast to S-N-S and S'-S-S' junctions where heat conductivity is suppressed in the superconducting banks. In our model Joule dissipation is taken into account only in the S constriction, because in the SN bilayer it is considerably lower due to the much lower resistivity and lower current density. Because of the small length of the constriction and the large difference in diffusion coefficients and thicknesses in constriction and banks we can neglect heat flow to phonons and substrate in the constriction (the main cooling of the junction comes from the diffusion of hot electrons to SN banks). In the SN bilayer $D_N \gg D_S$ and heat diffusion occurs mainly along the N layer. With above assumptions we obtain the following equation for δT_e:

$$\begin{gathered}\frac{d^2\delta T_e}{dx^2} + \rho_S\left(j_c\right)^2 / \kappa_S = 0, |x| \le a/2, \\ \frac{d^2\delta T_e}{dx^2} - \frac{\delta T_e}{\lambda_T^2} = 0, |x| \ge a/2,\end{gathered} \qquad (10)$$

where $\kappa_S = 2D_S\pi^2 N(0)k_B^2 T/3$ is the electron heat conductivity of the S layer in the normal state, and $N(0)$ is the one-spin density of states on the Fermi level,

$$\lambda_T = \sqrt{D_N\tau_0}\left(\frac{T_{c0}}{T}\right)^{3/2}\sqrt{\frac{\pi^2(1+\beta)}{720\zeta(5)}} \qquad (11)$$

is the thermal healing length, $\beta = [\gamma\tau_{esc}\ 450\zeta(5)T/[\tau_0\pi^4 T_{c0}]$, $\zeta(5) \approx 1.03$, τ_{esc} is the escape time of nonequilibrium phonons to the substrate, $\gamma = 8\pi^2 C_e(T_{c0})/C_p(T_{c0})$ is the ratio between electron and phonon heat capacity at $T = T_{c0}$ and τ_0 determines the strength of electron–phonon inelastic scattering in the S and the N layer (see Equations 4 and 6 in [25]). For τ_0 we use the smallest time for S and N materials due to the assumably good transfer of electrons between the S and the N layer and the small thickness of the layers. On the boundary between S and SN regions we use a continuity of the electron temperature, $\delta T_e|_{a/2-0} = \delta T_e|_{a/2+0}$, and of the heat flux

$$d_c D_S \left.\frac{\delta T_e}{dx}\right|_{a/2-0} = d_N D_N \left.\frac{\delta T_e}{dx}\right|_{a/2+0}.$$

Using Equation 10 and above boundary conditions, we find the maximal temperature increase in the constriction:

$$\frac{\delta T_e^{\max}}{T} = 0.23\left(\frac{a}{\xi_c}\right)^2\left(\frac{T_{c0}}{T}\right)^2\left(\frac{I_c}{I_{dep}(0)}\right)^2\left(\frac{D_S d_c}{D_N d_N}\frac{4\lambda_T}{a} + 1\right). \qquad (12)$$

In the following estimations we use the parameters of NbN (S layer) and Cu (N layer): T_{c0} = 10 K, D_S = 0.5 cm^2/s, ρ_S = 200 μΩ·cm, D_N = 40 cm^2/s, ρ_N = 2 μΩ·cm, τ_0 = 1 ns (theoretical estimation for NbN taken from [25]), ξ_c = 6.4 nm, γ = 9, $d_S = 1.25\xi_c$, $d_N = 2\xi_c$, $\tau_{esc} = 4(d_N + d_S)/u \approx 41$ ps ($u = 2\cdot10^5$ cm^2/s is the mean speed of sound), T/T_{c0} = 0.3, T_c/T_{c0} = 0.43, $a = 0.5\xi_c$, $d_c = 0.5\xi_c$. With these parameters $\beta \approx 0.53$, $I_c \approx 0.22 I_{dep}(0)$ (see Figure 4b) and $\delta T_e^{\max}/T \approx 0.24$ is small, thanks to $D_N \gg D_S$ and $d_N \gg d_c$.

Discussion

We use an Usadel model to calculate the current–phase relation of a SN-S-SN Josephson junction based on a high-resistivity superconductor and a low-resistivity normal metal. In [15], from comparison of experiment and theory it was concluded that the Usadel model underestimates proximity-induced superconductivity in the N layer and overestimates the inverse proximity effect in the S layer in NbN/Al, NbN/Ag and MoN/Ag bilayers. Namely, the suppression of the critical temperature of the SN bilayer is smaller while the change in magnetic field penetration depth of the SN bilayer is larger than the Usadel model predicts. Therefore, the present results should be considered only as a route for a possible experimental realization of SN-S-SN Josephson junctions. They demonstrate that the thickness of the S layer should not exceed ca. $1.5\xi_c$, otherwise the current–phase relation is not single-valued for reasonable lengths and thicknesses of the S constriction. The thickness of the N layer should not be too small (a small d_N leads to large overheating) and not too large (a larger d_N leads to lower T_c and smaller I_c at a fixed substrate temperature).

Our results show that the SN-S-SN Josephson junction in many respects resembles Dayem bridge, variable-thickness, S’-S-S’ or S-N-S junctions. The product

$$V_c = I_c R_n = \frac{\Delta(0)}{|e|}\frac{a}{\xi_c}\frac{I_c}{I_{dep}(0)}, \qquad (13)$$

can reach $0.5\Delta(0)/|e|$ at a low temperature ($T = 0.1T_{c0}$) and $a = \xi_c$ (see Figure 4c) due to use of a superconductor in the constriction area, instead of a normal metal as in [13]. In case of NbN with T_{c0} = 10 K one may have V_c = 0.75 mV but according to Equation 12), $\delta T_e^{\max}$ will be larger than T when using these parameters. However there is the hope, that the critical temperature of a real SN bilayer is higher than the Usadel model predicts (see discussion above) and therefore large I_c values could be reached at higher operating temperatures T/T_{c0}, leading to a drastic reduction of $\delta T_e^{\max}$ (see Equation 12).

SN-S-SN junctions made of a NbN/Al bilayer have been fabricated recently [26] and indications of the Josephson effect (the presence of Shapiro steps and a Fraunhofer-like dependence of the critical current on the magnetic field) have been observed. But due to not optimized parameters ($d_S = d_c \approx 15$ nm $\approx 2.3\ \xi_c$, $d_N \approx 29$ nm $\approx 4.5\ \xi_c$, a = 20 nm $\approx 3.1\ \xi_c$) the IV curves were hysteretic already at temperatures close to the critical temperature and the width of Shapiro steps did not follow the theoretical expectations [26]. Modern technology allows one to fabricate constrictions with lengths of about 5 nm, which is smaller than ξ_c in NbN, with the help of helium ion beam lithography. The successful implementation of this method could lead to the creation of low-temperature nanoscale Josephson junctions and arrays of them. For example, SN-S-SN junctions can be promising to use in programmable voltage standards [1], where a large value of V_c allows for a reduction of the number of junctions and for the use of Shapiro steps of orders higher than one. Nonhysteretic current–voltage characteristics with large V_c at low temperatures allow for the use of these structures for various low-temperature applications, e.g., particle detectors [3].

Conclusion

We have calculated the current–phase relation of a Josephson junction based on a SN-S-SN strip of variable thickness, where S is a dirty superconductor with large normal-state resistivity and N is a low-resistivity normal metal. We find a range of parameters for which the CPR is single-valued, is close to a sinusoidal shape, and $I_c R_n \leq \Delta(0)/2|e|$. Our estimations demonstrate that a relatively thick N layer serves as effective heat conductor yielding weak overheating and a nonhysteretic current–voltage characteristic of the SN-S-SN Josephson junction.

Funding

P. M. M. acknowledges support from Russian Scientific Foundation (project No. 20-42-04415 – results presented in sections 2 and 3) and D. Yu. V. acknowledges support from the Foundation for the Advancement of Theoretical Physics and Mathematics BASIS (program No. 18-1-2-64-2 – results presented in sections 4 and 5).

ORCID® iDs

Pavel M. Marychev - https://orcid.org/0000-0002-9779-7807
Denis Yu. Vodolazov - https://orcid.org/0000-0002-9846-8036

Preprint

A non-peer-reviewed version of this article has been previously published as a preprint https://arxiv.org/abs/2002.07552

References

1. Jeanneret, B.; Benz, S. P. *Eur. Phys. J.: Spec. Top.* **2009,** *172,* 181–206. doi:10.1140/epjst/e2009-01050-6
2. Martínez-Pérez, M. J.; Koelle, D. *Phys. Sci. Rev.* **2017,** *2,* 20175001. doi:10.1515/psr-2017-5001
3. Tarte, E. J.; Moseley, R. W.; Kölbl, M. R.; Booij, W. E.; Burnell, G.; Blamire, M. G. *Supercond. Sci. Technol.* **2000,** *13,* 983–988. doi:10.1088/0953-2048/13/7/313
4. Likharev, K. K.; Semenov, V. K. *IEEE Trans. Appl. Supercond.* **1991,** *1,* 3–28. doi:10.1109/77.80745
5. Soloviev, I. I.; Klenov, N. V.; Bakurskiy, S. V.; Kupriyanov, M. Y.; Gudkov, A. L.; Sidorenko, A. S. *Beilstein J. Nanotechnol.* **2017,** *8,* 2689–2710. doi:10.3762/bjnano.8.269
6. Skocpol, W. J.; Beasley, M. R.; Tinkham, M. *J. Appl. Phys.* **1974,** *45,* 4054–4066. doi:10.1063/1.1663912
7. Courtois, H.; Meschke, M.; Peltonen, J. T.; Pekola, J. P. *Phys. Rev. Lett.* **2008,** *101,* 067002. doi:10.1103/physrevlett.101.067002
8. Hazra, D.; Pascal, L. M. A.; Courtois, H.; Gupta, A. K. *Phys. Rev. B* **2010,** *82,* 184530. doi:10.1103/physrevb.82.184530
9. Biswas, S.; Winkelmann, C. B.; Courtois, H.; Gupta, A. K. *Phys. Rev. B* **2018,** *98,* 174514. doi:10.1103/physrevb.98.174514
10. Lam, S. K. H.; Tilbrook, D. L. *Appl. Phys. Lett.* **2003,** *82,* 1078–1080. doi:10.1063/1.1554770
11. Mück, M.; Rogalla, H.; Heiden, C. *Appl. Phys. A: Solids Surf.* **1988,** *47,* 285–289. doi:10.1007/bf00615934
12. Kumar, N.; Winkelmann, C. B.; Biswas, S.; Courtois, H.; Gupta, A. K. *Supercond. Sci. Technol.* **2015,** *28,* 072003. doi:10.1088/0953-2048/28/7/072003
13. Hadfield, R. H.; Burnell, G.; Booij, W. E.; Lloyd, S. J.; Moseley, R. W.; Blamire, M. G. *IEEE Trans. Appl. Supercond.* **2001,** *11,* 1126–1129. doi:10.1109/77.919546
14. Chen, K.; Cui, Y.; Li, Q.; Xi, X. X.; Cybart, S. A.; Dynes, R. C.; Weng, X.; Dickey, E. C.; Redwing, J. M. *Appl. Phys. Lett.* **2006,** *88,* 222511. doi:10.1063/1.2208555
15. Vodolazov, D. Y.; Aladyshkin, A. Y.; Pestov, E. E.; Vdovichev, S. N.; Ustavshikov, S. S.; Levichev, M. Y.; Putilov, A. V.; Yunin, P. A.; El'kina, A. I.; Bukharov, N. N.; Klushin, A. M. *Supercond. Sci. Technol.* **2018,** *31,* 115004. doi:10.1088/1361-6668/aada2e
16. Kuprianov, M. Y.; Lukichev, V. F. *Sov. Phys. - JETP* **1988,** *67,* 1163–1168.
17. Baratoff, A.; Blackburn, J. A.; Schwartz, B. B. *Phys. Rev. Lett.* **1970,** *25,* 1096–1099. doi:10.1103/physrevlett.25.1096
18. Zubkov, A. A.; Kupriyanov, M. Y. *Sov. J. Low Temp. Phys.* **1983,** *9,* 279.
19. Vijay, R.; Sau, J. D.; Cohen, M. L.; Siddiqi, I. *Phys. Rev. Lett.* **2009,** *103,* 087003. doi:10.1103/physrevlett.103.087003
20. Blackburn, J. A.; Schwartz, B. B.; Baratoff, A. *J. Low Temp. Phys.* **1975,** *20,* 523–545. doi:10.1007/bf00120866
21. Kupriyanov, M. Y.; Lukichev, V. F. *Sov. J. Low Temp. Phys.* **1981,** *7,* 137.
22. Golikova, T. E.; Hübler, F.; Beckmann, D.; Klenov, N. V.; Bakurskiy, S. V.; Kupriyanov, M. Y.; Batov, I. E.; Ryazanov, V. V. *JETP Lett.* **2013,** *96,* 668–673. doi:10.1134/s0021364012220043
23. Skryabina, O. V.; Egorov, S. V.; Goncharova, A. S.; Klimenko, A. A.; Kozlov, S. N.; Ryazanov, V. V.; Bakurskiy, S. V.; Kupriyanov, M. Y.; Golubov, A. A.; Napolskii, K. S.; Stolyarov, V. S. *Appl. Phys. Lett.* **2017,** *110,* 222605. doi:10.1063/1.4984605
24. Perrin, N.; Vanneste, C. *Phys. Rev. B* **1983,** *28,* 5150–5159. doi:10.1103/physrevb.28.5150
25. Vodolazov, D. Yu. *Phys. Rev. Appl.* **2017,** *7,* 034014. doi:10.1103/physrevapplied.7.034014
26. Levichev, M. Y.; El'kina, A. I.; Bukharov, N. N.; Petrov, Y. V.; Aladyshkin, A. Y.; Vodolazov, D. Y.; Klushin, A. M. *Phys. Solid State* **2019,** *61,* 1544–1548. doi:10.1134/s1063783419090142

License and Terms

The definitive version of this article is the electronic one which can be found at:
doi:10.3762/bjnano.11.71

BEILSTEIN JOURNAL OF NANOTECHNOLOGY

Band tail state related photoluminescence and photoresponse of ZnMgO solid solution nanostructured films

Vadim Morari[1], Aida Pantazi[2], Nicolai Curmei[3], Vitalie Postolache[4], Emil V. Rusu[1], Marius Enachescu[2], Ion M. Tiginyanu[4] and Veaceslav V. Ursaki*[4]

Full Research Paper

Open Access

Address:
[1]D.Ghitu Institute of Electronic Engineering and Nanotechnologies, Chisinau MD-2028, Republic of Moldova, [2]Center for Surface Science and NanoTechnology, University Politehnica of Bucharest, 060042-Bucharest, Romania, [3]Institute of Applied Physics, Chisinau MD-2028, Republic of Moldova and [4]National Center for Materials Study and Testing, Technical University of Moldova, Chisinau MD-2004, Republic of Moldova

Email:
Veaceslav V. Ursaki* - vvursaki@gmail.com

* Corresponding author

Keywords:
aerosol spray pyrolysis deposition; energy band tails; photodetector; photoluminescence; photosensitivity; spin coating; thin films; ZnMgO semiconductor alloy

Beilstein J. Nanotechnol. **2020,** *11,* 899–910.
doi:10.3762/bjnano.11.75

Received: 20 February 2020
Accepted: 14 May 2020
Published: 12 June 2020

This article is part of the thematic issue "Functional nanostructures for electronics, spintronics and sensors".

Guest Editor: A. S. Sidorenko

Abstract

A series of $Zn_{1-x}Mg_xO$ thin films with the composition range x = 0.00–0.40 has been prepared by sol–gel spin coating on Si substrates with a post-deposition thermal treatment in the temperature range of 400–650 °C. The morphology of the films was investigated by scanning electron microscopy and atomic force microscopy while their light emission properties were studied by photoluminescence spectroscopy under excitation at 325 nm. It was found that annealing at 500 °C leads to the production of macroscopically homogeneous wurtzite phase films, while thermal treatment at higher or lower temperature results in the degradation of the morphology, or in the formation of ZnO particles embedded into the ZnMgO matrix, respectively. Local compositional fluctuations leading to the formation of deep band tails in the gap were deduced from photoluminescence spectra. A model for the band tail distribution in the bandgap is proposed as a function of the alloy composition. Thin films were also prepared by aerosol spray pyrolysis deposition using the same sol–gel precursors for the purpose of comparison. The prepared films were tested for photodetector applications.

Introduction

The ZnMgO solid solution system is of interest due to the possibility to tailor many important physical properties by varying their composition. This alloy system covers a wide ultraviolet (UV) spectral range between the direct bandgaps of 3.36 eV for ZnO and 7.8 eV for MgO at room temperature, making it very attractive for short-wavelength optical applications such as UV detectors [1-5] and light emitters [6-9].

Various techniques have been used for the preparation of ZnMgO films such as radio-frequency plasma-assisted molecular beam epitaxy (RF-MBE) [2,7,10,11], DC [12,13] and RF [1,3,6] magnetron sputtering, pulsed laser deposition (PLD) [14,15], plasma-enhanced atomic layer deposition (PE-ALD) [16], chemical vapor deposition (CVD) [17], metal–organic chemical vapor deposition (MOCVD) [18,19], hydrothermal [4], chemical bath deposition (CBD) [20], sol–gel spin coating [21-29], and spray pyrolysis [28-34]. Among these techniques, the sol–gel spin coating method has the advantage of ensuring easy control and handling of chemicals and substrates, as well as excellent control over stoichiometry. Because the process does not require vacuum conditions and can be performed at low temperature, it is suitable for the fabrication of high quality, large area thin films at a fast rate and low cost. This method also offers the possibility for easy doping and preparation of homogeneous films with good electrical and optical properties.

The films are prepared on various substrates such as ZnO [6], MgO [17], Si [2-4,23], CaF_2 [12], Al_2O_3 [18], sapphire [7,10,11,13-16,19,31,32], glass and quartz [1,20,21,23-30,33,34]. The choice of the substrate is determined by the application. In particular, glass, quartz or sapphire substrates are usually used for photodetectors in the metal–semiconductor–metal (MSM) configuration, including Schottky photodetectors [1,19,24,25,28-32]. A comparison of MSM photodetectors based on ZnMgO films prepared by spin coating and spray pyrolysis performed recently revealed that the sensitivity of the structures prepared by spin coating is higher as compared to those obtained by spray pyrolysis, while the photoresponse to UV irradiation is faster in devices based on spray pyrolysis films [29].

Solar-blind UV photodetectors with the highest responsivity to date were demonstrated on sapphire substrates by introducing ZnO or Al_2O_3 buffer layers [11,16]. With respect to photodetectors with p–n junctions, some photodetectors have been demonstrated on p-type Si [2,4] because p-type doping is still a big challenge to ZnO-based semiconductors. Liang et al. demonstrated a ZnMgO/p-Si heterojunction solar-blind UV photodetector with a BeO buffer layer [35].

In terms of the crystal structure of ZnMgO films used in photodetectors, three types of structures are used, namely, hexagonal wurtzite structure (w-ZnMgO), cubic rock salt structure (c-ZnMgO) and films with mixed-phase (m-ZnMgO) [5]. Since the crystal structure of the alloy changes from w-ZnMgO to c-ZnMgO with increasing Mg content, the coexistence of two structures in ZnMgO films is unavoidable in the structure transformation process, in a certain interval of Mg concentrations. The phase segregation process was investigated in detail by means of X-ray diffraction, element-specific near-edge X-ray absorption fine structure (NEXAFS), electron dispersive spectroscopy (EDS), atomic force microscopy (AFM), UV–vis spectroscopy, photoluminescence (PL) and resistivity measurements in $Zn_{1-x}Mg_xO$ thin films deposited by the sol–gel spin-coating route in the composition range $x = 0.00–0.40$ [23]. It was found that the phase segregation manifests itself starting at a Mg content of $x = 0.25$. However, the results showed that films are deposited with wurtzite structure as the dominant phase even after phase segregation in the investigated Mg concentration interval. The issue of phase segregation was also investigated via selective resonant Raman scattering in a wider composition range of $x = 0.00–0.78$ for $Zn_{1-x}Mg_xO$ thin films grown by reactive DC magnetron co-sputtering [12]. It was shown that this investigation technique is highly sensitive for the detection of embedded structural inhomogeneities, and it was found that the phase segregation occurs in the range of $x = 0.35–0.65$ with coexistence of both wurtzite and NaCl structures.

In addition to crystallographic structure fluctuations, compositional fluctuations at the microscopic level are even more likely in $Zn_{1-x}Mg_xO$ alloys. Compositional fluctuations have been deduced from photoluminescence (PL), photoluminescence excitation (PLE) and optical absorption (OA) spectroscopy investigations in w-ZnMgO films produced by RF-MBE in the composition range $x = 0.00–0.37$ [36] and $x = 0.27–0.55$ [10], respectively. The observed Stokes shifts were indicative of the presence of band tail states introduced by alloying, while the “S-shaped” temperature dependence of the maximum PL emissions was explained in terms of exciton localization in potential traps induced by Mg compositional fluctuations. The fluctuations in the local arrangement of Mg and Zn atoms have been also recently investigated by means of cathodoluminescence (CL) and OA spectroscopy in c-ZnMgO films produced by CVD in the composition range $x = 0.61–0.81$ [17], where a relatively large Stokes-like shift of 0.7–0.8 eV was observed. The understanding of the influence of compositional fluctuations in sol–gel spin-coated ZnMgO thin films on their properties is of particular importance. Towards this goal, the present study explores the PL characteristics of $Zn_{1-x}Mg_xO$ films in the composition range $x = 0.00–0.40$, under excitation with sub-bandgap photon energies from the 325 nm line of a He–Cd laser. Some possible applications of these films as UV photodetectors are also discussed.

Results and Discussion

Figure 1a compares the morphology of ZnMgO films deposited by spin coating and aerosol spray pyrolysis methods. Both methods produce thin films with uniform morphology. However, the roughness of films prepared by spin coating is larger as compared to those prepared by aerosol spray pyrolysis. The roughness parameters of films were determined from the analysis of AFM images as published in our previous paper [28]. Graphical representations of the AFM profiles for films prepared by spin coating and aerosol spray pyrolysis are presented in Figure 1b. The RMS values deduced from the AFM profiles were found to be of 12 nm and 5 nm for ZnMgO films prepared by spin coating and aerosol deposition, respectively.

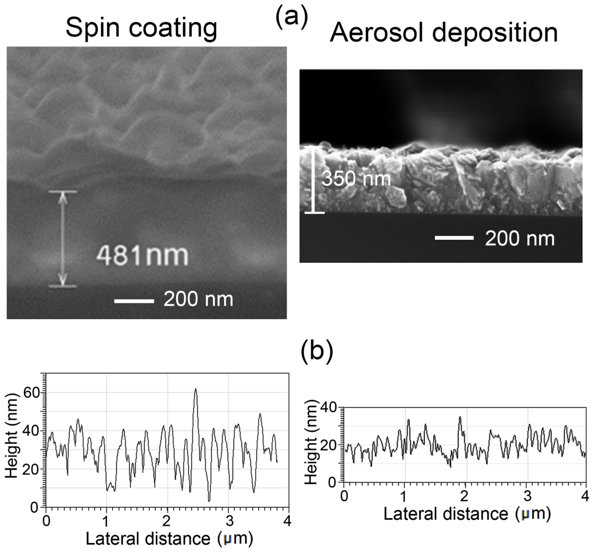

Figure 1: a) SEM images of ZnMgO films deposited on p-Si substrates by spin coating (left column) and aerosol deposition (right column) methods. b) Graphical representations of the AFM profiles for ZnMgO films.

As described in the experimental section, the thickness of films prepared by spin coating is determined by the number of cycles applied. One should note that the morphology of films deposited by spin coating and subjected to post-deposition annealing at 400 °C and 500 °C is similar. However, the morphology degrades for films annealed at temperatures higher than 600 °C. Figure 2 compares the surface morphology of films prepared by aerosol spray pyrolysis and spin coating annealed at 500 °C with the morphology of the film prepared by spin coating annealed at 650 °C. The analysis of the morphology in Figure 2a and Figure 2b corroborate the results of the AFM analysis revealing a larger roughness of films prepared by spin coating as compared to those prepared by aerosol spray pyrolysis. At the same time, the annealing of films at 650 °C (see Figure 2c) leads to deterioration of the morphology resulting in numerous cracks.

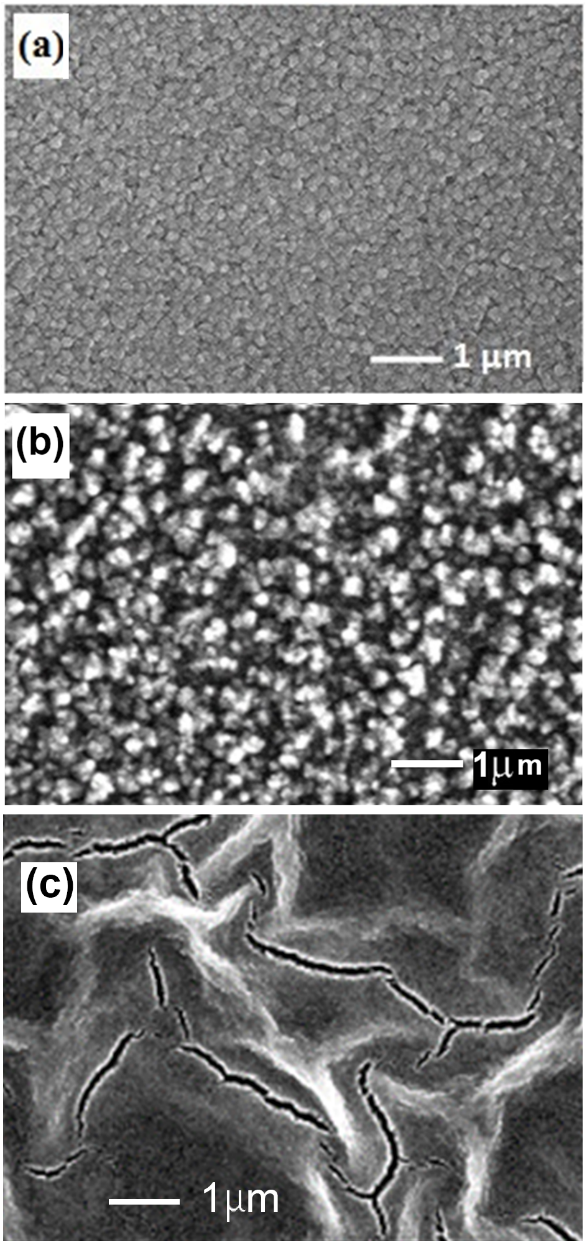

Figure 2: a) SEM image of a ZnMgO film prepared by aerosol spray pyrolysis. b) SEM image of a ZnMgO film prepared by spin coating and annealed at 500 °C. c) SEM image of a ZnMgO film prepared by spin coating and annealed at 650 °C.

We suppose that the difference in roughness of films prepared by the two methods is determined by the specific features of the technology. Namely, the deposition of films by spray pyrolysis occurs in a single technological step, while ten cycles are applied in spin coating, and the deposited film is annealed in the eleventh step. Apart from that, the deposition of films with spray pyrolysis is performed at a relatively high temperature of the substrate (400–650 °C), while the substrate is maintained at room temperature during the spin coating.

The influence of the film thickness on the morphology was not investigated specifically in this paper. However, it was observed that the film roughness increases with increasing film thickness from 100 nm to 500 nm. Thus, the morphology parameters, as well as the electrical parameters, should be compared for films with as close as possible thicknesses. The roughness of films prepared by spin coating is also determined by the viscosity and concentration of the solution used as well as by the rotational speed of the substrate.

The composition of the prepared films was determined by energy dispersive X-ray analysis (EDAX). Examples of the elemental composition analysis are presented in Figure 3 for ZnO and $Zn_{0.6}Mg_{0.4}O$ films. The results of measurements demonstrate stoichiometric compositions within limits of the errors defined by instrumental accuracy.

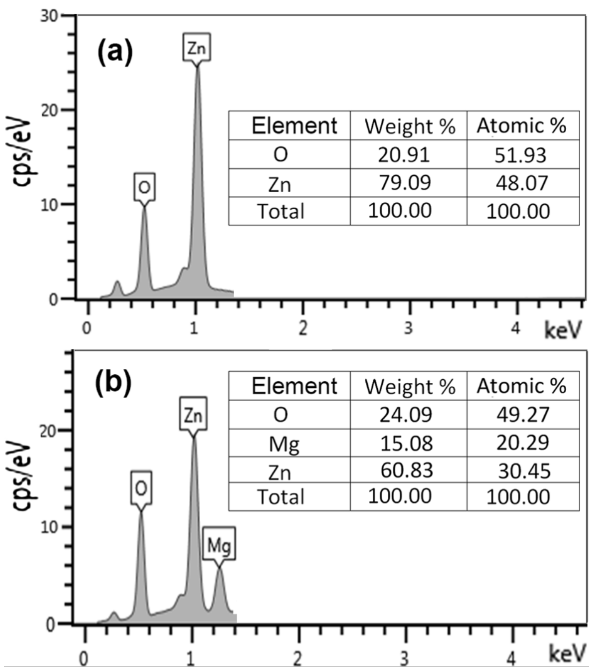

Element	Weight %	Atomic %
O	20.91	51.93
Zn	79.09	48.07
Total	100.00	100.00

Element	Weight %	Atomic %
O	24.09	49.27
Mg	15.08	20.29
Zn	60.83	30.45
Total	100.00	100.00

Figure 3: Elemental composition of a ZnO (a) and a $Zn_{0.6}Mg_{0.4}O$ (b) film determined by EDAX analysis.

The luminescence was investigated in films annealed at 400 °C and 500 °C. As seen from Figure 4, the PL spectra of films annealed at 500 °C consist of a broad emission band at both room temperature and low temperatures, which shifts to higher photon energies with increasing Mg content in the alloy. However, the position of the PL band does not follow the increase of the alloy bandgap with increasing *x* value. The higher the *x* value, the larger the difference between the bandgap and the PL band maximum.

Table 1 compares the position of the PL band with the bandgap of the alloy. Moreover, the luminescence is excited by the photon energy (3.81 eV) much lower than the bandgap for the thin film with the x value of 0.40 (4.28 eV).

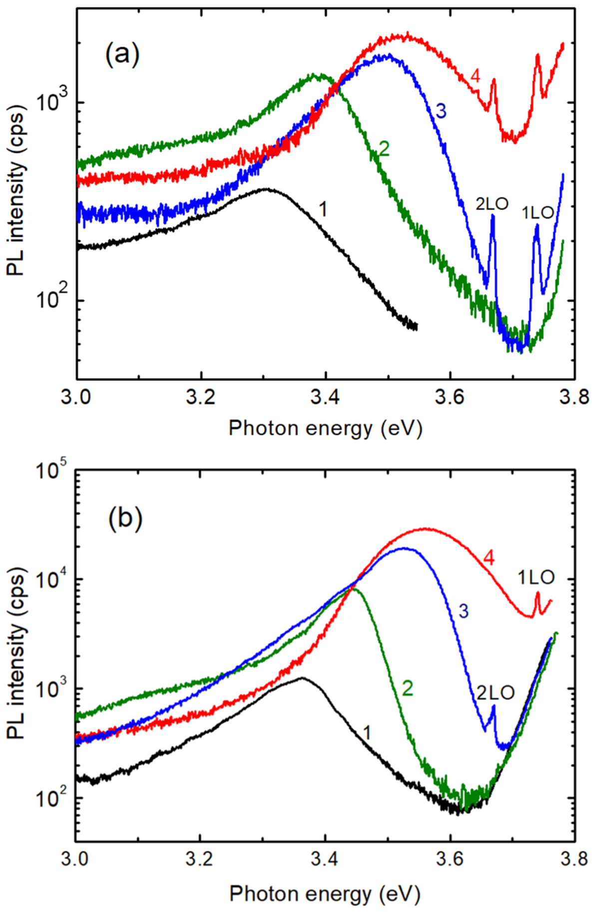

Figure 4: PL spectra of $Zn_{1-x}Mg_xO$ films deposited by spin coating with *x* values of 0.00 (1); 0.05 (2); 0.15 (3); and 0.40 (4), annealed at 500 °C and measured at a) 300 K and b) 20 K.

Table 1: The PL band spectral position and the bandgap value for ZnMgO films at room temperature.

x value	PL band maximum (eV)	Alloy bandgap (eV)[a]
0.00	3.30	3.36
0.05	3.39	3.47
0.15	3.50	3.70
0.40	3.53	4.28

[a]From [37].

The same is true for the luminescence measured at low temperature (Table 2). The bandgap of the alloy at low temperature was recalculated from the known values at room temperature, taking into account that the bandgap increases by around 80 meV with the decrease of temperature from 300 K to 20 K [38].

These observations are explained by the formation of large band tails in the density of states of solid solutions. It was shown that large random local-potential fluctuations occur in highly doped

Table 2: The PL band spectral position and the bandgap value for ZnMgO films at 20 K.

x value	PL band maximum (eV)	Alloy bandgap (eV)
0.00	3.36	3.44
0.05	3.45	3.55
0.15	3.53	3.78
0.40	3.56	4.36

and compensated semiconductors [39] and solid solutions [40] due to the microscopic inhomogeneity caused by impurity distribution in the first case and composition distribution in the second case. This spatially fluctuating band structure results in the formation of deep band tails in the gap.

As for the samples annealed at 400 °C, the luminescence spectra revealed the presence of two PL bands, as shown in Figure 5, which is indicative of the presence of two components in the samples. The lower energy PL band comes from ZnO crystallites embedded into the ZnMgO alloy matrix, which is responsible for the high energy broad PL band. To demonstrate that the low energy PL band is related to ZnO crystallites, it is compared to the spectrum of a high quality ZnO crystal measured at low temperature (curve 4 in Figure 5b). One can see that the spectral position of the main PL bands coincides well. In the ZnO single crystal, the main PL band at 3.359 eV is associated with the radiative recombination of neutral donor bound excitons (D^0X) [38,41,42]. The shoulder at higher photon energies is due to the recombination of free A excitons, while the PL bands at lower photon energies represent the LO-phonon replicas of the AX and D^0X bands at 3.29–3.31 eV, and the 2LO-phonon replicas at 3.22–3.24 eV. The PL band at 3.359 eV in films comes also from the recombination of D^0X excitons in ZnO crystallites, while the PL bands at 3.324 eV, 3.267 eV and 3.202 eV are related most likely to free-to-bound transitions due to some impurities in the ZnO crystallites.

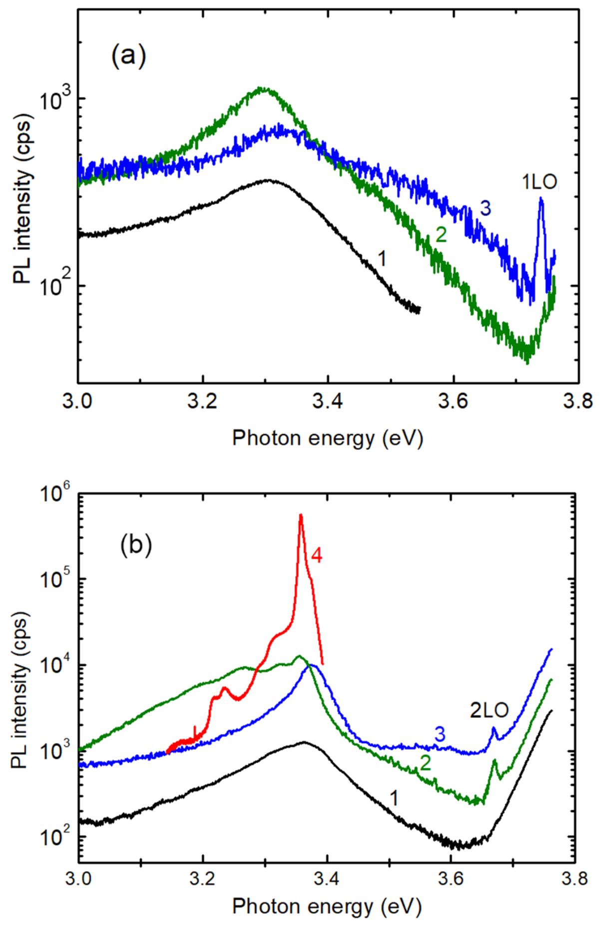

Figure 5: PL spectra of $Zn_{1-x}Mg_xO$ films deposited by spin coating with x values of 0.00 (1); 0.10 (2); and 0.25 (3), annealed at 400 °C and measured at a) 300 K and b) 20 K. For comparison, the spectrum of a bulk ZnO single crystal is shown by curve (4).

Therefore, the annealing temperature of 400 °C is not enough for the production of single phase ZnMgO films by sol–gel spin coating. On the other hand, ZnMgO:ZnO composite films with ZnO nanoparticles embedded into the ZnMgO matrix are useful for fast electron transport and high charge balance in quantum dot light emitting diodes [22].

The multiphase composition of films prepared by spin coating and annealed at temperatures lower that 450 °C was revealed by X-ray diffraction (XRD) analysis. As one can see from Figure 6b, reflexes related to ZnO inclusions (PDF Card No. 01-075-1533) are observed in the film annealed at 400 °C, along with those related to $Zn_{0.8}Mg_{0.2}O$ (PDF Card No. 01-078-3032). The peak around 43° can be assigned to some trace of MgO, while those at 38.5° and 44° could be due to some Zn clusters [43]. A peak at 40.5° marked with an asterisk in Figure 6b was previously found in ZnO nanopowders prepared by the sol–gel method with zinc acetate dihydrate as a precursor [44]. In contrast to this, only peaks related to the $Zn_{0.8}Mg_{0.2}O$ phase are observed in the film annealed at 500 °C. Silicon substrates were used for films annealed at temperatures higher than 500 °C to avoid softening of the glass substrate.

Table 3 summarizes the PL band position at 20 K and at room temperature in ZnMgO films prepared by sol–gel spin coating.

A model for the band tail distribution and the PL position at 20 K is proposed in Figure 7 for ZnMgO films.

For the films of $Zn_{0.90}Mg_{0.10}O$ and $Zn_{0.85}Mg_{0.15}O$, the laser line excitation energy is higher than the bandgap, while for the films of $Zn_{0.75}Mg_{0.25}O$ and $Zn_{0.60}Mg_{0.40}O$ the photon excita-

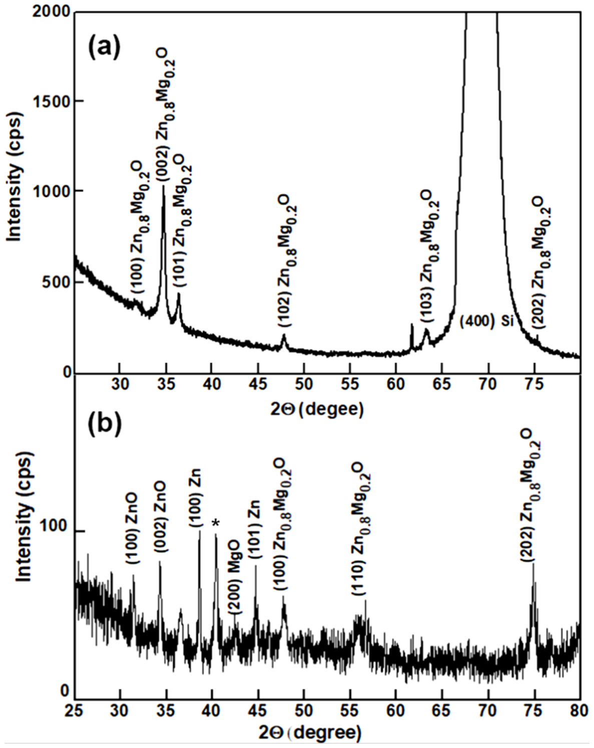

Figure 6: a) XRD pattern of a $Zn_{0.8}Mg_{0.2}O$ film deposited by spin coating on a Si substrate and annealed at 500 °C. b) XRD pattern of a $Zn_{0.8}Mg_{0.2}O$ film deposited by spin coating on a glass substrate and annealed at 400 °C.

Table 3: The summarized PL band maximum in $Zn_{1-x}Mg_xO$ films.

x value	PL band position at 20 K (eV)	PL band position at 300 K (eV)
0.00	3.36	3.30
0.05	3.45	3.39
0.10	3.52	3.45
0.15	3.53	3.50
0.25	3.56	3.50
0.40	3.56	3.53

tion energy is lower that the bandgap, and the luminescence is excited by transitions between the states from the band tails. After excitation, the carriers relax to the minimum possible energy in the band tails, which determines the spectral position of the PL band. With increasing *x* value from 0 to 0.40, the deepness of band tails in the gap increases to about 400 meV.

One can see from Figure 4 and Figure 5 that narrow emission lines related to resonance Raman scattering (RRS) are present in the emission spectrum from the ZnMgO films in addition to the broad PL bands, which is indicative of the high optical prop-

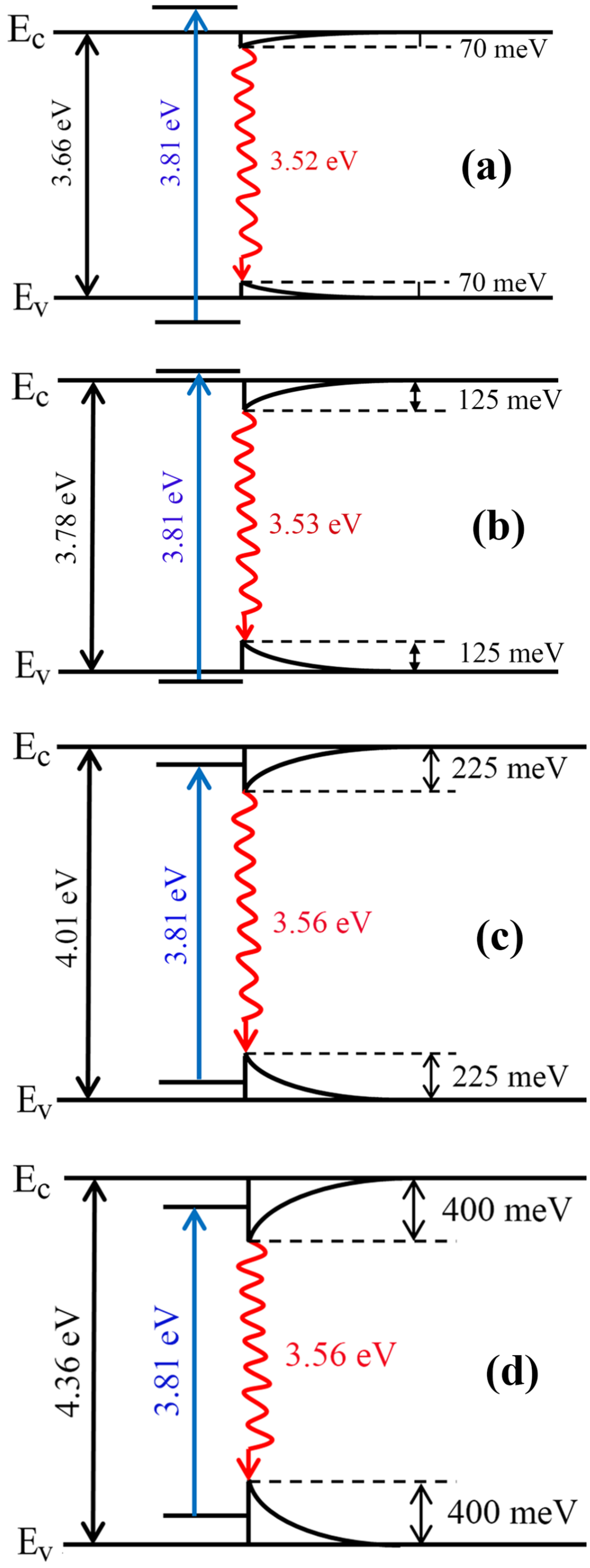

Figure 7: A model for the band tails distribution at 20 K in $Zn_{1-x}Mg_xO$ films with the *x* value composition of a) 0.10; b) 0.15; c) 0.25 and d) 0.40.

erties of the films produced by sol–gel spin coating. RRS from solids can be observed if the energy of the incoming or scattered photons matches real electronic states in the material. One refers to incoming and outgoing resonance, respectively [38,45-47]. Taking into account the band gap value and the width of band tails in ZnMgO thin films with various compositions at temperatures at which the emission spectra were measured (20 K and 300 K), and their correlations with the energy of the incident excitation photons (3.81 eV) and the energy of photons scattered by 1LO (3.74 eV) and 2LO (3.67 eV) phonons, Table 4 summarizes the conditions of RRS at the respective temperatures.

Therefore, according to Table 4, clear 2LO RRS peaks are observed in Figure 5b for the $Zn_{0.90}Mg_{0.10}O$ and $Zn_{0.75}Mg_{0.25}O$ samples at low temperature, and a 1LO RRS peak is found in Figure 5a for the $Zn_{0.75}Mg_{0.25}O$ sample at room temperature. For the sample $Zn_{0.85}Mg_{0.15}O$, the 2LO RRS peak is observed at low temperature in Figure 4b, and the peaks corresponding to 1LO RRS and 2LO RRS lines are revealed in Figure 4a at room temperature. Finally, lines corresponding to 1LO RRS and 2LO RRS processes are observed in Figure 4a and Figure 4b due to the interaction of the large band tails with both the incident and scattered photons in the $Zn_{0.60}Mg_{0.40}O$ sample.

The prepared ZnMgO thin films were tested for photodetector applications in the metal–semiconductor–metal (MSM) design configuration with coplanar metal Pd contacts in our previous paper [29]. The films demonstrated photosensitivity under UV light irradiation, where the photosensitivity was much higher in samples prepared by spin coating as compared to those prepared by aerosol spray pyrolysis. Additionally, the resistivity of films deposited by spin coating was found to be much higher. Apart from that, a long duration relaxation of photoconductivity was shown to be characteristic for films prepared by spin coating, while a fast response to irradiation was observed in samples prepared by aerosol spray pyrolysis.

Similar to the issues about the influence of the technology on the morphology of films discussed above, we suppose that the difference in the electrical parameters of films prepared by the two methods is determined by the specific features of the technology. The concentration of unintentionally introduced impurities and intrinsic defects is different with the two methods, particularly due to different numbers of technological steps and the different temperature of the substrate during the deposition processes. In our opinion, the higher resistivity of the films prepared by spin coating as compared to those obtained by spray pyrolysis indicates a higher degree of conductivity compensation, due to the higher concentration of acceptor levels introduced during spin coating.

Long duration relaxation of photoconductivity and persistent photoconductivity was previously observed in highly doped and compensated semiconductors [39], porous semiconductors [48] and solid solutions [40]. The origin of these phenomena was assumed to be the same in different materials, and it was attributed to random local-potential fluctuations. As mentioned above, the random local-potential fluctuations are also responsible for the emergence of broad PL bands in the near bandgap spectral region. These potential fluctuations lead to the formation of potential barriers, which have to be overcome for the recombination of photoexcited carrier to occur during the relaxation processes. On the other hand, the mechanisms for attaining such potential fluctuations were found to be different. In highly doped semiconductors, the amplitude of potential fluctuations is determined by the degree of doping and conductivity compensation. In porous semiconductors the amplitude is determined by the degree of porosity, while it is a function of local fluctuations of the composition in solid solutions, includ-

Table 4: The conditions of resonance Raman scattering in ZnMgO films for various compositions and temperatures.

Thin film composition	*T* = 20 K	*T* = 300 K
$Zn_{0.90}Mg_{0.10}O$	Bandgap (3.66 eV) in resonance with the 2LO scattered photon (3.67 eV). (Outgoing resonance)	No RRS lines
$Zn_{0.85}Mg_{0.15}O$	Bandgap (3.78 eV) in resonance with the incident photon (3.81 eV). (Ingoing resonance)	Bandgap (3.70 eV) in resonance with the 1LO scattered photon (3.74 eV). Band tails in resonance with the 2LO scattered photon (3.67 eV). (Outgoing resonance).
$Zn_{0.75}Mg_{0.25}O$	Band tails in resonance with the incident photon and with the 2LO scattered photon. (Combined resonance)	Band tails in resonance with the incident photon. (Ingoing resonance)
$Zn_{0.60}Mg_{0.40}O$	Band tails in resonance with the incident photon and with the 1LO scattered photon. (Combined resonance)	Band tails in resonance with the incident photon and with the 1LO scattered photon. (Combined resonance)

ing ZnMgO. The observation of the long duration component in the relaxation of photoconductivity in ZnMgO films deposited by spin-coating corroborates the data deduced from the analysis of photoluminescence spectra. At the same time, the lack of such a component in films prepared by aerosol deposition may be interpreted as reduced local composition fluctuations and lower local-potential fluctuations in such films. This statement is corroborated by the comparison of PL spectra of films prepared by the two methods. For example, Figure 8 compares the PL spectra of two films with the composition of $Zn_{0.85}Mg_{0.15}O$ prepared by spin coating and aerosol spray pyrolysis, measured at low temperature (20 K) and room temperature.

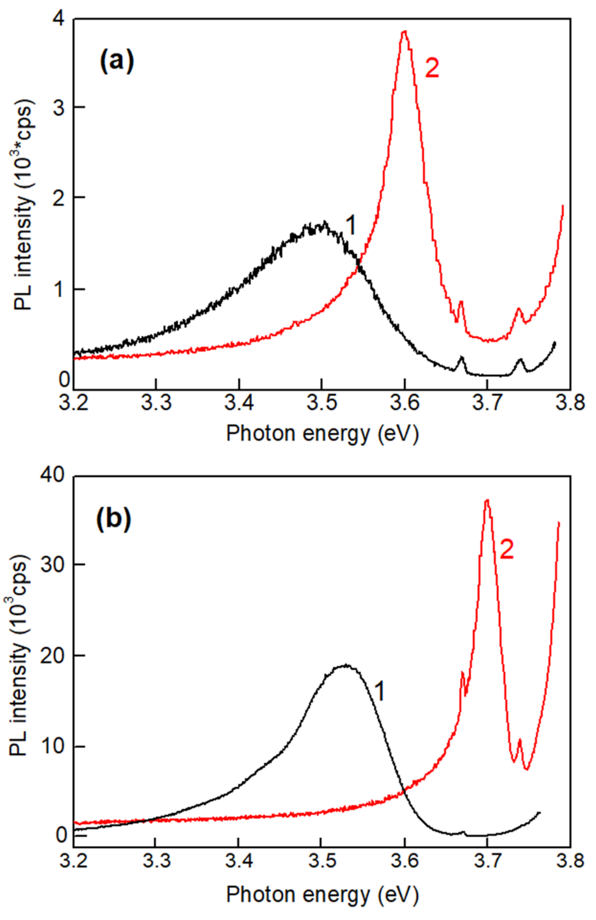

Figure 8: PL spectra of $Zn_{0.85}Mg_{0.15}O$ films by spin coating (curve 1) and aerosol spray pyrolysis (curve 2) measured a) at room temperature and b) at 20 K with a linear intensity axis.

One can see that the PL band in the film prepared by spay pyrolysis is much narrower as compared to the band in the film prepared by spin coating, and it is shifted to higher photon energy, i.e., closer to the bandgap position. Apart from that, the luminescence in films prepared by aerosol spray pyrolysis is not excited, when the x value is higher than 0.15. This observation indicates that the band tails are very narrow, if there are any. It could also be that the local-potential fluctuations in films prepared by spray pyrolysis are due to inhomogeneous distribution of intrinsic defects or unintentional doping impurities, as previously observed in undoped [38,49] or Cu, Ni, Co, or Al doped [46,50] ZnO materials, instead of local composition fluctuations.

Usually, the full width at half maximum (FWHM) of the PL band in ZnO with carrier concentration in the range of 10^{18} cm^{-3} to 10^{19} cm^{-3} is less than 50 meV. The concentration should be in the range of 10^{20} cm^{-3} to 10^{21} cm^{-3} to reach a FWHM value of 200 meV, i.e., the material should be highly conductive. On the other hand, the FWHM of PL bands in films prepared by spin coating reaches values of 200 meV, while the material is highly resistive, as mentioned above. This means that the formation of large band tails in films prepared by spin coating cannot be attributed to doping with impurities or to intrinsic defects, but to local composition fluctuations. The observed PL band also cannot be attributed to low concentration impurities or intrinsic defects since the PL bands related to such impurities in the region of the absorption edge are narrow (they are due to either free-to-bound transitions or donor-acceptor transitions) [41]. Wider PL bands related to impurities are observed in the visible spectral range, but this is not the subject of this paper.

Finally, the ZnMgO films deposited on p-type Si substrates were tested for photodetector applications in a heterostructure design with a metallic contact deposited on the n-ZnMgO film and another contact on the p-type Si substrate. Figure 9 and Figure 10 compare the current–voltage characteristics of p-Si/n-$Zn_{1-x}Mg_xO$ heterojunctions for two films deposited by spin coating with x values of 0.10 (Figure 9) and 0.40 (Figure 10). One can see from Figure 9b and Figure 10b that in both cases the current–voltage characteristic does not fit the classical formula for a p–n junction, $I = I_S\left[\exp\left(\frac{qU}{nkT}\right)-1\right]$, which should be a straight line for the forward bias in the semi-logarithmic coordinates. On the contrary, the characteristics are fit to straight lines in the double logarithmic coordinates (Figure 9c and Figure 10c). Moreover, the investigated heterojunctions work as photodetectors at forward bias, while a classical p–n junction should function as a photodetector at reverse bias.

Since the current–voltage characteristics are fit to straight lines in the log–log coordinates, it means that they correspond to a power function $I \propto U^n$, according to the Lampert theory [51]. For the heterojunction with a $Zn_{0.9}Mg_{0.1}O$ film in the dark, the n value is about 4, while it becomes equal to 2 under illumination, which corresponds to the space charge limited (SCL) current injection according to the Mott–Gurney (MG) law [52]. For

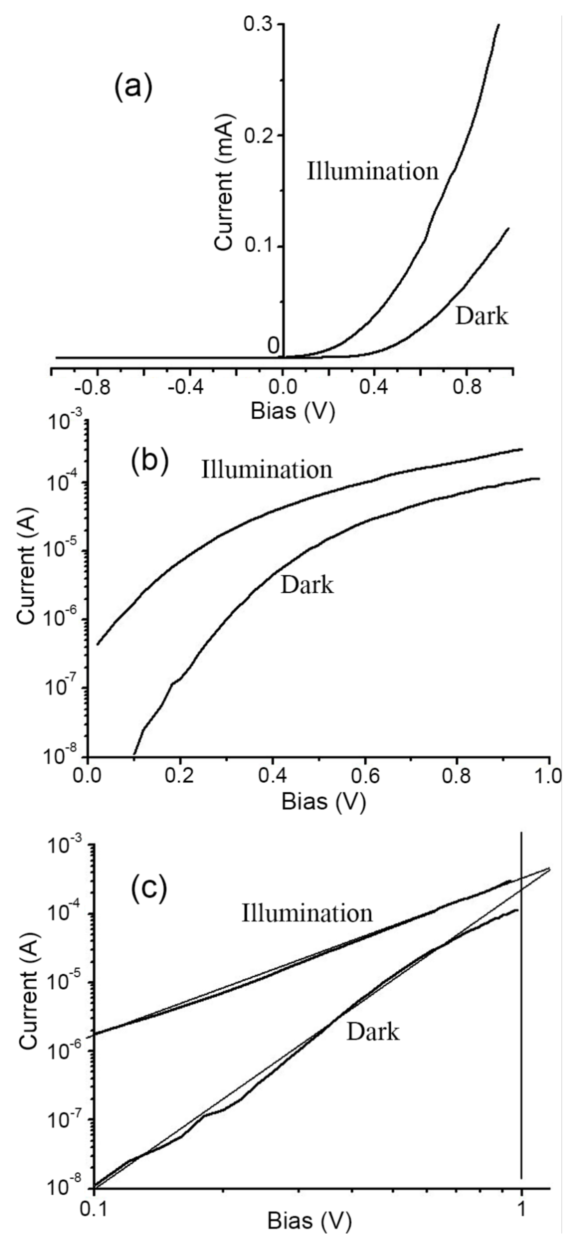

Figure 9: Current–voltage characteristics in dark and under UV illumination for a p-Si/n-$Zn_{0.9}Mg_{0.1}O$ heterostructure plotted on linear (a), semi-logarithmic (b) and double logarithmic coordinates (c).

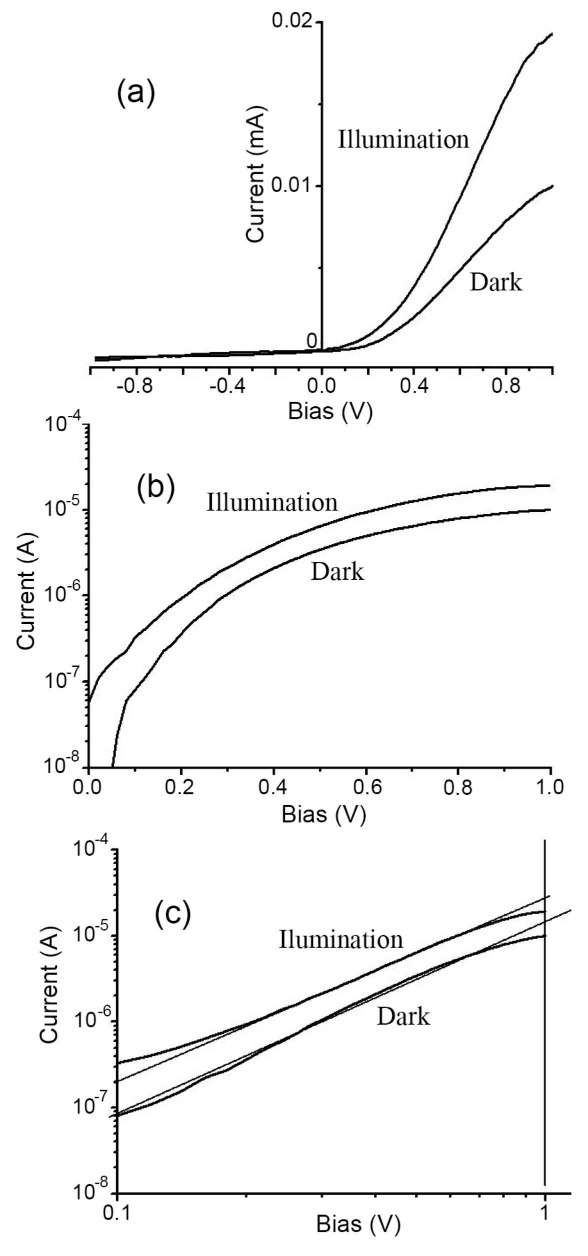

Figure 10: Current–voltage characteristics in dark and under UV illumination for a p-Si/n-$Zn_{0.6}Mg_{0.4}O$ heterostructure plotted on linear (a), semi-logarithmic (b) and double logarithmic coordinates (c).

the heterojunction with a $Zn_{0.6}Mg_{0.4}O$ film, the current–voltage characteristics fit to the MG law both in the dark and under illumination (see Figure 10c). These observations suggest that the investigated heterojunctions work at forward bias as injection photodiodes [53,54].

A more detailed investigation of photodetectors developed on ZnMgO films, including correlations between PL and sensing properties, is in progress in our laboratory, but the results will be published in a separate paper.

Conclusion

The results of this study demonstrate the preparation of ZnMgO thin films by spin-coating on Si substrates with homogeneous morphology at the macrosopic level. However, compositional fluctuations of the alloy are deduced at the microscopic level from the investigation of photoluminescence spectra. The local potential fluctuations induced by compositional fluctuations lead to the formation of deep band tails in the gap, which make it possible to excite photoluminescence with under-bandgap photon energies. The potential fluctuations also result in a long duration relaxation of photoconductivity in photodetectors prepared on these films. The p-Si/n-$Zn_{1-x}Mg_xO$ heterojunction photodetectors work at forward bias as injection photodiodes. The performed investigations demonstrate that post-deposition annealing at 500 °C is needed for the production of wurtzite single crystallographic phase $Zn_{1-x}Mg_xO$ films in the composition range of $x = 0.00–0.40$. Annealing at higher temperature leads to morphology degradation, while thermal treatment at lower temperatures is not enough for producing single phase films, ZnO nanoparticles being embedded into the ZnMgO matrix, as deduced from photoluminescence spectra and XRD analysis. Nevertheless, such films could also find specific applications, for instance in quantum dot light emitting diodes.

Experimental

ZnMgO thin films were prepared by spin coating from sol–gel solutions containing $Zn(CH_3CO_2)_2$ and $Mg(C_2H_3O_2)_2$ acetates in respective proportions dissolved in 20 mL of 2-methoxyethanol + 0.5 mL of diethanolamine (DEA). 0.35 M solutions with Mg/Zn from 0 to 2/3 were prepared in an ultrasonic bath for 30 min at a temperature of 50–60 °C. Spin coating was performed at room temperature on glass or (100) on p-Si substrates in multiple coating cycles at a rotational speed of 2000 rpm with the rotation taking 20 s followed by drying the coated layer at 150 °C for 10 min. After the deposition of 10 layers, the sample was treated at a temperature in the range of 400–650 °C in air for one hour. For the purpose of comparison, thin films were also prepared by the aerosol spray pyrolysis method. A solution of zinc acetate dihydrate with 99.999% purity and magnesium acetate tetrahydrate with purity ≥ 99%, both purchased from Sigma-Aldrich, dissolved in ethanol (C_2H_5OH), was sprayed onto the substrate using a homemade sprayer with an O_2 gas flow. The substrate was heated in the temperature range of 400 °C to 650 °C during the deposition. 0.35 M zinc acetate and magnesium acetate solutions were mixed in an ultrasonic bath in various proportions to produce ZnMgO films with Mg content from 5% to 40%. A distance of 18 cm was experimentally chosen between the sprayer and the heated substrate in view of producing a uniform coverage of the film on the substrate. The solution was injected into the oxygen gas flow by means of a syringe controlled by a stepper motor (Jova Solutions TIMS-0201™), operated by a computer. The produced film thickness is determined by the rate of precursor solution injection and the duration of deposition process. Usually, an injection rate of 0.33 mL/min was used, and the deposition process lasted for 15 min.

The morphology and chemical composition microanalysis of the produced films were studied using a Zeiss Sigma SEM, Hitachi SU 8230, equipped with tools for energy dispersive X-ray analysis (EDAX). Atomic force microscopy (AFM) measurements were performed in tapping mode with a SOLVER Next (NT-MDT) instrument equipped with cone-shaped tips from monocrystalline silicon (tip radius ≈ 10 nm) on cantilevers with a stiffness of about 17 N/m. The root mean square (RMS) roughness parameters were calculated from the acquired topographic images using image processing software.

The continuous wave (cw) PL was excited by the 325 nm line of a He–Cd Kimmon laser and analyzed with a double spectrometer, ensuring a spectral resolution better than 1 meV. The samples were mounted on the cold station of a LTS-22-C-330 optical cryogenic system. The current–voltage characteristics and the photocurrent of the photodetector structures were measured with a Keithley 2400 Source Meter Unit (SMU).

Funding

The following sources of funding are acknowledged: National Agency for Research and Development of the Republic of Moldova (Grant No. 19.80013.50.07.02A/BL), Horizon 2020 research and innovation programme of the European Union (Grant No. 810652, NanoMedTwin project), Romanian Executive Agency for Higher Education, Research, Development and Innovation Funding (project ROFCC, Contract No. 25PCCDI/2018), Romanian Ministry of Research (project R3-PowerUP – ECSEL-JU POC 2014-2020 Contract No. 1/1.1.3/31.01.2018).

ORCID® iDs

Vadim Morari - https://orcid.org/0000-0003-3625-251X
Veaceslav V. Ursaki - https://orcid.org/0000-0003-4488-850X

References

1. Wu, C.-Z.; Ji, L.-W.; Liu, C.-H.; Peng, S.-M.; Young, S.-J.; Lam, K.-T.; Huang, C.-J. *J. Vac. Sci. Technol., A* **2011,** *29,* 03A118. doi:10.1116/1.3575552
2. Hou, Y. N.; Mei, Z. X.; Liang, H. L.; Ye, D. Q.; Gu, C. Z.; Du, X. L. *Appl. Phys. Lett.* **2013,** *102,* 153510. doi:10.1063/1.4802486
3. Shiau, J.-S.; Brahma, S.; Liu, C.-P.; Huang, J.-L. *Thin Solid Films* **2016,** *620,* 170–174. doi:10.1016/j.tsf.2016.09.037
4. Maity, S.; Sahu, P. P.; Bhunia, C. T. *IEEE Sens. J.* **2018,** *18,* 6569–6575. doi:10.1109/jsen.2018.2849089
5. Yang, J.-L.; Liu, K.-W.; Shen, D.-Z. *Chin. Phys. B* **2017,** *26,* 047308. doi:10.1088/1674-1056/26/4/047308
6. Kang, J.-W.; Choi, Y.-S.; Kim, B.-H.; Goo Kang, C.; Hun Lee, B.; Tu, C. W.; Park, S.-J. *Appl. Phys. Lett.* **2014,** *104,* 051120. doi:10.1063/1.4864282
7. Morshed, M. M.; Suja, M.; Zuo, M. Z.; Liu, J. L. *Appl. Phys. Lett.* **2014,** *105,* 211107. doi:10.1063/1.4902921
8. Kozuka, Y.; Tsukazaki, A.; Kawasaki, M. *Appl. Phys. Rev.* **2014,** *1,* 011303. doi:10.1063/1.4853535
9. Suja, M.; Bashar, S. B.; Debnath, B.; Su, L.; Shi, W.; Lake, R.; Liu, J. *Sci. Rep.* **2017,** *7,* 2677. doi:10.1038/s41598-017-02791-0
10. Liu, Z. L.; Mei, Z. X.; Wang, R.; Zhao, J. M.; Liang, H. L.; Guo, Y.; Kuznetsov, A. Y.; Du, X. L. *J. Phys. D: Appl. Phys.* **2010,** *43,* 285402. doi:10.1088/0022-3727/43/28/285402

11. Schoenfeld, W. V.; Wei, M.; Boutwell, R. C.; Liu, H. Y. *Proc. SPIE* **2014,** *8987,* 89871P. doi:10.1117/12.2045555
12. Thapa, D.; Huso, J.; Che, H.; Huso, M.; Morrison, J. L.; Gutierrez, D.; Grant Norton, M.; Bergman, L. *Appl. Phys. Lett.* **2013,** *102,* 191902. doi:10.1063/1.4805005
13. Thapa, D.; Huso, J.; Miklos, K.; Wojcik, P. M.; McIlroy, D. N.; Morrison, J. L.; Corolewski, C.; McCluskey, M. D.; Williams, T. J.; Grant Norton, M.; Bergman, L. *J. Mater. Sci.: Mater. Electron.* **2017,** *28,* 2511–2520. doi:10.1007/s10854-016-5825-2
14. Ohtomo, A.; Kawasaki, M.; Koida, T.; Masubuchi, K.; Koinuma, H.; Sakurai, Y.; Yoshida, Y.; Yasuda, T.; Segawa, Y. *Appl. Phys. Lett.* **1998,** *72,* 2466–2468. doi:10.1063/1.121384
15. Wang, X.; Saito, K.; Tanaka, T.; Nishio, M.; Nagaoka, T.; Arita, M.; Guo, Q. *Appl. Phys. Lett.* **2015,** *107,* 022111. doi:10.1063/1.4926980
16. Lee, H.-Y.; Tsai, W.-H.; Lin, Y.-C.; Lee, C.-T. *J. Vac. Sci. Technol., B: Nanotechnol. Microelectron.: Mater., Process., Meas., Phenom.* **2016,** *34,* 051207. doi:10.1116/1.4962745
17. Onuma, T.; Ono, M.; Ishii, K.; Kaneko, K.; Yamaguchi, T.; Fujita, S.; Honda, T. *Appl. Phys. Lett.* **2018,** *113,* 061903. doi:10.1063/1.5031174
18. Emanetoglu, N. W.; Muthukumar, S. N.; Wu, P.; Wittstruck, R. H.; Chen, Y.; Lu, Y. *IEEE Trans. Ultrason., Ferroelectr., Freq. Control* **2003,** *50,* 537–543. doi:10.1109/tuffc.2003.1201466
19. Wang, L. K.; Ju, Z. G.; Zhang, J. Y.; Zheng, J.; Shen, D. Z.; Yao, B.; Zhao, D. X.; Zhang, Z. Z.; Li, B. H.; Shan, C. X. *Appl. Phys. Lett.* **2009,** *95,* 131113. doi:10.1063/1.3238571
20. Chawla, S.; Jayanthi, K.; Chander, H. *Phys. Status Solidi A* **2008,** *205,* 271–274. doi:10.1002/pssa.200723149
21. Chen, X.; Ruan, K.; Wu, G.; Bao, D. *Appl. Phys. Lett.* **2008,** *93,* 112112. doi:10.1063/1.2987514
22. Zhang, Q.; Gu, X.; Zhang, Q.; Jiang, J.; Jin, X.; Li, F.; Chen, Z.; Zhao, F.; Li, Q. *Opt. Mater. Express* **2018,** *8,* 909–918. doi:10.1364/ome.8.000909
23. Singh, A.; Vij, A.; Kumar, D.; Khanna, P. K.; Kumar, M.; Gautam, S.; Chae, K. H. *Semicond. Sci. Technol.* **2013,** *28,* 025004. doi:10.1088/0268-1242/28/2/025004
24. Tsay, C.-Y.; Chen, S.-T.; Fan, M.-T. *Coatings* **2019,** *9,* 277. doi:10.3390/coatings9040277
25. Rana, V. S.; Rajput, J. K.; Pathak, T. K.; Purohit, L. P. *J. Alloys Compd.* **2018,** *764,* 724–729. doi:10.1016/j.jallcom.2018.06.139
26. Wei, M.; Deng, H.; Chen, H.; Chen, J. J. *Adv. Mater. Res.* **2009,** *60-61,* 110–113. doi:10.4028/www.scientific.net/amr.60-61.110
27. Chebil, W.; Boukadhaba, M. A.; Madhi, I.; Fouzri, A.; Lusson, A.; Vilar, C.; Sallet, V. *Phys. B (Amsterdam, Neth.)* **2017,** *505,* 9–16. doi:10.1016/j.physb.2016.10.028
28. Morari, V.; Brincoveanu, O.; Mesterca, R.; Balan, D.; Rusu, E.; Zalamai, V.; Prodana, M.; Ursachi, V.; Enachescu, M. Synthesis of $Mg_xZn_{1-x}O$ thin films by spin coating and aerosol deposition methods. In *The 9th ICMCS & The 6th CFM*, Publications by Technical University of Moldova, Chisinau, 19–21 Oct 2017, p. 483. ISBN 978–9975-4264-8-0.
29. Morari, V.; Postolache, V.; Mihai, G.; Rusu, E.; Monaico, E.; Ursachi, V. V.; Nielsch, K.; Tiginyanu, I. M. Electrical and Photoelectrical Properties of Zn1−xMgxO Thin Films Obtained by Spin Coating and Aerosol Deposition Method. 4th International Conference on Nanotechnologies and Biomedical Engineering, IFMBE; Tiginyanu, I. M.; Sontea, V.; Railean, S., Eds.; Springer Nature: Switzerland, 2020; pp 105–109. doi:10.1007/978-3-030-31866-6_23
30. Winkler, N.; Wibowo, R. A.; Kautek, W.; Dimopoulos, T. *J. Mater. Chem. C* **2019,** *7,* 3889–3900. doi:10.1039/c8tc06097e
31. Lopez-Ponce, M.; Hierro, A.; Marín-Borrás, V.; Tabares, G.; Kurtz, A.; Albert, S.; Agouram, S.; Muñoz-Sanjosé, V.; Muñoz, E.; Ulloa, J. M. *Semicond. Sci. Technol.* **2015,** *30,* 105026. doi:10.1088/0268-1242/30/10/105026
32. Hierro, A.; Tabares, G.; Lopez-Ponce, M.; Ulloa, J. M.; Kurtz, A.; Munoz, E.; Marin-Borras, V.; Munoz-Sanjose, V.; Chauveau, J. M. *Proc. SPIE* **2016,** *9749,* 97490W. doi:10.1117/12.2213697
33. Winkler, N.; Edinger, S.; Kaur, J.; Wibowo, R. A.; Kautek, W.; Dimopoulos, T. *J. Mater. Sci.* **2018,** *53,* 12231–12243. doi:10.1007/s10853-018-2482-2
34. Yan, W.; Tan, J.; Zhang, W.; Liang, Y.; Feng, S.; Lei, X.; Wang, H. *Superlattices Microstruct.* **2013,** *60,* 407–413. doi:10.1016/j.spmi.2013.05.021
35. Liang, H. L.; Mei, Z. X.; Zhang, Q. H.; Gu, L.; Liang, S.; Hou, Y. N.; Ye, D. Q.; Gu, C. Z.; Yu, R. C.; Du, X. L. *Appl. Phys. Lett.* **2011,** *98,* 221902. doi:10.1063/1.3595342
36. Wassner, T. A.; Laumer, B.; Maier, S.; Laufer, A.; Meyer, B. K.; Stutzmann, M.; Eickhoff, M. *J. Appl. Phys.* **2009,** *105,* 023505. doi:10.1063/1.3065535
37. Yin, H.; Chen, J.; Wang, Y.; Wang, J.; Guo, H. *Sci. Rep.* **2017,** *7,* 41567. doi:10.1038/srep41567
38. Ursaki, V. V.; Tiginyanu, I. M.; Zalamai, V. V.; Rusu, E. V.; Emelchenko, G. A.; Masalov, V. M.; Samarov, E. N. *Phys. Rev. B* **2004,** *70,* 155204. doi:10.1103/physrevb.70.155204
39. Sheinkman, M. K.; Shik, A. Y. *Sov. Phys. - Semicond.* **1976,** *10,* 128–136.
40. Jiang, H. X.; Brown, G.; Lin, J. Y. *J. Appl. Phys.* **1991,** *69,* 6701–6708. doi:10.1063/1.348889
41. Meyer, B. K.; Alves, H.; Hofmann, D. M.; Kriegseis, W.; Forster, D.; Bertram, F.; Christen, J.; Hoffmann, A.; Straßburg, M.; Dworzak, M.; Haboeck, U.; Rodina, A. V. *Phys. Status Solidi B* **2004,** *241,* 231–260. doi:10.1002/pssb.200301962
42. Ursaki, V. V.; Tiginyanu, I. M.; Zalamai, V. V.; Masalov, V. M.; Samarov, E. N.; Emelchenko, G. A.; Briones, F. *J. Appl. Phys.* **2004,** *96,* 1001–1006. doi:10.1063/1.1762997
43. Qasim, I.; Mumtaz, M.; Nadeem, K.; Qamar Abbas, S. *J. Nanomater.* **2016,** 9781790. doi:10.1155/2016/9781790
44. Hasnidawani, J. N.; Azlina, H. N.; Norita, H.; Bonnia, N. N.; Ratim, S.; Ali, E. S. *Procedia Chem.* **2016,** *19,* 211–216. doi:10.1016/j.proche.2016.03.095
45. Yu, P. Y.; Cardona, M. *Fundamentals of Semiconductors: Physics and Materials Properties,* 4th ed.; Springer-Verlag: Berlin, Heidelberg, 2010. doi:10.1007/978-3-642-00710-1_4
46. Phan, T. L.; Vincent, R.; Cherns, D.; Nghia, N. X.; Ursaki, V. V. *Nanotechnology* **2008,** *19,* 475702. doi:10.1088/0957-4484/19/47/475702
47. Phan, T.-L.; Vincent, R.; Cherns, D.; Dan, N. H.; Yu, S.-C. *Appl. Phys. Lett.* **2008,** *93,* 082110. doi:10.1063/1.2968307
48. Monaico, E.; Postolache, V.; Borodin, E.; Ursaki, V. V.; Lupan, O.; Adelung, R.; Nielsch, K.; Tiginyanu, I. M. *Semicond. Sci. Technol.* **2015,** *30,* 035014. doi:10.1088/0268-1242/30/3/035014
49. Zalamai, V. V.; Ursaki, V. V.; Rusu, E. V.; Arabadji, P.; Tiginyanu, I. M.; Sirbu, L. *Appl. Phys. Lett.* **2004,** *84,* 5168–5170. doi:10.1063/1.1763980
50. Ursaki, V. V.; Lupan, O. I.; Chow, L.; Tiginyanu, I. M.; Zalamai, V. V. *Solid State Commun.* **2007,** *143,* 437–441. doi:10.1016/j.ssc.2007.06.001
51. Lampert, M. A. *Rep. Prog. Phys.* **1964,** *27,* 329–367. doi:10.1088/0034-4885/27/1/307

52. Mott, N. F.; Gurney, R. W. *Electronic processes in ionic crystals,* 2nd ed.; Oxford Clarendon Press, 1948.
53. Mirsagatov, S. A.; Leiderman, A. Y.; Ataboev, O. K. *Phys. Solid State* **2013,** *55,* 1635–1646. doi:10.1134/s1063783413080192
54. Mirsagatov, S. A.; Sapayev, I. B. *Semiconductors* **2014,** *48,* 1363–1369. doi:10.1134/s1063782614100212

License and Terms

The definitive version of this article is the electronic one which can be found at:
doi:10.3762/bjnano.11.75

BEILSTEIN JOURNAL OF NANOTECHNOLOGY

Microwave photon detection by an Al Josephson junction

Leonid S. Revin*[1,2], Andrey L. Pankratov[1,2,3], Anna V. Gordeeva[2], Anton A. Yablokov[1,2], Igor V. Rakut[2,3], Victor O. Zbrozhek[2] and Leonid S. Kuzmin[2,4]

Full Research Paper

Open Access

Address:
[1]Institute for Physics of Microstructures of RAS, GSP-105, Nizhny Novgorod, 603950, Russia, [2]Center of Cryogenic Nanoelectronics, Nizhny Novgorod State Technical University, Nizhny Novgorod, Russia, [3]Lobachevsky State University of Nizhny Novgorod, Nizhny Novgorod, Russia and [4]Chalmers University of Technology, SE-41296 Gothenburg, Sweden

Email:
Leonid S. Revin* - rls@ipmras.ru

* Corresponding author

Keywords:
aluminium; Josephson junction; microwaves; phase diffusion; photon counter; switching current distribution

Beilstein J. Nanotechnol. **2020,** *11,* 960–965.
doi:10.3762/bjnano.11.80

Received: 08 April 2020
Accepted: 10 June 2020
Published: 23 June 2020

This article is part of the thematic issue "Functional nanostructures for electronics, spintronics and sensors".

Guest Editor: A. S. Sidorenko

Abstract

An aluminium Josephson junction (JJ), with a critical current suppressed by a factor of three compared with the maximal value calculated from the gap, is experimentally investigated for application as a threshold detector for microwave photons. We present the preliminary results of measurements of the lifetime of the superconducting state and the probability of switching by a 9 GHz external signal. We found an anomalously large lifetime, not described by the Kramers' theory for the escape time over a barrier under the influence of fluctuations. We explain it by the phase diffusion regime, which is evident from the temperature dependence of the switching current histograms. Therefore, phase diffusion allows for a significant improvement of the noise immunity of a device, radically decreasing the dark count rate, but it will also decrease the single-photon sensitivity of the considered threshold detector. Quantization of the switching probability tilt as a function of the signal attenuation for various bias currents through the JJ is observed, which resembles the differentiation between N and $N + 1$ photon absorption.

Introduction

Currently, an important problem is the creation of single-photon counters in the gigahertz frequency range. Such devices are in demand in several areas, such as the search for axions, the alleged particles of dark matter [1-4] and quantum computing [5]. Commercially available single-photon detectors operate at frequencies of hundreds of terahertz and higher [6,7]. For the lower-frequency range, a new class of single-microwave-photon detectors is needed. With regard to this, a current-biased Josephson junction (JJ) is of particular interest for applications as a threshold detector since its phase dynamics is altered even by a weak probe field. Rich dynamics of the JJ constantly inspires new applications, such as thermometry [8,9], noise statistics [10-12] and single-photon detection [13].

There are, at least, two different approaches for the practical realization of single-photon detectors based on Josephson junctions, both having their advantages and disadvantages. The first approach relies on a continuous current sweep at a constant repetition rate and the measurements of the switching current distributions, from which the response and sensitivity can be determined [14-16]. In particular, in [16] the tunneling properties of a current-biased Josephson junction coupled with a resonator directly depend on the number of microwave photons in the resonator. The main disadvantages of this approach are the long initialization and freezing times of the detector. The detector works by slowly increasing the bias current from zero. This ramp takes seconds to avoid non-adiabatic excitation in a JJ. As soon as the detector switches, it must be reset by setting the current back to zero and waiting when a Josephson phase relaxes in a potential well. This implies a low repetition rate.

The second approach for experimental microwave detection [17,18] uses the switching events of a biased Josephson junction resulting from a single absorption. In contrast to the previous approach, this one requires less downtime of the detector, determined by the biasing time to the desired current only. However, the operation in this mode does not provide information on the number of absorbed photons and only above-threshold signals can be detected. Also, special care must be taken to minimize the false switching events of the detector due to thermal fluctuations and macroscopic quantum tunneling.

In this article the second approach is applied to a prototype of a single-photon counter described in [4]. We study the possibility of detecting photons in the gigahertz frequency range using an aluminium Josephson junction with a suppressed critical current. The main requirement to this counter is an extremely large lifetime (thousands of seconds), orders of magnitude larger than the switching time after the photon absorption (typically less than nanoseconds). In [4] it was shown theoretically that both the required sensitivity and the noise immunity can be reached at the same time in JJ with a suppressed critical current. Besides that, the mesoscopic junctions with low critical currents have received a great deal of interest themselves, since they exhibit Josephson phase diffusion [19-23].

The Josephson phase diffusion in small junctions has been studied both experimentally [24,25] and theoretically [26]. Recently, this regime has been observed also in layered high-temperature superconductors [27]. The significance of this effect depends on the ratio of thermal fluctuations k_BT, the damping parameter α and the Josephson energy E_J. Here we will consider a small tunnel junction with the thermal noise intensity of $\gamma = k_BT/E_J \geq 2 \times 10^{-2}$ and $\alpha > 0.1$, and show experimentally an unusually large lifetime of the superconducting state, which we attribute to phase diffusion according to [20]. The increase of the lifetime of the superconducting state due to phase diffusion was also observed in [28] under similar conditions. However, phase diffusion is expected to decrease the sensitivity to single photons for the same reason that it improves the noise immunity. To our knowledge, to date there are no works dedicated to the role of phase diffusion in the response to single photons. In the last section of the article, we show the experimental results of the switching probability induced by a weak microwave signal and discuss some features of the measured response, which may indicate the sensitivity to several photon bunches.

The analysis of the phase-diffusion phenomena is a special case of a general problem of the motion of a Brownian particle in a washboard potential in the framework of the resistively and capacitively shunted junction (RCSJ) model for the dynamics of the Josephson phase [29,30]. The tilt of the washboard potential is controlled by the bias current I and is defined as $E_J(I/I_C)$, where I_C is the critical current and $E_J = \hbar I_C/2e$. The particle moves along the potential in the presence of friction, the strength of which is characterized by $\alpha = \omega_p/\omega_c$, where $\omega_p = \sqrt{2eI_C / \hbar C}$ is the plasma frequency, $\omega_c = 2eI_CR_N/\hbar$ is the characteristic frequency, R_N is the normal state resistance and C is the capacitance.

The superconducting state of the JJ corresponds to the particle at rest in one well of the potential. The exit from this metastable state corresponds to the appearance of a finite voltage at the junction. In the case of low damping (but depending also on the barrier height and noise intensity), the particle, jumping over the barrier, gains enough energy to move along the potential in the running state. When the damping α is sufficiently large, the escape due to the thermal or quantum fluctuations does not necessarily lead to the appearance of the running state. After an escape event, the particle can move down the potential for several wells and then relax into one of the potential minima [24]. When barrier and noise are large, the exit from the well and the subsequent retrapping processes may occur many times at a given bias current.

The most evident signature of the phase diffusion phenomenon is the temperature dependence of the switching current distribution [21,31]. For underdamped junctions ($\alpha \ll 1$), the width of the switching current distributions monotonically decreases with decreasing temperature. In the case of moderately damped junctions ($\alpha > 0.2$), the switching dynamics changes due to phase diffusion, i.e., the width of the distribution decreases with increasing temperature. A change in the sign of the derivative of the second moment of the distribution is a reliable indicator of retrapping processes. Another sign of phase diffusion is an increase in the lifetime of the superconducting state in comparison with the classical Kramers' theory [32,33]. The exit of the particle from the well due to fluctuations does not lead to the instantaneous appearance of a final voltage at the Josephson junction, which can be seen in experiment as an increase of the noise immunity of the system.

The principle of operation of a single-photon counter based on a Josephson junction is the following: At an initial moment of time, the junction is in a superconducting state with bias current I close to the critical current. In standby mode, there is no voltage at the junction. An incoming external signal from a photon (current oscillations) can change the state of the system by switching it to a resistive state with a finite resistance value. At the same time the detector may be triggered spontaneously due to thermal fluctuations in the classical region of temperatures and tunneling through the barrier in the quantum case [15,34].

Experimental

Following the line proposed in [4], an aluminium Al/AlO$_x$/Al tunnel junction 0.4 × 2 μm^2 was fabricated using a self-aligned shadow evaporation technique. Its current–voltage characteristic shown in the inset of Figure 1 (see below) has a well-defined hysteresis. The double voltage gap of the junction is 0.38 mV, corresponding to the critical temperature of Al, T_C(Al) = 1.2 K, the capacitance is C ≈ 0.036 pF, the critical current density is 3.8×10^{-3} kA/cm^2 and the normal resistance is R_N = 2300 Ω, which gives the maximal possible value of the critical current $I_C^{\max} = 1.764\, kT_C/eR_N \approx 80$ nA. The measured critical current is I_C = 28 nA at a temperature of 20 mK. The damping of the Josephson junction calculated for the measured I_C is $\alpha = 0.24$.

The sample was mounted in an rf-proof box with a superconducting shielding on the coldest plate of a Triton 200 dry dilution refrigerator. The dc-bias wires were filtered with feed-through capacitors at the room temperature and RC filters at the 10 mK cryostat plate, minimizing the effect of unwanted low-frequency noise. In order to avoid ground loops, the measurement scheme was designed with a single ground.

For the switching current measurements, the bias current of the junction was ramped up at a constant rate of $\dot{I} = 5\times10^{-8}$ A/s. The voltage was measured using a low-noise room-temperature differential amplifier AD745 and was fed to a high-speed NI ADC-card. This signal was used to trigger a fast record of the switching current value. This procedure was repeated at least 5×10^3 times at each temperature, and as a result the switching current histograms were compiled in the temperature range between 1 K and 20 mK. For the lifetime measurements, the experimental setup was the same, except that the bias current was set to a predetermined value for 20 ms to prevent particle excitation caused by a rapid decrease in the barrier, and remained constant until the appearance of a gap voltage due to thermal noise or quantum tunneling. The lifetime measurements were repeated at least 200 times for each value of the bias current.

For a high-frequency experiment, a microwave signal was fed into the cryostat via a 2 m long phosphor bronze twisted-pair wiring with an attenuation of −15 dB/m at 9 GHz, and with a loop antenna near the JJ. The rf-signal from the external microwave synthesizer was attenuated using the voltage-controlled room-temperature attenuator, preliminarily calibrated with a commercial spectrum analyzer. The high-frequency signal was varied from a high power, at which the Shapiro steps and photon-assisted tunneling steps are well pronounced at the I–V-curve, to a low power, the presence of which can be observed only in the switching histograms and in the decrease of the superconducting state lifetime. While it is difficult to calibrate the whole rf path due to uncertainties in the twisted-pair wiring and the loop antenna, one can make estimates, based on the comparison of the potential barrier height of the JJ at 23 nA bias current and I_C = 28 nA (see the fit of the lifetime below). In this case, the potential barrier height is 1.3×10^{-24} J, while the photon energy at 9 GHz is 6×10^{-24} J. Thus, we are in the range where few-photon detection is possible.

Results and Discussion

In this section, we present preliminary results of the first measurements. First, we assemble the switching current distributions (Figure 1) and extract values for the mean switching current $\langle I_{SW} \rangle$ and standard deviation σ, which are plotted in Figure 2 for different temperatures of the chip. The decrease of $\langle I_{SW} \rangle$ with temperature increase indicates that here the thermal activation of the phase is the main switching mechanism. At

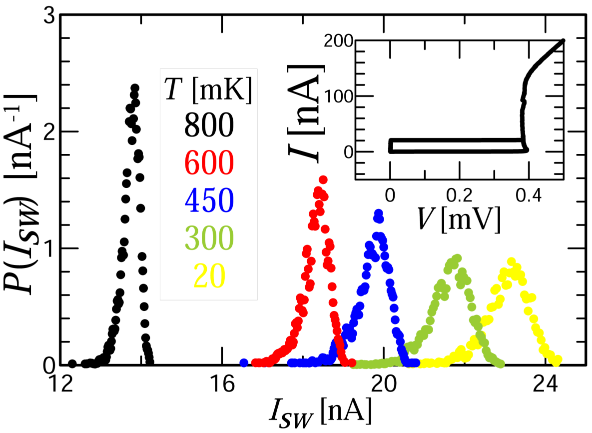

Figure 1: Experimentally measured histogram $P(I_{SW})$ of switching the Josephson junction to the resistive state for the current I_{SW} at the indicated temperatures. The inset shows the I–V curve of the junction at 20 mK.

temperatures below $T \approx 300$ mK there is a saturation both in $\langle I_{SW} \rangle$ and σ. The behavior of σ(T) in the entire temperature range of the experiment shows the well-known signature of phase diffusion, observed for example in [21,25,31].

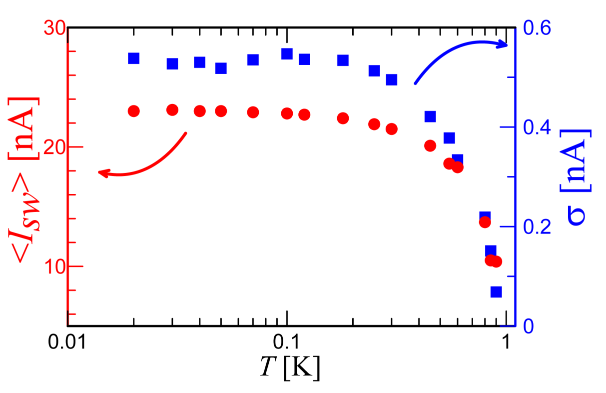

Figure 2: Temperature dependence of the mean switching current (left axis, red dots) and its standard deviation (right axis, blue squares).

The presence of phase diffusion can also explain the results of the lifetime (the inverse of the escape rate) measurements, shown in Figure 3. The lifetime of the superconducting state corresponds to the mean time of dark counts of a single-photon detector. We have measured the dependences of the lifetime for different bias currents and temperatures and without high-frequency signal. One can see the linear slope of the lifetime as a function of the bias current for 2–3 orders of magnitude on a logarithmic scale, which means the exponential dependence of the lifetime on the potential barrier height. The gentle slope of the experimental points, actually forming a plateau below 0.03 s in Figure 3, is due to time constants of the measurement setup. To find out more about the switching conditions the experimental curves have been fitted by the Kramers' formula for the lifetime in the following form [30,32,33] (for the overdamped case, see [35]):

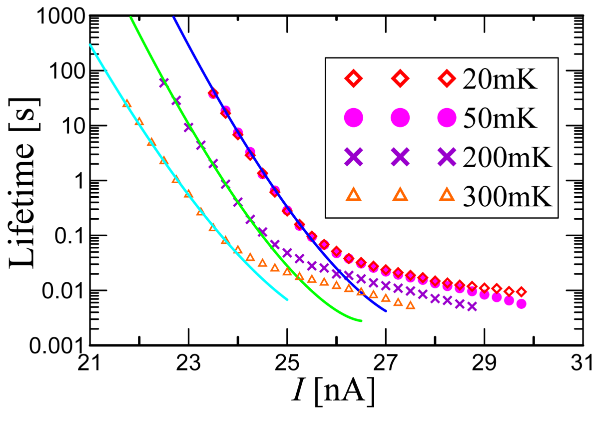

Figure 3: Experimental lifetime as function of the bias current for different sample temperatures (symbols) and fit with Equation 1 (solid curves).

$$\tau = \frac{f(\alpha)\exp(\Delta u/\gamma)}{\sqrt{1-i^2}}, \tag{1}$$

where $i = I/I_C$ is the dimensionless bias current, $\Delta u = 2\sqrt{1-i^2} + i[2\arcsin(i) - \pi]$ is the potential barrier height and $\gamma = I_T/I_C$ is the noise intensity and $I_T = 2ek_BT/\hbar$ is the fluctuational current, which can be calculated for a given temperature T as I_T [μA] = 0.042T [K] [29]. If the well and the barrier of a potential profile can be approximated by parabolas, then $f(\alpha)$ does not depend on the working temperature [36]. However, for $\alpha \approx 1$, the exact prefactor $f(\alpha)$ is unknown [33], therefore we use $f(\alpha)$ as a fit parameter.

Inserting a temperature of 300 mK into γ for our experimental parameters, one obtains $\gamma = 0.48$. For such large fluctuations the barrier height even with zero bias current is comparable to the noise intensity and the corresponding lifetime must be much smaller than measured in the experiment. If we use γ as a fit parameter together with $f(\alpha)$, we get the best fit for the following parameters: $f(\alpha) = 0.00035$ s for all curves, I_C = 26.5, 27 and 28 nA, and noise intensity γ = 0.0137, 0.0112 and 0.011 for temperatures of 300, 200 and 50 mK, respectively. One can see that I_C in this case corresponds to the measured values.

Thus, the comparison of measurements and fit shows that the average time between dark counts significantly exceeds the time predicted by Kramers' theory, with mean values reaching hundreds of seconds or even thousands of seconds in single measurements. Qualitatively similar discrepancies between experimental results and Kramers' theory have been reported before [21,28] and require further studies. However, if it is the phase diffusion regime that significantly suppresses the dark count rate, the next important question will be to figure out how it influences the sensitivity to photons. In order to do so we perform measurements of the detection probability as a function of the attenuator voltage of 9 GHz photons in a 50 ms pulse, incident on the sample area, for three values of bias current I, shown in Figure 4.

The left vertical axis shows the experimental data, i.e., the number of detector counts divided by the total number of pulses (200 pulses). The horizontal axis corresponds to the attenuation (output power) of the external high-frequency signal. For high incident photon fluxes, the detector switches for all 200 pulses, i.e., it counts all pulses. For smaller fluxes our experimental data show that for 2.5 orders of magnitude, the detection proba-

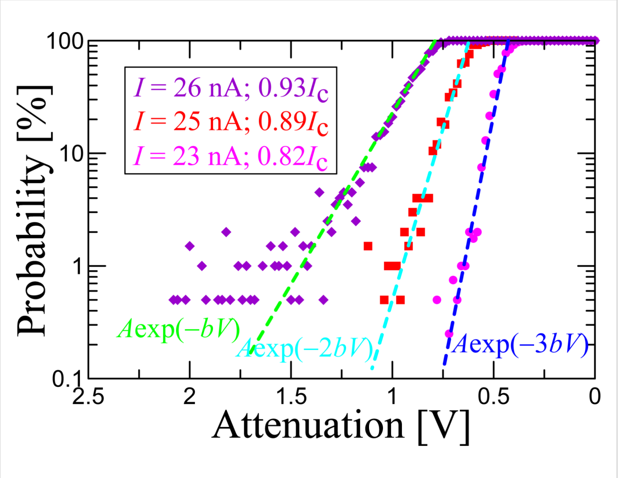

Figure 4: Detection probability of 9 GHz 50 ms pulses of different power (signal attenuation) for different values of the bias current. Dashed lines indicate slopes with exponential factors 1, 2 and 3.

bility decreases linearly (on a logarithmic scale) with the decrease of the incident power (average number of incident photons), and the probability slopes for various bias currents are well fitted by a function $A \cdot \exp(-nbV)$, and are quantized. Here A and b are fit parameters and b is the same for all three curves. This resembles the multi-photon detection [6], where for a smaller bias current (I = 23 nA), the slope is larger, ca. $A \cdot \exp(-3bV)$, than for larger bias current, ca. $A \cdot \exp(-2bV)$ for I = 25 nA and ca. $A \cdot \exp(-bV)$ for I = 26 nA.

Although we see a consistent switching due to 9 GHz signal even at 23 nA, at the moment we cannot estimate the absorption efficiency, because of the uncertainty in the determination of losses in the twisted-pair wiring at the frequency of 9 GHz and of the absorption efficiency in the junction. Therefore, we do not convert the attenuation to the power to avoid the introduction of an additional insecure parameter. The experiments will be continued with better statistics and signal calibration to extract the number of detected photons. We expect that the sensitivity of the considered threshold detector will be decreased in comparison with the situation without phase diffusion. However, further studies are required to answer this question.

Conclusion

Temporal and detecting characteristics of a low-critical-current Al Josephson junction have been studied experimentally. From measurements of switching current distributions and the dark count time intervals, the operation in a phase diffusion regime is evident. It is shown by comparison with theory that the phase diffusion regime allows to significantly improve noise immunity of a device, radically increasing the mean time between dark counts. However, in the same way, the phase diffusion should decrease the single-photon sensitivity of the considered threshold detector, which will be studied in future experiments.

The plot of the detection probability as a function of the attenuation voltage shows quantization of the tail slopes, which resembles few-photon detection. The use of such a device for supersensitive detection has essential applications. In particular, such a detector can be used in the search for axions and to measure signals generated by quantum circuits at a frequency of 6–9 GHz. In the future, it is planned to improve the measurement setup and conduct research on the detection of test signals in the range of 8–14 GHz.

Acknowledgements

The authors wish to thank M. Tarasov for the help in the sample fabrication and G. N. Gol’tsman for discussions and critical comments. The samples were fabricated in the Chalmers Nanotechnology Center and the measurements were performed using the facilities of the Center of Cryogenic Nanoelectronics of NNSTU.

Funding

The work is supported by Russian Science Foundation (Project No. 19-79-10170).

ORCID® iDs

Andrey L. Pankratov - https://orcid.org/0000-0003-2661-2745
Igor V. Rakut - https://orcid.org/0000-0001-9314-2363
Leonid S. Kuzmin - https://orcid.org/0000-0002-8051-484X

Preprint

A non-peer-reviewed version of this article has been previously published as a preprint doi:10.3762/bxiv.2020.47.v1

References

1. Barbieri, R.; Braggio, C.; Carugno, G.; Gallo, C. S.; Lombardi, A.; Ortolan, A.; Pengo, R.; Ruoso, G.; Speake, C. C. *Phys. Dark Universe* **2017,** *15,* 135–141. doi:10.1016/j.dark.2017.01.003
2. Crescini, N.; Alesini, D.; Braggio, C.; Carugno, G.; D’Agostino, D.; Di Gioacchino, D.; Falferi, P.; Gambardella, U.; Gatti, C.; Iannone, G.; Ligi, C.; Lombardi, A.; Ortolan, A.; Pengo, R.; Ruoso, G.; Taffarello, L.; QUAX Collaboration. *Phys. Rev. Lett.* **2020,** *124,* 171801. doi:10.1103/physrevlett.124.171801
3. McAllister, B. T.; Flower, G.; Ivanov, E. N.; Goryachev, M.; Bourhill, J.; Tobar, M. E. *Phys. Dark Universe* **2017,** *18,* 67–72. doi:10.1016/j.dark.2017.09.010
4. Kuzmin, L. S.; Sobolev, A. S.; Gatti, C.; Di Gioacchino, D.; Crescini, N.; Gordeeva, A.; Il’ichev, E. *IEEE Trans. Appl. Supercond.* **2018,** *28,* 2400505. doi:10.1109/tasc.2018.2850019
5. Inomata, K.; Lin, Z.; Koshino, K.; Oliver, W. D.; Tsai, J.-S.; Yamamoto, T.; Nakamura, Y. *Nat. Commun.* **2016,** *7,* 12303. doi:10.1038/ncomms12303

6. Gol'tsman, G. N.; Okunev, O.; Chulkova, G.; Lipatov, A.; Semenov, A.; Smirnov, K.; Voronov, B.; Dzardanov, A.; Williams, C.; Sobolewski, R. *Appl. Phys. Lett.* **2001,** *79,* 705–707. doi:10.1063/1.1388868
7. Baeva, E. M.; Sidorova, M. V.; Korneev, A. A.; Smirnov, K. V.; Divochy, A. V.; Morozov, P. V.; Zolotov, P. I.; Vakhtomin, Y. B.; Semenov, A. V.; Klapwijk, T. M.; Khrapai, V. S.; Goltsman, G. N. *Phys. Rev. Appl.* **2018,** *10,* 064063. doi:10.1103/physrevapplied.10.064063
8. Guarcello, C.; Valenti, D.; Spagnolo, B.; Pierro, V.; Filatrella, G. *Nanotechnology* **2017,** *28,* 134001. doi:10.1088/1361-6528/aa5e75
9. Zgirski, M.; Foltyn, M.; Savin, A.; Norowski, K.; Meschke, M.; Pekola, J. *Phys. Rev. Appl.* **2018,** *10,* 044068. doi:10.1103/physrevapplied.10.044068
10. Guarcello, C.; Braggio, A.; Solinas, P.; Giazotto, F. *Phys. Rev. Appl.* **2019,** *11,* 024002. doi:10.1103/physrevapplied.11.024002
11. Guarcello, C.; Valenti, D.; Spagnolo, B.; Pierro, V.; Filatrella, G. *Phys. Rev. Appl.* **2019,** *11,* 044078. doi:10.1103/physrevapplied.11.044078
12. Guarcello, C.; Braggio, A.; Solinas, P.; Pepe, G. P.; Giazotto, F. *Phys. Rev. Appl.* **2019,** *11,* 054074. doi:10.1103/physrevapplied.11.054074
13. Anghel, D. V.; Kulikov, K.; Galperin, Y. M.; Kuzmin, L. S. *Phys. Rev. B* **2020,** *101,* 024511. doi:10.1103/physrevb.101.024511
14. Wallraff, A.; Duty, T.; Lukashenko, A.; Ustinov, A. V. *Phys. Rev. Lett.* **2003,** *90,* 037003. doi:10.1103/physrevlett.90.037003
15. Oelsner, G.; Revin, L. S.; Il'ichev, E.; Pankratov, A. L.; Meyer, H.-G.; Grönberg, L.; Hassel, J.; Kuzmin, L. S. *Appl. Phys. Lett.* **2013,** *103,* 142605. doi:10.1063/1.4824308
16. Oelsner, G.; Andersen, C. K.; Rehák, M.; Schmelz, M.; Anders, S.; Grajcar, M.; Hübner, U.; Mølmer, K.; Il'ichev, E. *Phys. Rev. Appl.* **2017,** *7,* 014012. doi:10.1103/physrevapplied.7.014012
17. Chen, Y.-F.; Hover, D.; Sendelbach, S.; Maurer, L.; Merkel, S. T.; Pritchett, E. J.; Wilhelm, F. K.; McDermott, R. *Phys. Rev. Lett.* **2011,** *107,* 217401. doi:10.1103/physrevlett.107.217401
18. Poudel, A.; McDermott, R.; Vavilov, M. G. *Phys. Rev. B* **2012,** *86,* 174506. doi:10.1103/physrevb.86.174506
19. Yu, H. F.; Zhu, X. B.; Peng, Z. H.; Cao, W. H.; Cui, D. J.; Tian, Y.; Chen, G. H.; Zheng, D. N.; Jing, X. N.; Lu, L.; Zhao, S. P.; Han, S. *Phys. Rev. B* **2010,** *81,* 144518. doi:10.1103/physrevb.81.144518
20. Yu, H. F.; Zhu, X. B.; Peng, Z. H.; Tian, Y.; Cui, D. J.; Chen, G. H.; Zheng, D. N.; Jing, X. N.; Lu, L.; Zhao, S. P.; Han, S. *Phys. Rev. Lett.* **2011,** *107,* 067004. doi:10.1103/physrevlett.107.067004
21. Longobardi, L.; Massarotti, D.; Rotoli, G.; Stornaiuolo, D.; Papari, G.; Kawakami, A.; Pepe, G. P.; Barone, A.; Tafuri, F. *Phys. Rev. B* **2011,** *84,* 184504. doi:10.1103/physrevb.84.184504
22. Lisitskiy, M.; Massarotti, D.; Galletti, L.; Longobardi, L.; Rotoli, G.; Russo, M.; Tafuri, F.; Ruggiero, B. *J. Appl. Phys.* **2014,** *116,* 043905. doi:10.1063/1.4890317
23. Koval, Y.; Fistul, M. V.; Ustinov, A. V. *Phys. Rev. Lett.* **2004,** *93,* 087004. doi:10.1103/physrevlett.93.087004
24. Martinis, J. M.; Kautz, R. L. *Phys. Rev. Lett.* **1989,** *63,* 1507–1510. doi:10.1103/physrevlett.63.1507
25. Vion, D.; Götz, M.; Joyez, P.; Esteve, D.; Devoret, M. H. *Phys. Rev. Lett.* **1996,** *77,* 3435–3438. doi:10.1103/physrevlett.77.3435
26. Grabert, H.; Ingold, G.-L.; Paul, B. *Europhys. Lett.* **1998,** *44,* 360–366. doi:10.1209/epl/i1998-00480-8
27. Franz, A.; Koval, Y.; Vasyukov, D.; Müller, P.; Schneidewind, H.; Ryndyk, D. A.; Keller, J.; Helm, C. *Phys. Rev. B* **2004,** *69,* 014506. doi:10.1103/physrevb.69.014506
28. Massarotti, D.; Longobardi, L.; Galletti, L.; Stornaiuolo, D.; Rotoli, G.; Tafuri, F. *Low Temp. Phys.* **2013,** *39,* 294–298. doi:10.1063/1.4795203
29. Likharev, K. K. *Dynamics of Josephson junctions and circuits;* Gordon and Breach Science Publishers: New York, NY, USA, 1986.
30. Blackburn, J. A.; Cirillo, M.; Grønbech-Jensen, N. *Phys. Rep.* **2016,** *611,* 1–33. doi:10.1016/j.physrep.2015.10.010
31. Longobardi, L.; Massarotti, D.; Stornaiuolo, D.; Galletti, L.; Rotoli, G.; Lombardi, F.; Tafuri, F. *Phys. Rev. Lett.* **2012,** *109,* 050601. doi:10.1103/physrevlett.109.050601
32. Kramers, H. A. *Physica (Amsterdam)* **1940,** *7,* 284–304. doi:10.1016/s0031-8914(40)90098-2
33. Hänggi, P.; Talkner, P.; Borkovec, M. *Rev. Mod. Phys.* **1990,** *62,* 251–341. doi:10.1103/revmodphys.62.251
34. Caldeira, A. O.; Leggett, A. J. *Phys. Rev. Lett.* **1981,** *46,* 211–214. doi:10.1103/physrevlett.46.211
35. Malakhov, A. N.; Pankratov, A. L. *Phys. C (Amsterdam, Neth.)* **1996,** *269,* 46–54. doi:10.1016/0921-4534(96)00426-1
36. Malakhov, A. N.; Pankratov, A. L. *Adv. Chem. Phys.* **2002,** *121,* 357–438. doi:10.1002/0471264318.ch6

License and Terms

The definitive version of this article is the electronic one which can be found at:
doi:10.3762/bjnano.11.80

BEILSTEIN JOURNAL OF NANOTECHNOLOGY

Electrochemical nanostructuring of (111) oriented GaAs crystals: from porous structures to nanowires

Elena I. Monaico[1], Eduard V. Monaico*[1], Veaceslav V. Ursaki[1,2], Shashank Honnali[3], Vitalie Postolache[1], Karin Leistner[3], Kornelius Nielsch[3] and Ion M. Tiginyanu[1,2]

Full Research Paper

Open Access

Address:
[1]National Center for Materials Study and Testing, Technical University of Moldova, Chisinau MD-2004, Republic of Moldova, [2]Academy of Sciences of Moldova, Chisinau MD-2001, Republic of Moldova and [3]Leibniz IFW Dresden, Helmholtzstr. 20, 01069 Dresden, Germany

Email:
Eduard V. Monaico* - eduard.monaico@cnstm.utm.md

* Corresponding author

Keywords:
anodization; crystallographically oriented pores; gallium arsenide (GaAs); nanowires; neutral electrolyte; photocurrent; porous GaAs

Beilstein J. Nanotechnol. **2020,** *11,* 966–975.
doi:10.3762/bjnano.11.81

Received: 29 March 2020
Accepted: 27 May 2020
Published: 29 June 2020

This article is part of the thematic issue "Functional nanostructures for electronics, spintronics and sensors".

Guest Editor: A. S. Sidorenko

Abstract

A comparative study of the anodization processes occurring at the GaAs(111)A and GaAs(111)B surfaces exposed to electrochemical etching in neutral NaCl and acidic HNO_3 aqueous electrolytes is performed in galvanostatic and potentiostatic anodization modes. Anodization in NaCl electrolytes was found to result in the formation of porous structures with porosity controlled either by current under the galvanostatic anodization, or by the potential under the potentiostatic anodization. Possibilities to produce multilayer porous structures are demonstrated. At the same time, one-step anodization in a HNO_3 electrolyte is shown to lead to the formation of GaAs triangular shape nanowires with high aspect ratio (400 nm in diameter and 100 µm in length). The new data are compared to those previously obtained through anodizing GaAs(100) wafers in alkaline KOH electrolyte. An IR photodetector based on the GaAs nanowires is demonstrated.

Introduction

Electrochemical technology became an established and cost-effective approach for the preparation of porous semiconductor matrices and arrays of nanowires with tailored architecture at the submicrometer scale [1-3]. Semiconductor nanotemplates provide many possibilities for nanofabrication through electrochemically filling the pores with metallic nanostructures such as nanowires or nanotubes, resulting in the production of 2D metallo-semiconductor interpenetrating networks, which are promising for various nanoelectronic, optoelectronic, plasmonic, and nanophotonic applications [4-6]. While the growth of crystallographically oriented and current line oriented pores has been demonstrated in a variety of semiconductors [1-3], to date, only crystallographically oriented pores were observed in GaAs crystalline wafers. This observation is a factor limiting the possibilities for the preparation of various GaAs nanostructures, including nanowires.

Semiconductor nanowires, particularly III–V compound nanowires, show potential for their use as active components in solar cells [7-10], photodetectors [11], light-emitting diodes [12], transistors [13], and other applications. A uniform array of parallel nanowires with diameters of about 50 nm and oriented normally to a InP wafer, i.e., along the crystallographic [100] orientation, was obtained after anodic etching at elevated applied voltages [14]. High-aspect-ratio GaAs pillar arrays with triangular cross section were prepared by combining colloidal crystal templating, anisotropic chemical etching, localized anodic etching, and isotropic anodic oxidation [15,16]. However, this is a complex multistep technology. A more simple and cost-effective technology was applied for obtaining triangular GaAs nanowires through electrochemical etching of GaAs(100) surfaces in aqueous KOH solution [17]. However, this process was difficult to control. The bundles of GaAs nanowires were formed only in some regions of the surface and the orientation of the arrays was basically random.

Usually, acidic or alcaline electrolytes are used for the electrochemical preparation of porous semiconductors although the anodization in environmentally friendly electrolytes, including aqueous solutions of NaCl, has attracted increasing attention during the last decade [5,18-21].

In this paper, we report on the electrochemical porosification of GaAs(111) wafers in neutral NaCl and acidic HNO_3 electrolytes, and on optimized technological conditions for the one-step formation of GaAs nanowires with triangular shape and well oriented perpendicularly to the substrate.

Results and Discussion

In order to study the influence of the applied anodization conditions on the porosification process of (111) oriented GaAs crystals, three different current densities and three different voltages were used for galvanostatic and potentiostatic modes, respectively. SEM images of a GaAs crystal anodized on both surfaces in 1.75 M NaCl electrolyte are given in Figure 1. The porous features produced by GaAs anodization in NaCl electrolyte are similar to those previously observed in GaAs samples with the same carrier concentration anodized in HCl electrolyte [1]. This observation corroborates the results obtained from other III–V semiconductors, which state that the etching behavior depends mainly on the anions rather than the cations [22], because the anions of NaCl and HCl electrolytes are the same. The morphology of the porous structure produced by galvanostatic anodization of GaAs(111)A surface (Figure 1A) consists of two sets of ⟨111⟩ crystallographically oriented pores intersecting each other [2]. According to previous studies, the main property of crystallographically oriented pores is their growth along definite crystallographic directions. On substrates with sphalerite crystal structures, the pores grow along the ⟨111⟩B crystallographic directions, regardless of the initial surface orientation, with an angle of approximately 109° between the pores. The pores tend to have a triangular cross section while the pore walls and tips exhibit a pronounced crystallographic anisotropy. A specific characteristic feature of crystallographically oriented pores is their ability to intersect each other without changing their direction of propagation during growth.

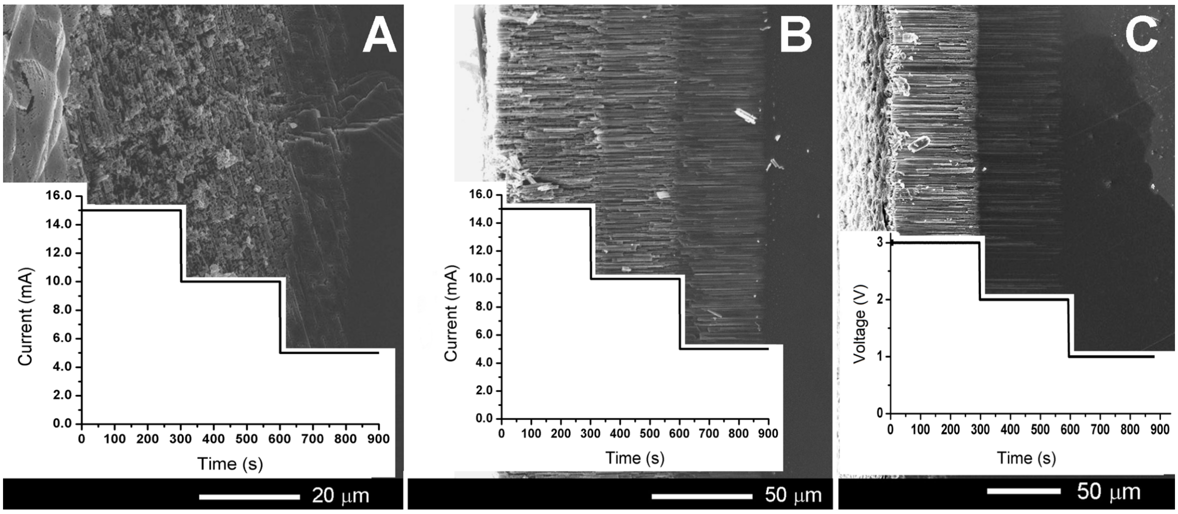

Figure 1: SEM images in cross section of porous GaAs layers for three different conditions of anodization in 1.75 M NaCl: (A) galvanostatic regime on the GaAs(111)A surface; (B) galvanostatic regime on the GaAs(111)B surface; (C) potentiostatic regime on the GaAs(111)B surface. The substrate is on the right side of the images. The inserted plots represent the applied currents (A, B) and the applied potential (C) during anodization.

As one can see from Figure 1A, the degree of porosity decreases with decreasing the anodization current density.

The situation is different when the GaAs crystals are anodized on the (111)B surface. During anodization in the galvanostatic mode at current densities similar to those applied during anodizing the (111)A surface (15, 10, and 5 mA), three porous layers are formed with different degrees of porosity, but the pores are parallel to each other and they grow perpendicularly to the crystal surface (Figure 1B). The same propagation of pores was observed for the potentiostatic mode of anodization (Figure 1C). Switching the anodization voltage to 1 V stops the formation of the porous layer, since this value is below the pore nucleation potential (1.8 V) established from the *I–V* characteristic, which is in agreement with the doping level of the used crystal. We will focus further on the results obtained by anodization of the (111)B surface because the resulting morphology is of great interest for the development of porous nanotemplates and elaboration of free-standing nanomembranes based on GaAs.

The results of a comparative anodization study of the GaAs(111)B surface in galvanostatic and potentiostatic regimes are illustrated in the SEM images of Figure 2. Along with pores

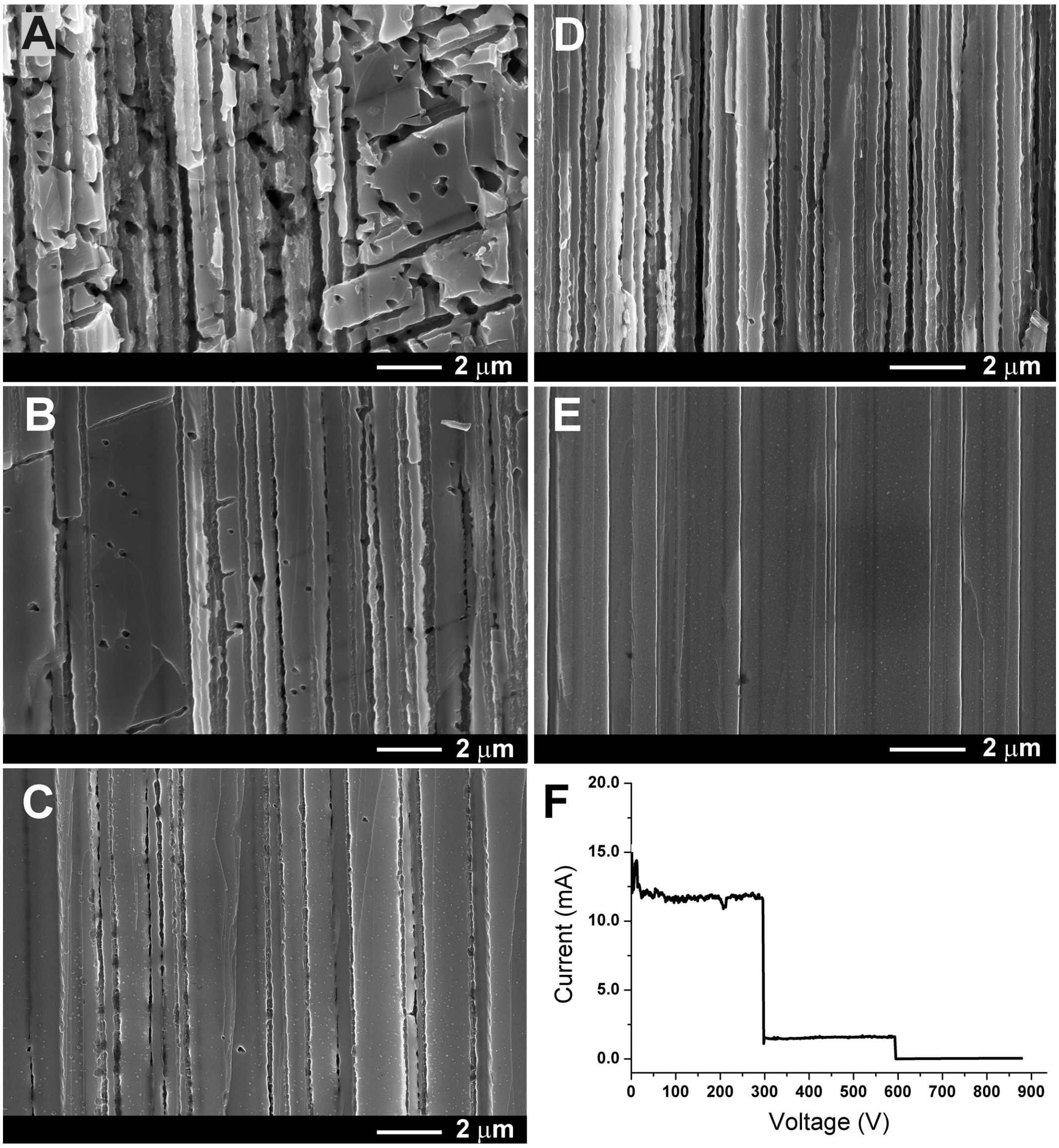

Figure 2: (A–C) SEM images in cross section at higher magnification of the porous layers obtained by anodization of the GaAs(111)B surface in galvanostatic regime, corresponding to the images illustrated in Figure 1B. (D, E) SEM images of samples anodized in potentiostatic regime, corresponding to images illustrated in Figure 1C. (F) Evolution of the current during anodization in potentiostatic regime of the GaAs(111)B surface at applied voltages of 3, 2 and 1 V.

propagating perpendicularly to the substrate surface, pores growing in other directions are observed in the cross-sectional view (Figure 2A), hinting at the formation of pores that are tilted and intersect each other. However, with the decrease of the current density (Figure 2B,C), the number of tilted pores is drastically reduced, and pores oriented perpendicularly to the surface predominate in the produced porous layer (Figure 2C). The morphology of the layer produced by anodization in the potentiostatic regime presented in Figure 2D,E looks more uniform (note that the pores grow perpendicularly to the surface). It should be mentioned, however, that the pore walls are not smooth, which is observed for both potentiostatic and galvanostatic anodization regimes. This can be explained by analyzing the current as a function of the time at constant voltage (Figure 2F). At the applied potential of 3 V, the registered current is practically stable at a value of 13 mA, but some fluctuations in the current can be easily observed. Reducing the anodization voltage to 2 V leads to a decrease of the current down to 5 mA. This value remains quite stable. So, by anodizing the sample in the potentiostatic mode at relatively low voltage, which does not introduce self-oscillations in the registered current, it is possible to obtain pores with smooth walls (Figure 2E).

According to Li and co-workers [17], the anodization of GaAs with a carrier concentration of about 10^{18} cm^{-3} in a KOH electrolyte can be categorized into three etching modes, deduced from the analysis of the current–voltage plot at a scan rate of 5 $mV{\cdot}s^{-1}$. Practically no etching occurs when the applied voltage is below 3 V, which is the pore formation potential. The first etching mode is characterized by the formation of triangular nanowires, which occurs at an applied potential in the range of 3.0–4.5 V. The second mode corresponds to surface texturing occurring at an applied potential in the range of 4.5–6.5 V. At an applied potential higher than 6.5 V the sample is electropolished. Taking these observations into account, we increased the applied potential in our experiments to 4 V, with the purpose of producing GaAs nanowires. However, the analysis of SEM images after anodization in NaCl electrolyte with an applied potential of 4 V revealed that no nanowires are formed. Instead a higher number of tilted pores was formed, similar to the morphology produced under anodization in the galvanostatic regime with a current of 14 mA (Figure 2A). Moreover, an increase of the applied potential to 6 V leads to the formation of GaAs nanowires, but the number of tilted pores that intersect the vertical nanowires increases, resulting in the formation of interrupted nanowires (Figure 3A). A further increase of the applied voltage is not recommended, because the formed nanowires are destroyed. We are interested in the fabrication of pores strictly perpendicular to the crystal surface, which would enable us to fabricate stable nanowires.

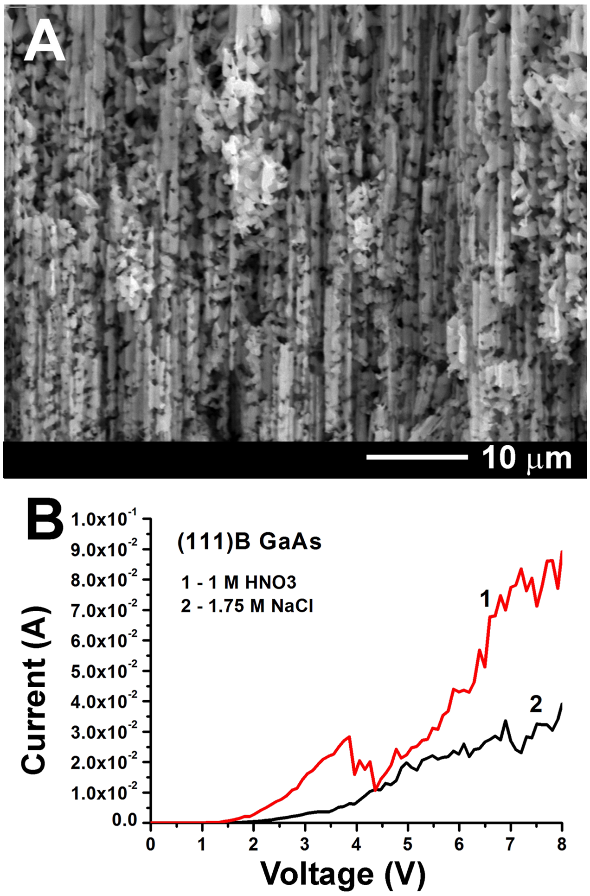

Figure 3: (A) SEM images of the formation of interrupted GaAs nanowires on the (111)B surface anodized in NaCl electrolyte at 6 V. (B) The polarization curves measured at a scan rate of 50 $mV{\cdot}s^{-1}$ at the beginning of the anodization process of a GaAs(111)B crystal in 1 M HNO_3 (curve 1) and 1.75 M NaCl (curve 2).

One can conclude that anodizations in NaCl electrolyte and in aqueous HCl solution are suitable for the production of porous layers with various morphologies, rather than for the fabrication of GaAs nanowires. Since, on one hand, nanowires were produced through anodization in alkaline KOH electrolyte [17] and, on the other hand, the etching behavior in acidic electrolytes is mainly determined by the anions [22], we tried to obtain GaAs nanowires through anodization in acidic electrolyte with another type of anion. A comparison of the polarization curves measured at the beginning of the anodization process of a GaAs(111)B crystal in 1 M HNO_3 or 1.75 M NaCl electrolyte is presented in Figure 3B. It can be observed that current oscillations occur at applied potentials higher than 4 V for both electrolytes. We suppose that these self-induced oscillations are related to the simultaneous formation of pores along the ⟨111⟩B directions and an increasing contribution of tilted pores. At high anodizing voltages electropolishing occurs in both electrolytes. The potential for initiating electropolishing is 4.5 V and 6 V for anodization in HNO_3 and NaCl electrolyte, respectively. Note that the value for anodizing in NaCl electrolyte agrees with previously reported data [17].

Arrays of GaAs nanowires with a very high aspect ratio and well oriented perpendicularly to the (111)B crystal surface were produced under anodization at an applied potential of 3 V for 20 min in 1 M HNO_3 electrolyte (Figure 4A). The obtained triangular nanowires with a diameter of 400 nm are 100 µm in length, i.e., the aspect ratio is around 250. The uniform distribution of the nanowires across the sample surface is illustrated in Figure 4C. Interestingly, the anodization potential for producing nanowires in the acidic 1 M HNO_3 electrolyte is similar to that required for producing GaAs nanowires in alkaline 5% KOH electrolyte [17].

Thus, triangular-shape GaAs nanowires with a diameter ranging from 200 to 400 nm can be produced by electrochemical etching of GaAs(100) wafers with a carrier concentration of the order of 10^{18} cm^{-3} in KOH electrolyte, or by etching of GaAs(111)B substrates in HNO_3 electrolyte. However, the bundles of GaAs nanowires are formed only in some regions of the surface anodized in KOH electrolyte, and the orientation of the arrays is basically random, while the nanowires produced in HNO_3 electrolyte are highly oriented perpendicularly to the wafer surface. No nanowires were reported after GaAs anodization in H_2SO_4 electrolyte, which was used for uniform pore nucleation in a two-step anodization process and the preparation of porous structures consisting of crossing pores [1,23]. GaAs nanocolumns with a diameter of about 200 nm were obtained previously through anodization of GaAs(100) substrates in aqueous HCl solution [24], but the nanocolumns were penetrated by a large number of tilted pores. One can conclude that etching in HNO_3 electrolyte suppresses the nucleation of tilted pores as compared to anodization in HCl or H_2SO_4 electrolyte, resulting in the fabrication of non-porous GaAs nanowires, which are better suitable for photodetector applications. High-aspect-ratio arrays of spatially ordered triangular GaAs nanopillars with diameters of about 1.5 µm were previously fabricated by a combination of electrochemical etching in HCl electrolyte of a pre-etched GaAs(111) substrate and anisotropic chemical etching [15,16]. However, this is a multistep process requiring the use of photolithography with colloidal crystal templating in the first pre-etching step. Fabrication of GaAs nanopillars by metal-assisted chemical etching (MacEtch) also requires lithographic methods for catalytic metal patterning [25,26]. Among non-lithographic methods based on electrochemical etching, to the best of our knowledge, there is only one report on the preparation of high-aspect-ratio vertically aligned GaAs nanowires with a diameter of about 200 nm and a length of 100 µm on GaAs(111)B wafers with a carrier concentration in the range of (1–2) × 10^{18} cm^{-3} [27]. Bundles of these nanowires were tested for field emission, but not for photodetector applications. The nanowires were produced using electrochemical etching under optimized conditions in a mixed H_3PO_4/HCl electrolyte followed by chemical etching for reducing the diameter down to 150 nm. The authors of the work did not discuss the diameter distribution of nanowires produced by the process, effectively utilizing a structural feature of spontaneously generated

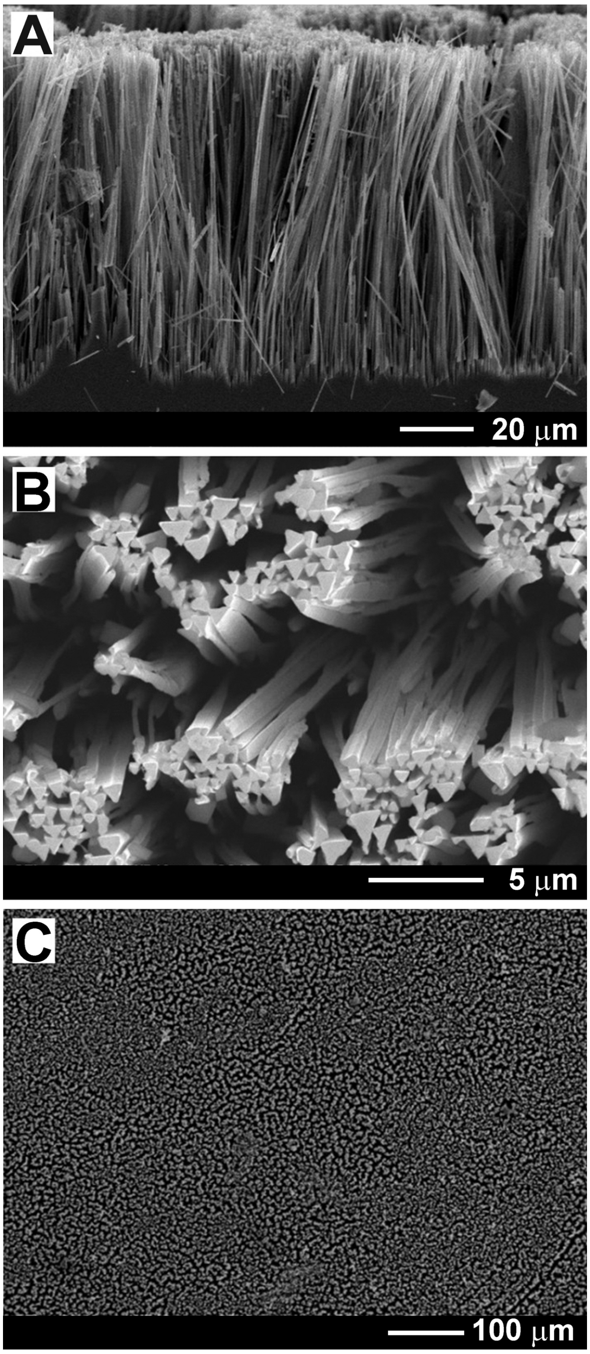

Figure 4: (A) SEM image in cross section of a GaAs(111)B sample anodized at 3 V for 20 min in 1 M HNO_3. (B, C) Top-view SEM images.

patterns. According to the presented scanning electron microscope images, however, there is a relatively broad distribution.

The nanowires produced in the present work also exhibit a diameter distribution with a certain width. However, we believe that the distribution could be narrowed by further optimization of the technological processes. Note that the diameter of a particular nanowire is determined by the width of the space charge region (SCR) set up within the nanopore wall at the interface with the electrolyte during anodization [23], and it equals ca. 2 × SCR [17]. As a result, for higher carrier concentrations in the GaAs wafer thinner nanowires are obtained. The density of the nanowires is quite homogeneous on a large scale (Figure 4C), while the nanowires tend to form bundles at the micrometer scale, similar to the results presented in [27].

Figure 5 compares the photoluminescence (PL) spectra of the as-grown and anodized GaAs samples measured at low temperature. One can see that the shapes of the spectra are similar. The only difference is the emission intensity, which is higher by a factor of about two in the anodized GaAs sample. This means that the PL spectra can be attributed to identical recombination channels. In both samples the PL is dominated by an emission band around 1.32 eV with a weaker PL band at 1.485 eV. The PL band at 1.32 eV is usually attributed to Si impurities at the Ga sites forming different complexes, such as ($\mathrm{Si_{Ga}V_{Ga}}$) [28,29] or ($\mathrm{Si_{Ga}Ga_{As}}$) [30]. Since Si impurities exhibit an amphoteric behavior in GaAs, they give rise to an acceptor $\mathrm{Si_{As}}$ state in addition to the $\mathrm{Si_{Ga}}$ shallow donor state. The second PL band at 1.485 eV is related to the recombination of electrons from the conduction band with holes trapped by the $\mathrm{Si_{As}}$ state the energy level of which is situated 35 meV above the valence band [31]. The higher intensity of the emission from the anodized GaAs sample is indicative of an effective passivation during anodization of the huge internal surface of the porous sample [18].

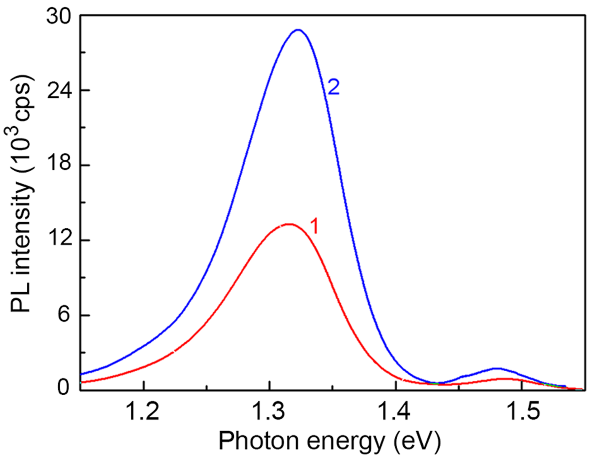

Figure 5: PL spectra of bulk (curve 1) and anodized (curve 2) GaAs samples measured at a temperature of 10 K.

The preservation of the quality of the GaAs compound after anodization is also confirmed by the results of XRD analysis (Figure 6). The high quality of the material produced by anodization is indicated by narrow reflexes with a full width at half maximum (FWHM) of about 0.08°. The predominance of (111) and (333) reflexes in the XRD pattern indicates also to the preservation of the initial (111)B crystallographic orientation of the sample.

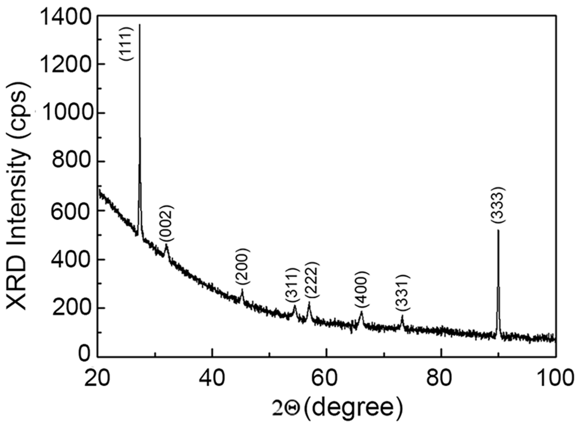

Figure 6: XRD pattern of the anodized GaAs(111)B sample.

To demonstrate the applicability of the nanowires for device fabrication, a photodetector for the IR region of the spectrum was tested, as described in the Experimental section. A special design of contacts was applied via laser beam lithography on selected nanowires. As illustrated in Figure 7A, defined regions (bright regions) were opened in the photoresist (dark regions) for further metal deposition. Note that the nanowire was visible in the optical microscope due to its length of 70 µm, despite the small diameter. The distance between the contacts is 20 µm. A photograph of five contacted nanowires on a glass substrate after Cr/Au deposition and lift-off is presented in the inset of the Figure 7A. The photocurrent build-up and relaxation for a photodetector produced on a nanowire with a diameter of 400 nm is presented in Figure 7B for an IR illumination density of 800 mW·cm^{-2}. One can see that the current increases by a factor of four in magnitude under illumination with IR light.

The current–voltage characteristics measured with and without illumination reveal a good ohmic quality of the prepared Cr/Au contacts (Figure 8). Therefore, one can conclude that the detector works in the photoconductor mode.

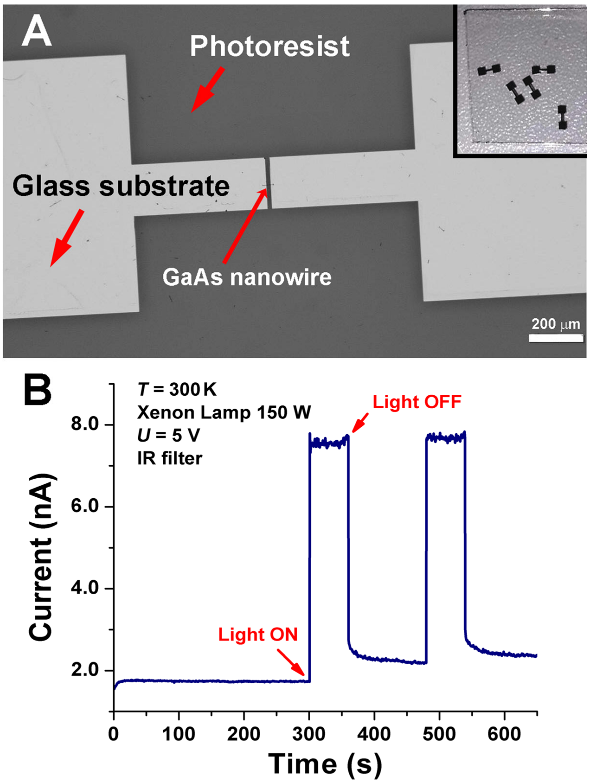

Figure 7: (A) Optical microscopy image of the opened regions in the photoresist on the glass substrate for deposition of the metal contacts on the selected GaAs nanowire. The inset in (A) shows a photo of five contacted GaAs nanowires on the same glass substrate. (B) Photocurrent build-up and relaxation of the photodetector measured for an IR illumination density of 800 mW·cm^{-2}.

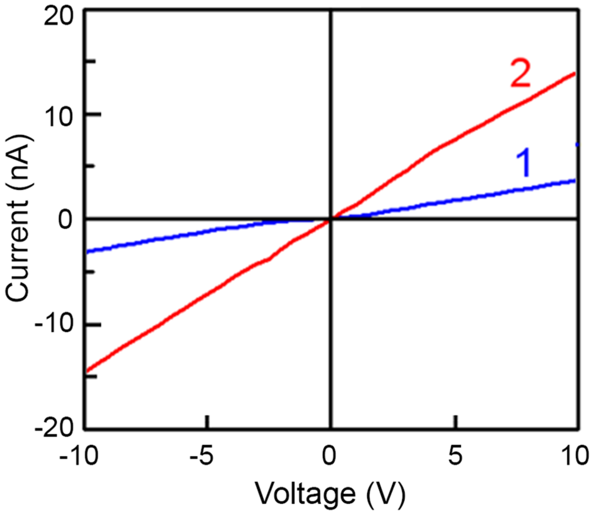

Figure 8: Current–voltage characteristics measured in dark (curve 1) and under IR illumination with power density of 800 mW·cm^{-2} (curve 2) for the GaAs nanowire photodetector with the design shown in Figure 7.

The responsivity of the detector is defined as

$$R = \frac{I_{\text{photo}} - I_{\text{dark}}}{P_{\text{ill}}}, \qquad (1)$$

where I_{photo} is the photocurrent of the photodetector, I_{dark} is the dark current, and P_{ill} is the illumination power on the photodetector. The calculated responsivity of the GaAs nanowire photodetector equals 100 mA·W^{-1}, according to the data presented in Figure 7B for a nanowire with a diameter of 400 nm and a length of 20 µm biased at 5 V.

The estimation of the detectivity D*, which is defined as

$$D^* = \frac{R\sqrt{A}}{\sqrt{2eI_{\text{dark}}}}, \qquad (2)$$

where A is the active area of the photodetector, and e is the elementary charge, gives a value of ca. 1.2×10^9 cm·Hz$^{1/2}$·W^{-1}, under the assumption that shot noise is the primary source of noise in the detector [32].

Taking into account that the photodetector works in the photoconductor mode, the photocurrent increases linearly with increasing bias. This results in increasing responsivity and detectivity with increasing bias. For instance, the responsivity increases by a factor of three after increasing the bias from 5 to 20 V. The measured parameters vary among the five investigated devices basically due to the different diameters of the nanowires. The responsivity measured at the same excitation power density of 800 mW·cm^{-2} at a bias of 5 V decreases with decreasing nanowire diameter. The detectivity also decreases with decreasing diameter, but to a lesser extent.

The obtained values of responsivity and detectivity are comparable with those previously reported for a graphene/GaAs NW photodetector with a Schottky junction working at 532 nm radiation [33]. The detectivity of our photodetector is better than that reported for a GaAsSb NW IR detector (1300 nm), although the responsivity of the GaAsSb NW detector is better [34]. A photodetector based on a single GaAs nanowire with a responsivity of 1.2 mA·W^{-1} has been recently reported on a nanowire prepared by chemical beam epitaxy (CBE) with a vapor–liquid–solid (VLS) growth procedure [35]. This value is by two orders of magnitude lower than the responsivity of our photodetector. However, one should take into account that it was fabricated with a nanowire that is one order of magnitude thinner than our nanowire prepared by electrochemical etching. The detectivity of our GaAs nanowire detector working in the photoconductor mode is by a factor of 1.5 better than the value obtained recently on molecular beam epitaxy (MBE)-grown Si-doped GaAs nanowires with a carrier concentration of 1.47×10^{17} cm^{-3}, working in the field-effect transistor (FET) mode at similar excitation power densities (around 800 $mW \cdot cm^{-2}$) but with radiation of 532 nm wavelength [36]. At the same time, the authors of [36] succeeded to improve the detectivity of the NW FET detector by one order of magnitude and also to attain record responsivities of the order of 1 $kA \cdot W^{-1}$ after optimization of the carrier concentration in the GaAs NWs and of the photodetector design. We suppose that the parameters of IR photodetectors based on nanowires prepared by anodization can also be significantly improved after corresponding optimization.

A drawback of photoconductive detectors based on semiconductor nanowires is related to their long-relaxation phenomena caused by the strong surface band bending effects [37]. In contrast, much shorter relaxation times are inherent to photodetectors based on interdigitated metal–semiconductor–metal structures with Schottky diodes. However, a very low feature size is needed for such structures, which makes photolithography challenging [38].

Conclusion

This study demonstrates possibilities to produce porous GaAs structures with a controlled degree of porosity through the anodization of GaAs(111) wafers in a neutral, environmentally friendly NaCl electrolyte. Porous morphologies with pores oriented perpendicularly to the wafer surface are obtained through potentiostatic anodization of GaAs(111)B surfaces at low applied potentials. With increasing the applied potential in the potentiostatic anodization mode, or the current in the galvanostatic anodizing mode, a higher number of tilted pores are produced in addition to those oriented perpendicularly to the wafer surface. When the anodization is performed on the GaAs(111)A surface, a porous morphology with crossing pores is obtained, and the degree of porosity increases with increasing the anodizing current. Since these results are similar to those previously observed after anodization of GaAs wafers in HCl electrolytes, one can conclude that the etching behavior is mainly determined by the type of anions. No nanowires are produced under any anodizing conditions in NaCl electrolyte. On the other hand, high-aspect-ratio triangular shape GaAs nanowires are obtained by anodizing in a HNO_3 electrolyte at an applied potential of 3 V, and the uniformity and orientation of these nanowire arrays are much better than those produced previously with anodizing in alkaline KOH electrolytes. The produced GaAs nanowires prove to be suitable for the development of IR photodetectors with good sensitivity and dynamic characteristics.

Experimental

Electrochemical anodization. Crystalline 500 µm thick (111)-oriented substrates of Si-doped n-GaAs with a free electron concentration of 2×10^{18} cm^{-3} were used in this study. The samples were sonicated in acetone for 15 min, cleaned in distilled water and dried. In order to remove the native oxide from the surface, the samples were dipped in a HCl/H_2O (1:3) solution for 2 min. The electrical contacts to the sample were prepared with silver paste, then the samples were pressed against an O-ring in a Teflon cell with the 0.2 cm^2 area exposed to the electrolyte. The electrolytes used in this study were 1.75 M NaCl and 1 M HNO_3. The experiments were performed in a three-electrode configuration, with a Pt mesh with a surface area of 6 cm^2 acting as counter electrode, a saturated Ag/AgCl reference electrode and the sample as working electrode. The anodization was performed in galvanostatic as well as potentiostatic regimes at room temperature (T = 23 °C). Analysis of morphology and chemical composition of the anodized GaAs crystals was carried out using scanning electron microscopy (Zeiss Sigma and TESCAN Vega TS 5130 MM equipped with an Oxford Instruments INCA Energy EDX system operated at 20 kV). The photoluminescence spectra were measured with a double spectrometer with resolution better than 1 meV under excitation by the 514 nm line of an Ar^+ SpectraPhysics laser. The samples were mounted on the cold station of a LTS-22-C-330 cryogenic system. X-ray diffraction analysis of the samples was performed with a Philips X-Pert MPD System with Cu $K\alpha_1$ radiation.

Electrical contacts to GaAs nanowires. The contacts were realized using laser leam lithography (µPG 101, Heidelberg Instruments). After the formation of nanowires via anodization, the GaAs substrates were treated in an ultrasound bath for 15 s in ethanol. Subsequently, a few drops of the ethanol suspension containing nanowires were deposited on a glass substrate followed by a gentle blow drying to remove the ethanol. A double-layer resist (LOR 3B and ma-P 1205) was spin-coated on the glass substrate with the GaAs nanowires and was exposed with the pattern containing the contact pad structure of 1.5 mm × 1.5 mm using the laser writer. After the development of the exposed contact pad structure, a thin layer of 50 nm Cr followed by 250 nm Au layer was sputtered using a magnetron from Torr International Inc model No: CRC622-2G2-RF-DC and lift-off was performed with Microposit remover 1165 at 50 °C.

Photoelectrical characterization. To excite photoconductivity in the GaAs nanowires, the radiation from a Xenon lamp DKSS-150 was used. An optical filter was used to select radiation from the near-IR spectral range (700–2500 nm, optical power 130 mW). The current through the samples was measured by means of a Keithley's Series 2400 source measure unit. Since the photoconductivity decay time is long enough, a mechanical shutter was used in the relaxation experiments. The signal from the source measure unit was fed to computer via IEEE-488 interface for further data processing. The measurements were performed at 300 K.

Acknowledgements

The manuscript contains contributions from all authors. All authors have given approval to the final version of the manuscript.

Funding

Eduard Monaico thanks the Alexander von Humboldt Foundation for support. The authors acknowledge financial support from the Ministry of Education, Culture and Research of Moldova under the Grant #20.80009.5007.20. This work has received partial funding from the bilateral Moldova-Belarus Program under the grant 19.80013.50.07.03A/BL as well as from the European Commission under the Grant #810652 "NanoMedTwin".

ORCID® iDs

Elena I. Monaico - https://orcid.org/0000-0002-9486-2589
Eduard V. Monaico - https://orcid.org/0000-0003-3293-8645
Veaceslav V. Ursaki - https://orcid.org/0000-0003-4488-850X
Vitalie Postolache - https://orcid.org/0000-0002-0391-1526
Karin Leistner - https://orcid.org/0000-0002-8049-4877
Kornelius Nielsch - https://orcid.org/0000-0003-2271-7726
Ion M. Tiginyanu - https://orcid.org/0000-0003-0893-0854

References

1. Föll, H.; Langa, S.; Carstensen, J.; Christophersen, M.; Tiginyanu, I. M. *Adv. Mater. (Weinheim, Ger.)* **2003,** *15,* 183–198. doi:10.1002/adma.200390043
2. Föll, H.; Carstensen, J.; Frey, S. *J. Nanomater.* **2006,** 91635. doi:10.1155/jnm/2006/91635
3. Kochergin, V.; Föll, H. *Porous Semiconductors;* Springer, 2009. doi:10.1007/978-1-84882-578-9
4. Tiginyanu, I.; Monaico, E.; Monaico, E. *Electrochem. Commun.* **2008,** *10,* 731–734. doi:10.1016/j.elecom.2008.02.029
5. Tiginyanu, I. M.; Ursaki, V. V.; Monaico, E.; Enachi, M.; Sergentu, V. V.; Colibaba, G.; Nedeoglo, D. D.; Cojocaru, A.; Föll, H. *J. Nanoelectron. Optoelectron.* **2011,** *6,* 463–472. doi:10.1166/jno.2011.1197
6. Bian, Y.; Zheng, Z.; Zhao, X.; Liu, L.; Su, Y.; Xiao, J.; Liu, J.; Zhu, J.; Zhou, T. *J. Lightwave Technol.* **2013,** *31,* 1973–1979. doi:10.1109/jlt.2013.2263217
7. Wallentin, J.; Anttu, N.; Asoli, D.; Huffman, M.; Åberg, I.; Magnusson, M. H.; Siefer, G.; Fuss-Kailuweit, P.; Dimroth, F.; Witzigmann, B.; Xu, H. Q.; Samuelson, L.; Deppert, K.; Borgström, M. T. *Science* **2013,** *339,* 1057–1060. doi:10.1126/science.1230969
8. Service, R. F. *Science* **2013,** *339,* 263. doi:10.1126/science.339.6117.263
9. Cui, Y.; Wang, J.; Plissard, S. R.; Cavalli, A.; Vu, T. T. T.; van Veldhoven, R. P. J.; Gao, L.; Trainor, M.; Verheijen, M. A.; Haverkort, J. E. M.; Bakkers, E. P. A. M. *Nano Lett.* **2013,** *13,* 4113–4117. doi:10.1021/nl4016182
10. Czaban, J. A.; Thompson, D. A.; LaPierre, R. R. *Nano Lett.* **2009,** *9,* 148–154. doi:10.1021/nl802700u
11. Wang, J.; Gudiksen, M. S.; Duan, X.; Cui, Y.; Lieber, C. M. *Science* **2001,** *293,* 1455–1457. doi:10.1126/science.1062340
12. Duan, X.; Huang, Y.; Cui, Y.; Wang, J.; Lieber, C. M. *Nature* **2001,** *409,* 66–69. doi:10.1038/35051047
13. Tomioka, K.; Yoshimura, M.; Fukui, T. *Nature* **2012,** *488,* 189–192. doi:10.1038/nature11293
14. Monaico, E.; Tiginyanu, I.; Volciuc, O.; Mehrtens, T.; Rosenauer, A.; Gutowski, J.; Nielsch, K. *Electrochem. Commun.* **2014,** *47,* 29–32. doi:10.1016/j.elecom.2014.07.015
15. Asoh, H.; Kotaka, S.; Ono, S. *Electrochem. Commun.* **2011,** *13,* 458–461. doi:10.1016/j.elecom.2011.02.020
16. Ono, S.; Kotaka, S.; Asoh, H. *Electrochim. Acta* **2013,** *110,* 393–401. doi:10.1016/j.electacta.2013.06.025
17. Li, X.; Guo, Z.; Xiao, Y.; Um, H. D.; Lee, J. H. *Electrochim. Acta* **2011,** *56,* 5071–5079. doi:10.1016/j.electacta.2011.03.084
18. Tiginyanu, I. M.; Ursaki, V. V.; Monaico, E.; Foca, E.; Föll, H. *Electrochem. Solid-State Lett.* **2007,** *10,* D127–D129. doi:10.1149/1.2771076
19. Volciuc, O.; Monaico, E.; Enachi, M.; Ursaki, V. V.; Pavlidis, D.; Popa, V.; Tiginyanu, I. M. *Appl. Surf. Sci.* **2010,** *257,* 827–831. doi:10.1016/j.apsusc.2010.07.074
20. Schwab, M. J.; Han, J.; Pfefferle, L. D. *Appl. Phys. Lett.* **2015,** *106,* 241603. doi:10.1063/1.4922702
21. Monaico, E.; Moise, C.; Mihai, G.; Ursaki, V. V.; Leistner, K.; Tiginyanu, I. M.; Enachescu, M.; Nielsch, K. *J. Electrochem. Soc.* **2019,** *166,* H3159–H3166. doi:10.1149/2.0251905jes
22. Zhang, C.; Yuan, G.; Bruch, A.; Xiong, K.; Tang, H. X.; Han, J. *J. Electrochem. Soc.* **2018,** *165,* E513–E520. doi:10.1149/2.1181810jes
23. Langa, S.; Carstensen, J.; Christophersen, M.; Steen, K.; Frey, S.; Tiginyanu, I. M.; Föll, H. *J. Electrochem. Soc.* **2005,** *152,* C525–C531. doi:10.1149/1.1940847
24. Prunici, P.; Irmer, G.; Monecke, J.; Sirbu, L.; Tiginyanu, I. *Phys. Status Solidi A* **2005,** *202,* 1562–1566. doi:10.1002/pssa.200461183
25. DeJarld, M.; Shin, J. C.; Chern, W.; Chanda, D.; Balasundaram, K.; Rogers, J. A.; Li, X. *Nano Lett.* **2011,** *11,* 5259–5263. doi:10.1021/nl202708d
26. Song, Y.; Oh, J. *J. Mater. Chem. A* **2014,** *2,* 20481–20485. doi:10.1039/c4ta05095a
27. Asoh, H.; Kotaka, S.; Ono, S. *Mater. Res. Express* **2014,** *1,* 045002. doi:10.1088/2053-1591/1/4/045002
28. Capizzi, M.; Emiliani, V.; Frova, A.; Sarto, F. *Phys. Rev. B* **1993,** *47,* 4301–4306. doi:10.1103/physrevb.47.4301
29. Sauncy, T.; Palsule, C. P.; Holtz, M.; Gangopadhyay, S.; Massie, S. *Phys. Rev. B* **1996,** *53,* 1900–1906. doi:10.1103/physrevb.53.1900
30. Yu, P. W.; Fischer, D. W.; Sizelove, J. R. *Semicond. Sci. Technol.* **1992,** *7,* 556–561. doi:10.1088/0268-1242/7/4/020
31. Deepak; Lakshminarayana, N. *Bull. Mater. Sci.* **2001,** *24,* 225–229. doi:10.1007/bf02710106

32. Sirkeli, V. P.; Yilmazoglu, O.; Hajo, A. S.; Nedeoglo, N. D.; Nedeoglo, D. D.; Preu, S.; Küppers, F.; Hartnagel, H. L. *Phys. Status Solidi RRL* **2018,** *12,* 1700418. doi:10.1002/pssr.201700418
33. Luo, Y.; Yan, X.; Zhang, J.; Li, B.; Wu, Y.; Lu, Q.; Jin, C.; Zhang, X.; Ren, X. *Nanoscale* **2018,** *10,* 9212–9217. doi:10.1039/c8nr00158h
34. Li, Z.; Yuan, X.; Fu, L.; Peng, K.; Wang, F.; Fu, X.; Caroff, P.; White, T. P.; Hoe Tan, H.; Jagadish, C. *Nanotechnology* **2015,** *26,* 445202. doi:10.1088/0957-4484/26/44/445202
35. García Núñez, C.; Braña, A. F.; López, N.; Pau, J. L.; García, B. J. *Nanotechnology* **2020,** *31,* 225604. doi:10.1088/1361-6528/ab76ee
36. Chen, X.; Wang, D.; Wang, T.; Yang, Z.; Zou, X.; Wang, P.; Luo, W.; Li, Q.; Liao, L.; Hu, W.; Wei, Z. *ACS Appl. Mater. Interfaces* **2019,** *11,* 33188–33193. doi:10.1021/acsami.9b07891
37. Chen, H.-Y.; Chen, R.-S.; Rajan, N. K.; Chang, F.-C.; Chen, L.-C.; Chen, K.-H.; Yang, Y.-J.; Reed, M. A. *Phys. Rev. B* **2011,** *84,* 205443. doi:10.1103/physrevb.84.205443
38. Berger, P. R. *Proc. SPIE* **2001,** *4285,* 198–207. doi:10.1117/12.426888

License and Terms

The definitive version of this article is the electronic one which can be found at:
doi:10.3762/bjnano.11.81

BEILSTEIN JOURNAL OF NANOTECHNOLOGY

Gas-sensing features of nanostructured tellurium thin films

Dumitru Tsiulyanu

Full Research Paper

Open Access

Address:
CIMAN Research Centre of Department of Physics, Technical University, bul. Dacia 41, MD-2060 Chisinau, Moldova

Email:
Dumitru Tsiulyanu - tsiudima@gmail.com

Keywords:
gas-sensing properties; NO_2; tellurium thin films; nanocrystalline films

Beilstein J. Nanotechnol. **2020,** *11,* 1010–1018.
doi:10.3762/bjnano.11.85

Received: 20 March 2020
Accepted: 29 May 2020
Published: 10 July 2020

This article is part of the thematic issue "Functional nanostructures for electronics, spintronics and sensors".

Guest Editor: A. S. Sidorenko

Abstract

Nanocrystalline and amorphous nanostructured tellurium (Te) thin films were grown and their gas-sensing properties were investigated at different operating temperatures with respect to scanning electron microscopy and X-ray diffraction analyses. It was shown that both types of films interacted with nitrogen dioxide, which resulted in a decrease of electrical conductivity. The gas sensitivity, as well as the response and recovery times, differed between these two nanostructured films. It is worth mentioning that these properties also depend on the operating temperature and the applied gas concentration on the films. An increase in the operating temperature decreased not only the response and recovery times but also the gas sensitivity of the nanocrystalline films. This shortcoming could be solved by using the amorphous nanostructured Te films which, even at 22 °C, exhibited higher gas sensitivity and shorter response and recovery times by more than one order of magnitude in comparison to the nanocrystalline Te films. These results were interpreted in terms of an increase in disorder (amorphization), leading to an increase in the surface chemical activity of chalcogenides, as well as an increase in the active surface area due to substrate porosity.

Introduction

Tellurium (Te) is a multifunctional chemical element used for the development of many devices, such as diodes with high (10^6) rectification ratios, thin-film field-effect transistors, optical recording media, infrared and UV detectors, strain-sensitive devices and others (see [1,2] for extended reviews on the topic). In the last decade, Te has also become an attractive element with great biological applicability since it can be used as quantum dots in imaging and diagnostics and has antibiotic properties [3]. Even though Te has a biological relevance, it is largely used in the development of thin films in chemical-sensing applications, especially for toxic gas sensing. Szaro [4] pioneered the studies regarding the effects of oxygen and nitrogen, diluted in either dry or wet air, on the electrical properties of Te films. The results showed an increase in the hole concentration during the adsorption process but not in the mobility of these holes. However, the changes in the electrical properties induced by these gases were very small and irreversible and were, later on, confirmed and explained in a systematic, relevant work [5]. In the early 2000s, Tsiulyanu and coworkers [6] started to thoroughly investigate the use of Te thin films as an active element in gas sensor manufacturing. They showed that microcrystalline Te thin films, grown by thermal vacuum evaporation, exhibit high sensitivity to low concentrations (ppm range) of nitrogen dioxide (NO_2) even at room temperature. Subsequent studies showed that it was possible to increase the concentration range sensitivity to more than 300 ppm NO_2 by growing single-crystalline microtubes. In order to do that, Te metal was evaporated onto quartz substrates under an inert argon gas at ambient pressure [7]. Later, it was also found that microcrystalline Te films have remarkable, sensitive properties toward ammonia [8,9] and hydrogen sulfide [10] and, to a lesser extent, to carbon oxides and amines [11]. In the last years, due to the increase in the general interest toward nanodimensional devices and structures, significant attention has been given to growing, studying and applying nanostructured Te. To achieve these goals, different and sometimes quite sophisticated chemical, electrochemical and physical methods have been developed. In line with this, Wang and collaborators [12] used thermal decomposition of Te dietyldithiocarbamato film to grow Te nanoflakes. In order to synthesize Te nanowires, Liang and collaborators [13] performed chemical reactions of Na_2TeO_3, in aqueous solution, via hydrothermal treatment, whereas Ma and colleagues [14] used a solvothermal approach on glass substrates. To synthesize Te nanotubes, techniques such as galvanic displacement of sacrificial cobalt nanowires were employed [15]. Lastly, to grow one-dimensional nanostructures, either template-free electrodeposition of Te, from an ionic liquid binary mixture [16], or thermal evaporation in a furnace under argon gas flow [17] were strategies utilized.

The present work is related to investigations of the interaction between nanostructured Te films and toxic gases. According to the literature, such investigations firstly have been provided utilizing the nanocrystalline Te films grown onto Pyrex glass, alumina (Al_2O_3), oxidized silicon or sapphire substrates via thermal vacuum evaporation of pure Te [18-20]. Tests were performed in those films in order to access their ability to detect both oxidizing (NO_2) and reducing (H_2S) toxic gases at temperatures between 77 and 423 K. Depending on the experimental conditions in which the films were prepared (such as temperature, type and concentration of the target gas), their sensing characteristics were found to vary. For instance, the best response and recovery time values toward NO_2 were around 30 s and 7 min, respectively, at 40% sensitivity (defined as the relative variation of the resistance). Such sensing parameters did not differ much from the similar parameters obtained earlier for microcrystalline Te films. Further investigations have been extended to Te nanotubes grown on quartz or Si(111) substrates through a catalyst-free growing process in a furnace filled with argon [21]. Another study used the high-vacuum deposition technique in order to grow Te nanotubes on silicon substrates containing previously deposited nanoparticles of silver or gold [22]. In both cases, 50 nm diameter Te nanotubes were obtained. When exposed to low concentrations of different toxic gases, including NO_2, the Te nanotube-based sensors showed similar (or sometimes lower) numbers regarding sensitivity and response/recovery times in comparison to Te single-crystalline microtube-based gas sensors [7]. An increase in the gas-sensing performance was achieved by growing single-crystal Te-based nanotubes and nanowires via hydrothermal recrystallization [23]. The response time range of NH_3 gas sensors based on such nanocomponents was 5–18 s but the recovery time ranged between 170–720 s. From comparison with state-of-the-art devices, it can be observed that the physically nanostructured Te thin films exhibit great potential for applications in development in advanced gas sensors and, so far, are the only Te-based nanostructured sensors tested with this purpose. Besides, it can also be observed that nanostructuring is mostly performed via phase transformations, such as hydrothermal recrystallization and growth of Te nanocrystals, nanotubes or nanowires from the gas phase under vacuum or argon atmosphere. On the other hand, nanostructuring can be performed mechanically as indicated by the possibility of growth of nanocrystalline gas sensors via rf sputtering (13.6 MHz) of Te in an ultra-high-purity argon atmosphere [24].

The main aims of the present work were to investigate and improve the gas-sensing parameters of nanostructured Te films by using a mechanical nanostructuring approach. Crystalline and amorphous Te films were grown, respectively, on glass or porous, nanostructured, dielectric substrates. These two physically nanostructured Te films were studied with a special focus on the gas-response kinetics.

Results and Discussion

Sample preparation, morphology and structure

Two methods were used to nanostructure Te-based films: growth of Te nanocrystals on Pyrex glass substrates or deposition of amorphous Te films onto nanostructured (porous) Al_2O_3 substrates. In both cases, the polycrystalline Te (purity 99.999%) was evaporated under 10^{-4} Pa vacuum conditions. The evaporation was carried out using VUP-5 equipment (SUMI, Ukraine) from a tantalum boat, keeping the same distance (20 cm) between the evaporation boat and substrate, without any cooling or heating of the latter. To grow films with a nanocrystalline structure, a growth rate of about 10 nm/s was used whereas, for amorphous thin films, the growth rate was increased to 30 nm/s. The deposition rate was increased by raising the temperature of the evaporator. The calibration was performed via measuring the final thickness of the grown film versus the time of deposition at given temperature of the evaporator. Under these conditions, the amorphous Te films were grown on either continuous (Pyrex glass) or porous (Al_2O_3) nanostructured substrates. Then, rectangular 70 mm^2 samples were cut from nanocrystalline and nanostructured amorphous Te films, which were either prepared for further morphological and structural analysis or for fabrication of gas-sensitive devices. After preparation, the thickness and shape of the films were studied using a SIS SCAN Control C (PhotoniTech Pte Ltd., Singapore) atomic force microscope. The surface morphology of the films was investigated using either a TESLA BS 340 or a VEGA TESCAN TS 5130 MM (TESCAN, Czech Republic) scanning electron microscope (SEM). To investigate the structural features of the grown films, X-ray analysis was performed using a DRONE–YM1 (Burevestnik, Russia) diffractometer with Fe Kα radiation. The rotational velocity of the scintillation counter was set to be either 2 or 4°/min. For the electrical and gas-sensing characterization, the samples were supplied with symmetrical gold or platinum electrodes, identified in our preliminary works as ohmics [25,26], which form electrically transparent contacts with Te. The gold or copper wires were then attached to the electrodes with a silver paste. Figure 1A shows the surface morphology of a Te film grown on a Pyrex glass substrate at a rate of 10 nm/s. As shown, the film contains a dense nanocrystalline layer with randomly oriented crystals with sizes ranging from 50–100 nm. Figure 1B shows the surface morphology of an amorphous Te film grown on preliminary nanostructured Al_2O_3. Pure amorphous films grown on Pyrex glass substrates were uniform and did not exhibit a striking morphological structure; therefore, their SEM image was omitted.

At the same time, the Te films grown on the Al_2O_3 substrate (Figure 1B) exhibited a nanostructured morphology, corresponding to the substrate template, which consists of ≈100 nm diameter dotted holes, separated 400 nm from one another. No Te crystallites were observed in this case.

The structural phase state of the grown films was adequately confirmed by X-ray diffraction (XRD). Figure 2 shows the XRD patterns of Te films grown on either Pyrex glass (Figure 2A) or nanostructured Al_2O_3 substrates (Figure 2B).

According to Figure 2A, the XRD pattern of films grown on Pyrex glass substrates reveals a highly crystalline structure with a predominant Te hexagonal phase. The positions of the most intense peaks matched the reference values: from right to left, the first peak occurs due to the reflection from the (100) crystal plane, the second peak is observed due to the reflection from the (101) crystal plane and the third peak appears due to the reflection from the (110) crystal plane. The nearly equal intensities of these peaks as well as the appearance of other refraction peaks indicates the absence of a predominant growth orientation of the nanocrystals. As a counter example, the XRD pattern of a Te film grown on Al_2O_3 substrates with a higher deposition rate ≈30 nm/s (Figure 2B, adapted from [27]) only shows two weak Te peaks (ASTM, 4-554). These type of films are considered amorphous. It should also be mentioned that the XRD pattern of samples grown on Pyrex glass substrates at the same rate of 30 nm/s (data not shown) does not show features of crystalline Te.

Gas-sensing characterization, methods and response kinetics

For the gas-sensing characterization of fabricated films, NO_2 was chosen since it is one of the most active toxic gases known to interact with Te [1].

NO_2 vapor, with a concentration of either 0.5 or 1.0 ppm, was obtained by using the experimental set up described in our previous paper [28]. Gaseous NO_2 media was obtained using a

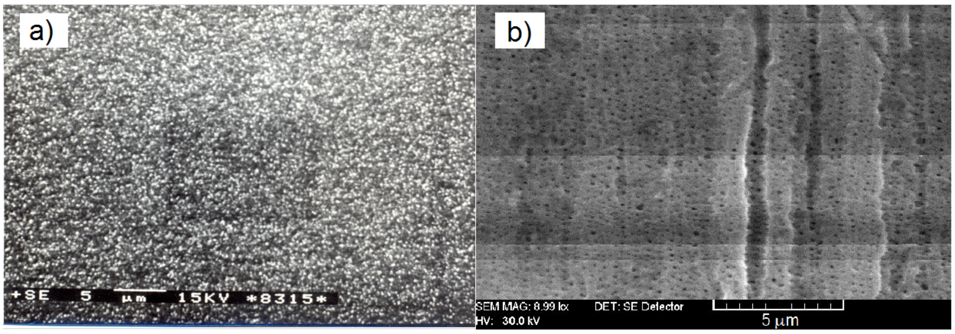

Figure 1: SEM of Te films grown: a) on Pyrex glass at a rate of 10 nm/s and b) on nanostructured Al_2O_3 substrates at a rate of 30 nm/s. Scale bar is 5 µm.

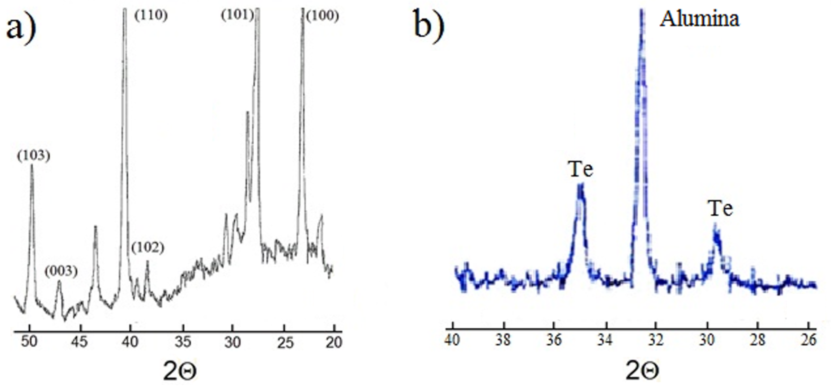

Figure 2: XRD diffraction patterns of Te films grown on Pyrex glass (A) or nanostructured Al_2O_3 (B) substrates.

calibrated permeation tube (Vici Metronics, USA), which was introduced into the experimental setup. Ambient air was used as both the carrier and the reference gas. Nanostructured Te-based gas-sensing devices were put into a 10 mL test cell and the NO_2 diluted in ambient air was injected at a 100 mL/min flow rate parallel to the film surface. To perform both the heating and the annealing of the samples, the test cell was mounted inside a furnace. A platinum temperature detector (PT-100, Cliptec Kabeltechnik, Germany) was placed close to the film and was used to assist with the temperature control.

The data was processed using a PC equipped with a data acquisition board (National Instruments Inc., USA). Characteristic transient current response curves were collected at a constant applied voltage (5 V), using different NO_2 concentrations at different temperatures. The switching between the mixture of NO_2 vapor and reference gases was computer-controlled. The time delay between measurements was 2 s, which was, simultaneously, much smaller than the sensor response time and much higher than the assessed dielectric relaxation time value. In order to transform the resistance signal into a voltage signal, the sample was connected in series to a load resistance using a dc voltage supplier. In all measurements, the load resistance was chosen to be approximately one order of magnitude lower than the sample resistance.

Figure 3 shows the dynamic response of both nanocrystalline (blue) and amorphous (black) nanostructured Te-based gas-sensitive devices to a concentration pulse of 1.0 ppm NO_2 at room temperature (22 °C). As a comparison, and under the same conditions, the response of a microcrystalline film grown on a Pyrex glass substrate at a deposition rate of 1 nm/s was also added. The morphological and structural features of microcrystalline films were previously described in detail [5,6]. It can be observed in Figure 3 that both the response current and the time to reach the saturation decrease with the reduction of the crystallite structural block dimension, i.e., from microcrystalline (red) to nanocrystalline (blue) states. On the other hand, the behavior of the nanostructured amorphous films (black curve) is significantly different from the crystalline ones. It is worth noting that these parameters also depend on the film thickness, temperature and gas concentration.

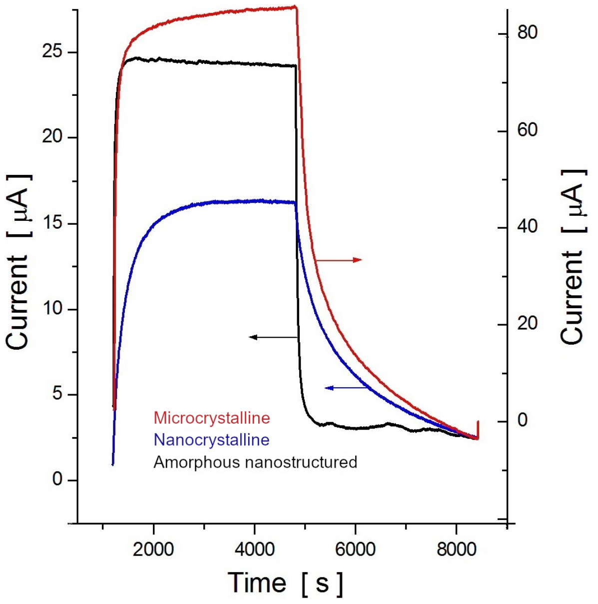

Figure 3: Normalized dynamic response of a microcrystalline (red), nanocrystalline (blue) and amorphous (black) nanostructured Te-based gas-sensitive device to a rectangular pulse of 1.0 ppm NO_2 at room temperature (22 °C).

The effect of temperature and gas concentration on nanocrystalline films

Figure 4 shows the current flow through a ≈100 nm thick nanocrystalline film submitted to repeated switching on–off cycles of the NO_2 gas mixture at a constant bias voltage and 22 °C operating temperature. Square pulses of NO_2 vapor

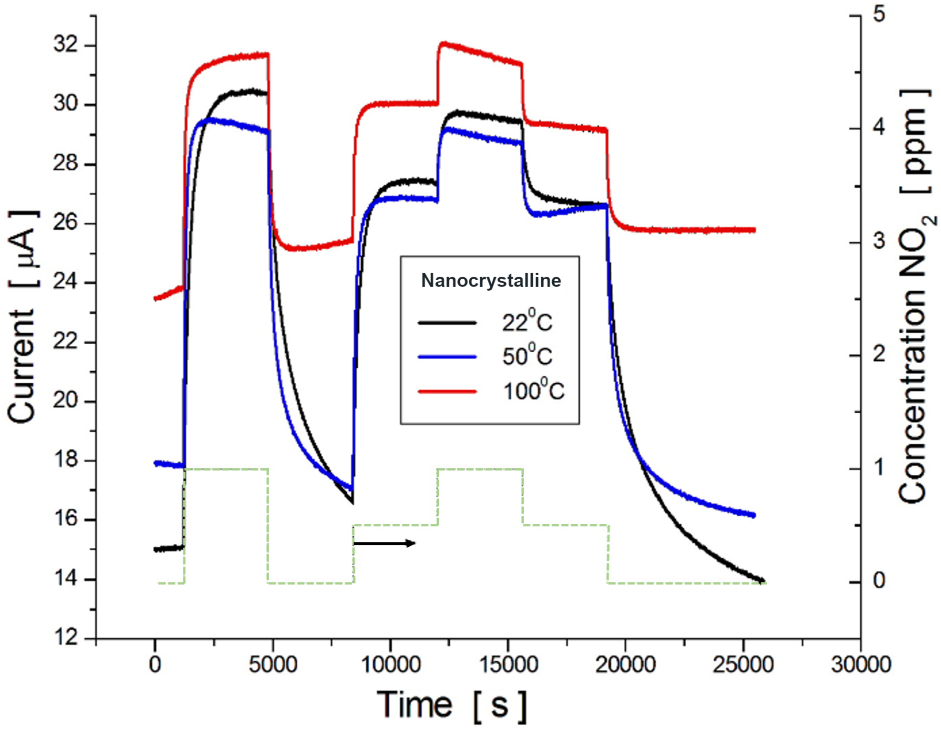

Figure 4: Transient characteristics of gas-induced current in nanocrystalline Te films, at different temperatures, due to the exposure to various NO$_2$ concentrations, according to the profile shown by the green dashed line at the bottom.

at concentrations of 0 ppm, 0.5 ppm, and 1.0 ppm were applied. The dashed green line shows the switching profile. It is seen that the current follows the same pattern but the baseline strongly increases with temperature, as depicted in Table 1. Table 1 also shows the film sensitivity, which is calculated from the response kinetics to 1.0 ppm NO$_2$, as a relative percent increase in current (in %/ppm) according to Equation 1:

$$S = 100(I_g - I_a)/C \cdot I_g \qquad (1)$$

where I_a and I_g are the currents flowing through the specimen in air and in the presence of NO$_2$, respectively, and C is the gas concentration.

Figure 4 shows that, independent of the operating temperature, the recovery time (t_{rv}) is longer than the response time (t_{rs}). These parameters, listed in Table 1, were estimated to be the time to reach and to lose 50% of the maximum value of I_g.

According to Table 1, both t_{rs} and t_{rv} decrease with the temperature increase; however, the sensitivity of the films diminishes. In the following subsection, interesting results will be explored in terms of solving this sensitivity issue by nanostructuring amorphous Te-based films.

Amorphous nanostructured films

Figure 5 illustrates the transient characteristics of the gas-induced current in both nanocrystalline Te films, grown on Pyrex glass substrate, and amorphous Te films, grown on a nanostruc-

Table 1: Gas-sensing parameters of nanostructured Te films. t_{rv} is the recovery time and t_{rs} is the response time upon exposure to 1.0 ppm of NO$_2$.

Films	T [°C]	Baseline [µA]	Sensitivity [%/ppm]	t_{rs} [s]	t_{rv} [s]
nanocrystalline	22	15	50	160	600
	50	18	40	70	200
	100	24	25	50	50
amorphous nanostructured	22	11	65	15	30

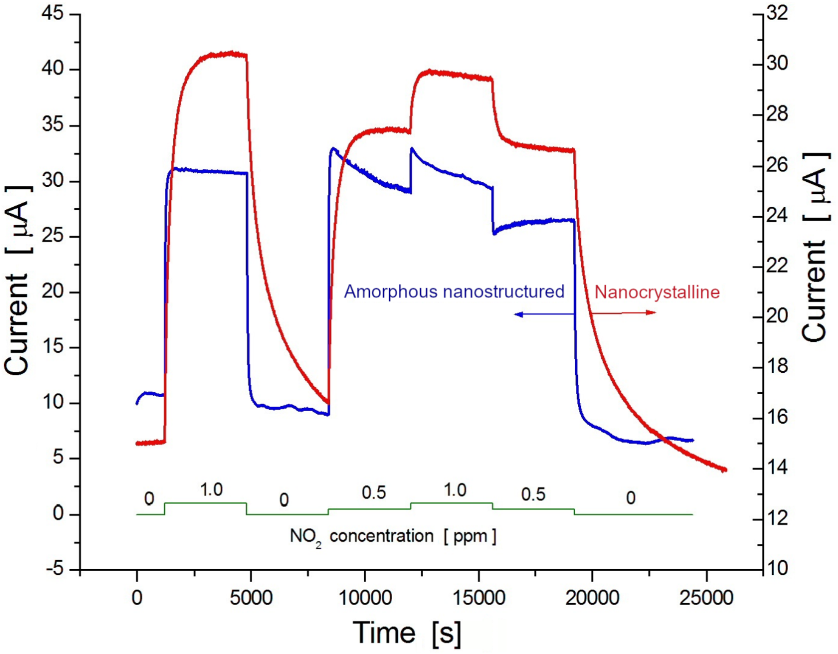

Figure 5: Transient characteristics of gas-induced current in amorphous nanostructured Te films (blue curve) at room temperature (22 °C) due to exposure to various concentrations of NO_2, according to the profile shown by the green continuous line at the bottom. The transient characteristic profile for nanocrystalline film (red curve) is given for comparison.

tured Al_2O_3 substrate. The NO_2 exposure profile curve is shown by the green continuous line at the bottom. The operating temperature was maintained at 22 °C. There is no noticeable baseline drift in either the nanocrystalline or in the amorphous nanostructured films; however, a dramatic change in the response kinetics can be clearly observed. These changes consist of a decrease in both the response and recovery times for amorphous Te films grown on preliminary nanostructured Al_2O_3 substrates. As shown in Figure 6A, in such films, the response time is approximately only 15 s whereas the recovery time is about twice as long (see red bars). Interestingly, the reduction in both the response and recovery times is accompanied by an impressive increase in gas sensitivity reaching 65%/ppm, which is the highest among the values obtained for the nanostructured films studied. The diagram presented in Figure 6B illustrates this result.

Another peculiarity of the transient characteristics of amorphous nanostructured films is a spontaneous reduction (or increase) in the gas-induced current in terms of step change concentration of the target gas.

Discussion

This paper presents a study regarding two different types of nanostructured Te films physically built either in the form of nanocrystals, grown onto flat substrates, or vitreous Te, deposited onto nanostructured (porous) dielectric templates. It was expected that the physical properties, including the adsorptive ones, of these films would differ from each other and also from those observed in the microcrystalline Te-based films. In fact, this assumption, previously mentioned in our review paper [29], was confirmed by our results presented in Figure 3, which shows the normalized response kinetics to the target gas NO_2 when in contact with microcrystalline, nanocrystalline or amorphous nanostructured Te-based films. Since that review was dedicated to exploring only the fabrication and investigation of gas-sensing properties of nanocrystalline Te films, it was only superficially mentioned that the amorphous films could improve the response kinetic parameters in detriment of sensitivity. One way to enhance both the response time and sensitivity to NO_2 seems to be the mechanical nanostructuring of amorphous Te films, which is investigated and discussed in this paper. So far, nanocrystalline Te films have been grown using either the thermal vacuum evaporation of pure Te [17-20] or its sputtering under a pure argon atmosphere [24] onto glass, Al_2O_3 or sapphire substrates. It was shown that the film morphology as well as the gas sensitivity is controlled by several factors, such as the nature and temperature of the substrate, the type and concentration of the target gas molecules, film thickness, post-preparation thermal treatment and operating temperature. It is more or less generally accepted that the films grown on glass substrates at room temperature exhibit a maximum sensitivity to gases such as NO_2, H_2S or ammonia. This is the main reason why this method was used in this work to manufacture and ex-

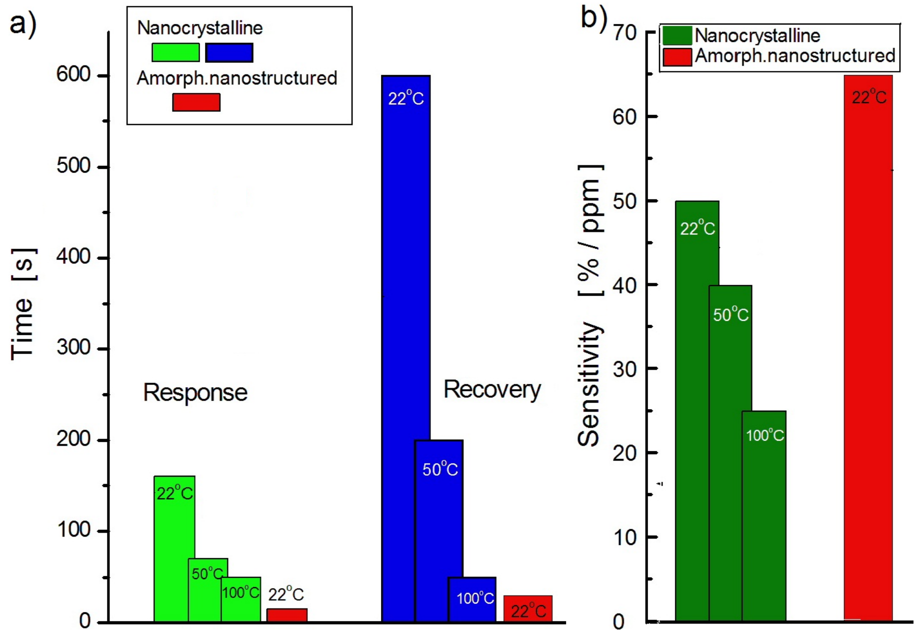

Figure 6: Comparison of the gas-sensing properties of nanocrystalline and amorphous nanostructured Te-based films to NO_2 at different temperatures: A) response and recovery times; B) sensitivity.

amine Te films. According to the SEM image shown in Figure 1A, nanocrystalline Te films grown on glass substrates present a uniform and dense distribution of randomly oriented nanocrystalline grains with an approximate average size of 100 nm. Assuming the neutrality of the Au/Te contacts, the electrical conductivity of the film is mainly controlled by the bulk, surface and grain boundary resistances. On the other hand, due to the peculiarities of chalcogens and chalcogenide materials [1,30], a region enriched in holes is formed at the surface and at grain boundary and intragrain regions. Therefore, when the films are exposed to NO_2, the surface and grain boundaries are the most affected by the gas reaction. Although the gas sensing occurs due to the variation in hole density at the enriched region (surface and grain boundary), in the presence of gaseous media, the bulk is responsible for the observed increase in the baseline current when the temperature increases (Figure 4). Elevated temperatures result in the decrease of the gas (NO_2) sensitivity, as shown in Figure 6B. At the same time, the increase in the operating temperature values affects the gas response kinetics (Figure 4), essentially decreasing both the response and recovery times (Figure 6A). The decrease in both the response and recovery times with an increase in temperature can be partially explained by Maxwell's dielectric relaxation time (τ_r). As $\tau_r = \varepsilon\varepsilon_0\rho$ (ρ is the bulk resistivity, ε and ε_0 are the permittivity and the electric constant, respectively), it is clear that τ_r decreases since there is a reduction in the resistivity when the temperature increase and the system reaches steady state in less time. Another suitable explanation for the reduction in the response and recovery times with the increase in temperature might be the shift in the adsorption–desorption equilibrium, pointed out in Langmuir's theory [31].

The nanostructuring of Te-based films by growing amorphous Te on nanoporous Al_2O_3 substrates (Figure 1B) allows for a reduction in the response and recovery times and a simultaneous increase in the sensitivity to NO_2. As show in Figure 6A and Table 1, both the response and recovery times for these films are, respectively, more than 10 and 20 times shorter in comparison to the nanocrystalline film kinetics. In addition, the sensitivity to 1 ppm of NO_2 increases by 15%/ppm. It is worth noting that such remarkable improvement in gas sensing parameters is achieved without heating, since the working temperature is kept at 22 °C (room temperature). The reason for such behavior seems to be due to the increase in the chemical activity of chalcogenides at the surface when disorder (amorphization) increases [32,33] and to the increase in the active area caused by substrate porosity. Another interesting feature observed in the experiments was the spontaneous reduction (or sometimes increase) in the gas-induced current upon step-change concentration of the target gas. This can be explained based on the concentration-induced phenomenon that induces sensitivity damping in ultrathin films [34]. It is safe to assume that, given the high rate at which the films are grown (30 nm/s), their thickness remains low (<40 nm) since the film is deposited on the walls of the porous surface. On the one hand, these ultrathin films show a considerably short response time, but on the other hand, the increase in gas concentration damps their sensitivity due to the formation of a catalytic gate at the surface.

Conclusion

The nanostructuring of Te-based films by growing vitreous Te on a pre-nanostructured (porous) dielectric template significantly improves their gas sensing capabilities. At room temperature (22 °C), the response and recovery times decrease by approximately 10 and 20 times, respectively, in comparison with nanocrystalline Te films. In addition, there is an increase in the gas sensitivity by 15%/ppm. These achievements can be attributed to two main factors: the increase in chemical activity of chalcogenides at the surface due to increase in disordering (amorphization) and an increase in the active surface area due to increased substrate porosity.

Acknowledgements

The author expresses his gratitude to Dr. M. Enache at NCMST of TUM for the porous Al_2O_3 substrates and SEM analysis, as well as to Dr. G. F.Volodina at IAF ASM for XRD analysis.

Funding

This work was supported by the National Agency for Research and Development of Moldova, project PS 20.80009.5007.21.

ORCID® iDs

Dumitru Tsiulyanu - https://orcid.org/0000-0003-3711-4434

References

1. Tsiulyanu, D. Tellurium Thin Films in Sensor Technology. In *Nanotechnological Basis for Advanced Sensors. NATO Science for Peace and Security Series B: Physics and Biophysics;* Reithmaier, J.; Paunovic, P.; Kulisch, W.; Popov, C.; Petcov, P., Eds.; Springer: Dordrecht, The Netherlands, 2011; pp 363–380. doi:10.1007/978-94-007-0903-4_38
2. He, Z.; Yang, Y.; Liu, J.-W.; Yu, S.-H. *Chem. Soc. Rev.* **2017,** *46,* 2732–2753. doi:10.1039/c7cs00013h
3. Ba, L. A.; Döring, M.; Jamier, V.; Jacob, C. *Org. Biomol. Chem.* **2010,** *8,* 4203–4216. doi:10.1039/c0ob00086h
4. Szaro, L. *Thin Solid Films* **1986,** *139,* 9–13. doi:10.1016/0040-6090(86)90042-8
5. Tsiulyanu, D.; Stratan, I.; Tsiulyanu, A.; Liess, H.-D.; Eisele, I. *Sens. Actuators, B* **2007,** *121,* 406–413. doi:10.1016/j.snb.2006.04.068
6. Tsiulyanu, D.; Marian, S.; Miron, V.; Liess, H.-D. *Sens. Actuators, B* **2001,** *73,* 35–39. doi:10.1016/s0925-4005(00)00659-6
7. Siciliano, T.; Filippo, E.; Genga, A.; Micocci, G.; Siciliano, M.; Tepore, A. *Sens. Actuators, B* **2009,** *142,* 185–190. doi:10.1016/j.snb.2009.07.050
8. Bianchetti, M. F.; Heredia, E.; Oviedo, C.; Walsöe de Reca, N. E. *J. Argent. Chem. Soc.* **2005,** *93,* 27–34.
9. Sen, S.; Muthe, K. P.; Joshi, N.; Gadkari, S. C.; Gupta, S. K.; Jagannath; Roy, M.; Deshpande, S. K.; Yakhmi, J. V. *Sens. Actuators, B* **2004,** *98,* 154–159. doi:10.1016/j.snb.2003.10.004
10. Sen, S.; Bhandarkar, V.; Muthe, K. P.; Roy, M.; Deshpande, S. K.; Aiyer, R. C.; Gupta, S. K.; Yakhmi, J. V.; Sahni, V. C. *Sens. Actuators, B* **2006,** *115,* 270–275. doi:10.1016/j.snb.2005.09.013
11. Tsiulyanu, D.; Marian, S.; Liess, H.-D. *Sens. Actuators, B* **2002,** *85,* 232–238. doi:10.1016/s0925-4005(02)00113-2
12. Wang, S.; Wen, H.; Guan, W.; Zhang, L.; Ma, D.; Huang, S.; Wang, J. *Thin Solid Films* **2010,** *518,* 4215–4220. doi:10.1016/j.tsf.2009.12.081
13. Liang, F.; Qian, H. *Mater. Chem. Phys.* **2009,** *113,* 523–526. doi:10.1016/j.matchemphys.2008.07.101
14. Ma, J.; Liu, X.; Wu, L.; Zheng, W. *Cryst. Res. Technol.* **2008,** *43,* 1297–1299. doi:10.1002/crat.200800185
15. Rheem, Y.; Chang, C. H.; Hangarter, C. M.; Park, D. Y.; Lee, K. H.; Jeong, Y. S.; Myung, N. V. *Electrochim. Acta* **2010,** *55,* 2472–2476. doi:10.1016/j.electacta.2009.12.002
16. Thiebaud, L.; Legeai, S.; Stein, N. *Electrochim. Acta* **2016,** *197,* 300–306. doi:10.1016/j.electacta.2015.12.084
17. Sen, S.; Bhatta, U. M.; Kumar, V.; Muthe, K. P.; Bhattacharya, S.; Gupta, S. K.; Yakhmi, J. V. *Cryst. Growth Des.* **2008,** *8,* 238–242. doi:10.1021/cg070185m
18. Tsiulyanu, D.; Marian, S.; Liess, H.-D.; Eisele, I. *Sens. Actuators, B* **2004,** *100,* 380–386. doi:10.1016/j.snb.2004.02.005
19. Bhandarkar, V.; Sen, S.; Muthe, K. P.; Kaur, M.; Kumar, M. S.; Deshpande, S. K.; Gupta, S. K.; Yakhmi, J. V.; Sahni, V. C. *Mater. Sci. Eng., B* **2006,** *131,* 156–161. doi:10.1016/j.mseb.2006.04.017
20. Tsiulyanu, D.; Marian, T.; Tiuleanu, A.; Liess, H.-D.; Eisele, I. *Thin Solid Films* **2009,** *517,* 2820–2823. doi:10.1016/j.tsf.2008.11.073
21. Her, Y. C.; Huang, S. L. *Nanotechnology* **2013,** *24,* 215603. doi:10.1088/0957-4484/24/21/215603
22. Kumar, V.; Sen, S.; Sharma, M.; Muthe, K. P.; Jagannath; Gaur, N. K.; Gupta, S. K. *J. Nanosci. Nanotechnol.* **2009,** *9,* 5278–5282. doi:10.1166/jnn.2009.1185
23. Wang, Z.; Wang, L.; Huang, J.; Wang, H.; Pan, L.; Wei, X. *J. Mater. Chem.* **2010,** *20,* 2457–2463. doi:10.1039/b924462j
24. Siciliano, T.; Di Giulio, M.; Tepore, M.; Filippo, E.; Micocci, G.; Tepore, A. *Sens. Actuators, B* **2008,** *135,* 250–254. doi:10.1016/j.snb.2008.08.018
25. Ciobanu, M.; Tsiulyanu, D. Electric conductivity of tellurium-based chalcogenides thin films with Au and Ag contacts. In *ICTEI-2015: International Conference on Telecommunications, Electronics and Informatics. Proceedings,* May 20–23, 2015; Kantser, V.; Andronic, S., Eds.; Chisinau, Maldova, 2015; pp 236–238.
26. Ciobanu, M.; Tsiulyanu, D. *Chalcogenide Lett.* **2018,** *15,* 19–24.
27. Tsiulyanu, D.; Mocreac, O. Impedance characterization of Te based gas sensitive films. In *Proceedings 6th International Conference on Telecomunications, Electronics and Informatics,* Chisinau, Maldova, 2018; pp 166–169.
28. Tsiulyanu, D.; Ciobanu, M. *Glass Phys. Chem.* **2019,** *45,* 53–59. doi:10.1134/s1087659619010140
29. Tsiulyanu, D.; Moraru, A. Nanocrystalline Tellurium Films: Fabrication and Gas Sensing Properties. In *Nanoscience Advances in CBRN Agents Detection, Information and Energy Security;* Petkov, P.; Tsiulyanu, D.; Kulisch, W.; Popov, C., Eds.; Springer: Dordrecht, The Netherlands, 2015; pp 389–408. doi:10.1007/978-94-017-9697-2_40
30. Mott, N. F.; Davis, E. A. *Electronic processes in non-crystalline materials;* Clarendon Press: Oxford, U.K., 1979.

31. Wolkenstein, T. *Electronic Processes on Semiconductor Surfaces During Chemosorption;* Consultants Bureau: New York, 1987.
32. Ciobanu, M. Contacts and surface phenomena in quaternary glassy chalcogenides based on S and Te. Ph.D. Thesis, Technical University of Moldova, Moldova, 2018.
33. Mamontova, T. N.; Kochemirovskii, A. S.; Pivovarova, L. V. *Phys. Status Solidi A* **1988,** *107,* 11–43. doi:10.1002/pssa.2211070102
34. Tsiulyanu, D.; Mocreac, O. *Sens. Actuators, B* **2013,** *177,* 1128–1133. doi:10.1016/j.snb.2012.12.022

License and Terms

The definitive version of this article is the electronic one which can be found at:
doi:10.3762/bjnano.11.85

BEILSTEIN JOURNAL OF NANOTECHNOLOGY

Excitonic and electronic transitions in Me–Sb_2Se_3 structures

Nicolae N. Syrbu*[1], Victor V. Zalamai[2], Ivan G. Stamov[3] and Stepan I. Beril[3]

Full Research Paper

Address:
[1]Laboratory of Micro-Optoelectronics, Technical University of Moldova, 168 Stefan cel Mare Avenue, 2004 Chisinau, Republic of Moldova, [2]National Center for Materials Study and Testing, Technical University of Moldova, Bv. Stefan cel Mare 168, Chisinau 2004, Republic of Moldova and [3]T.G. Shevchenko State University of Pridnestrovie, 25 Oktyabrya street 107, 3300 Tiraspol, Republic of Moldova

Email:
Nicolae N. Syrbu* - sirbunn@yahoo.com

* Corresponding author

Keywords:
anisotropy; antimony triselenide; band structure; excitons; optical spectroscopy; reflection and absorption spectra

Beilstein J. Nanotechnol. **2020,** *11,* 1045–1053.
doi:10.3762/bjnano.11.89

Received: 28 February 2020
Accepted: 25 June 2020
Published: 16 July 2020

This article is part of the thematic issue "Functional nanostructures for electronics, spintronics and sensors".

Guest Editor: A. S. Sidorenko

Abstract

The optical anisotropy of the Sb_2Se_3 crystals was investigated at 300 and 11 K. Excitonic features of four excitons (A, B, C, and D) were observed in the optical spectra of the Sb_2Se_3 single crystals and in the photoelectric spectra of the Me–Sb_2Se_3 structures. The exciton parameters, such as the ground (n = 1) and excited (n = 2) state positions and the binding energy (Ry), were determined. The effective mass of the electrons at the bottom of the conduction band ($m_c^* = 0.67m_0$) as well as the holes at the four top valence bands ($m_{v1}^* = 3.32m_0$, $m_{v2}^* = 3.83m_0$, $m_{v3}^* = 3.23m_0$ and $m_{v4}^* = 3.23m_0$) were calculated in the Γ-point of the Brillouin zone. The magnitude of the valence band splitting V_1–V_2 due to the spin–orbit interaction (Δ_{so} = 35 meV) and the crystal field (Δ_{cf} = 13 meV) were estimated in the Brillouin zone center. The energy splitting between the bands V_3–V_4 was 191 meV. The identified features were discussed based on both the theoretically calculated energy band structure and the excitonic band symmetry in the Brillouin zone (k = 0) for crystals with an orthorhombic symmetry (*Pnma*). The photoelectric properties of the Me–Sb_2S_3 structures were investigated in the spectral range 1–1.8 eV under E||c and E⊥c polarization conditions and at different applied voltages.

Introduction

Antimony selenide (Sb_2Se_3) is an inorganic semiconductor compound with interesting photoelectric properties. This material has a high absorption coefficient (≈10^5 cm^{-1}) in the region of maximum solar energy radiation [1,2] which is corroborated by a 6.5% rapid increase in solar cell efficiency when Sb_2Se_3 is present [3-5]. Interestingly, this high absorption coefficient is 10^3 times higher than the absorption in silicon [5-7] and encompasses a wide portion of the spectrum ranging from 1.0 eV to 2–3 eV. The crystalline structure of Sb_2Se_3 is quite uniform and stable which minimizes the energy loss due to radiation [3,7,8]. In combination, the binary arrangement (Sb, Se), high crystalline stability, low toxicity and low deposition temperature (melting point ≈611 °C) reduce the production costs [3-10]. It has been shown that Sb_2Se_3 has many applications in photovoltaic devices and thermoelectric systems where it can be used as a thin film [11], in thermovoltaic and switch devices [12], in optical data storage [13] and in optoelectronics as a 2D anisotropic material [14,15].

In order to use Sb_2Se_3 to build high-performance devices it is necessary to study its crystalline nanostructure in terms of band structure and optical and optoelectronic properties, especially in the bandgap region in which ambiguous and contradictory results have been obtained. For example, the energy range of the bandgap was found to be 1.2 eV [15,16], 1.1–1.3 eV [17,18] and 1.25–1.46 eV [19] and these discrepancies have been pointed out in a different study [20]. There are also discrepancies in terms of which type of electronic transitions are responsible for determining the minimal bandgap. Several studies have shown that the bandgap is established due to allowed transitions that happen within 1.0 and 1.9 eV [6,8,10], whereas other studies show that the bandgap is determined by forbidden transitions [21-23]. In addition, the energy band structure and the theoretical calculations in the Brillouin zone space are also ambiguous [6,8,10,19,20].

The crystalline properties of Sb_2Se_3, such as optical absorption, reflection, and photoconductivity, were studied in this work. In order to determine the bandgap, the nature of electronic transitions, among other properties, the absorption, reflection and excitonic spectra were obtained. The Sb_2Se_3 crystalline anisotropy of the ground and excited states of four excitonic series were determined at 300 and 11 K.

Due to the crystal field (Δ_{cf}) and spin–orbit (Δ_{so}) interactions, the high valence band splittings were estimated in the Brillouin zone center. The effective mass of the electrons and holes was calculated as well as the anisotropy of the latter. The photoconductivity measurements were performed in the excitonic region at positive and negative voltages applied to the Me–Sb_2Se_3 contacts. A similar investigation using the Sb_2S_3 single crystals was carried out by our group [24]. Since Sb_2S_3 and Sb_2Se_3 have a similar band structure, the four excitonic states (A, B, C and D) were also obtained for the Sb_2S_3 single crystals. Based in our previous work [24], the exciton binding energies, valence band parameters, valence band splitting, as well as the effective mass of electrons and holes were estimated for Sb_2Se_3 single crystals.

Experimental

Bulk Sb_2Se_3 crystals were obtained by fusion ($T \approx$ 700–730 °C) of antimony (Sb) and selenium (Se) taken in the stoichiometric ratio. The growth method used for Sb_2S_3 [24] was adapted here for lower temperatures. Sb and Se, at a semiconductor purity B5 level (99.9999%), were used as the initial precursors and placed into a container that was evacuated to a residual pressure of 10^{-5} mmHg. For a thorough mixing of the reacting components in the liquid phase, a rocking device and an electromagnetic vibrator, at a frequency of $f = 2$ Hz, were used and the reaction lasted between six and eight hours. The ampoule with the synthesized material was placed in a temperature-gradient furnace. The synthesized Sb_2Se_3 was placed in the highest temperature zone of the furnace (720–730 °C) whereas the other end the of ampoule was designated as the crystal growth zone (670–680 °C). The ampoule was maintained at this temperature gradient for 80 h to allow for the crystal growth process. Due to the temperature gradient, the material was transferred to the crystal growth zone, which was set at the lower temperature range. The temperature difference between the two zones was approximately 50–60 °C which enabled single-crystalline growth. Easily-cleaved crystal ingots (1 × 1 × 1.5 cm) were the final product, from which mirrored layers of various thicknesses (100 µm–3 mm), were obtained. Thinner layers (1.3–10 µm) could also be obtained from the crystal with the aid of adhesive tape. X-ray diffraction was performed in order to verify the quality of the crystalline sheets and their spatial crystalline groups.

Optical transmission and reflection spectra were obtained on a double-grating spectrometer SDL-1 with a 1:2 aperture and 7 Å/mm linear dispersion. The crystals were placed in a closed helium cryostat LTS-22 C 330 perpendicular to the *b* axis and their spectra were obtained at low temperatures with ≈0.5 meV resolution since both the spectrometer entrance and exit slits did not exceed 70 µm. The crystal layers were characterized by a high reflectance, which is characteristic of metallic aluminum mirrors. Some measurements were also carried out on the spectrometer DFS-32 coupled with a Specord M-40 and a Jasco V-670. The photoconductivity spectra were obtained on a single spectrometer (MDR-2) with a 1:2 aperture and 7 Å/mm linear dispersion.

Results and Discussion

The quality and composition of the single crystals were verified by optical and X-ray diffraction (XRD) analysis. The position of the atoms relative to the crystal lattice axes and the crystal XRD pattern is shown in Figure 1. A typical Sb_2Se_3 diffractogram is shown in Figure 1B. This result indicates the complete miscibility of the components during the synthesis process. The Sb_2Se_3 lattice parameters were determined based on the XRD analysis. The experimental interplanar distances *dhkl*, obtained from the X-ray data for Sb_2Se_3, are consistent with the previously published data [11]. The analysis shows that the prepared Sb_2Se_3 crystals are single phase and have an orthorhombic-type structure with a *Pnma* space group (a = 11.6901, b = 3.9210, c = 11.4894 Å) [21,25]. According to Figure 1A, which shows a fragment of the Sb_2S_3 crystal lattice, Sb_2Se_3 is a 2D semiconductor with a layered structure in which the Sb and Se atoms are connected with three other atoms of the opposite type, which in turn are connected within the crystal through weak secondary bonds.

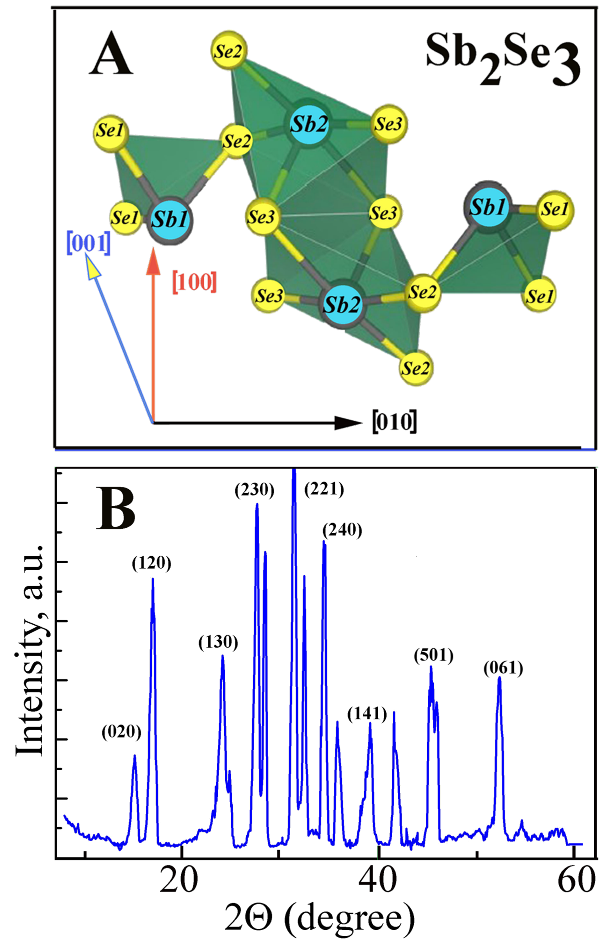

Figure 1: (A) Positions of the Sb and Se atoms in the Sb_2Se_3 crystals. (B) The Sb_2Se_3 crystalline XRD pattern.

Figure 2 shows the absorption spectra of the Sb_2Se_3 crystal (thickness d = 113 μm) measured at different temperatures (300–11 K) under $E||c$ and $E \perp c$ polarization conditions. The results demonstrate that the absorption edge is shifted towards higher energies when the temperature decreases. The largest difference in the absorption edge (E_{ed}) values is observed at $\approx 2 \cdot 10^3$ cm^{-1} and at 300 K ($\Delta E = E_{ed}(E \perp c) - E_{ed}(E||c)$ = 29 meV). When the temperature decreases to 100 K, ΔE decreases to 9 meV; however, a further decrease in the temperature to 11 K leads to an increase in ΔE to 16 meV (Table 1). Such absorption characteristics suggest that the absorption edge, under these polarization conditions, is formed due to the electronic transitions from different valence bands to a conduction band. Estimated values for the edge positions can be obtained by extrapolating the absorption curve to the energy axis, as shown by the black dotted lines in Figure 2.

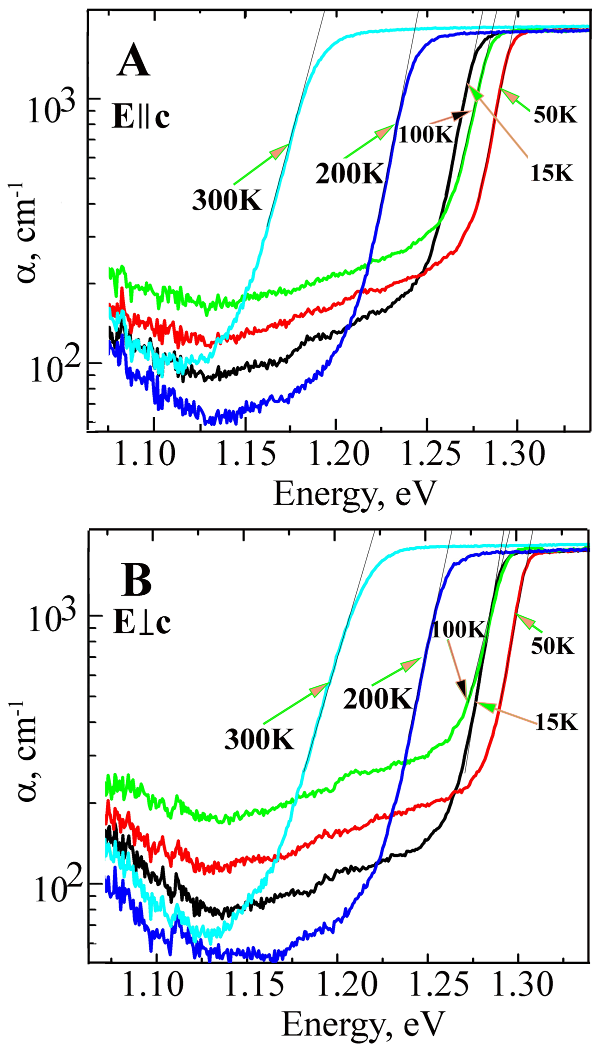

Figure 2: The absorption spectra of the Sb_2Se_3 crystals, with thickness d = 113 μm, measured at different temperatures (300 K: cyan, 200 K: blue, 100 K: green, 50 K: red and 15 K: black) for $E||c$ (A) and $E \perp c$ (B) polarization conditions.

Table 1: The differences (ΔE) in the absorption edge positions (E_{ed}) for $E||c$ ($E_{ed}(E \perp c)$) and $E \perp c$ ($E_{ed}(E||c)$) polarization conditions at different temperatures.

T, K	E_{ed}, $E \perp c$, eV	E_{ed}, $E \| c$, eV	ΔE, meV
300	1.220	1.191	29
200	1.264	1.244	20
100	1.296	1.287	9
50	1.307	1.296	11
11	1.294	1.278	16

Figure 3A illustrates the absorption spectra of the Sb_2Se_3 single crystal with a 13 μm thickness measured at room temperature under $E||c$ and $E \perp c$ polarization conditions. The spectra show the high absorption coefficients with maxima at 1.162 eV (marked as A, *E*||c) and 1.185 eV (marked as B, *E*⊥c) at the absorption level of 2×10^4 cm^{-1}. The onset of edge absorption starts at 1.09 eV (*E*||c) and 1.1 (*E*⊥c). In conclusion, the absorption edge splitting (with a high absorption coefficient of $\approx 10^4$ cm^{-1}) measured at room temperature is 23 meV.

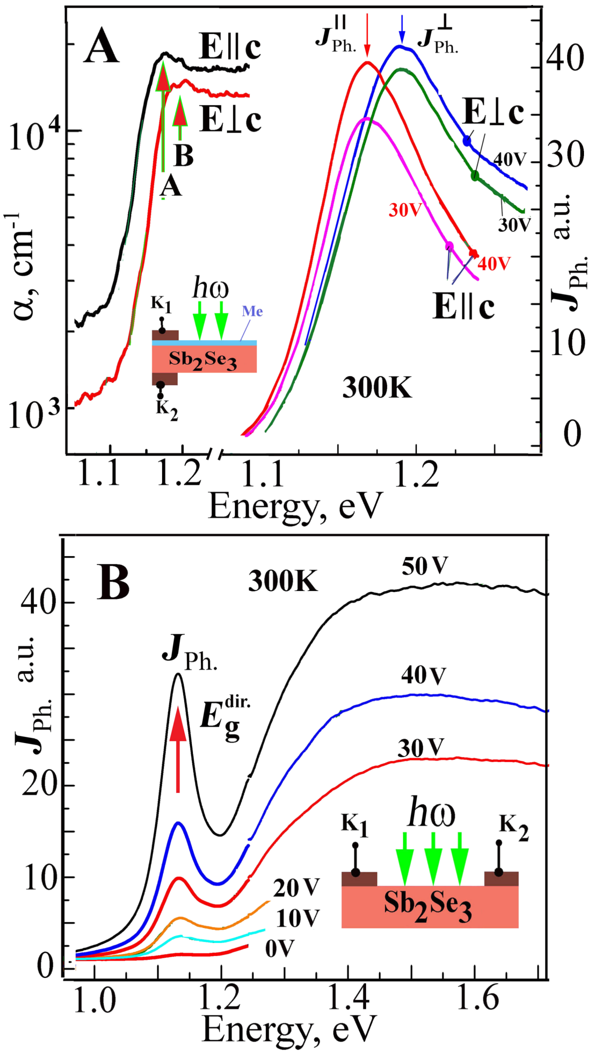

Figure 3: (A) The spectra showing the edge absorption (α) and photoconductivity (J_{Ph}) for the Sb_2Se_3 crystals measured under *E*||c and *E*⊥c polarization conditions and at room temperature (insert shows the structure used for the photoconductivity measurements). (B) The photoconductivity spectra measured at room temperature for various voltages applied to the In–Sb_2Se_3 contact (insert illustrates this structure).

In order to investigate the electrical and photoelectric properties of the metal–antimony selenide (In–Sb_2Se_3) contacts, the structures were obtained by either thermal sputtering under vacuum or electrochemical deposition onto the cleaved faces of single crystals (Figure 3A). Current–voltage characteristics suggest that the contacts have an ohmic behavior. The impedance has a frequency dependence that is characteristic of the conductivity hopping mechanism which in turn is independent of the metal type and the deposition method used. The photocurrent increases when the energy of the photons increases in the Schottky barriers when the transparent contacts are illuminated. The structures with the contacts deposited onto one side of the crystal are photosensitive. At the same time, the contact deposition onto opposite sides of the crystal planes leads to the appearance of a photo-electromotive force (EMF) with a magnitude of up to 150 mV. The photocurrent increases when a positive voltage is applied to the illuminated electrode and it decreases to zero when a negative voltage is applied. The nature of the photoelectric effect cannot be associated with the contact-EMF effect since there is no band bending at the semiconductor surface region. On the other hand, the photo-EMF effect, in this case, may be associated with the Dember effect.

The photoconductivity and photo-EMF spectra in the absorption edge region show a broad band with maximum values at 1.187 eV (*E*⊥c) and 1.167 eV (*E*||c) (Figure 3A) which are associated with the light absorption at the direct transitions in the interband gap minimum region. It is highly likely that the photoconductivity maxima are due to excitonic ground states ($n = 1$) in the aforementioned polarization conditions. In addition, the photocurrent increases when the bias increases. For the unpolarized light case, the photoconductivity spectra have a narrow maximum at 1.15 eV when different voltages are applied to the K_1 and K_2 contacts belonging to the structure shown in the Figure 3B insert. The maximum intensity increases when the voltage between the contacts increase which can be associated with the electronic transitions in the absorption spectra at 1.17 eV and 1.19 eV. When the applied voltage increases the photocurrent signal also increases in the region of higher energies (1.2–1.8 eV), reaching a maximum at 1.5–1.6 eV. The maximum photocurrent value at 1.15 eV is due to excitonic states at the direct electronic transitions between V_1–C_1 bands. The increase in intensity with the applied voltage confirms the excitonic character of the maximum, which is consistent with the fact that the binding energy of these excitons is 130–136 meV.

The In–Sb_2Se_3 structures, in which the contacts were deposited by electrochemical methods, show photosensitivity over a wide energy range (1–1.8 eV, Figure 4). When a voltage range from 0 to 2 V was applied to the indium contacts, the photoconductivity maximum was registered at 1.168 eV for both polarization cases (*E*⊥c and *E*||c). This happens due to the direct electronic transitions in the bandgap minimum. The maxima D at 1.46 eV and F at 1.67 eV are observed in the photoconductivity spectra at the energy range between 1.3–1.8 eV for the *E*⊥c polarization case (Figure 4). For the *E*||c polarization condition, a lower maximum S is observed at 1.60 eV. All these maxima can be attributed to the direct electronic transitions in the Brillouin zone.

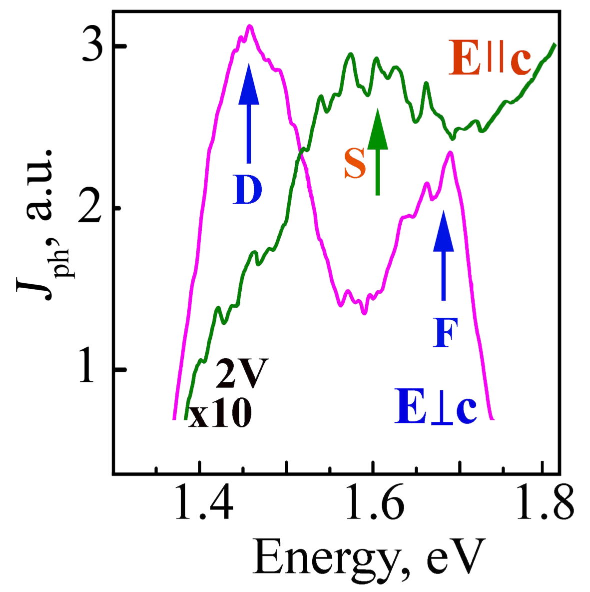

Figure 4: The photoconductivity spectra registered when 2 V is applied to the In–Sb_2Se_3 contacts (Figure 3A, insert) under the *E*||c and *E*⊥c polarization conditions.

The maxima observed for the reflection spectra (room temperature, *E*||c) are at 1.164 eV and 1.325 eV due to the ground states $\boldsymbol{n}^A = 1$ and $\boldsymbol{n}^C = 1$ for the A and C excitonic series, respectively. For the *E*⊥c case, the reflection spectra maxima are at 1.191 eV and 1.467 eV due to the ground states for B and D excitons, respectively. A weaker shoulder S at 1.6 eV and a maximum G at 1.807 eV are measured for the *E*||c polarization case at higher energies. For *E*⊥c the polarization maximum F is at 1.671 eV (Figure 5A). There is good agreement between the maxima in the reflection (Figure 5) and in the photoconductivity spectra (Figure 4); therefore, these values can be attributed to the direct excitonic state transitions in the Brillouin zone.

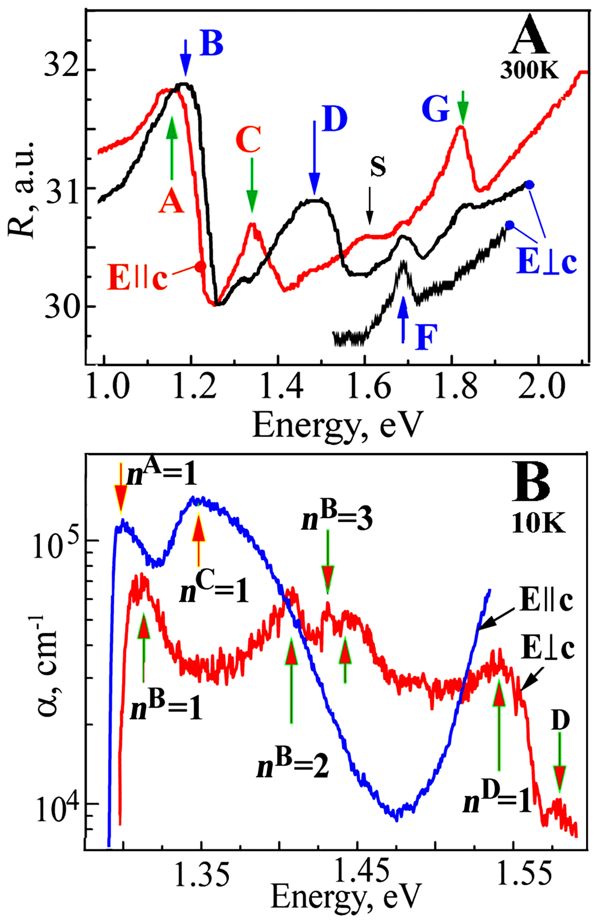

Figure 5: (A) The reflection spectra of the Sb_2Se_3 crystal measured at room temperature for both *E*||c and *E*⊥c polarization conditions. (B) The edge absorption of the Sb_2Se_3 crystal with a thickness *d* = 1.3 μm for *E*||c and *E*⊥c polarization conditions at a temperature of 10 K.

The excitonic nature of the maxima detected in the reflection spectra is also confirmed by the absorption spectra measurements performed at low temperatures (Figure 5B). For the *E*||c case, when the temperature decreases to 10 K, a maximum is detected at 1.299 eV which is caused by the exciton ground states $\boldsymbol{n}^A = 1$, conventionally designated as the A series. For the same polarization case, another maximum $\boldsymbol{n}^C = 1$ is detected at 1.347 eV, which is caused by the ground state of the C excitonic series. For the *E*⊥c polarization case six maxima are detected. In the long-wavelength region, a maximum is detected at 1.312 eV, which is caused by the B series. At 1.410 eV and 1.429 eV, the excited states $\boldsymbol{n}^B = 2$ and $\boldsymbol{n}^B = 3$ of the B excitonic series are observed. In the high-energy region, the maximum $\boldsymbol{n}^D = 1$ is detected at 1.538 eV and a weaker peak is detected at 1.588 eV, which is formed by the D excitonic series in the vicinity of another pair of bands. To determine the main parameters of the excitonic series, the profiles of the measured reflection spectra of the A and B excitons (experimental data) are calculated based on the dispersion ratios in the single-oscillator and multi-oscillator models, according to a method described in our previous work [26].

Figure 6 shows the experimentally measured and the calculated profiles of the reflection spectra for both *E*||c and *E*⊥c polarization cases at 300 K. The calculations showed that for the polarization *E*||c the background dielectric constant (ε_b) is equal to 7.5, the energy of the transversal exciton (ω_T) is 1.192 eV, the longitudinal-transversal splitting (ω_{LT}) is 15 meV, the damping factor (γ) is 110 and the translational mass of the exciton (*M*) is

$3.5m_0$ (Table 2). For the excitonic series C the following parameters were calculated: $\omega_T = 1.310$ eV, $\omega_{LT} = 17$ meV, $\gamma = 150$ and $M = 3.9m_0$. For the $E{\perp}c$ polarization case the calculations of the reflection spectra profiles gave the following parameters: $\varepsilon_b = 7.5$, $\omega_T = 1.219$ eV, $\omega_{LT} = 14$ meV, $\gamma = 161$, and $M = 4.5m_0$.

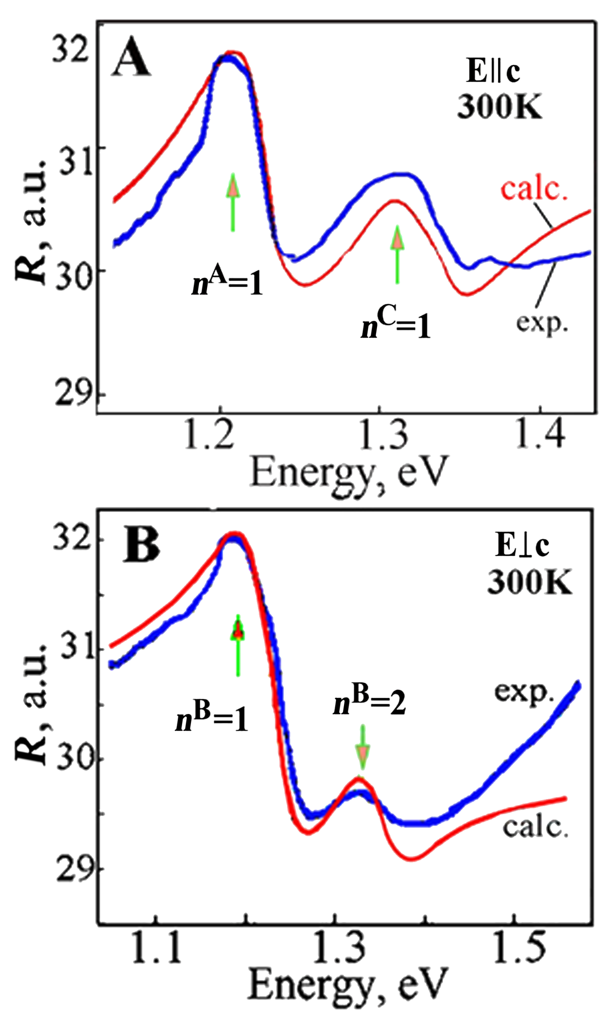

Figure 6: The experimentally measured (exp.) and calculated (calc.) profiles of the reflection spectra for the $E||c$ (A) and $E{\perp}c$ (B) polarization cases at 300 K.

Table 2: Exciton parameters of the Sb_2Se_3 crystals (data outside brackets: from the reflection spectra, data inside brackets: from the absorption spectra).

Exciton state	$E\|\|c$, A-exc.	$E{\perp}c$, B-exc.	$E{\perp}c$, C-exc.	$E{\perp}c$, D-exc.
	R, 300 K/ (α, 11 K)	*R*, 300 K/ (α, 11 K)	*R*, 300 K/ (α,11 K)	*R*, 300 K/ (α, 11 K)
$n = 1$, eV	1.164/ (1.299)	1.191/ (1.312)	1.310/ (1.347)	1.522/ (1.538)
$n = 2$, eV	–	1.317/ (1.410)	1.372	/ (1.588)
$n = 3$, eV	–	(1.429)	–	–
$\omega_{LT,}$ meV	15.0	14.0	17.0	–
Ry, eV	–	0.168/ (0.130)	0.082	0.067
E_g, eV	–	1.359/ (1.442)	1.392	1.589
ε_b	7.5	7.5	–	8.5
μ^*, m_0	0.56	0.56	–	0.49
M, m_0	3.5	4.5	3.9	3.9
$m_c{}^*$, m_0	0.67	0.67	0.67	0.67
$m_{v1}{}^*$, m_0	3.32	–	–	–
$m_{v2}{}^*$, m_0	–	3.83	–	–
$m_{v3}{}^*$, m_0	–	–	3.23	–
$m_{v4}{}^*$, m_0	–	–	–	3.32

By using the obtained experimental data and the known relation $\mu^* = \varepsilon_b^2 \mathrm{Ry} / R_H$, where R_H is the Rydberg energy of a hydrogen atom (13.6 eV) and Ry is the binding energy for the corresponding exciton (Rydberg constant), the reduced effective mass (μ^*) is calculated for the excitons A, B, C and D. For excitons A and B when the background dielectric constant is $\varepsilon_b = 7.5$ and the binding energy is Ry = 130–136 meV the reduced exciton mass is $\mu^* = 0.56m_0$. For the exciton series C at $\varepsilon_b = 7.5$ and at the binding energy Ry = 82 meV, the reduced mass of the exciton is $\mu^* = 0.49m_0$. The Bohr radius (α_B) for the S state of the A exciton is 0.3×10^{-5} cm and for the B exciton it is $\alpha_B = 0.2 \times 10^{-5}$ cm. Considering that the exciton mass M is equal to the sum of the masses of holes and electrons, $m_v{}^* + m_c{}^*$, and the reduced mass $1/\mu^*$ is equal to $(1/m_v{}^*) + (1/m_c{}^*)$, from the experimentally estimated mass values of M and μ^*, the effective mass is estimated for the electrons in the conduction band $m_c{}^* = 0.67m_0$ and for the holes in the valence bands $m_{v1}{}^* = 3.32m_0$, $m_{v2}{}^* = 3.83m_0$, $m_{v3}{}^* = 3.23m_0$ and $m_{v4}{}^* = 3.32m_0$ (Table 2). The excitonic parameters calculated here correlate with the previously published data [18], where it was stated that Frenkel excitons exist in the Sb_2S_3 crystals with a binding energy Ry = 0.1 eV and effective mass $m_c{}^* = 1.035m_0$, $m_{v1}{}^* = 1.843m_0$. A similar approach that was used in our previous work to study the Sn_2S_3 crystals was also used here for the calculation of the effective mass of electrons and holes in the bands located at the Brillouin zone center. The magnitudes of the effective mass of the electrons ($m_c{}^* = 1.08m_0$) at the bottom of the conduction band and of the holes at the top of four valence bands ($m_{v1}{}^*$, $m_{v2}{}^* = 2.91m_0$ and $m_{v3}{}^*$, $m_{v4}{}^* = 3.12m_0$) were estimated [24]. The bandgap was calculated based on the positions of the ground and excited states of the observed excitons. The well-known formula $E_g = E_i + \mathrm{Ry}/n^2$ was used for this calculation, where E_g is the bandgap energy, E_i corresponds to the positions of the ground ($n = 1$) and excited ($n = 2, 3, 4\ldots$) states of the exciton, Ry is the exciton binding energy (Rydberg constant) and $n = 1, 2, 3 \ldots$ are the main quantum numbers. First, from the positions of the ground and excited states, the Rydberg constant was calculated. Then the bandgap energy is estimated.

In the Sb_2Se_3 and Sb_2S_3 crystals, the theoretical calculation of the band structure over a wide energy range was performed in several studies [6,8,10,19]; however, the obtained results were contradictory and the inconsistencies were related to the assignment of the actual points in the Brillouin zone. For all the previous studies [6,8,10,19] the valence bands had the maximum in the Brillouin zone center (in $k = 0$, Γ-point) whereas the minimum in the conduction band was found to be in different points of the Brillouin zone. For example, a few studies [8,10,19] showed that the minimum was localized in the Z point whereas others [6] found the minimum in the X point. In addition, for the Sb_2S_3 crystals [20], the minimum energy interval corresponded to direct transitions in the center of the Brillouin zone (Γ-point). For the Sb_2Se_3 crystals the top of the valence band was positioned between the Γ and S points, while the bottom of the conduction band was in the Γ point. Given the inconsistency in the literature, our results were discussed based on theoretical calculations performed by Koç and collaborators [20]. A similar approach was used to interpret our previous data for the Sb_2S_3 crystals [24]. Based on the results by Koç et al. [20], Figure 7 illustrates the band structure fragment in the interband minimum region. As mentioned previously, Koç and collaborators [20] calculated and built a wavevector space for both crystals (Sb_2S_3 and Sb_2Se_3) band structures. Based on these data an interpretation was made in terms of the electron transitions in the framework of the calculated band structure. As mentioned, a few previous studies have shown that the absorption edge was formed by indirect transitions in Sb_2Se_3. However, the data presented here does not confirm entirely the previous findings and it does not refute the existence of indirect transitions given that more studies (like the ones made for Ge, Si, GaP, etc.) need to be performed in order to clarify those issues, ideally with purely grown crystals. We do not negate the existence of indirect transitions as we do not have such experimental data. Therefore, a focus will be given on the direct transitions that were experimentally observed (Figure 7).

The excitonic series A, B, C, and D is formed by the electrons in the conduction band C_1 (with Γ_6 symmetry) and the holes in the valence bands V_1, V_2, V_3, and V_4 (with Γ_7, Γ_6, Γ_7, and Γ_6 symmetries), respectively [27]. Considering that the bands originate from the structures with a higher symmetry (tetragonal) to the structures with an orthorhombic symmetry (D_{2h}), it should be noted that the bands in $k = 0$ are split by a crystal field and a spin–orbit interaction [27]. The lower conduction band is formed from the Γ_1 states and acquires the Γ_6 (Γ_7) symmetry, while the upper valence bands of V_1, V_2, V_3, and V_4 have the Γ_7, Γ_6, Γ_7, and Γ_6 symmetry, respectively. The interaction between the electrons from the Γ_6 conduction band and the holes from the Γ_7 valence band is determined by the product of the irreducible representation $\Gamma_1 \times \Gamma_6 \times \Gamma_7 = \Gamma_3 + \Gamma_4 + \Gamma_5$. As a result of this interaction, in the long-wavelength region, an exciton Γ_4 is allowed in polarization $E||c$, Γ_5 is allowed in polarization $E \perp c$ and Γ_3 is forbidden in both polarization conditions. The interaction between the electrons from the C_1 conduction band (Γ_6 symmetry) with the holes from the V_2 valence band (Γ_6 symmetry) causes the appearance of three excitonic series: Γ_1, Γ_2 and Γ_5. According to the selection rules for the $E \perp c$ polarization case, the Γ_5 excitons are allowed whereas the Γ_1 and Γ_2 excitons are both forbidden. A similar approach was used when the Sb_2S_3 single crystals were investigated [24]. Since the Sn_2S_3 and Sn_2Se_3 crystals have the same crystal structure and a similar band structure (only with a different bandgap) the excitons observed had the same symmetries. Based on the obtained experimental data, the splitting between the upper valence bands, V_1 and V_2, in the center of the Bril-

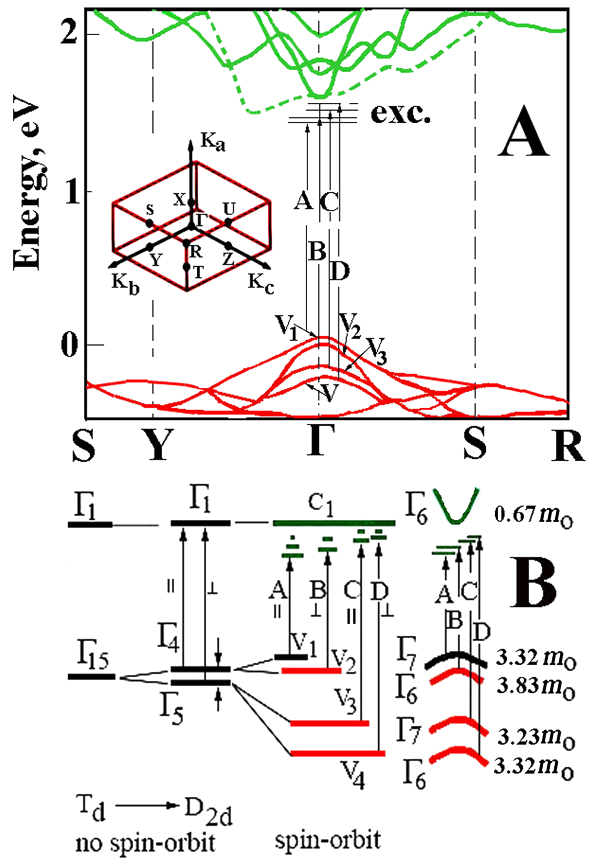

Figure 7: (A) The energy band structure of the Sb_2Se_3 crystals. Insert illustrates the Brillouin zone. (B) Transformation from the tetrahedral to orthorhombic symmetry due to the spin–orbit interaction and the crystal field in the center of the Brillouin zone. Figure 7B adapted with permission from [24], copyright 2020 Elsevier.

louin zone is 13 meV, whereas the splitting between V_2 and V_3 is 35 meV and between V_3 and V_4 is 191 meV.

Besides the excitonic peaks (A, B, C and D), the features a1 (2.090 eV), a2 (3.059 eV), a3 (3.365 eV), a4 (3.822 eV), a5 (4.432 eV), a6 (5.009 eV), a7 (5.281 eV), a8 (5.466 eV) and a9 (5.815 eV) are also observed in the reflection spectra (Figure 8). These spectra were measured at room temperature over a wide energy range (1–6 eV) under the E||c and E⊥c polarization conditions. The observed reflection peaks can be associated with the direct electronic transitions at actual points of the Brillouin zone. In the E⊥c polarization, the reflection spectra maxima b1 (2.167 eV), b2 (2.439 eV), b3 (2.875 eV), b4 (3.191 eV), b5 (3.485 eV), b6 (4.040 eV), b7 (4.509 eV), b8 (5.391 eV), b9 (5.685 eV) and b10 (6.045 eV) can be identified. The maxima a1, b1, b2, and b3 are most likely due to the electronic transitions from the valence bands V_1, V_2, V_3 and V_4 to the conduction band C_2 in the Brillouin zone center. The maxima localized in the high-energy region of the reflection spectra a2, a3, a4, a5, b4, b5, b6 and b7 are most likely associated with the transitions from the upper valence bands V_1, V_2, V_3 and V_4 to the conduction bands C_3 and C_4 also in $k = 0$. The maxima of the reflection spectra in the high-energy range (4–6 eV) are possibly from the valence band maxima in the Y and S points of the Brillouin zone.

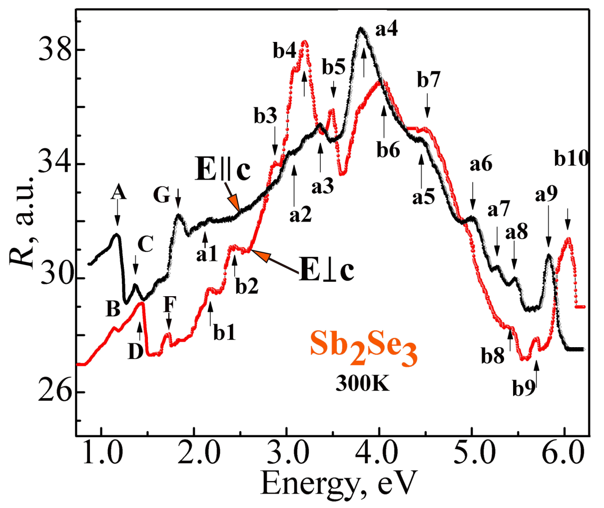

Figure 8: The reflection spectra of the Sb_2Se_3 crystals measured at room temperature under E||c and E⊥c polarization conditions.

Conclusion

The ground and excited states of four excitonic series (A, B, C, and D) formed in the bandgap minimum region were identified based on the studies of the optical properties of the Sb_2Se_3 single crystals performed at different temperatures. Taking into account the energy position of the excitonic ground and excited states, the binding energy of the excitons and the valence bands V_1–V_4 were determined. In the Brillouin zone Γ-point, the calculated electron effective mass m_c* was $0.67m_0$, and the values of the hole effective masses m_{v1}*, m_{v2}*, m_{v3}* and m_{v4}* were $3.32m_0$, $3.83m_0$, $3.23m_0$ and $3.32m_0$, respectively. The V_1–V_2 valence band splitting in the center of the Brillouin zone by a crystal field (Δ_{cr} = 13 meV) and the spin–orbit interaction (Δ_{so} = 35 meV) were determined. The bands V_3–V_4 were split by 191 meV. The observed features were discussed based on the theoretical calculation of the energy band structures and the excitonic band symmetries in the Brillouin zone center for crystals with an orthorhombic symmetry (*Pnma*). The In–Sb_2Se_3 structures were generated either by thermal sputtering under vacuum or by electrochemical deposition. The photoconductivity spectra at different applied voltages were investigated. The features associated with the excitonic states were shown in the measured photoconductivity spectra.

Funding

The authors acknowledge the financial support from the Ministry of Education, Culture and Research of Moldova under the Grants #20.80009.5007.20.

ORCID® iDs

Nicolae N. Syrbu - https://orcid.org/0000-0001-9368-6096
Victor V. Zalamai - https://orcid.org/0000-0002-1882-2622

References

1. Zhou, Y.; Wang, L.; Chen, S.; Qin, S.; Liu, X.; Chen, J.; Xue, D.-J.; Luo, M.; Cao, Y.; Cheng, Y.; Sargent, E. H.; Tang, J. *Nat. Photonics* **2015,** *9,* 409–415. doi:10.1038/nphoton.2015.78
2. Zeng, K.; Xue, D.-J.; Tang, J. *Semicond. Sci. Technol.* **2016,** *31,* 063001. doi:10.1088/0268-1242/31/6/063001
3. Wang, L.; Li, D.-B.; Li, K.; Chen, C.; Deng, H.-X.; Gao, L.; Zhao, Y.; Jiang, F.; Li, L.; Huang, F.; He, Y.; Song, H.; Niu, G.; Tang, J. *Nat. Energy* **2017,** *2,* 17046. doi:10.1038/nenergy.2017.46
4. Chen, C.; Wang, L.; Gao, L.; Nam, D.; Li, D.; Li, K.; Zhao, Y.; Ge, C.; Cheong, H.; Liu, H.; Song, H.; Tang, J. *ACS Energy Lett.* **2017,** *2,* 2125–2132. doi:10.1021/acsenergylett.7b00648
5. Messina, S.; Nair, M. T. S.; Nair, P. K. *J. Electrochem. Soc.* **2009,** *156,* H327. doi:10.1149/1.3089358
6. El-Shair, H.; Ibrahim, A.; Abd El-Wahabb, E.; Afify, M.; Abd El-Salam, F. *Vacuum* **1991,** *42,* 911–914. doi:10.1016/0042-207x(91)90557-y
7. Zhou, Y.; Leng, M.; Xia, Z.; Zhong, J.; Song, H.; Liu, X.; Yang, B.; Zhang, J.; Chen, J.; Zhou, K.; Han, J.; Cheng, Y.; Tang, J. *Adv. Energy Mater.* **2014,** *4,* 1301846. doi:10.1002/aenm.201301846
8. Chen, C.; Li, W.; Zhou, Y.; Chen, C.; Luo, M.; Liu, X.; Zeng, K.; Yang, B.; Zhang, C.; Han, J.; Tang, J. *Appl. Phys. Lett.* **2015,** *107,* 043905. doi:10.1063/1.4927741
9. Voutsas, G. P.; Papazoglou, A. G.; Rentzeperis, P. J.; Siapkas, D. *Z. Kristallogr.* **1985,** *171,* 261–268. doi:10.1524/zkri.1985.171.3-4.261
10. Mueller, R.; Wood, C. *J. Non-Cryst. Solids* **1972,** *7,* 301–308. doi:10.1016/0022-3093(72)90266-9

11. Ko, T.-Y.; Shellaiah, M.; Sun, K. W. *Sci. Rep.* **2016,** *6,* 35086. doi:10.1038/srep35086
12. Fourspring, P. M.; DePoy, D. M.; Rahmlow, T. D., Jr.; Lazo-Wasem, J. E.; Gratrix, E. J. *Appl. Opt.* **2006,** *45,* 1356–1358. doi:10.1364/ao.45.001356
13. Arun, P.; Vedeshwar, A. G.; Mehra, N. C. *J. Phys. D: Appl. Phys.* **1999,** *32,* 183–190. doi:10.1088/0022-3727/32/3/001
14. Song, H.; Li, T.; Zhang, J.; Zhou, Y.; Luo, J.; Chen, C.; Yang, B.; Ge, C.; Wu, Y.; Tang, J. *Adv. Mater. (Weinheim, Ger.)* **2017,** *29,* 1700441. doi:10.1002/adma.201700441
15. Kurumada, M.; Suzuki, H.; Kimura, Y.; Saito, Y.; Kaito, C. *J. Cryst. Growth* **2003,** *250,* 444–449. doi:10.1016/s0022-0248(02)02463-6
16. Gilbert, L. R.; Van Pelt, B.; Wood, C. *J. Phys. Chem. Solids* **1974,** *35,* 1629–1632. doi:10.1016/s0022-3697(74)80175-7
17. Kutasov, V. A. Shifting the maximum figure-of-merit of (Bi, Sb)2(Te, Se)3 thermoelectrics to lower temperatures. *Thermoelectrics Handbook;* CRC Press: Boca Raton, FL, USA, 2005; pp 18–37.
18. Liu, X.; Chen, J.; Luo, M.; Leng, M.; Xia, Z.; Zhou, Y.; Qin, S.; Xue, D.-J.; Lv, L.; Huang, H.; Niu, D.; Tang, J. *ACS Appl. Mater. Interfaces* **2014,** *6,* 10687–10695. doi:10.1021/am502427s
19. Zhang, Y.; Li, G.; Zhang, B.; Zhang, L. *Mater. Lett.* **2004,** *58,* 2279–2282. doi:10.1016/j.matlet.2004.02.006
20. Koç, H.; Mamedov, A. M.; Deligoz, E.; Ozisik, H. *Solid State Sci.* **2012,** *14,* 1211–1220. doi:10.1016/j.solidstatesciences.2012.06.003
21. Černošková, E.; Todorov, R.; Černošek, Z.; Holubová, J.; Beneš, L. *J. Therm. Anal. Calorim.* **2014,** *118,* 105–110. doi:10.1007/s10973-014-4000-3
22. El-Sayad, E. A. *J. Non-Cryst. Solids* **2008,** *354,* 3806–3811. doi:10.1016/j.jnoncrysol.2008.05.004
23. Vadapoo, R.; Krishnan, S.; Yilmaz, H.; Marin, C. *Phys. Status Solidi B* **2011,** *248,* 700–705. doi:10.1002/pssb.201046225
24. Beril, S. I.; Stamov, I. G.; Tiron, A. V.; Zalamai, V. V.; Syrbu, N. N. *Opt. Mater.* **2020,** *101,* 109737. doi:10.1016/j.optmat.2020.109737
25. Green, M. A.; Emery, K.; Hishikawa, Y.; Warta, W.; Dunlop, E. D.; Levi, D. H.; Ho-Baillie, A. W. Y. *Prog. Photovoltaics* **2017,** *25,* 3–13. doi:10.1002/pip.2855
26. Syrbu, N. N.; Ursaki, V. V. Exciton polariton dispersion in multinary compounds. In *Exciton Quasiparticles: Theory, Dynamicsand Applications;* Bergin, R. M., Ed.; Nova Science Publishers Inc., 2010; pp 1–130.
27. Kovalev, O. V. *Irreducible and Induced Representations and Corepresentations of Fedorov Groups;* Nauka: Moscow, Russia, 1986. (in Russian).

License and Terms

The definitive version of this article is the electronic one which can be found at:
doi:10.3762/bjnano.11.89

BEILSTEIN JOURNAL OF NANOTECHNOLOGY

Ultrasensitive detection of cadmium ions using a microcantilever-based piezoresistive sensor for groundwater

Dinesh Rotake*[1], Anand Darji[1] and Nitin Kale[2]

Full Research Paper

Address:
[1]Department of Electronics Engineering, Sardar Vallabhbhai National Institute of Technology, Surat, Gujarat, India and [2]The Chief Technology Officer, NanoSniff Technologies Pvt. Ltd., F-14, 1st Floor, IITB Research Park, Old CSE Building, IIT Bombay, Powai, Mumbai – 76, India.

Email:
Dinesh Rotake* - dinesh.rotake@gmail.com

* Corresponding author

Keywords:
BioMEMS; heavy metal ions (HMIs); limit of detection (LOD); microcantilevers; microfluidics; micro-electromechanical systems (MEMS); piezoresistive sensors; SAM (self-assembled monolayers); World Health Organization (WHO)

Beilstein J. Nanotechnol. **2020,** *11,* 1242–1253.
doi:10.3762/bjnano.11.108

Received: 04 April 2020
Accepted: 29 July 2020
Published: 18 August 2020

This article is part of the thematic issue "Functional nanostructures for electronics, spintronics and sensors".

Guest Editor: A. S. Sidorenko

Abstract

This paper proposes the selective and ultrasensitive detection of Cd(II) ions using a cysteamine-functionalized microcantilever-based sensor with cross-linked DL-glyceraldehyde (DL-GC). The detection time for various laboratory-based techniques is generally 12–24 hours. The experiments were performed to create self-assembled monolayers (SAMs) of cysteamine cross-linked with DL-glyceraldehyde on the microcantilever surface to selectively capture the targeted Cd(II). The proposed portable microfluidic platform is able to achieve the detection in 20–23 min with a limit of detection (LOD) of 0.56 ng (2.78 pM), which perfectly describes its excellent performance over other reported techniques. Many researchers used nanoparticle-based sensors for the detection of heavy metal ions, but daily increasing usage and commercialization of nanoparticles are rapidly expanding their deleterious effect on human health and the environment. The proposed technique uses a blend of thin-film and microcantilever (micro-electromechanical systems) technology, which mitigate the disadvantages of the nanoparticle approaches, for the selective detection of Cd(II) with a LOD below the WHO limit of 3 µg/L.

Introduction

Water is fundamentally essential for sustaining life, and an increase in the global population has led to an exponential increase in waste disposal, which causes significantly increased requirements regarding the control of water quality [1]. Clean water is one of the main priorities of the 21st century worldwide, and negligence to this may have a significant effect on maintaining the safety and security of human beings [2,3]. One common water contamination is caused by cadmium ions. There are numerous sources of Cd ions in groundwater, including industrial wastewater, mining industry, fossil fuels, iron and steel industry, cement manufacturing units, electroplating industry, manufacturing units of PVC, Ni–Cd batteries, fertilizers, pesticides, photovoltaic devices, soil, and sediments. Cadmium is a highly toxic heavy metal ion (HMI). Cadmium poisoning may cause fatigue, headaches, nausea, vomiting, abdominal cramps, bone degeneration, diarrhea, osteoporosis, renal dysfunction, cancer, anemia, and neurological disorders such as Parkinson's disease or Alzheimer's disease [4,5]. The WHO has set a water contamination limit of 3 μg/L Cd(II) [6]. We conclude from the WHO limit that cadmium is hazardous, and smaller Cd concentrations below the limit is also hazardous. Hence, it is essential to sense Cd(II) in the picomolar (pM) range well below the specified WHO limit.

The ion-selective electrodes (ISEs) fabricated by [7] are stable and precise for HMI detection, but the measurement requires by laboratory equipment. Sensors based on nanotubes, nanorods, nanoneedles, or nanoplates are also used to detect HMIs selectively down to the nanomolar range [8-11]. Many authors used adsorption methods to extract heavy metal ions from groundwater [12-16]. However, this is only useful when a pollution source has been already identified. Sensors based on luminescence or fluorescence sensors have been used by many researchers to selectively detect HMIs [17-22]. However, this method also requires laboratory equipment for analysis and detection. Also, most of the reported fluorescent probes reply only on absorption and fluorescence change and need dynamic acquisition [23]. A magnetic field powered pressure sensor proposed by Khan et al. [24] is capable of measuring pressure in the range of kilopascals but the suitability for the very low pressure caused by HMIs needs to be examined. A reduced graphene oxide (RGO)-based sensor and a microfluidic platform fabricated by [25-27] can be used with some surface modification for HMIs, but it is mostly capable of detecting in the micromolar range. A polymer-based microcantilever using an encapsulated piezoresistor has been proposed by Kale et al. [28], but it is not suitable for other high-temperature sputtering processes. Microcantilevers based on SiO_2 have been manufactured by Tang et al. [29] to enhance the sensitivity of cantilever sensors. Many authors use optical setups for microcantilevers. However, an optical output has several disadvantages during operation in water when the refractive index of water changes [30,31].

Many authors have proposed electrode-based approaches for the selective sensing of Cd(II) [32], but the limits of detection were always in the micromolar to nanomolar ranges. Some of the authors used fluorescent [5,33] and calorimetric [34] approaches to selectively detect the Cd(II). But these approaches required laboratory equipment for analysis and the LODs were also in the nanomolar range. All these methods are reliable for the qualitative and quantitative determination of Cd(II), but they are time-consuming, expensive, and not suitable for on-site determination. The calorimetric approach proposed by [34-37] is free from these problems but not capable of differentiating between two nearby ranges and the LOD is also on the higher side. The electrochemical sensor described in [38] is a good approach, but it also requires a lab instrument for measurement.

We have previously investigated SAMs of homocysteine (HCys) and pyridinedicarboxylic acid (PDCA) for the selective sensing of Hg(II) ions using a portable piezoresistive platform [39,40]. Experimental results confirmed that proposed setup is capable of sensing in the picomolar range. In this paper, we have used the previously designed portable piezoresistive platform for the selective capture Cd(II) in the picomolar range. Preliminary results show that the fabricated device has an excellent response within 20–23 minutes with 0.56 ng/mL (2.78 pM) LOD, which is well below the WHO limit for cadmium ions.

The paper describes the methodology, the formation of SAMs and their characterization using field-emission scanning electron microscopy (FESEM), the use of the portable experimental platform with the MEMS-based piezoresistive device to selective capture Cd(II) at the picomolar level and the verification of the experimental results using energy-dispersive X-ray spectroscopy (EDX).

Fabrication and Calibration of the Piezoresistive Device

Previously, a polysilicon-based piezoresistive sensor was fabricated using a standard microfabrication process. It was calibrated using atomic force microscopy (AFM) [40]. The process begins with thermal oxidation of Si at 1000 °C using an oxidation furnace to obtain a thermally grown SiO_2 layer followed by masking and etching to get the desired pattern. The polysilicon is deposited in a low-pressure chemical vapor deposition (LPCVD) furnace at 630 °C and boron doping (10^{18} per cm^3) is carried out using ion implantation at 35 keV. The upper SiO_2 layer is formed by re-oxidizing the polysilicon in an oxidation furnace [40]. The stiffness (k) of the fabricated piezoresistive sensor measured using AFM is 131–146 mN/m, which is well below the stiffness required for BioMEMS applications (1000 mN/m [41,42]). COMSOL 5.3 software is used to perform design and simulation of the piezoresistive sensor to optimize the dimensions for better stiffness and sensitivity [43]. The fabricated piezoresistive sensor layer structure with thickness, FESEM image, PCB, and the experimental platform is shown in Figure 1.

For using the microcantilever device for selectively detecting Cd(II) a surface modification is required. The surface modifica-

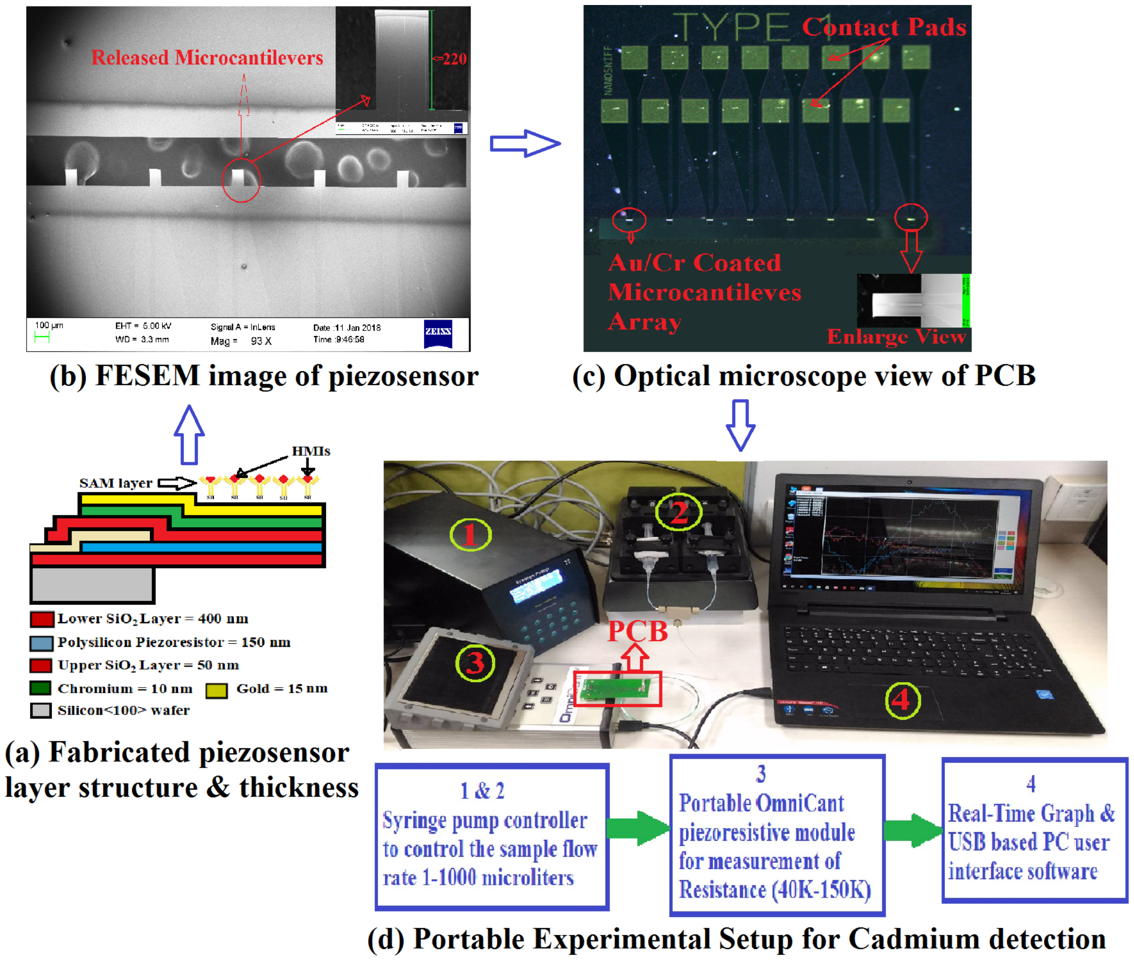

Figure 1: Fabricated piezoresistive sensor and experimental platform for Cd(II) detection.

tion of the sensor is basically a selective thiol coating on top of a gold surface. Here, SAMs of cysteamine–glyceraldehyde were created on top of microcantilever-based sensors with integrated piezoresistive readout to get the change in resistance due to changes in surface stress. Until now, many people have used lab-based optical setups to measure the change in surface stress of the cantilever sensors. Moreover, the proposed piezoresistive device has capabilities to directly capture the surface stress make this a better option for HMI applications.

Microfluidic Platform with Piezosensor

In the proposed method, the benefits of three different technologies are combined, namely thin film, nanoparticles (NPs), and MEMS, to selectively target Cd(II) in the picomolar range. Also, excessive commercialization of nanoparticles leads to increasing their harmful effect on life and the environment by [44-46]. In this article, an attempt is made to expand the AuNP-based technology proposed by [34] for the ultrasensitive sensing of Cd(II) with cysteamine-functionalized DL-glyceraldehyde (Cys-DL-GC) using the advanced MEMS-based piezoresistive platform. The MEMS-based sensor has very high sensitivity compared to any other technique. The complete process flow and the sensing scheme for the piezoresistive microcantilever-based biosensor is shown in Figure 2.

Here, the fabricated microfluidic platform with a microcantilever-based piezoresistive sensor is used to capture Cd(II) in the picomolar range. The amine group (–NH_2) of cysteamine has an affinity to all types of HMIs and it needs to be cross-linked for selectivity. We have cross-linked the amine group with DL-glyceraldehyde at pH 7 to obtain a free –OH group (a Lewis acid) for capturing Cd(II). The pKa value of 12.6 of DL-glyceraldehyde yield a strong copmplex of the –OH group with cadmium [34] after blocking the –NH_2 group of cysteamine.

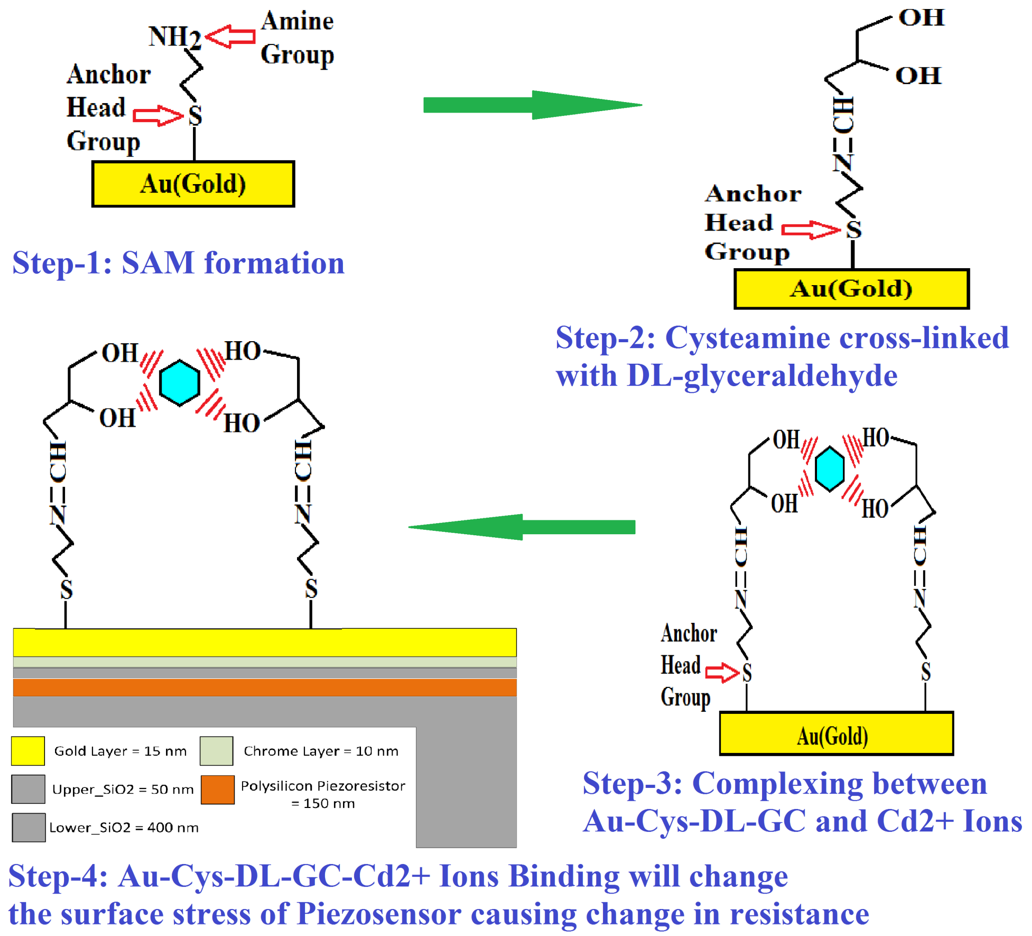

Figure 2: Process flow of biosensor for selective detection of Cd(II) ions.

Results and Discussion

The performance of the fabricated device in the selective detection of Cd(II) in a microfluidic environment is evaluated using the OmniCant setup shown in Figure 1d. The non-stress calibrated resistance values of the piezoresistive sensor using SAMs of cysteamine cross-linked with DL-glyceraldehyde (Cys-DL-GC) is in the range of 56268–63813 Ω. The non-stress resistance values of the fabricated piezoresistive die in the OmniCant microfluidic platform are shown in Figure 3. The microcantilever in channel 2 was blocked with acetyl chloride and selected as a reference for the Cys-DL-GC experiments. The values shows that the microcantilevers in channels 1 and 8 broke during the wire bonding and are not present in the analysis. The piezoresistive MEMS devices exhibit a fast response to changes in the resistance depending on the additional mass of Cd(II) loaded on the surface.

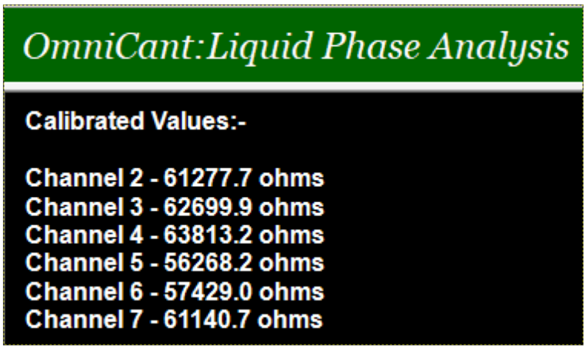
OmniCant:Liquid Phase Analysis

Calibrated Values:-

Channel 2 - 61277.7 ohms
Channel 3 - 62699.9 ohms
Channel 4 - 63813.2 ohms
Channel 5 - 56268.2 ohms
Channel 6 - 57429.0 ohms
Channel 7 - 61140.7 ohms

Figure 3: Non-stress calibrated values for used piezoresistive die.

Results of the SAM detecting cadmium ions

The proposed microfluidic platform provides real-time monitoring of Cd(II) in groundwater. We performed the experiment using the coating of cysteamine thiol with cross-linked DL-glyceraldehyde (Cys-DL-GC). We have already discussed that the methods based on Au/Ag nanoparticles require the laboratory equipment such as fluorescence spectroscopy, which ultimately leads to a non-portable platform. Hence, our primary focus is the selective detection of the Cd(II) using the fabricated portable experimental platform.

We used the following experimental procedure. A stock solution of cysteamine ([Cys] = 10 mM/10 mL) was prepared. The piezoresistive devices were gently dipped into a petri-dish containing cysteamine thiol for at least 12–24 hours. Longer times yield a better packing density of the SAM. In addition, a 2% (0.2 g/10 mL) solution of DL-glyceraldehyde (DL-GC) in phosphate buffer saline (PBS, pH 7) according to [34] was prepared. The cysteamine SAM was allowed to cross-link with the DL-glyceraldehyde solution for at least 2–3 hours by covering the container using silver foil. Stock solutions of 1 mM/10 mL of different salts ($AlCl_3$, $MnCl_2$, $CrCl_3$, $HgCl_2$, $PbCl_2$, $CdCl_2$) were used for the experiments. The flow rate was kept constant at 30 μL/min during the experiments. Before the measurement, DI water was used to stabilize the microcantilever in a liquid environment for a period of 7 min. Subsequently, the different heavy metal ion solutions were injected separately and the corresponding change in piezoresistance was measured. The Cd(II) solution was injected and the corresponding change in piezoresistance was measured.

The change in piezoresistance (ΔR) is calculated using a formula:

$$\Delta R = \left[\Delta R_{\text{Block}} - \Delta R_{\text{Unblock}}\right], \tag{1}$$

where ΔR_{Block} is the change in piezoresistance of the microcantilever blocked with acetyl chloride and $\Delta R_{\text{Unblock}}$ is the change in piezoresistance of the unblocked microcantilever. The change in piezoresistance of unblocked microcantilever compared to that of the blocked microcantilever of acetyl chloride (channel 2) is shown in Figure 4.

Initially, we used DI water to stabilize the microcantilever for a period of 7 min. The change of piezoresistance remained constant during this period. When the different heavy metal ion solutions (except Cd(II)) were injected after 7 min, the change in piezoresistance was minimal (5–30 Ω). When cadmium ions were injected after 7 min, the change in piezoresistance was around 200–300 Ω for each microcantilever. These results show the selectivity of the proposed method for Cd(II) with respect to other HMIs. It is also evident that the microcantilever in channel 5 (Figure 4c) shows a non-linear response. The rationale behind this is that no binding sites are available for cadmium ions on the microcantilever surface. Two microcantilevers exhibit a decrease in resistance because of tensile stress due to a small number of biomolecules (Cd(II)) binding to the surface (Figure 4b,d), while the other three microcantilevers exhibit an increase in the resistance because of compressive surface stress when a large number of biomolecules bind to the microcantilever surface (Figure 4a,c,e) [47].

Figure 5 demonstrates the average change in piezoresistance of a sensor based on Au-Cys-DL-GC-coated cantilevers for different heavy metals ($AlCl_3$, $MnCl_2$, $CrCl_3$, $HgCl_2$, $PbCl_2$, $CdCl_2$).

The average value of change in piezoresistance is the difference between the average change in piezoresistance for DI water and the particular heavy metal injected. Our results show that the SAM of cysteamine with cross-linked DL-glyceraldehyde(Cys-DL-GC) has a higher selectivity for Cd(II) than for other heavy metals. The average value of change in piezoresistance of the Au-Cys-DL-GC-coated microcantilevers is approximately 130–240 Ω for Cd(II) and 5–30 Ω for the other injected heavy metals. The total value of the average change in piezoresistance for a concentration of 0.56 ng Cd(II) is 877.72 Ω.

Characterization using Fourier-transform infrared spectroscopy (FTIR)

FTIR is a mature technique for elemental analysis and the identification of functional groups. The FTIR results show –OH stretching in the range of 2900–3750 cm^{-1} and N–H bending (1350–1750 cm^{-1}) [48-51]. The FTIR analysis of a Cd(II)/DL-GC/Cys/Au/Cr coating is shown in Figure 6.

The FTIR results of the Cys/Au/Cr coating show a single band at 3367 cm^{-1} associated to the –OH group and three bands at 1420, 1651, and 1732 cm^{-1} associated to the $–NH_2$ group. After coating with DL-glyceraldehyde (DL-GC/Cys/Au/Cr), the FTIR spectra show four bands at 1320, 1473, 1571, and 1647 cm^{-1} associated to the $–NH_2$ group and two bands at 2922 and 3311 cm^{-1} associated to the –OH group. After exposure to Cd(II) two bands related to –OH disappear and only single band at 3500 cm^{-1} is present due Cd(II) binding to the –OH groups. Similarly, for $–NH_2$ group), three bands disappear, and only single modified band is present at 1583 cm^{-1} due Cd(II) binding. This modification of the FTIR spectra after exposure to Cd(II) indicates the selective binding of cysteamine cross-linked DL-glyceraldehyde (Cys-DL-GC) to cadmium.

Verification of performed experiment results using EDX

In general, the thiol groups can bind to all types of HMIs. Thus, to selectively bind and detect Cd(II) the thiols goups need to be modified or functionalized with materials that are selective for Cd(II). The experimental results show that the fabricated MEMS-based sensor is capable of selective Cd(II) detection using SAMs of cysteamine with cross-linked DL-glyceraldehyde (Cys-DL-GC). To characterize the SAM on the microcantilever device only a few analytical techniques are available because of the fragile nature of the cantilever. FESEM/EDX is the preeminent tool to characterize the SAM on the top of the

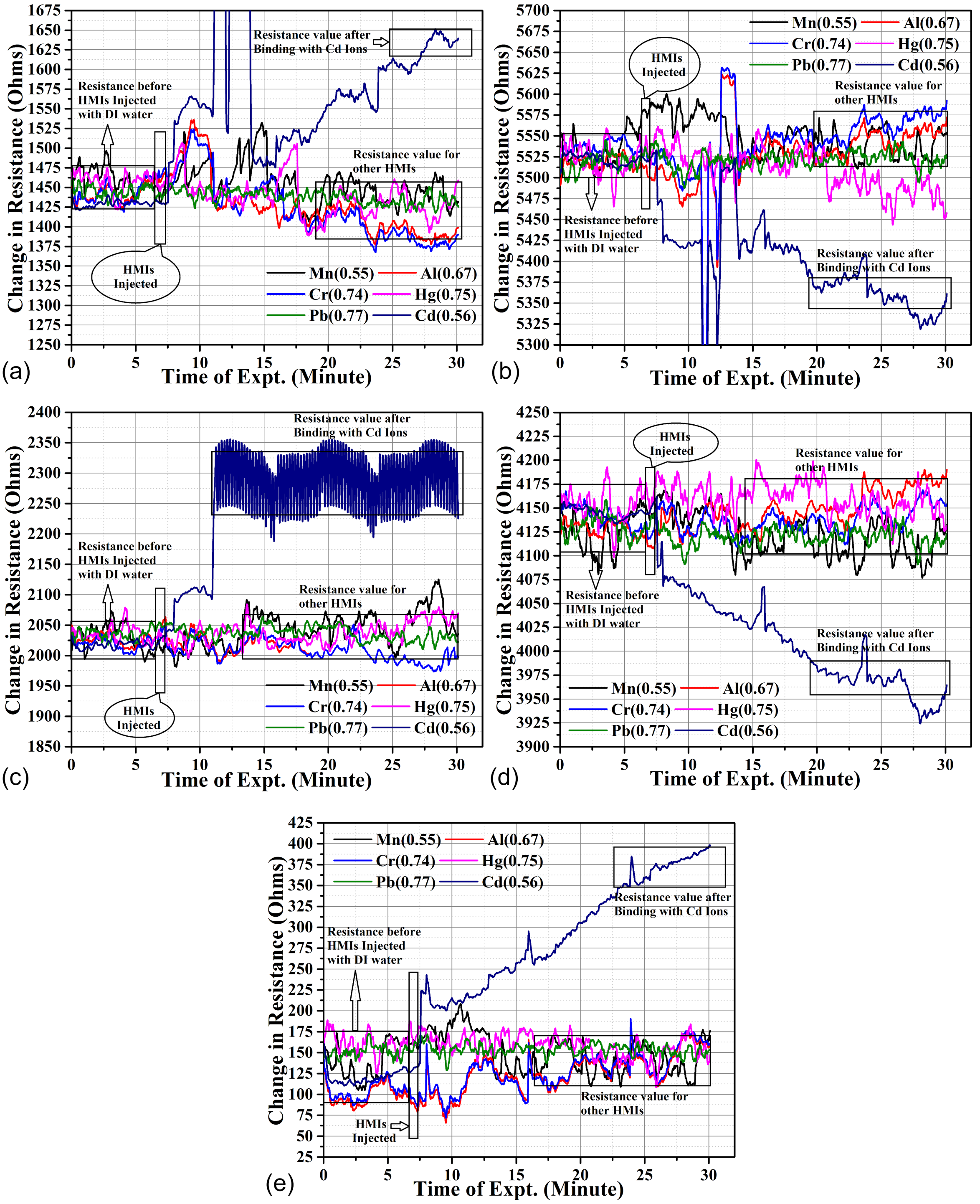

Figure 4: The change in piezoresistance of the unblocked cantilevers with respect to the cantilever blocked with acetyl chloride(channel 2): (a) Cys-DL-GC (channel 3), (b) Cys-DL-GC (channel 4), (c) Cys-DL-GC (channel 5), (d) Cys-DL-GC (channel 6) and (e) Cys-DL-GC (channel 7).

cantilever without damaging the device. The EDX measurement of the sensor with a SAM of cysteamine cross-linked DL-glyceraldehyde (Cys-DL-GC) on top of a Au surface is shown in Figure 7.

The EDX measurement shows that no cadmium ions are detected before exposure to $CdCl_2$. The EDX measurement of the microcantilever-based MEMS sensor with SAM of cysteamine cross-linked DL-glyceraldehyde (Cys-DL-GC) on

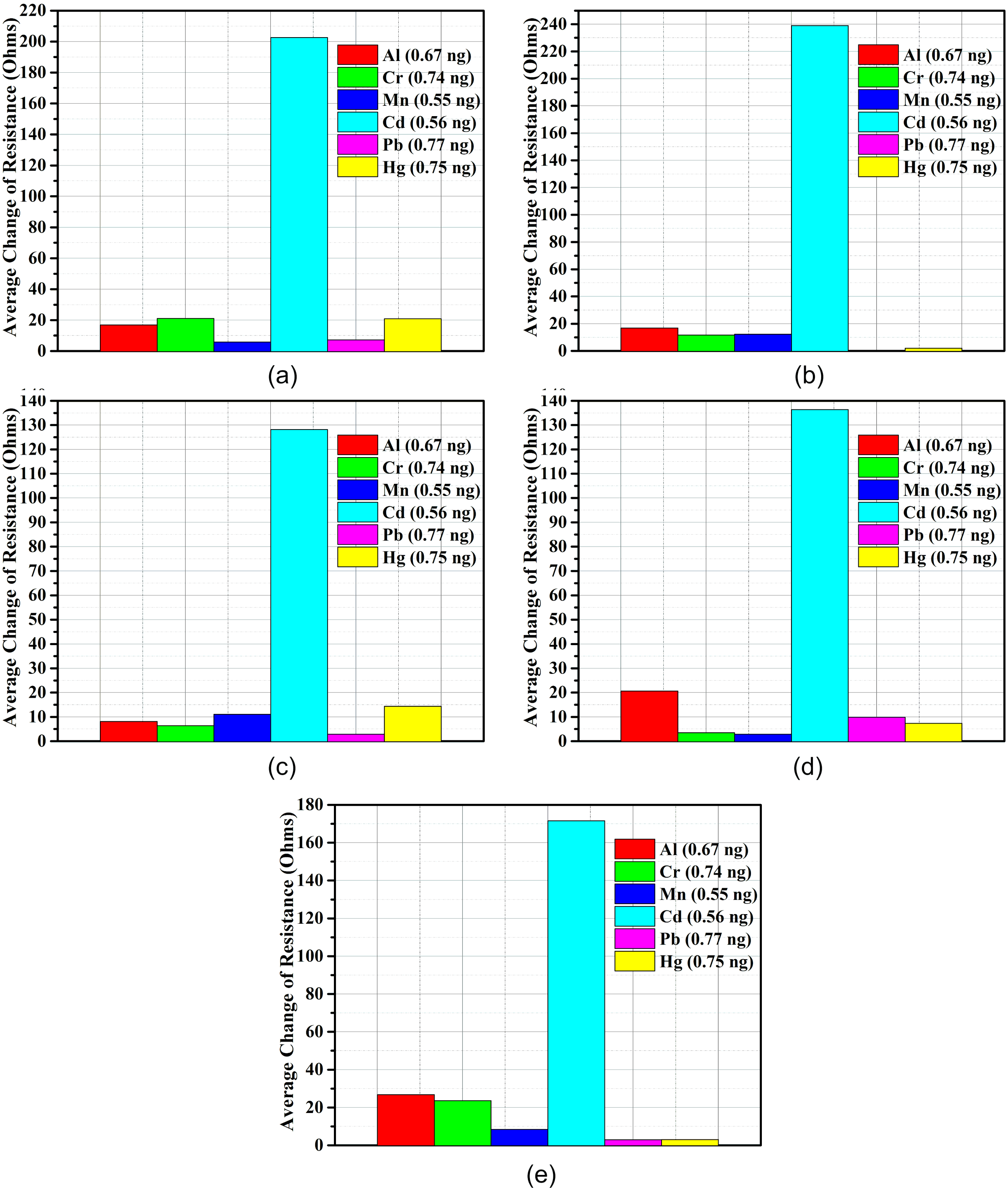

Figure 5: The average change in piezoresistance of microcantilevers: a) Au-Cys-DL-GC(3), b) Au-Cys-DL-GC(4), c) Au-Cys-DL-GC(5), d) Au-Cys-DL-GC(6) and e) Au-Cys-DL-GC(7).

top of a Au surface after exposure to $CdCl_2$ is shown in Figure 8. The table with the mass percentages (Figure 8b) explicitly shows the presence of Cd(II), and the percentage number of molecules captured in that scan region.

Table 1 presents a comparative analysis of different techniques to selectively capture Cd(II) in the picomolar range. We found that the fabricated piezoresistive sensor needs 20–23 min for selectively capturing Cd(II). At a flow of 30 µL/min, the total

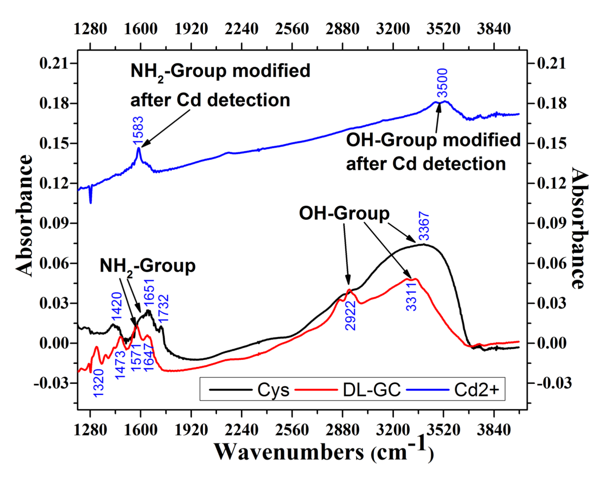

Figure 6: FTIR absorbance spectra of a Cd(II)/DL-GC/Cys/Au/Ti coating.

injected volume is 0.69 mL for a maximum of 23 min. Therefore, the corresponding mass of $AlCl_3$, $MnCl_2$, $CrCl_3$, $CdCl_2$, $PbCl_2$, and $HgCl_2$ is 0.67 ng, 0.55 ng, 0.74 ng, 0.56 ng, 0.77 ng, and 0.75 ng, respectively (refer to [40,52] for LOD calculation).

From the comparison in Table 1, it is clear that the proposed microfluidic platform has the ability to selectively capture Cd(II) at amounts as small as 2.78 pM/mL (LOD) and outperforms other approaches, which require sophisticated measuring instruments. The methods proposed by [4,62,63,65] have outstanding potential for a picomolar range of detection but require costly, sophisticated analytical tools [62,63,65]. The method proposed by [66] has excellent detection in the picomolar range but authors have not studied the sensor response with respect to time, necessary for real-time sensing. Many authors have used colorimetric or fluorescence techniques for selective HMI

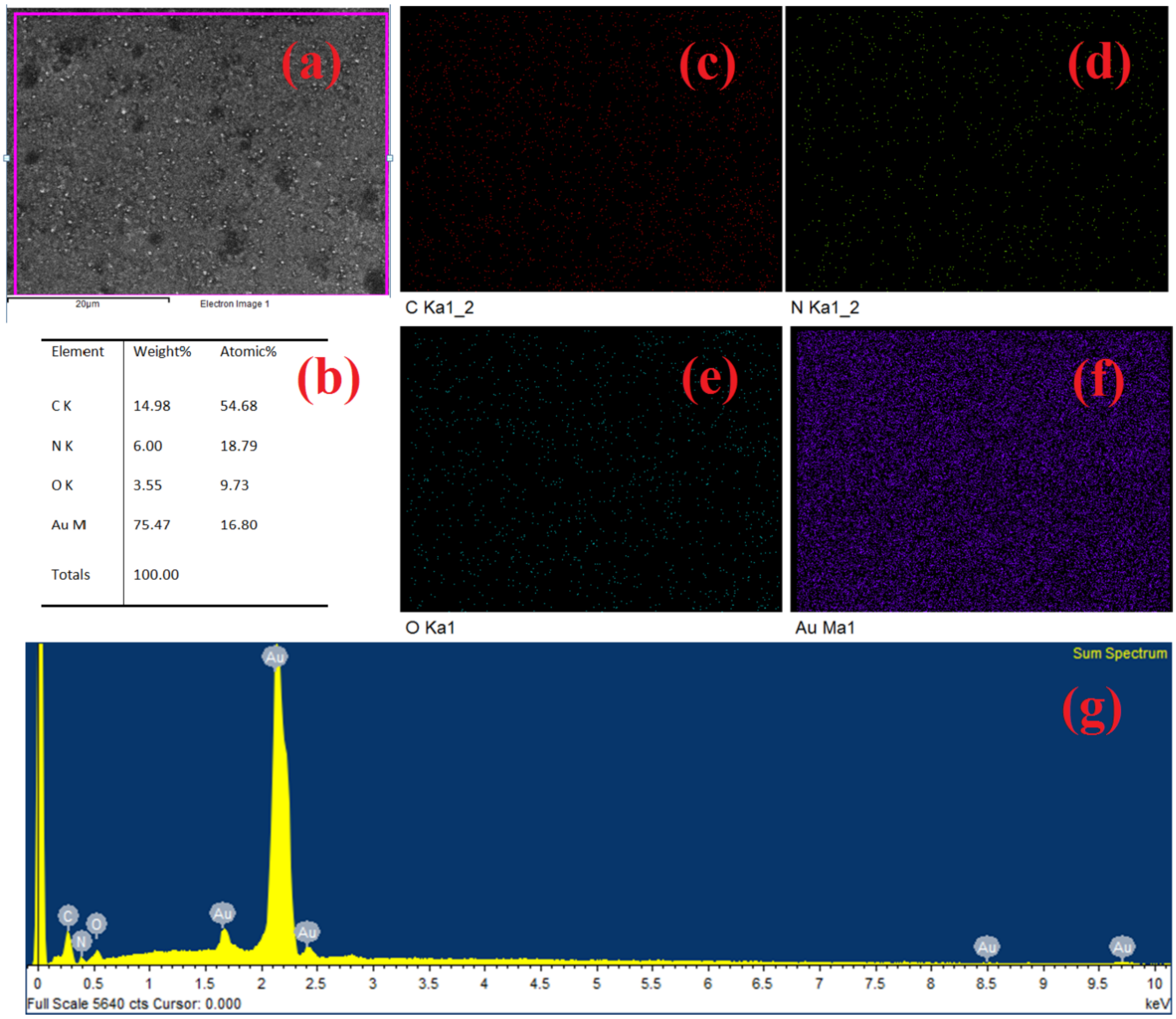

Element	Weight%	Atomic%
C K	14.98	54.68
N K	6.00	18.79
O K	3.55	9.73
Au M	75.47	16.80
Totals	100.00	

Figure 7: EDX measurement of a SAM of cysteamine (Cys)-cross-linked DL-glyceraldehyde (Cys-DL-GC). (a) Scan area for analysis, (b) table with detected elements, (c–f) color mappings of detected elements, (g) EDX spectrum.

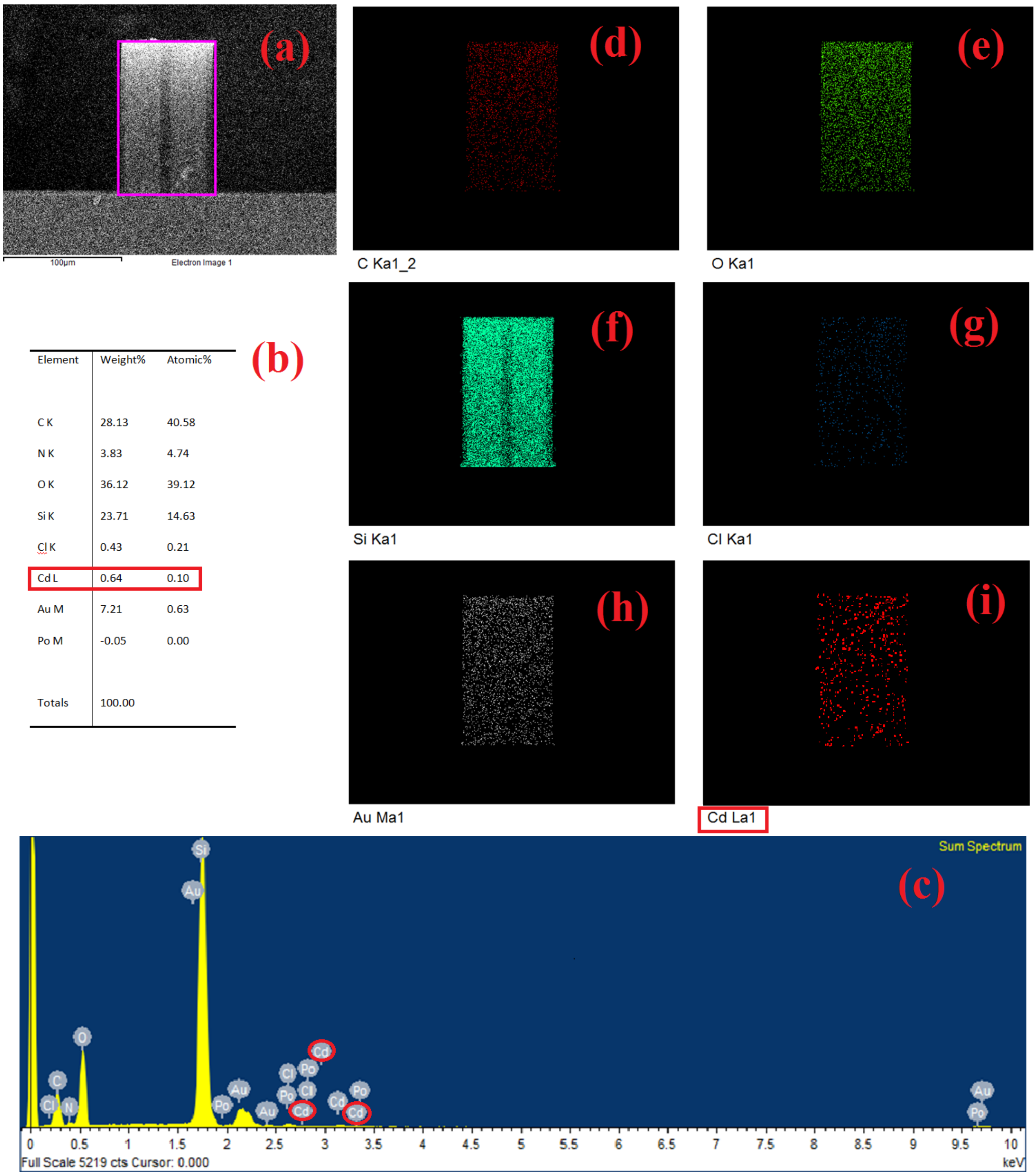

Element	Weight%	Atomic%
C K	28.13	40.58
N K	3.83	4.74
O K	36.12	39.12
Si K	23.71	14.63
Cl K	0.43	0.21
Cd L	0.64	0.10
Au M	7.21	0.63
Po M	-0.05	0.00
Totals	100.00	

Figure 8: EDX measurement of a SAM of cysteamine (Cys)-cross-linked DL-glyceraldehyde (Cys-DL-GC) after exposure to Cd(II). (a) Scan area for analysis, (b) table with detected elements, (c) EDX spectrum, and (d–i) color mappings of detected elements.

detection but they are highly sensitive to variation of pH values [67]. In a colorimetric sensor, the concentration variation is shown by different shades of color and it is challenging to exactly identify the shades for the different ranges of concentrations. Both the colorimetric and the fluorescence techniques use NPs and lead to an excessive commercialization of nanoparticles, quickly expanding their harmful effect on life and environment, as discussed earlier.

Conclusion

The proposed microcantilever-based device was tested in a microfluidic setup for the selective detection of cadmium and

Table 1: Comparison of different methods for cadmium detection.

reference	Analyte (HMI)	Limit of detection (LOD)	Method used	Detection technique
[4]	Cd(II)	100 pM	microstructured/optical fiber	fluorescence/absorption spectra
[5]	Cd(II)	0.5 nM	ratiometric fluorescence	UV–vis spectroscopy/fluorescence spectra
[32]	Cd(II)	1 µM	carbon paste electrode	XRF/XRD/anodic stripping voltammetry
[33]	Cd(II)	2.15 nM	fluorescent aptamer probe	F-4500/UV-2450 spectrophotometer
[34]	Cd(II)	21 nM	AuNP based probes	colorimetric/FT-IR/DLS
[35]	Cd(II)	10 µM	AuNP based electrode	colorimetric/UV–vis spectroscopy
[38]	Cd(II)	1.33 nM	polymeric-NPs/sol–gel	anodic stripping voltammetry (ASV)/FTIR
[53]	Cd(II)	800 µM	LSPR technique	optical fiber setup
[54]	Cd(II)	2.26 nM	AlGaN/GaN HEMT	high electron mobility transistor (HEMT)
[55]	Cd(II)	65 µM	gold nanoclusters/graphene	fluorescent probe/UV–vis spectroscopy
[56]	Cd(II)	1 µM	gold bioluminescent	fluorescent/microalgae-based
[57]	Cd(II)	1.062 µM	FRET probe-ZnS QD	FTIR/UV–vis/DLS/TEM/(Lab based)
[58]	Cd(II)	5.56 nM	AuNPs-based	colorimetric system/UV–vis spectra/TEM
[59]	Cd(II)	18.5 µM	fluorometric chemosensor	colorimetric/UV–vis/fluorescent spectra
[60]	Cd(II), Pb(II)	2.23 nM	carbon stencil printed electrode	Raman scattering
[61]	Cd(II)	4.95 µM	silver nanoparticles (AgNPs)	UV–vis/FTIR/TEM
[62]	Cd(II), Hg(II)	10–100 pM	electrochemical sensors	PGSTAT potentiostat
[63]	Cd(II), Pb(II)	49.67 pM	cantilever nanobiosensor	atomic force microscope (AFM) setup
[64]	Cd(II)	1 nM	antibody-modified microcantilever	atomic force microscope (AFM) setup
[65]	Pb(II), Cd(II)	1.72–1.58 pM	electrochemical sensor	stripping voltammetry (SWASV)
[66]	Cd(II)	0.3 pM	electrochemical biosensor	AUTOLAB PGSTAT 30
this work	Cd(II)	2.78 pM	piezoresistive sensor	portable setup (real-time analysis)

was found to achieve sensing in 20–23 min. The 0.56 ng/mL (2.78 pM) limit of detection is possible with a SAM of cysteamine cross-linked DL-glyceraldehyde (Cys-DL-GC). The average value of change in piezoresistance of the Au-Cys-DL-GC-coated microcantilever is approximately 130–240 Ω for cadmium ions and 5–30 Ω range for other injected HMIs. The total value of average change in piezoresistance for the concentration of 0.56 ng/mL for Cd(II) is 877.72 Ω. The most significant feature of this approach is the need for a sample volume of one milliliter. It is also evident from EDX spectra that no other HMIs except Cd(II) have been found. This EDX finding shows that the fabricated microcantilever-based piezoresistive sensor does not have cross selectivity. In conclusion, this approach could serve as a portable framework for on-site, ultrasensitive, and selective Cd(II) detection in the picomolar range.

Funding

The authors would like to thank Director of Indian Institute of Technology, Bombay for the support of atomic force microscopy under “Indian Nanoelectronics Users Program” and “Visvesvaraya Ph.D. Scheme for Electronics and IT” funded by the MeitY and FESEM support under PUMP, NCPRE funded by the MNRE, Government of India.

ORCID® iDs

Dinesh Rotake - https://orcid.org/0000-0003-2036-463X

Preprint

A non-peer-reviewed version of this article has been previously published as a preprint doi:10.3762/bxiv.2020.44.v1

References

1. Vaseashta, A.; Duca, G.; Culighin, E.; Bogdevici, O.; Khudaverdyan, S.; Sidorenko, A. Smart and Connected Sensors Network for Water Contamination Monitoring and Situational Awareness. *Functional Nanostructures and Sensors for CBRN Defence and Environmental Safety and Security;* Springer, 2020; pp 293–296.
2. Nastasiuc, L. N.; Bogdevici, O. P.; Overcenco, A. V.; Smîslov, V. V.; Iacunin, V. S.; Sidorenko, A. S.; Vaseashta, A. *Water contaminants monitoring in Moldova;* 2015; p 112.
3. Nastasiuc, L.; Bogdevici, O.; Aureliu, O.; Culighin, E.; Sidorenko, A.; Vaseashta, A. *Pol. J. Environ. Stud.* **2016,** *25,* 221–230. doi:10.15244/pjoes/58888
4. Heng, S.; Mak, A. M.; Stubing, D. B.; Monro, T. M.; Abell, A. D. *Anal. Chem. (Washington, DC, U. S.)* **2014,** *86,* 3268–3272. doi:10.1021/ac500619z

5. Qian, J.; Wang, K.; Wang, C.; Ren, C.; Liu, Q.; Hao, N.; Wang, K. *Sens. Actuators, B* **2017,** *241,* 1153–1160. doi:10.1016/j.snb.2016.10.020
6. Thompson, T.; Fawell, J.; Kunikane, S.; Jackson, D.; Appleyard, S.; Callan, P.; Bartram, J.; Kingston, P. *Chemical safety of drinking-water: Assessing priorities for risk management;* World Health Organization, 2007; pp 1–142.
7. Criscuolo, F.; Lobello, L.; Taurino, I.; Demarchi, D.; Carrara, S.; De Micheli, G. Mixed Gold and Platinum Nanostructured Layers for All-Solid-State Ion Sensors. *2018 IEEE SENSORS;* IEEE, 2018; pp 1–4.
8. Gutierrez, F. A.; Gonzalez-Dominguez, J. M.; Ansón-Casaos, A.; Hernández-Ferrer, J.; Rubianes, M. D.; Martínez, M. T.; Rivas, G. *Sens. Actuators, B* **2017,** *249,* 506–514. doi:10.1016/j.snb.2017.04.026
9. Ramírez, M. L.; Tettamanti, C. S.; Gutierrez, F. A.; Gonzalez-Domínguez, J. M.; Ansón-Casaos, A.; Hernández-Ferrer, J.; Martínez, M. T.; Rivas, G. A.; Rodríguez, M. C. *Microchem. J.* **2018,** *141,* 271–278. doi:10.1016/j.microc.2018.05.007
10. Jin, L.; Li, J.; Liu, L.; Wang, Z.; Zhang, X. *Appl. Nanosci.* **2018,** *8,* 1189–1196. doi:10.1007/s13204-018-0755-3
11. Krasovska, M.; Gerbreders, V.; Mihailova, I.; Ogurcovs, A.; Sledevskis, E.; Gerbreders, A.; Sarajevs, P. *Beilstein J. Nanotechnol.* **2018,** *9,* 2421–2431. doi:10.3762/bjnano.9.227
12. Hemavathy, R. R. V.; Kumar, P. S.; Suganya, S.; Swetha, V.; Varjani, S. J. *Bioresour. Technol.* **2019,** *281,* 1–9. doi:10.1016/j.biortech.2019.02.070
13. Christopher, F. C.; Anbalagan, S.; Kumar, P. S.; Pannerselvam, S. R.; Vaidyanathan, V. K. *IET Nanobiotechnol.* **2017,** *11,* 433–442. doi:10.1049/iet-nbt.2016.0166
14. Yan, Y.; Li, J.; Kong, F.; Jia, K.; He, S.; Wang, B. *Beilstein J. Nanotechnol.* **2017,** *8,* 2680–2688. doi:10.3762/bjnano.8.268
15. Kumar, N.; Fosso-Kankeu, E.; Ray, S. S. *ACS Appl. Mater. Interfaces* **2019,** *11,* 19141–19155. doi:10.1021/acsami.9b03853
16. Kumar, N.; Reddy, L.; Parashar, V.; Ngila, J. C. *J. Environ. Chem. Eng.* **2017,** *5,* 1718–1731. doi:10.1016/j.jece.2017.03.014
17. Song, Z.; Wang, F.; Qiang, J.; Zhang, Z.; Chen, Y.; Wang, Y.; Zhang, W.; Chen, X. *J. Lumin.* **2017,** *183,* 212–216. doi:10.1016/j.jlumin.2016.11.052
18. Liu, C.; Xiao, T.; Wang, Y.; Wang, F.; Chen, X. *Tetrahedron* **2017,** *73,* 5189–5193. doi:10.1016/j.tet.2017.07.012
19. Ma, Y.; Mei, J.; Bai, J.; Chen, X.; Ren, L. *Mater. Res. Express* **2018,** *5,* 055605. doi:10.1088/2053-1591/aac419
20. Rao, A. V. R. K.; Reddy, R. B.; Sengupta, S.; Chelvam, V. *Appl. Nanosci.* **2018,** *8,* 1973–1987. doi:10.1007/s13204-018-0875-9
21. Makwana, B. A.; Vyas, D. J.; Bhatt, K. D.; Darji, S.; Jain, V. K. *Appl. Nanosci.* **2016,** *6,* 555–566. doi:10.1007/s13204-015-0459-x
22. Basu, T.; Rana, K.; Das, N.; Pal, B. *Beilstein J. Nanotechnol.* **2017,** *8,* 762–771. doi:10.3762/bjnano.8.79
23. Li, J.; Ge, J.; Zhang, Z.; Qiang, J.; Wei, T.; Chen, Y.; Li, Z.; Wang, F.; Chen, X. *Sens. Actuators, B* **2019,** *296,* 126578. doi:10.1016/j.snb.2019.05.055
24. Khan, M. A.; Alfadhel, A.; Kosel, J.; Bakolka, M. Fabrication and characterization of magnetic composite membrane pressure sensor. 2016 IEEE Sensors Applications Symposium (SAS); 2019; pp 1–5.
25. Salem, M.; Javanmard, M. *IEEE Sens. Lett.* **2018,** *2,* 1–4. doi:10.1109/lsens.2018.2839090
26. Javanmard, M.; Davis, R. W. *Sens. Actuators, B* **2011,** *154,* 22–27. doi:10.1016/j.snb.2010.03.067
27. Javanmard, M.; Davis, R. W. *IEEE Sens. J.* **2012,** *12,* 2733–2734. doi:10.1109/jsen.2012.2198463
28. Kale, N. S.; Nag, S.; Pinto, R.; Rao, V. R. *J. Microelectromech. Syst.* **2009,** *18,* 79–87. doi:10.1109/jmems.2008.2008577
29. Tang, Y.; Fang, J.; Yan, X.; Ji, H.-F. *Sens. Actuators, B* **2004,** *97,* 109–113. doi:10.1016/j.snb.2003.08.003
30. Thaysen, J. Cantilever for bio-chemical sensing integrated in a microliquid handling system. Ph.D. Thesis, Technical University of Denmark, Lyngby, Denmark, 2001.
31. Haiden, C.; Wopelka, T.; Jech, M.; Keplinger, F.; Vellekoop, M. J. *IEEE Sens. J.* **2016,** *16,* 1182–1189. doi:10.1109/jsen.2015.2501355
32. Ourari, A.; Tennah, F.; Ruíz-Rosas, R.; Aggoun, D.; Morallón, E. *Int. J. Electrochem. Sci.* **2018,** *13,* 1683–1699. doi:10.20964/2018.02.35
33. Zhu, Y.-F.; Wang, Y.-S.; Zhou, B.; Yu, J.-H.; Peng, L.-L.; Huang, Y.-Q.; Li, X.-J.; Chen, S.-H.; Tang, X.; Wang, X.-F. *Anal. Bioanal. Chem.* **2017,** *409,* 4951–4958. doi:10.1007/s00216-017-0436-1
34. Yadav, R.; Patel, P. N.; Lad, V. N. *Res. Chem. Intermed.* **2018,** *44,* 2305–2317. doi:10.1007/s11164-017-3230-y
35. Chen, N.; Chen, J.; Yang, J.-H.; Bai, L.-Y.; Zhang, Y.-P. *J. Nanosci. Nanotechnol.* **2016,** *16,* 840–843. doi:10.1166/jnn.2016.11618
36. Sung, H. K.; Oh, S. Y.; Park, C.; Kim, Y. *Langmuir* **2013,** *29,* 8978–8982. doi:10.1021/la401408f
37. Greis, K.; Bethke, K.; Stückrath, J. B.; Ingber, T. T. K.; Valiyaveettil, S.; Rademann, K. *Clean: Soil, Air, Water* **2019,** *47,* 1900179. doi:10.1002/clen.201900179
38. Ghanei-Motlagh, M.; Taher, M. A. *Chem. Eng. J.* **2017,** *327,* 135–141. doi:10.1016/j.cej.2017.06.091
39. Rotake, D. R.; Darji, A. D.; Kale, N. S. *Microelectron. Int.* **2019,** *37,* 10–28. doi:10.1108/mi-05-2019-0025
40. Rotake, D.; Darji, A.; Kale, N. *IET Nanobiotechnol.* **2020,** *14,* 357–368. doi:10.1049/iet-nbt.2019.0277
41. Fritz, J.; Baller, M. K.; Lang, H. P.; Rothuizen, H.; Vettiger, P.; Meyer, E.; Güntherodt, H.-J.; Gerber, C.; Gimzewski, J. K. *Science* **2000,** *288,* 316–318. doi:10.1126/science.288.5464.316
42. Mathew, R.; Ravi Sankar, A. *Nano-Micro Lett.* **2018,** *10,* 35. doi:10.1007/s40820-018-0189-1
43. Rotake, D.; Darji, A. Stiffness and Sensitivity analysis of Microcantilever Based Piezoresistive Sensor for Bio-MEMS Application. IEEE SENSORS, International Symposium; 2018; pp 1584–1875.
44. Asharani, P. V.; lianwu, Y.; Gong, Z.; Valiyaveettil, S. *Nanotoxicology* **2011,** *5,* 43–54. doi:10.3109/17435390.2010.489207
45. Kovochich, M.; Xia, T.; Xu, J.; Yeh, J. I.; Nel, A. E. Principles and procedures to assess nanomaterial toxicity. *Environmental nanotechnology: applications and impacts of nanomaterials;* McGraw Hill: New York, NY, USA, 2007; pp 205–229.
46. Royce, S. G.; Mukherjee, D.; Cai, T.; Xu, S. S.; Alexander, J. A.; Mi, Z.; Calderon, L.; Mainelis, G.; Lee, K.; Lioy, P. J.; Tetley, T. D.; Chung, K. F.; Zhang, J.; Georgopoulos, P. G. *J. Nanopart. Res.* **2014,** *16,* 2724. doi:10.1007/s11051-014-2724-4
47. Wu, S.; Nan, T.; Xue, C.; Cheng, T.; Liu, H.; Wang, B.; Zhang, Q.; Wu, X. *Biosens. Bioelectron.* **2013,** *48,* 67–74. doi:10.1016/j.bios.2013.03.086
48. Patty, D. J.; Loupatty, G.; Sopalauw, F. *AIP Conf. Proc.* **2017,** *1801,* 060005. doi:10.1063/1.4973109
49. Kong, J.; Yu, S. *Acta Biochim. Biophys. Sin.* **2007,** *39,* 549–559. doi:10.1111/j.1745-7270.2007.00320.x

50. Liu, Y.; Wu, Y.; Guo, X.; Wen, Y.; Yang, H. *Sens. Actuators, B* **2019,** *283,* 278–283. doi:10.1016/j.snb.2018.12.043
51. Rotake, D. R.; Darji, A.; Singh, J. *Sens. Rev.* **2020,** *40,* 485–495. doi:10.1108/sr-12-2019-0313
52. Rotake, D.; Singh, J.; Darji, A.; Kumar, A. *IET Nanobiotechnol.* **2020,** *14,* in press. doi:10.1049/iet-nbt.2020.0109
53. Dhara, P.; Kumar, R.; Binetti, L.; Nguyen, H. T.; Alwis, L. S.; Sun, T.; Grattan, K. T. V. *IEEE Sens. J.* **2019,** *19,* 8720–8726. doi:10.1109/jsen.2019.2921701
54. Nigam, A.; Bhat, T. N.; Bhati, V. S.; Dolmanan, S. B.; Tripathy, S.; Kumar, M. *IEEE Sens. J.* **2019,** *19,* 2863–2870. doi:10.1109/jsen.2019.2891511
55. Ju, C.; Gong, X.; Song, W.; Zhao, Y.; Li, R. *Micro Nano Lett.* **2018,** *13,* 804–806. doi:10.1049/mnl.2017.0637
56. Wong, L. S.; Judge, S. K.; Voon, B. W. N.; Tee, L. J.; Tan, K. Y.; Murti, M.; Chai, M. K. *IEEE Sens. J.* **2018,** *18,* 2091–2096. doi:10.1109/jsen.2017.2787786
57. Safari, S.; Amiri, A.; Badiei, A. *Spectrochim. Acta, Part A* **2020,** *231,* 118062. doi:10.1016/j.saa.2020.118062
58. Gan, Y.; Liang, T.; Hu, Q.; Zhong, L.; Wang, X.; Wan, H.; Wang, P. *Talanta* **2020,** *208,* 120231. doi:10.1016/j.talanta.2019.120231
59. Pham, T. C.; Kim, Y. K.; Park, J. B.; Jeon, S.; Ahn, J.; Yim, Y.; Yoon, J.; Lee, S. *ChemPhotoChem* **2019,** *3,* 1133–1137. doi:10.1002/cptc.201900165
60. Kava, A. A.; Beardsley, C.; Hofstetter, J.; Henry, C. S. *Anal. Chim. Acta* **2020,** *1103,* 58–66. doi:10.1016/j.aca.2019.12.047
61. Jabariyan, S.; Zanjanchi, M. A. *Appl. Phys. A: Mater. Sci. Process.* **2019,** *125,* 872. doi:10.1007/s00339-019-3167-7
62. Popescu Mandoc, L.-R.; Moldoveanu, I.; Stefan-van Staden, R.-I.; Ungureanu, E. M. *Microsyst. Technol.* **2017,** *23,* 1141–1145. doi:10.1007/s00542-016-3039-4
63. Rigo, A. A.; Cezaro, A. M. D.; Muenchen, D. K.; Martinazzo, J.; Manzoli, A.; Steffens, J.; Steffens, C. *J. Environ. Sci. Health, Part B* **2020,** *55,* 239–249. doi:10.1080/03601234.2019.1685318
64. Velanki, S.; Kelly, S.; Thundat, T.; Blake, D. A.; Ji, H.-F. *Ultramicroscopy* **2007,** *107,* 1123–1128. doi:10.1016/j.ultramic.2007.01.011
65. Zeinu, K. M.; Hou, H.; Liu, B.; Yuan, X.; Huang, L.; Zhu, X.; Hu, J.; Yang, J.; Liang, S.; Wu, X. *J. Mater. Chem. A* **2016,** *4,* 13967–13979. doi:10.1039/c6ta04881a
66. Ebrahimi, M.; Raoof, J. B.; Ojani, R. *Int. J. Biol. Macromol.* **2018,** *108,* 1237–1241. doi:10.1016/j.ijbiomac.2017.11.023
67. Charbgoo, F.; Ramezani, M.; Darroudi, M. *Biosens. Bioelectron.* **2017,** *96,* 33–43. doi:10.1016/j.bios.2017.04.037

License and Terms

The definitive version of this article is the electronic one which can be found at:
doi:10.3762/bjnano.11.108

BEILSTEIN JOURNAL OF NANOTECHNOLOGY

Proximity effect in [Nb(1.5 nm)/Fe(x)]$_{10}$/Nb(50 nm) superconductor/ferromagnet heterostructures

Yury Khaydukov*[1,2,3], Sabine Pütter[4], Laura Guasco[1,2], Roman Morari[5], Gideok Kim[1],
Thomas Keller[1,2], Anatolie Sidorenko[5] and Bernhard Keimer[1]

Full Research Paper

Open Access

Address:
[1]Max-Planck-Institut für Festkörperforschung, Heisenbergstraße 1, D-70569 Stuttgart, Germany, [2]Max Planck Society Outstation at the Heinz Maier-Leibnitz Zentrum (MLZ), D-85748 Garching, Germany, [3]Skobeltsyn Institute of Nuclear Physics, Moscow State University, Moscow 119991, Russia, [4]Forschungszentrum Jülich GmbH, Jülich Centre for Neutron Science (JCNS) at Heinz Maier-Leibnitz Zentrum (MLZ), Lichtenbergstr. 1, D-85747 Garching, Germany and [5]Institute of Electronic Engineering and Nanotechnologies ASM, MD2028 Kishinev, Moldova

Email:
Yury Khaydukov* - y.khaydukov@fkf.mpg.de

* Corresponding author

Keywords:
ferromagnet; iron (Fe); mixed state; neutron reflectometry; niobium (Nb); proximity effects; superconductor

Beilstein J. Nanotechnol. **2020,** *11,* 1254–1263.
https://doi.org/10.3762/bjnano.11.109

Received: 26 November 2019
Accepted: 28 July 2020
Published: 21 August 2020

This article is part of the thematic issue "Functional nanostructures for electronics, spintronics and sensors".

Associate Editor: J. M. van Ruitenbeek

Abstract

We have investigated the structural, magnetic and superconduction properties of [Nb(1.5 nm)/Fe(x)]$_{10}$ superlattices deposited on a thick Nb(50 nm) layer. Our investigation showed that the Nb(50 nm) layer grows epitaxially at 800 °C on the Al$_2$O$_3$(1−102) substrate. Samples grown at this condition possess a high residual resistivity ratio of 15–20. By using neutron reflectometry we show that Fe/Nb superlattices with $x < 4$ nm form a depth-modulated FeNb alloy with concentration of iron varying between 60% and 90%. This alloy has weak ferromagnetic properties. The proximity of this weak ferromagnetic layer to a thick superconductor leads to an intermediate phase that is characterized by a suppressed but still finite resistance of structure in a temperature interval of about 1 K below the superconducting transition of thick Nb. By increasing the thickness of the Fe layer to $x = 4$ nm the intermediate phase disappears. We attribute the intermediate state to proximity induced non-homogeneous superconductivity in the structure.

Introduction

Superconductor(S)/ferromagnet(F) heterostructures are intensively studied systems, which are interesting for fundamental physics due to a big number of predicted and detected phenomena such as the appearance of non-uniform superconducting states (see reviews [1-3]). Among these phenomena are π–Josephson junctions [4-7] with a π-phase difference of superconducting correlations between two neighboring interfaces, long-range triplet superconductivity [8-16] generated in S/F systems with a non-collinear (NC) magnetic configuration of the F system, and re-entrant superconductivity as evidence of nonuniform LOFF-states [17-20]. Apart from the interest in basic science, the proximity effect in S/F structures has great technological importance for the creation of spintronics devices, where the transport properties of the structure are controlled via the manipulation of the magnetic order in the F subsystem [21-26].

One possible way to exert such a control is via interaction of superconductivity and interlayer exchange coupling (IEC) of F layers through a normal metal (NM) spacer. The IEC in a F/N/F system can be tuned by varying the thickness of the N spacer to organize antiparallel (AP), parallel (P) or non-collinearly aligned F layers [27]. Also, the presence of superconducting correlations in the same F/N/F system would favor AP alignment for singlet pairing or a NC configuration to generate a long-range triplet condensate. To the best of our knowledge the interaction of singlet superconductivity and exchange coupling was first considered theoretically in [28,29] and different magnetic re-ordering processes, such as the transition from parallel to antiparallel alignment [29] or the suppression of RKKY interaction below T_C were calculated [28]. Experimentally the interaction of exchange coupling can be studied by integral magnetometric methods such as SQUID magnetometry [30] or depth-resolved techniques such as polarized neutron reflectometry (PNR) [31].

One potentially interesting system for studying the interaction between superconductivity and IEC is the Fe/Nb system. Proximity effects in Fe/Nb systems were extensively studied before [32-36]. The antiferromagnetic coupling of Fe layers through a Nb(y) spacer with $y = (1.3 + 0.9 \times n)$ nm ($n = 0, 1, 2$) was found in [37,38] by means of PNR. In the following work of the same group [39] the modification of IEC by hydrogen uptake was reported. An advantage of niobium as N spacer is that it is the superconducting material with the highest bulk $T_C = 9.3$ K among all elemental superconductors. However, the thickest Nb spacer layer where AP alignment is still possible, $y \approx 3$ nm, is still two times smaller than the minimum thickness $d_S^{\text{crit}} \approx 6–8$ nm of thin Nb films in which superconductivity appears [19,20]. In order to provide superconducting correlations in a Fe/Nb superlattice (SL) we propose to deposit the Fe/Nb SL on top of a thick Nb(40–50 nm) layer. This thick superconducting layer will act as a reservoir of superconducting pairs, which will be transferred to the SL using the proximity effect. The aim of this work is the study of structural, magnetic and superconducting properties of such S/F heterostructures.

Experimental

Growth conditions and techniques

Samples of the nominal structure Pt(3 nm)/[Nb(1.5 nm)/Fe(x)]$_{10}$/Nb(50 nm) were prepared on $Al_2O_3(1\bar{1}02)$ substrates using a DCA M600 MBE system with a base pressure of 10^{-10} mbar. Before deposition, the substrates were cleaned from organic contaminations with ethanol and isopropanol ex situ and heated at 1000 °C in ultra high vacuum for 2–3 h. A 50 nm thick Nb layer was deposited at a typical rate of 0.6 Å/s and a substrate temperature of $T_{Nb} = 800$ °C for samples s1 to s5 and at $T_{Nb} = 33$ °C for sample s6. Subsequently, the substrate temperature was decreased to $T_{SL} = 30–100$ °C (see below Table 1) and a periodic structure [Nb(1.5 nm)/Fe(x)]$_{10}$ was deposited starting with the iron layer. The growth rates for both elements in the periodic structure were about 0.1 Å/s. On top, a 3 nm Pt cap layer was grown at about 0.3 Å/s at room temperature to protect the sample against oxidation. Fe was deposited by thermal evaporation from an effusion cell while Nb and Pt were grown by electron beam evaporation. Reflection high-energy electron diffraction (RHEED) was measured in situ during deposition to trace the structure of the atomic layer being deposited. For the RHEED experiment, an electron beam of 15 keV energy was directed along the $[20\bar{2}\bar{1}]$ azimuth of the sapphire substrate.

In order to check the crystal structure and the quality of the epitaxial growth, X-ray diffraction measurements were performed using a θ–2θ diffractometer. The diffractometer operates at the wavelength of λ = 1.54 Å and is equipped with a DECTRIS line detector, which allows for simultaneous measurement of both specular and off-specular reflections.

The polarized neutron reflectometry (PNR) experiments were conducted on the angle-dispersive reflectometer NREX (λ = 4.28 Å) at the research reactor FRM-II (Garching, Germany). During the experiments we applied a magnetic field in-plane and normal to the sample plane. Data were fitted to models using the exact solutions of the Schrödinger equation as described in our prior works [13,40,41].

For the transport experiment we used the device depicted in Figure 1b. The device consists of four metallic springs touching the surface of the sample. The tension of the springs is sufficiently high to ensure good contact with the sample surface and to measure the resistivity using a standard four-point contact method. The setup is designed to enable simultaneous PNR and transport experiments, though in this work we used it ex situ. For the measurements we used an ac current with an amplitude of 100–200 μA. In the experiment we measured the resistance of the samples $\mathcal{R}$ as a function of the temperature T and the magnetic field H, which was applied parallel to the sample sur-

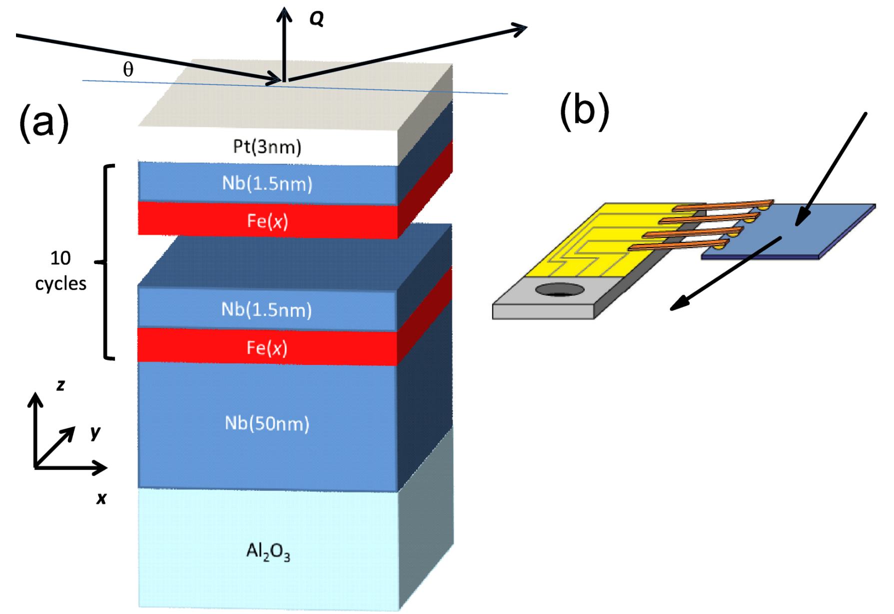

Figure 1: (a) Sketch of the experiment for structure and reflectometric measurements and (b) setup for the transport measurements. Black arrows show the direction of the neutron beam.

face. Before every H scan we waited 10–15 min to stabilize the temperature. From the transport measurements we derived the residual resistivity ratio RRR = $\mathcal{R}(300\text{K})/\mathcal{R}(10\text{K})$, the superconducting transition temperature T_C and its width ΔT_C. The latter two parameters were defined as the center and the width of derivative $\text{d}\mathcal{R}/\text{d}T$, respectively.

Reflectometry data analysis

To study the quality of layers and interfaces in a layered structure reflectometry techniques (X-ray or neutron) can be used. Using these methods, a reflectivity curve $R(Q)$ is measured as a function of momentum transfer $Q = 4\pi\sin(\theta)/\lambda$. In the kinematical approximation the reflectivity is proportional to the square of the Fourier transform of $\text{d}\rho(z)/\text{d}z$, where $\rho(z)$ is the depth profile of the scattering length density (SLD). The SLD is defined as the product of the averaged scattering length $\bar{b}$ and the density N. For a periodic structure with period D repeated n times one can write a simple expression for the reflectivity [42]:

$$R(Q) = \left|L_n(Q,D)F(Q,\rho)\right|^2, \qquad (1)$$

where $L_n(Q,D) = (1 - e^{inQD})/(1 - e^{iQD})$ is the Laue function and $F(Q,\rho)$ is the structure factor of the unit cell. The latter can be written for a Fe(x)/Nb(y) periodic bilayer as

$$F(Q,\rho) = \frac{4\pi\Delta\rho}{Q^2} e^{iQx}\left(1 - e^{iQy}\right), \qquad (2)$$

where $\Delta\rho = (\rho_\text{Fe} - \rho_\text{Nb})$ is the contrast between the SLDs of Fe and Nb. Thus, from Equation 1 and Equation 2 it follows that reflectometry measures the contrast between SLDs of neighboring layers. Using Equation 1 and Equation 2 we can write for the reflectivity R_1 at the first Bragg peak $Q_1 = 2\pi/D$:

$$\Delta\rho = \frac{\sqrt{R_1 Q_1^2}}{8\pi n}. \qquad (3)$$

Thus, the Bragg analysis allows us to determine the contrast between the SLDs of Fe and Nb. Interdiffusion will lead to suppression of the contrast and, hence, of R_1. Assuming that the packing density N_av is the same for both layers, we may estimate the concentration of Fe in the $\text{Fe}_c\text{Nb}_{1-c}$ alloy as

$$c = \frac{\bar{b} - b_\text{Nb}}{b_\text{Fe} - b_\text{Nb}}, \qquad (4)$$

where $\bar{b} = \rho/N_\text{av}$ is the averaged coherent scattering length of the corresponding layer, and b_Fe and b_Nb are the coherent scattering lengths of Fe and Nb. The X-ray SLDs of Fe and Nb differ only by a few percent, which makes the X-ray contrast very small even without interdiffusion. For neutrons, in contrast, the SLDs of Fe and Nb, $\rho_\text{Fe} = 8 \times 10^{-4}\ \text{nm}^{-2}$ and $\rho_\text{Nb} = 3.9 \times 10^{-4}\ \text{nm}^{-2}$, differ by a factor of two, which makes neutron reflectometry a better choice to study diffusion in periodic Fe/Nb structures. Another advantage of neutron reflectometry is its sensitivity to the magnetic depth profile. The total SLD for spin-up(+) and spin-down(−) neutrons can be written as $\rho^{\pm}(z) = \rho_0(z) \pm \rho_m(z)$, where ρ_0 and ρ_m are the nuclear and magnetic SLDs. The latter is proportional to the magnetization of a layer. Thus in addition to the chemical we can study magnetic depth profiles using PNR.

Results

Structural study

Growth analysis with RHEED

The RHEED pattern of the $Al_2O_3(1\bar{1}02)$ substrate (Figure 2a) reveals a crystalline structure with Laue rings and Kikuchi lines indicating a smooth and ordered surface. Nb deposition at 800 °C results in a streaky pattern and a Laue ring (Figure 2c) revealing epitaxial growth in agreement with previous results [43-46]. In particular, the epitaxial Nb growth of (100) orientation on $Al_2O_3(1\bar{1}02)$ substrates was reported in [46]. The peculiarity of this growth, also seen in our samples, is an angle of approx. 3° between the above mentioned planes of Nb and $Al_2O_3(1\bar{1}02)$. At T_{Nb} = 30 °C a transmission pattern (i.e., a regular arrangement of spots) and rings are visible in the RHEED pattern of the Nb layer, which indicate island growth and polycrystallinity (Figure 2d).

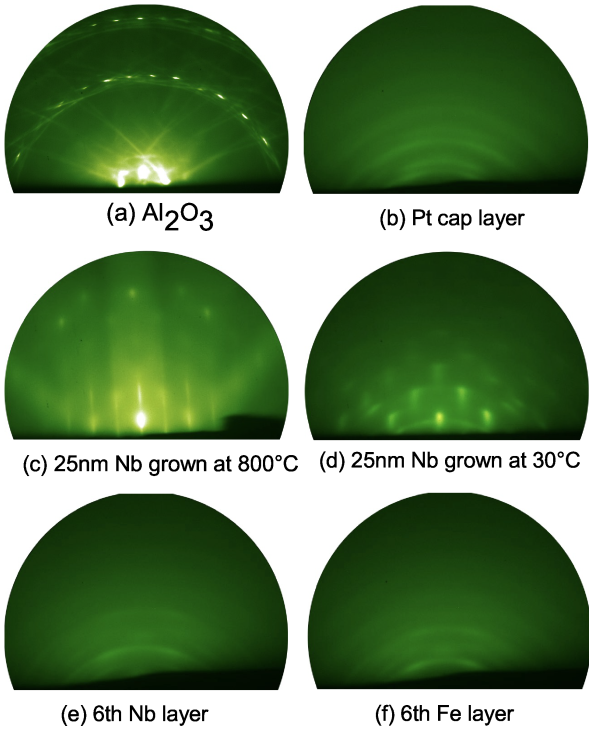
(a) Al_2O_3

(b) Pt cap layer

(c) 25nm Nb grown at 800°C

(d) 25nm Nb grown at 30°C

(e) 6th Nb layer

(f) 6th Fe layer

Figure 2: RHEED patterns of (a) the $Al_2O_3(1\bar{1}02)$ substrate, (b) the Pt cap layer, and the Nb buffer layer grown at (c) 800 °C and (d) 30 °C. (e, f) Growth stages of sample s6: (e) the 6th Fe layer, (f) the 6th Nb layer.

Subsequently, the Fe/Nb multilayers were grown on the 800 °C Nb buffer. The corresponding RHEED patterns exhibit amorphous growth, i.e., blurred screens (not shown). Increasing the Fe film thickness from 2 to 4 nm improves the film quality. The Fe layer becomes polycrystalline while the Nb layer remains amorphous. In contrast, for sample s6, which was grown on the 30 °C Nb buffer, both layers reveal polycrystallinity with a certain texture (Figure 2e,f). Finally, the Pt cap is always polycrystalline (Figure 2b).

X-ray diffraction

Figure 3a shows the diffraction pattern measured on sample s3. Together with two reflections from the substrate we observed a Nb(200) peak at 2θ = 55°with mosaicity of the same order as the substrate peak. In agreement with the observation by RHEED (Figure 4b) we observed that the Nb(200) peak is tilted off-specular by a few degrees, which is a well-known feature of Nb growth on $Al_2O_3(1\bar{1}02)$ substrates [45,46]. Similar patterns were measured for all samples, except for sample s6, which was

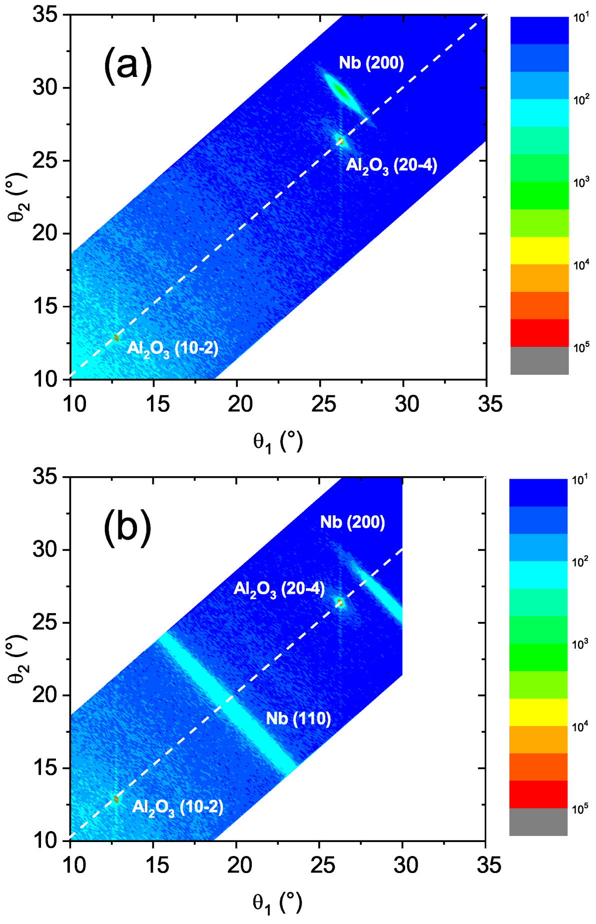

Figure 3: X-ray diffraction patterns of (a) sample s3 and (b) sample s6. Dashed tilted lines show the direction of specular reflection. The color bars show the logarithmic intensity scale.

grown at room temperature. For this sample we measured a typical polycrystalline pattern with coexisting Nb(100) and Nb(110) phases (Figure 3b).

Magnetic properties

SQUID measurements

Figure 4a shows hysteresis loops measured on sample s3 at $T = 300$ K and $T = 13$ K. At room temperature the sample saturates to a magnetic moment $m_{\mathrm{sat}} = 12$ μemu above a saturation field of only $H_{\mathrm{sat}} = 50$ Oe. At 13 K the saturation moment increases to $m_{\mathrm{sat}} = 40$ μemu and a field above $H_{\mathrm{sat}} \approx 2$ kOe is needed to saturate the magnetic moment of the sample. The temperature dependence of the magnetic moment at $H = 250$ Oe (Figure 4b) shows that the moment is constant down to $T \approx 100$ K, and grows upon further cooling to $T = 8.2$ K. Below this temperature a decrease of the magnetic moment due to the Meissner effect is observed.

Polarized neutron reflectometry

Figure 5a shows reflectivity curves measured on sample s3 at a temperature of $T = 13$ K in a magnetic field of $H = 4.5$ kOe. The curves are characterized by the total external reflection plateau, interference oscillations and the first Bragg peak at $Q_1 \approx 2.1$ nm^{-1}. The intensity of the Bragg peak $R(Q_1) \equiv R_1 \approx 4 \times 10^{-5}$ is one order of magnitude lower than calculated for the nominal SLDs, indicating high interdiffusion of Fe and Nb. Despite this high interdiffusion we observed a statistically significant difference of Bragg intensities for spin-up and spin-down neutrons (see inset in Figure 5a), which suggests the presence of magnetism in the periodic structure. A similar picture was also observed for the samples s1 and s2, which shows that the interdiffusion does not depend strongly on the deposition temperature T_{SL}. We fitted experimental curves to models with varying SLD, thickness, and rms roughness of all layers and varying magnetization of the Fe layer. The resulting depth profiles $\rho_0(z)$ and $M(z)$ are shown in Figure 5b. According to our model the SLD in the center of the Fe and Nb layers is $\rho_{\mathrm{Fe}} = 6.0(2) \times 10^{-4}$ nm^{-2} and $\rho_{\mathrm{Nb}} = 5.0(2) \times 10^{-4}$ nm^{-2}, respectively. Using Equation 4 for $N_{\mathrm{av}} = (N_{\mathrm{Fe}} + N_{\mathrm{Nb}})/2$ we can estimate the concentration of iron atoms in the nominal Fe and Nb layers as $c = 90\%$ and $c = 60\%$, respectively. In this estimation we used the bulk densities $N_{\mathrm{Fe}} = 0.085$ Å^{-3}, $N_{\mathrm{Nb}} = 0.06$ Å^{-3} and the scattering lengths $b_{\mathrm{Fe}} = 9.45$ fm and $b_{\mathrm{Nb}} = 7.05$ fm.

Samples s4 to s6 were measured at room temperature at $H = 4.5$ kOe and analyzed in the same way. The resulting SLDs and magnetization values are shown below in Table 1. All samples except s4 show strong intermixing of Fe and Nb atoms, which resulted in a suppressed magnetization of the order of 10% of the bulk value. For sample s4 with Fe(4 nm) we observed a much stronger Bragg peak with significantly stronger difference of spin-up and spin-down channels (Figure 5c). The fit shows (Figure 5d) that these reflectivities correspond to much higher nuclear and magnetic contrast.

Since the thickness of our Nb spacer, 1.3 nm, is close to the thickness at which antiferromagnetic coupling was observed in [37-39] we thoroughly searched for antiferromagnetic coupling in our structures. We remind that such a coupling will lead to the doubling of the magnetic period comparing to the chemical one and, hence, the appearance of Bragg peaks on positions $Q_{\mathrm{AF}} = 1/2\ Q_n$, where n is the order of the structural Bragg peak. In addition to the high-field measurements we performed PNR measurements at a low magnetic field of $H = 5$ Oe. None of our measurements revealed the appearance of additional peaks. An example is given in Figure 5c for sample s4 measured at room temperature in $H = 5$ Oe.

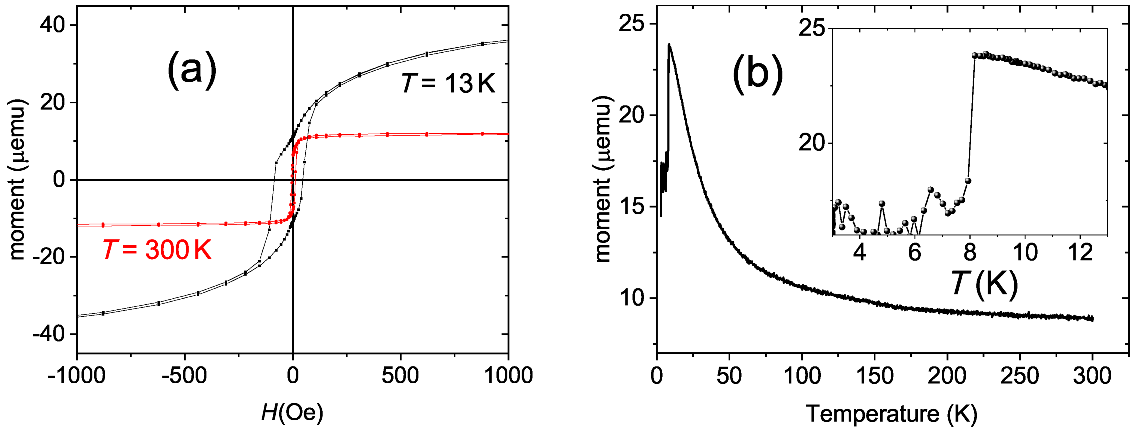

Figure 4: SQUID data of the s3 sample. (a) Hysteresis loop measured at $T = 300$ K (red) and $T = 13$ K (black). (b) Temperature dependence of the magnetic moment measured at $H = 250$ Oe. The inset shows the data in the vicinity of the superconducting transition.

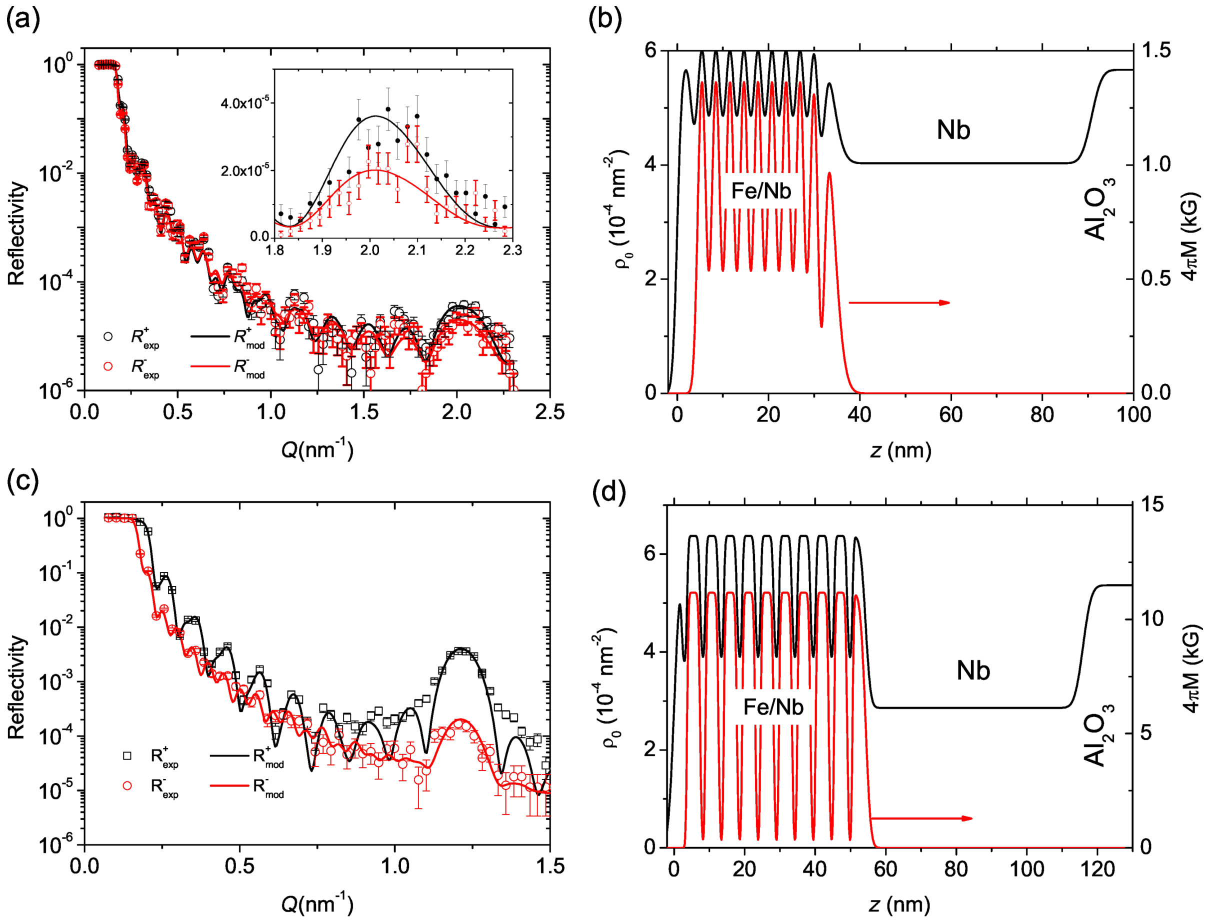

Figure 5: (a) Experimental (dots) and model (lines) reflectivity curves measured on sample s3 at T = 13 K and H = 4.5 kOe. (b) The depth profiles of SLD and magnetization for the same sample. (c) Reflectivity curves for sample s4 measured at T = 300 K and H = 5 Oe. (d) Corresponding depth profile of SLD and magnetization for sample s4.

Transport measurements

The inset of Figure 6a shows the resistance $\mathcal{R}(T)$ of samples s3 and s6 measured during cooling from room temperature to 10 K in magnetic field of H = 4.5 kOe. For s3 we measured RRR = 18.6, a value which is typical for MBE-prepared S/F structures in the epitaxial regime of growth [47,48]. Similar values of RRR from 16 to 20 were obtained for all samples except RRR = 3.4 for s6, which was deposited at room temperature and has polycrystalline quality (see below Table 1).

Figure 6a shows the $\mathcal{R}(T)$ curves for the s3 and s4 measured in zero magnetic field in the vicinity of the superconducting transition. For sample s3 we observed a 40% drop of resistance below T_{c1} = 8.9 K. A similar drop was observed for all samples, except for s4, for which the initial drop was only 3%. Finally, below $T_{c2} \approx 8$ K the resistance falls to zero (down to the accuracy of the setup-related background resistance of 5 mΩ) for all samples, evidencing the superconducting transition. The second transition coincides with the transition seen by SQUID (inset in Figure 4b).

Figure 6b shows the $\mathcal{R}(H,T)$ phase diagram for sample s3. The superconducting transition can be well described by the expression $T_{c2}(H) = T_{c2}(0)\,[1 - (H/H_{c2}(0))^2]$ with $H_{c2}(0)$ = 12 kOe. This expression can be re-written in the well known form for 2D superconductors: $H_{c2}(T) = H_{c2}(0)\sqrt{1 - T/T_{c2}(0)}$. From $H_{c2}(0)$ we can estimate the superconducting correlation length ξ_S = 12 nm. We note that 2D superconductivity was reported earlier for various structures with Nb layer thicknesses of 100 nm or less [5,33,35,36,41].

Discussion

In this work we studied the structural, magnetic and superconduction properties of [Fe(x)/Nb(1.5 nm)]$_{10}$ superlattices on top of a thick Nb(50 nm) layer. The main characteristics are summarized in Table 1. Our investigation has shown that the Nb

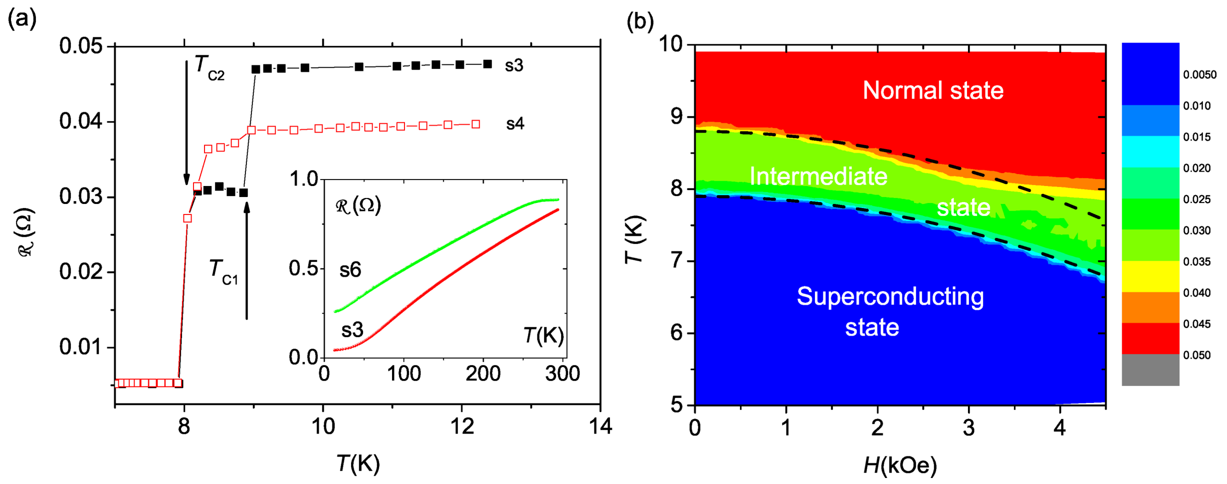

Figure 6: (a) $\mathcal{R}(T)$ for the samples s4 (black) and s3 (red) in the vicinity of the superconducting transition measured in zero magnetic field. The inset shows the resistance of samples s3 and s6 between room temperature and 10 K in H = 4.5 kOe. (b) The H–T dependence of resistance of the sample s3. The color bar depicts resistance in ohms. The bottom dashed line show the dependence $T_{c2}(H) = T_{c2}(0)\ [1 - (H/H_{c2}(0))^2]$ with $H_{c2}(0)$ = 12 kOe. The upper dashed line is shifted 0.9 K up from the bottom one to show borders of the intermediate state.

Table 1: Main characteristics of the prepared samples. Here x is the thickness of the Fe layers, the column “XRD” gives the corresponding Miller indices of the peaks observed in the experiment, T_{Nb} and T_{SL} are the temperatures of deposition of the thick Nb layer and the periodic structure, respectively, ρ_{Fe} and ρ_{Nb} are, respectively, the nuclear SLD at the center of the nominal Fe and Nb layers, and T_{c1} and T_{c2} are, respectively, the upper and lower transition temperature.

ID	x (Å)	XRD	T_{Nb} (°C)	T_{SL} (°C)	$\rho_{\mathrm{Fe}}/\rho_{\mathrm{Nb}}$	M_{Fe} (kG)	RRR	T_{c1} (K)	T_{c2} (K)
s1	15.4(1)	Nb(200)	800	100	6.1/5.1	1(1)	18.1	8.9(3)	8.1(3)
s2	15.6(4)	n/m	800	66	5.7/4.7	1.8(8)	16.9	8.9(1)	8.0(2)
s3	15.1(1)	Nb(200)	800	30	6.0/4.9	2(1)	18.6	8.8(2)	8.1(2)
s4	36.7(3)	Nb(200)	800	30	6.6/4.0	11.2(4)	19.6	8.8(2)	8.0(1)
s5	26.7(4)	Nb(200)	800	30	6.1/3.9	2(1)	16.3	8.9(1)	7.9(2)
s6	20.1(5)	Nb(110), Nb(200)	30	30	5.0/4.6	2.3(5)	3.4	9.1(1)	8.3(1)

layer grows epitaxially on the $\mathrm{Al_2O_3}(1\bar{1}02)$ substrate in the (100) direction at a substrate temperature during deposition of T_{Nb} = 800 °C. This result agrees with [45]. Furthermore the samples grown at this temperature show high residual resistivity ratios of 15–20. The sample deposited at room temperature, in contrast, possesses a polycrystalline structure of the Nb(50 nm) layer with a mixture of (100) and (110) phases and a rather low RRR of 3.4, which is attributed to enhanced scattering of conduction electrons at the grain boundaries.

Neutron reflectometry has shown that Fe/Nb superlattices with $x \leq 2.5$ nm form a depth-modulated FeNb alloy with the concentration of iron varying within the superlattice unit cell between 60% and 90%. Based on the SQUID data (Figure 4), we can attribute the magnetic signal at room temperature to the iron-rich $\mathrm{Fe_{0.9}Nb_{0.1}}$ alloy, while the signal below $T_m \approx 100$ K originates from $\mathrm{Fe_{0.6}Nb_{0.4}}$. Although the thickness of our Nb spacer, 1.3 nm, is close to the values in [37-39] we did not observe any antiferromagnetic coupling, neither at room temperature nor in low-temperature measurements. The reason of this disagreement may originate from the amorphous Nb spacers.

The proximity of this depth-modulated and weakly magnetic layer to a thick superconductor causes the appearance of an intermediate phase between the normal state ($T > T_{c1}$) with nonzero resistance and the superconducting state ($T < T_{c2}$) with zero resistance. This state is characterized by a ≈50% suppressed resistance and the absence of the Meissner effect. Similar steps were already observed in several works [19,30,49,50]. Up to now there exists no explanation of such steps except for cases related to different imperfections of the sample (e.g., thickness gradient, crystal inhomogeneity, or oxide at S/F interface) [19,30,49,50]. However, a detailed study of our systems using various structural methods allows us to exclude these cases. To discuss this effect we first need to pay attention to the peculiarities of our transport experiment. Since the contacts are attached to the surface, electrical current will tend to flow along the surface penetrating only to a certain depth λ. To calculate λ one needs to know the resistivity of all layers in z direction as well as the interfaces resistances. This will require additional experiments on simpler systems and/or with current applied normal to the surface. However, the following arguments allow us to say that the value of λ is comparable to the thickness of the entire structure, that is, the current flows not only along the SL but also through the thick niobium layer or at least through its upper part. First of all, we note that a stand-alone Fe/Nb SL structure itself hardly can be a superconductor due to the absence of a clean and oriented Nb phase. Secondly, we draw attention to the difference between the transport properties of samples s5 and s6. Lowering of the deposition temperature of thick niobium T_{Nb} led to polycrystalline growth of the thick Nb layer of sample s6 and a strong decrease of its RRR (Table 1). Such a sensitivity of the RRR on the crystal structure of thick Nb indicates that the transport experiment is sensitive to the thick niobium layer, i.e., the current does flow through it. If this is the case, then the transition of the thick niobium to the superconducting state should lead to a (almost) complete loss of resistance. This is indeed observed experimentally below T_{c2} for all samples, while for samples with $x \leq 2.5$ nm in the region of temperatures between T_{c1} and T_{c2} the loss is only partial. Taking into account all of these facts we can propose that the thick Nb layer in the intermediate state comprises superconducting and normal-state domains. This hypothesis allows us to explain the suppression of the resistance and the absence of the Meissner effect in the intermediate state. However, it requires further experimental and theoretical studies. For example covering the SL from both sides with thick superconductor layers would allow direct measurements of the proximity effect using PNR [41].

Conclusion

We studied the structural, magnetic and superconducting properties of $[\mathrm{Nb}(1.5\ \mathrm{nm})/\mathrm{Fe}(x)]_{10}$ superlattices deposited on a thick Nb(50 nm) layer. Our investigation showed that a high deposition temperature of T_{Nb} = 800 °C results in systems of high structural quality with an epitaxial Nb(50 nm) layer and high residual resistivity ratios of 15–20. By using neutron reflectometry we have shown that Fe/Nb superlattices with $x < 4$ nm form a depth-modulated FeNb alloy with the concentration of iron varying between 60% and 90%. This alloy has properties of a weak ferromagnet with a Curie temperature of $T_{\mathrm{m}} \approx 100$ K. The proximity of this weak F layer to a thick superconductor leads to the presence of an intermediate phase between normal and superconducting state. This phase is characterized by a suppressed resistance of the structure in the temperature range of T = 8–9 K below the superconducting transition of thick Nb. By increasing thickness of Fe layer to $x = 4$ nm this phase was destroyed.

Acknowledgements

We would like to thank G. Logvenov, F. Klose, and Ch. Rehm for the fruitful discussions. This work is partially based on experiments performed at the NREX instrument operated by Max-Planck Society at the Heinz Maier-Leibnitz Zentrum (MLZ), Garching, Germany. Sample preparation was performed in the thin film laboratory of the Jülich Centre for Neutron Science (JCNS) at Heinz Maier-Leibnitz Zentrum (MLZ), Garching, Germany.

Funding

YK, LG, TK, and BK would like to acknowledge financial support of German Research Foundation (Deutsche Forschungsgemeinschaft, DFG, Project No. 107745057 - TRR80). AS and RM would like to thank the support of the "SPINTECH" project of the HORIZON-2020 TWINNING program (2018-2020).

ORCID® iDs

Yury Khaydukov - https://orcid.org/0000-0001-9945-8342
Sabine Pütter - https://orcid.org/0000-0003-2694-0095
Laura Guasco - https://orcid.org/0000-0001-5823-3665
Anatolie Sidorenko - https://orcid.org/0000-0001-7433-4140

Preprint

A non-peer-reviewed version of this article has been previously published as a preprint: https://arxiv.org/abs/1911.10168

References

1. Buzdin, A. I. *Rev. Mod. Phys.* **2005,** *77,* 935–976. doi:10.1103/revmodphys.77.935
2. Eschrig, M. *Phys. Today* **2011,** *64,* 43. doi:10.1063/1.3541944
3. Sidorenko, A. S. *Low Temp. Phys.* **2017,** *43,* 766–771. doi:10.1063/1.4995623
4. Fominov, Y. V.; Chtchelkatchev, N. M.; Golubov, A. A. *Phys. Rev. B* **2002,** *66,* 014507. doi:10.1103/physrevb.66.014507
5. Khaydukov, Y. N.; Vasenko, A. S.; Kravtsov, E. A.; Progliado, V. V.; Zhaketov, V. D.; Csik, A.; Nikitenko, Y. V.; Petrenko, A. V.; Keller, T.; Golubov, A. A.; Kupriyanov, M. Y.; Ustinov, V. V.; Aksenov, V. L.; Keimer, B. *Phys. Rev. B* **2018,** *97,* 144511. doi:10.1103/physrevb.97.144511
6. Karabassov, T.; Stolyarov, V. S.; Golubov, A. A.; Silkin, V. M.; Bayazitov, V. M.; Lvov, B. G.; Vasenko, A. S. *Phys. Rev. B* **2019,** *100,* 104502. doi:10.1103/physrevb.100.104502
7. Vargunin, A.; Silaev, M. A. *Appl. Phys. Lett.* **2020,** *116,* 092601. doi:10.1063/1.5143269
8. Bergeret, F. S.; Volkov, A. F.; Efetov, K. B. *Phys. Rev. Lett.* **2001,** *86,* 4096–4099. doi:10.1103/physrevlett.86.4096
9. Volkov, A. F.; Bergeret, F. S.; Efetov, K. B. *Phys. Rev. Lett.* **2003,** *90,* 117006. doi:10.1103/physrevlett.90.117006
10. Fominov, Y. V.; Golubov, A. A.; Kupriyanov, M. Y. *JETP Lett.* **2003,** *77,* 510–515. doi:10.1134/1.1591981

11. Fominov, Y. V.; Golubov, A. A.; Karminskaya, T. Y.; Kupriyanov, M. Y.; Deminov, R. G.; Tagirov, L. R. *JETP Lett.* **2010,** *91,* 308–313. doi:10.1134/s002136401006010x
12. Zhu, L. Y.; Liu, Y.; Bergeret, F. S.; Pearson, J. E.; te Velthuis, S. G. E.; Bader, S. D.; Jiang, J. S. *Phys. Rev. Lett.* **2013,** *110,* 177001. doi:10.1103/physrevlett.110.177001
13. Khaydukov, Y. N.; Ovsyannikov, G. A.; Sheyerman, A. E.; Constantinian, K. Y.; Mustafa, L.; Keller, T.; Uribe-Laverde, M. A.; Kislinskii, Y. V.; Shadrin, A. V.; Kalaboukhov, A.; Keimer, B.; Winkler, D. *Phys. Rev. B* **2014,** *90,* 035130. doi:10.1103/physrevb.90.035130
14. Leksin, P. V.; Kamashev, A. A.; Schumann, J.; Kataev, V. E.; Thomas, J.; Büchner, B.; Garifullin, I. A. *Nano Res.* **2016,** *9,* 1005–1011. doi:10.1007/s12274-016-0988-y
15. Tagirov, L. R.; Kupriyanov, M. Y.; Kushnir, V. N.; Sidorenko, A. Superconducting Triplet Proximity and Josephson Spin Valves. *Functional Nanostructures and Metamaterials for Superconducting Spintronics;* NanoScience and Technology; Springer International Publishing: Cham, Switzerland, 2018; pp 31–47. doi:10.1007/978-3-319-90481-8_2
16. Diesch, S.; Machon, P.; Wolz, M.; Sürgers, C.; Beckmann, D.; Belzig, W.; Scheer, E. *Nat. Commun.* **2018,** *9,* 5248. doi:10.1038/s41467-018-07597-w
17. Sidorenko, A. S.; Zdravkov, V.; Kehrle, J.; Morari, R.; Obermeier, G.; Gsell, S.; Schreck, M.; Müller, C.; Ryazanov, V.; Horn, S.; Tagirov, L. R.; Tidecks, R. *J. Phys.: Conf. Ser.* **2009,** *150,* 052242. doi:10.1088/1742-6596/150/5/052242
18. Sidorenko, A. S.; Zdravkov, V. I.; Kehrle, J.; Morari, R.; Obermeier, G.; Gsell, S.; Schreck, M.; Müller, C.; Kupriyanov, M. Y.; Ryazanov, V. V.; Horn, S.; Tagirov, L. R.; Tidecks, R. *JETP Lett.* **2009,** *90,* 139–142. doi:10.1134/s0021364009140124
19. Zdravkov, V.; Sidorenko, A.; Obermeier, G.; Gsell, S.; Schreck, M.; Müller, C.; Horn, S.; Tidecks, R.; Tagirov, L. R. *Phys. Rev. Lett.* **2006,** *97,* 057004. doi:10.1103/physrevlett.97.057004
20. Zdravkov, V. I.; Kehrle, J.; Obermeier, G.; Gsell, S.; Schreck, M.; Müller, C.; Krug von Nidda, H.-A.; Lindner, J.; Moosburger-Will, J.; Nold, E.; Morari, R.; Ryazanov, V. V.; Sidorenko, A. S.; Horn, S.; Tidecks, R.; Tagirov, L. R. *Phys. Rev. B* **2010,** *82,* 054517. doi:10.1103/physrevb.82.054517
21. Zdravkov, V. I.; Lenk, D.; Morari, R.; Ullrich, A.; Obermeier, G.; Müller, C.; Krug von Nidda, H.-A.; Sidorenko, A. S.; Horn, S.; Tidecks, R.; Tagirov, L. R. *Appl. Phys. Lett.* **2013,** *103,* 062604. doi:10.1063/1.4818266
22. Lenk, D.; Morari, R.; Zdravkov, V. I.; Ullrich, A.; Khaydukov, Y.; Obermeier, G.; Müller, C.; Sidorenko, A. S.; von Nidda, H.-A. K.; Horn, S.; Tagirov, L. R.; Tidecks, R. *Phys. Rev. B* **2017,** *96,* 184521. doi:10.1103/physrevb.96.184521
23. Soloviev, I. I.; Klenov, N. V.; Bakurskiy, S. V.; Kupriyanov, M. Y.; Gudkov, A. L.; Sidorenko, A. S. *Beilstein J. Nanotechnol.* **2017,** *8,* 2689–2710. doi:10.3762/bjnano.8.269
24. Golubov, A. A.; Kupriyanov, M. Y. *Nat. Mater.* **2017,** *16,* 156–157. doi:10.1038/nmat4847
25. Sidorenko, A., Ed. *Functional Nanostructures and Metamaterials for Superconducting Spintronics;* Springer International Publishing: Cham, Switzerland, 2018. doi:10.1007/978-3-319-90481-8
26. Klenov, N.; Khaydukov, Y.; Bakurskiy, S.; Morari, R.; Soloviev, I.; Boian, V.; Keller, T.; Kupriyanov, M.; Sidorenko, A.; Keimer, B. *Beilstein J. Nanotechnol.* **2019,** *10,* 833–839. doi:10.3762/bjnano.10.83
27. Hoffman, J. D.; Kirby, B. J.; Kwon, J.; Fabbris, G.; Meyers, D.; Freeland, J. W.; Martin, I.; Heinonen, O. G.; Steadman, P.; Zhou, H.; Schlepütz, C. M.; Dean, M. P. M.; te Velthuis, S. G. E.; Zuo, J.-M.; Bhattacharya, A. *Phys. Rev. X* **2016,** *6,* 041038. doi:10.1103/physrevx.6.041038
28. Sá de Melo, C. A. R. *Phys. Rev. B* **2000,** *62,* 12303–12316. doi:10.1103/physrevb.62.12303
29. Proshin, Y. N.; Izyumov, Y. A.; Khusainov, M. G. *Phys. Rev. B* **2001,** *64,* 064522. doi:10.1103/physrevb.64.064522
30. Zhu, Y.; Pal, A.; Blamire, M. G.; Barber, Z. H. *Nat. Mater.* **2017,** *16,* 195–199. doi:10.1038/nmat4753
31. Hoppler, J.; Stahn, J.; Niedermayer, C.; Malik, V. K.; Bouyanfif, H.; Drew, A. J.; Rössle, M.; Buzdin, A.; Cristiani, G.; Habermeier, H.-U.; Keimer, B.; Bernhard, C. *Nat. Mater.* **2009,** *8,* 315–319. doi:10.1038/nmat2383
32. Mühge, T.; Garif'yanov, N. N.; Goryunov, Y. V.; Khaliullin, G. G.; Tagirov, L. R.; Westerholt, K.; Garifullin, I. A.; Zabel, H. *Phys. Rev. Lett.* **1996,** *77,* 1857–1860. doi:10.1103/physrevlett.77.1857
33. Mühge, T.; Garif'yanov, N. N.; Goryunov, Y. V.; Theis-Bröhl, K.; Westerholt, K.; Garifullin, I. A.; Zabel, H. *Phys. C (Amsterdam, Neth.)* **1998,** *296,* 325–336. doi:10.1016/s0921-4534(97)01819-4
34. Mühge, T.; Westerholt, K.; Zabel, H.; Garif'yanov, N. N.; Goryunov, Y. V.; Garifullin, I. A.; Khaliullin, G. G. *Phys. Rev. B* **1997,** *55,* 8945–8954. doi:10.1103/physrevb.55.8945
35. Verbanck, G.; Potter, C. D.; Metlushko, V.; Schad, R.; Moshchalkov, V. V.; Bruynseraede, Y. *Phys. Rev. B* **1998,** *57,* 6029–6035. doi:10.1103/physrevb.57.6029
36. Huang, S. Y.; Lee, S. F.; Liang, J.-J.; Yu, C. Y.; You, K. L.; Chiang, T. W.; Hsu, S. Y.; Yao, Y. D. *J. Magn. Magn. Mater.* **2006,** *304,* e81–e83. doi:10.1016/j.jmmm.2006.01.185
37. Rehm, C.; Klose, F.; Nagengast, D.; Pietzak, B.; Maletta, H.; Weidinger, A. *Phys. B (Amsterdam, Neth.)* **1996,** *221,* 377–381. doi:10.1016/0921-4526(95)00952-3
38. Rehm, C.; Nagengast, D.; Klose, F.; Maletta, H.; Weidinger, A. *Europhys. Lett.* **1997,** *38,* 61–72. doi:10.1209/epl/i1997-00535-4
39. Klose, F.; Rehm, C.; Nagengast, D.; Maletta, H.; Weidinger, A. *Phys. Rev. Lett.* **1997,** *78,* 1150–1153. doi:10.1103/physrevlett.78.1150
40. Khaydukov, Y.; Petrzhik, A. M.; Borisenko, I. V.; Kalabukhov, A.; Winkler, D.; Keller, T.; Ovsyannikov, G. A.; Keimer, B. *Phys. Rev. B* **2017,** *96,* 165414. doi:10.1103/physrevb.96.165414
41. Khaydukov, Y. N.; Kravtsov, E. A.; Zhaketov, V. D.; Progliado, V. V.; Kim, G.; Nikitenko, Y. V.; Keller, T.; Ustinov, V. V.; Aksenov, V. L.; Keimer, B. *Phys. Rev. B* **2019,** *99,* 140503. doi:10.1103/physrevb.99.140503
42. Andreeva, M. A.; Lindgren, B. *Phys. Rev. B* **2005,** *72,* 125422. doi:10.1103/physrevb.72.125422
43. Gutekunst, G.; Mayer, J.; Rühle, M. *Philos. Mag. A* **1997,** *75,* 1329–1355. doi:10.1080/01418619708209859
44. Gutekunst, G.; Mayer, J.; Vitek, V.; Rühle, M. *Philos. Mag. A* **1997,** *75,* 1357–1382. doi:10.1080/01418619708209860
45. Wildes, A. R.; Mayer, J.; Theis-Bröhl, K. *Thin Solid Films* **2001,** *401,* 7–34. doi:10.1016/s0040-6090(01)01631-5
46. Di Nunzio, S.; Theis-Bröhl, K.; Zabel, H. *Thin Solid Films* **1996,** *279,* 180–188. doi:10.1016/0040-6090(95)08197-6
47. Nowak, G.; Zabel, H.; Westerholt, K.; Garifullin, I.; Marcellini, M.; Liebig, A.; Hjörvarsson, B. *Phys. Rev. B* **2008,** *78,* 134520. doi:10.1103/physrevb.78.134520
48. Nowak, G.; Westerholt, K.; Zabel, H. *Supercond. Sci. Technol.* **2013,** *26,* 025004. doi:10.1088/0953-2048/26/2/025004

49. Chiodi, F.; Witt, J. D. S.; Smits, R. G. J.; Qu, L.; Halász, G. B.; Wu, C.-T.; Valls, O. T.; Halterman, K.; Robinson, J. W. A.; Blamire, M. G. *EPL* **2013,** *101,* 37002. doi:10.1209/0295-5075/101/37002
50. Satchell, N.; Witt, J. D. S.; Flokstra, M. G.; Lee, S. L.; Cooper, J. F. K.; Kinane, C. J.; Langridge, S.; Burnell, G. *Phys. Rev. Appl.* **2017,** *7,* 044031. doi:10.1103/physrevapplied.7.044031

License and Terms

The definitive version of this article is the electronic one which can be found at:
https://doi.org/10.3762/bjnano.11.109

BEILSTEIN JOURNAL OF NANOTECHNOLOGY

Cryogenic low-noise amplifiers for measurements with superconducting detectors

Ilya L. Novikov, Boris I. Ivanov*, Dmitri V. Ponomarev and Aleksey G. Vostretsov

Full Research Paper

Open Access

Address:
Novosibirsk State Technical University, K.Marx-Av.20, Novosibirsk
630073, Russia

Email:
Boris I. Ivanov* - to_ivanov_boris@yahoo.com

* Corresponding author

Keywords:
cryogenic amplifier; cryogenic low-noise amplifier; differential cryogenic amplifier; superconducting circuit readout

Beilstein J. Nanotechnol. **2020,** *11,* 1316–1320.
https://doi.org/10.3762/bjnano.11.115

Received: 05 June 2020
Accepted: 17 August 2020
Published: 02 September 2020

This article is part of the thematic issue "Functional nanostructures for electronics, spintronics and sensors".

Guest Editor: A. S. Sidorenko

Abstract

We designed, implemented, and characterized differential amplifiers for cryogenic temperatures based on Si bipolar junction transistor technology. The amplifiers show high gain values of more than 60 dB at 300, 77, and 48 K. The minimum voltage noise spectral density was achieved at 77 K and corresponded to 0.33 nV/Hz$^{0.5}$ with a flicker noise of 20 Hz. The maximum voltage gain was 70 dB at 77 K for a frequency range from DC to 17 kHz. We experimentally show that the parallel differential circuit design allows for a reduction of the voltage noise from 0.55 to 0.33 nV/Hz$^{0.5}$ at 77 K.

Introduction

Currently, superconducting detectors are the most sensitive devices in the electromagnetic field and find wide application in radioastronomy and quantum electronics. Sensors based on superconductors can detect microwaves close to the single-photon limit [1]. Most of such sensors are based on Josephson junctions and superconducting thin films. Experimental studies of such sensors require the design of low-noise cryogenic readout electronics with a direct coupling to the sample. For example, investigations of noise sources in low-temperature tunnel Josephson junctions are still ongoing for high-precision calibration of superconductor technology and for finding new noise sources in Josephson junctions, which lead to high decoherence in superconducting systems [2,3]. The most important part in a measurement readout is a low-noise amplifier. The modern low-temperature low-noise cryogenic amplifiers are widely used for superconducting circuit readout at a temperature of 4 K [4-10]. However, the operating frequency range of such amplifiers starts at 10 kHz or higher. This specific design of cryogenic amplifiers is mainly based on two technological concepts, i.e., high electron mobility transistor (HEMT) technology and SiGe bipolar heterojunction technology (HBT).

Low-frequency amplifiers are usually applied as first stage of SQUID readout electronics [11,12] or as the readout of cryogenic bolometers [13]. In both cases the amplifiers have a working temperature of 300 K. Modern low-frequency and low-noise amplifiers are commonly based on Si bipolar junction transistor (BJT) technology and junction field-effect transistor (JFET) technology. Since external interferences can be compensated by differential input circuits, differential amplifier designs are used for these applications. These amplifiers, including instrumentation amplifiers, are usually built as fully monolithic integrated circuits. Due to the complicated circuit design, their parameters are not stable at temperatures below 240 K and they can not be used at cryogenics. However, it is known that single BJT amplifiers can operate at temperatures down to 77 K [11,14,15]. In [11] the authors use a matched transistor pair to develop a low-noise preamplifier for room-temperature SQUID readout electronics and show the possible application in wide temperature range. They achieved a low voltage noise spectral density of 0.33 nV/$\sqrt{\text{Hz}}$ with a $1/f$ flicker noise corner frequency of 0.1 Hz but there is no information about gain and noise performance at 77 K. Moreover, it would be useful to compare room-temperature results of BJT-based differential amplifiers with results obtained at 77 K. Also, modern cryogenic applications are based on dry cryostats instead of coolants. The most common modern dry cryostats, including dilution refrigerators and He-7 sorption refrigerators, have a 50 K temperature stage as uppermost cooling stage where the DC cryogenic amplifier can be mounted.

In this paper, we show the potential applicability of commercially available Si bipolar transistors for cryogenics. Design and preliminary performance of cryogenic low-noise differential amplifiers, based on matched parallel connected pairs of commercially available bipolar junction transistors, at temperatures of 77 and 50 K are presented. This amplifier design is simple to modify, fast to implement, and requires only a proper selection of components. The amplifiers show a high gain value of 70 dB for a frequency range from DC to 17 kHz, a low voltage noise spectral density of 0.33 nV/$\sqrt{\text{Hz}}$ and low flicker noise at 77 K. The total power consumption for the parallel circuit amplifier design corresponds to 180 mW. We experimentally show that the parallel differential circuit design allows for the reduction of the voltage noise from 0.55 to 0.33 nV/$\sqrt{\text{Hz}}$ at 77 K. The performance of the amplifier in measurements with superconducting detectors requires improvements, which are currently under investigation.

Experimental

We designed the cryogenic differential amplifier with an active load as a current mirror using negative and positive power supplies. SSM2210 and SSM2220 transistors were used as the main elements. These are n-p-n and p-n-p matched transistor pairs. Each pair is fabricated on one chip. Both type of transistors are used in low-frequency low-noise room-temperature amplifiers for SQUID and bolometer readouts [16-18]. Since the current gain in the bipolar transistors decreases with a lowering of the temperature, the main goal of this circuit design was to achieve a high voltage gain level at cryogenic temperatures of 77 and 48 K. This led us to use transistor bias points at high currents up to 10 mA, which is beyond the optimal working points for minimum voltage and current noise criteria. Moreover, this circuit modifies the differential input to the common mode output, which might be easily connected to any coaxial cable in a cryostat. The first amplifier circuit was designed with one transistor pair (SSM2210) connected to the active load (SSM2220). In order to reduce the Johnson–Nyquist noise we used a second transistor pair of SSM transistors connected in parallel to the input differential circuit as it is shown in Figure 1. This design was used in the second cryogenic differential amplifier. We used a negative voltage supply for biasing the emitter circuits over the resistors R_3 and R_4, which were thermally anchored to the 48 K cooling stage. This way we formed a current source and reduced the noise coming from the room-temperature voltage biasing part. Since the resistors were cooled to 48 K their Johnson–Nyquist noise did not influence the circuit. The resistors were measured at 77 K before and a pair of resistors with low resistance spread was chosen. Each pair of the SSM2210 transistors was measured and the input and output I–V curves were obtained. Pairs with

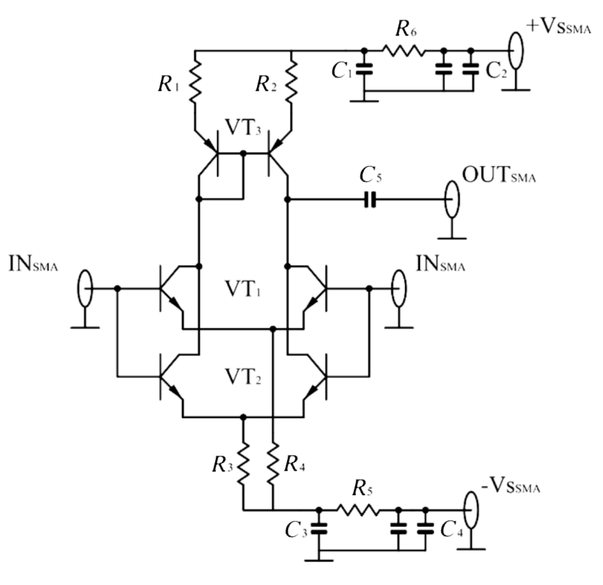

Figure 1: Schematic of the 0–120 kHz cryogenic LNA based on paired SSM2210 transistors. The important component values are: $R_1 = R_2 = 100\ \Omega$, $R_3 = R_4 = 4.3\ \text{k}\Omega$, $C_5 = 470$ nF. The capacitors are realized in 0402 package (C0G type) and the resistors are realized as uMELF. The other passive components are used for filtering of the bias lines.

similar transistor parameters were selected. We used simple RC filters in order to suppress any external interference coming from room-temperature voltage sources. The resistors R_1 and R_2 are the load resistors of the collector circuits, and the capacitor C_5 is the decoupling output capacitor, which has the unwanted effect of reducing the frequency bandwidth at low frequencies. The resistors used in the cryogenic amplifier are MELF-type resistors and the capacitors have a C0G-type of dielectric. All the components were mounted on the designed layout of the printed circuit board (PCB) from FR4 material. We did not solder the electrodes of the capacitors directly to the PCB in order to reduce the mechanical stress during the cooldown cycles. Instead, we used a small 0.25 mm Cu wire to provide a soldering connection to the PCB pads. The nominals for passive elements are given in the caption of Figure 1. The PCB with the cryogenic amplifier circuit was embedded inside a Cu box with SMA input and output connectors for signal lines. The biasing terminals were set up as feedthrough filters.

Results and Discussion

The main measurement instrument of the setup was a dynamic signal analyzer (SA) SR780 from Stanford Research Systems with a frequency range from DC to 102.4 kHz and imbedded analogue sweeping generator. It was used for gain and noise measurements. We performed measurements of two cryogenic differential amplifiers, i.e., one design with one pair of input transistors and another design with a parallel connection of transistor pairs (see Figure 1). The first design was measured at 300 and 77 K and the second design was characterized at three different temperatures, i.e., 300, 77, and 48 K. The first experimental temperature was room temperature. In order to measure the amplifiers at 77 K we used a liquid nitrogen dewar with good thermal isolation. The amplifier circuit mounted to the Cu case was immersed in a liquid nitrogen dewar. The low-temperature measurements at 48 K were made on the uppermost cooling stage of He-7 refrigerator with a Cryomech pulse tube cryocooler PT-405. Flexible shielded coaxial cables with SMA connectors were used for circuit biasing and for the input and output. We used an additional 40 dB attenuator at the SR780 generator output in order to reduce the voltage amplitude, so that the input voltage signal applied to the amplifiers corresponded to 100 µV. We estimated the dynamic behavior of the amplifiers while applying a sinusoidal analog signal with different amplitudes. The linear voltage range corresponded up to 5 mV at the input. At cryogenic temperatures the amplifiers were measured in two cooldown steps. First, the dependence of the gain on the frequency was obtained and during the next cooldown the voltage noise properties were characterized. The amplifier gain curves measured at two temperatures are presented in Figure 2. The gain of the amplifier corresponded to 73 dB in a frequency range from DC to 11 kHz at 77 K and 65 dB in a frequency range from DC to 9.6 kHz at 300 K.

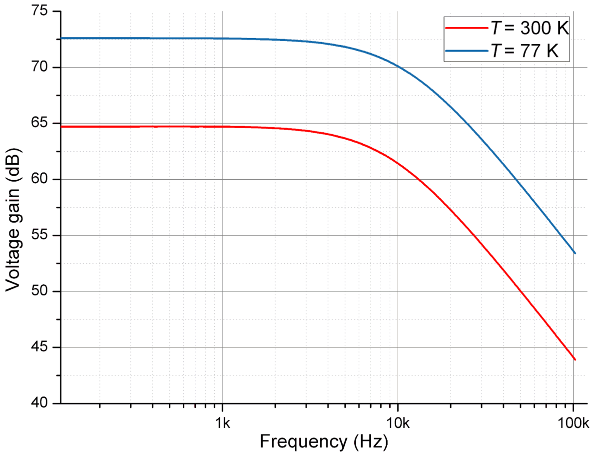

Figure 2: The gain of the cryogenic differential BJT amplifier depending on the frequency at 77 and 300 K.

The noise parameters of the amplifiers were measured using a standard measurement procedure. Both inputs of the amplifier were shorted to the ground and the total voltage noise spectral density was measured. The self voltage noise of the SA was previously characterized and it did not exceed 12 nV/$\sqrt{\text{Hz}}$. The measured total noise was defined only by the amplifiers since the voltage gain was more than 3000 for both designs. The voltage noise spectral density related to the input as a function of the frequency is presented in Figure 3. The minimum obtained noise was measured at 77 K and corresponded to 0.55 nV/$\sqrt{\text{Hz}}$. The important parameter for a low-frequency application is the value of the 1/*f* flicker noise frequency. It corresponds to 5 and 20 Hz (Figure 3).

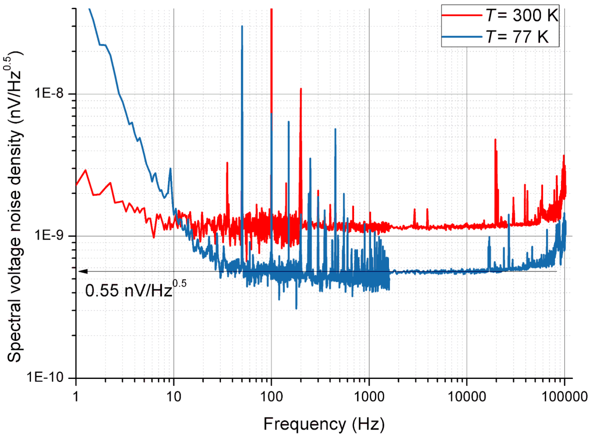

Figure 3: The voltage noise spectral density of the cryogenic differential BJT amplifier as a fucntion of the frequency at 77 and 300 K.

The second amplifier with a parallel design of SSM2210 transistors (see Figure 1) was conceived to reduce the voltage noise. It was measured at three different temperatures, i.e., 300, 77, and 48 K. In order to measure the amplifier at 48 K we used the uppermost stage of the He cryostat with He-7 sorption unit. The amplifier was fixed to the cooling plate with brass screws to have good thermal anchoring. The signal lines were connected to the cryostat CuBe coaxial cables. The amplifier gain curves measured at three temperatures are presented in Figure 4. The maximum gain of the amplifier was 75 dB, obtained at 77 K. The bandwidth of this amplifier ranged from DC to 17 kHz.

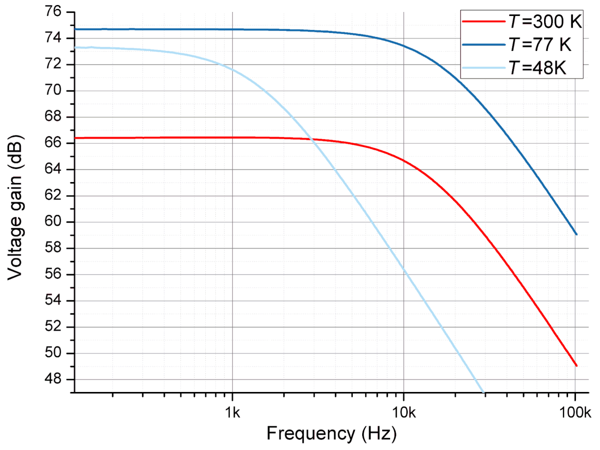

Figure 4: The gain of the cryogenic differential two-stage BJT amplifier as a function of the frequency at three different temperatures.

The voltage noise spectral density related to the input as a function of the frequency for three different temperatures is presented in Figure 5. The minimum obtained noise was measured at 77 K and corresponded to 0.33 nV/$\sqrt{\text{Hz}}$. The 1/*f* flicker noise corner frequency corresponded to 5, 20, and about 100 Hz for the different temperatures (Figure 5).

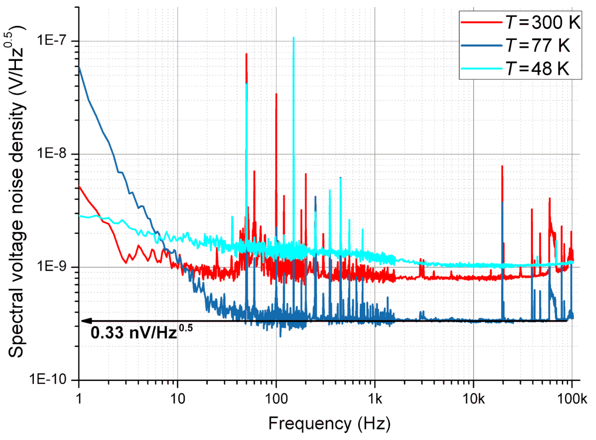

Figure 5: The voltage noise spectral density of the cryogenic differential parallel BJT amplifier as a function of the frequency for three different temperatures. A spurious interference at 50 Hz and its harmonics are visible in the spectrum.

We assume that the high level of 1/*f* noise at 48 K was caused by significant current noise due to a carrier freeze-out effect in the transistor base. Such an effect significantly increases the base current of the transistor to hundreds of milliamperes and increases the spread base resistance at our DC working points. Also, the current gain β was drastically decreased down to approximately five. The characteristics at 48 and 77 K differ, e.g., regarding the amplitude of the 50 Hz interference and its harmonics. This is explained by the different experimental conditions. The 77 K experiments were performed in a liquid nitrogen bath with shielded amplifier case and coaxial lines while the 48 K experiments were performed in the cryostat.

Conclusion

We have demonstrated differential cryogenic low-frequency low-noise bipolar junction transistor amplifiers. The amplifiers have a high gain value of more than 60 dB, with a voltage noise spectral density of less than 0.55 nV/$\sqrt{\text{Hz}}$ and a low flicker noise of 20 Hz at 77 K. We have shown experimentally that the parallel differential circuit design allows for a reduction of the voltage noise from 0.55 to 0.33 nV/$\sqrt{\text{Hz}}$. However, the amplifier characteristics were drastically degraded at 50 K. The bandwidth was reduced to 1.5 kHz and the voltage noise spectral density increased to 1 nV/$\sqrt{\text{Hz}}$. This may limit the usage of the amplifiers for some experimental needs. Generally, the amplifier performance is not sufficient to be a replacement of modern low-frequency amplifiers for SQUID or bolometer readouts. Comparing the performance of this amplifier at 77 K with that of the amplifier from [11] at room temperature we can see worse bandwidth, higher 1/*f* corner frequency and approximately the same voltage noise level. Also, the measurements of amplifier current noise were not carried out because the amplifier was biased by high currents.

However, we want to emphasize that our amplifier design was made to demonstrate the potential applicability of BJ transistors for cryogenic application, especially at 50 K. It was not optimized for SQUID or bolometer readouts. Also the type of transistors were chosen to be n-p-n and p-n-p pairs as in [11]. SSM transistors have the same producer, similar technology, and performance and were used to develop room-temperature SQUID readout electronics [16]. Taking into account a comparison of the performance of the two transistor types SSM and MAT, we are confident that the amplifier performance can be significantly improved. The amplifiers are easy to mount to most of the measurement setups since they have a SMA termination. Unfortunately, modern cryostats for low-temperature experiments do not have a cooling temperature stage corresponding to 77 K. Hence, the designed amplifiers are most applicable for the working temperature of liquid nitrogen, which is the main working temperature for high-temperature superconducting sensors and semiconductor detectors [19,20].

Acknowledgements

The authors thank E. Il'ichev for valuable discussions.

Funding

The research leading to these results has received funding from the Ministry of Science and Higher Education of the Russian Federation through the project number FSUN-2020-0007.

ORCID® iDs

Ilya L. Novikov - https://orcid.org/0000-0001-6328-9911
Boris I. Ivanov - https://orcid.org/0000-0003-3410-349X
Aleksey G. Vostretsov - https://orcid.org/0000-0002-4753-4304

References

1. Schmidt, M.; von Helversen, M.; López, M.; Gericke, F.; Schlottmann, E.; Heindel, T.; Kück, S.; Reitzenstein, S.; Beyer, J. *J. Low Temp. Phys.* **2018,** *193,* 1243–1250. doi:10.1007/s10909-018-1932-1
2. Yohannes, D.; Kirichenko, A.; Sarwana, S.; Tolpygo, S. K. *IEEE Trans. Appl. Supercond.* **2007,** *17,* 181–186. doi:10.1109/tasc.2007.897399
3. Roddatis, V. V.; Hübner, U.; Ivanov, B. I.; Il'ichev, E.; Meyer, H.-G.; Koval'chuk, M. V.; Vasiliev, A. L. *J. Appl. Phys.* **2011,** *110,* 123903. doi:10.1063/1.3670003
4. Wadefalk, N.; Mellberg, A.; Angelov, I.; Barsky, M. E.; Bui, S.; Choumas, E.; Grundbacher, R. W.; Kollberg, E. L.; Lai, R.; Rorsman, N.; Starski, P.; Stenarson, J.; Streit, D. C.; Zirath, H. *IEEE Trans. Microwave Theory Tech.* **2003,** *51,* 1705–1711. doi:10.1109/tmtt.2003.812570
5. Oukhanski, N.; Grajcar, M.; Il'ichev, E.; Meyer, H.-G. *Rev. Sci. Instrum.* **2003,** *74,* 1145–1146. doi:10.1063/1.1532539
6. Weinreb, S.; Bardin, J.; Mani, H.; Jones, G. *Rev. Sci. Instrum.* **2009,** *80,* 044702. doi:10.1063/1.3103939
7. Aja, B.; Schuster, K.; Schäfer, F.; Gallego, J. D.; Chartier, S.; Seelmann-Eggebert, M.; Kallfass, I.; Leuther, A.; Massler, H.; Schlechtweg, M.; Diez, C.; López-Fernandez, I.; Lenz, S.; Türk, S. *IEEE Microwave Wireless Compon. Lett.* **2011,** *21,* 613–615. doi:10.1109/lmwc.2011.2167502
8. Montazeri, S.; Grimes, P. K.; Tong, C.-Y. E.; Bardin, J. C. *IEEE Trans. Terahertz Sci. Technol.* **2016,** *6,* 133–140. doi:10.1109/tthz.2015.2498041
9. Ivanov, B. I.; Trgala, M.; Grajcar, M.; Il'ichev, E.; Meyer, H.-G. *Rev. Sci. Instrum.* **2011,** *82,* 104705. doi:10.1063/1.3655448
10. Ivanov, B. I.; Grajcar, M.; Novikov, I. L.; Vostretsov, A. G.; Il'ichev, E. *Tech. Phys. Lett.* **2016,** *42,* 380–383. doi:10.1134/s1063785016040076
11. Oukhanski, N.; Stolz, R.; Zakosarenko, V.; Meyer, H.-G. *Phys. C (Amsterdam, Neth.)* **2002,** *368,* 166–170. doi:10.1016/s0921-4534(01)01160-1
12. Oukhanski, N.; Stolz, R.; Meyer, H.-G. *J. Phys.: Conf. Ser.* **2006,** *43,* 1270–1273. doi:10.1088/1742-6596/43/1/310
13. Gordeeva, A. V.; Zbrozhek, V. O.; Pankratov, A. L.; Revin, L. S.; Shamporov, V. A.; Gunbina, A. A.; Kuzmin, L. S. *Appl. Phys. Lett.* **2017,** *110,* 162603. doi:10.1063/1.4982031
14. Dumke, W. P. *IEEE Trans. Electron Devices* **1981,** *28,* 494–500. doi:10.1109/t-ed.1981.20372
15. Cressler, J. D. *Cryogenics* **1990,** *30,* 1036–1047. doi:10.1016/0011-2275(90)90204-p
16. Drung, D. *Rev. Sci. Instrum.* **1997,** *68,* 4066–4074. doi:10.1063/1.1148348
17. Drung, D.; Hinnrichs, C.; Barthelmess, H.-J. *Supercond. Sci. Technol.* **2006,** *19,* S235–S241. doi:10.1088/0953-2048/19/5/s15
18. Zhao, J.; Zhang, Y.; Lee, Y.-H.; Krause, H.-J. *Rev. Sci. Instrum.* **2014,** *85,* 054707. doi:10.1063/1.4878342
19. Greenberg, Y. S.; Novikov, I. L.; Schultze, V.; Meyer, H.-G. *Eur. Phys. J. B* **2005,** *44,* 57–62. doi:10.1140/epjb/e2005-00099-1
20. Novikov, I. L.; Greenberg, Y. S.; Schultze, V.; Ijsselsteijn, R.; Meyer, H.-G. *Phys. C (Amsterdam, Neth.)* **2009,** *469,* 30–38. doi:10.1016/j.physc.2008.10.007

License and Terms

The definitive version of this article is the electronic one which can be found at:
https://doi.org/10.3762/bjnano.11.115

BEILSTEIN JOURNAL OF NANOTECHNOLOGY

Controlling the proximity effect in a Co/Nb multilayer: the properties of electronic transport

Sergey Bakurskiy[1], Mikhail Kupriyanov[1], Nikolay V. Klenov*[1,2,3], Igor Soloviev[1,4], Andrey Schegolev[2,3], Roman Morari[5,6], Yury Khaydukov[1,7] and Anatoli S. Sidorenko[6,8]

Full Research Paper

Open Access

Address:
[1]Lomonosov Moscow State University, Skobeltsyn Institute of Nuclear Physics, Moscow, 119991, Russia, [2]Lomonosov Moscow State University, Physics Department, Moscow, 119991, Russia, [3]Moscow Technical University of Communication and Informatics (MTUCI), 111024 Moscow, Russia, [4]Lobachevsky State University of Nizhny Novgorod, Nizhny Novgorod 603950, Russia, [5]Moscow Institute of Physics and Technology, State University, Dolgoprudny, Moscow Region 141700, Russia, [6]Institute of Electronic Engineering and Nanotechnologies ASM, MD2028 Kishinev, Moldova, [7]Max-Planck-Institut für Festkörperforschung, Heisenbergstraße 1, D-70569 Stuttgart, Germany and [8]Laboratory of Functional Nanostructures, Orel State University named after I.S. Turgenev, 302026, Orel, Russia

Email:
Nikolay V. Klenov* - nvklenov@gmail.com

* Corresponding author

Keywords:
cryogenic computing; spin-valve; superconducting neural network; superconducting spintronics

Beilstein J. Nanotechnol. **2020,** *11,* 1336–1345.
https://doi.org/10.3762/bjnano.11.118

Received: 05 June 2020
Accepted: 07 August 2020
Published: 07 September 2020

This article is part of the thematic issue "Functional nanostructures for electronics, spintronics and sensors".

Associate Editor: J. M. van Ruitenbeek

Abstract

We present both theoretical and experimental investigations of the proximity effect in a stack-like superconductor/ferromagnetic (S/F) superlattice, where ferromagnetic layers with different thicknesses and coercive fields are made of Co. Calculations based on the Usadel equations allow us to find the conditions at which switching from the parallel to the antiparallel alignment of the neighboring F-layers leads to a significant change of the superconducting order parameter in superconductive thin films. We experimentally study the transport properties of a lithographically patterned Nb/Co multilayer. We observe that the resistive transition of the multilayer structure has multiple steps, which we attribute to the transition of individual superconductive layers with the critical temperature, T_c, depending on the local magnetization orientation of the neighboring F-layers. We argue that such superlattices can be used as tunable kinetic inductors designed for artificial neural networks representing the information in a "current domain".

Introduction

Multilayer superconductor/ferromagnetic (S/F) heterostructures can be used for construction of tunable cryoelectronic elements, such as switches, Josephson junctions and inductors [1-8]. Here, we present theoretical and experimental investigations of an S/F "stranded wire" with a controllable proximity effect. The wire is composed of ferromagnetic (F) layers separated by thin superconducting layers, in which the superconducting order parameter is maintained due to the proximity to a thick superconducting bank (S-bank). Switching from the antiparallel (AP) to the parallel (P) alignment of neighboring F1 and F2 layers leads to a significant enhancement of the effective exchange field in this artificial ferromagnet. Previously, the properties of [Co(1.5 nm)/Nb(8 nm)/Co(2.5 nm)/Nb(8 nm)]$_6$ multilayer structures for cryogenic memory applications were studied using polarized neutron scattering and magnetometry techniques [9]. In particular, the parameter regions where the aforementioned switching between the P and AP orientations of the F1 and F2 layers is possible were found experimentally.

In this work, we perform theoretical and experimental analyses of electronic properties of Nb/Co multilayers with different F1 and F2 thicknesses and several stacking periods. It is demonstrated that the magnetization switching results in modulation of superconductivity in the superlattice with a corresponding change in the kinetic inductance of the superconducting parts of the wire core, due to the inverse proximity effect. We argue that this effect facilitates new possibilities for the development of tunable superconducting electronic components. For example, the considered “stranded wire” can be readily applied in a synaptic connection for a superconducting artificial neural network (ANN), where the information is represented in a “current domain” [10-21].

The paper is organized as follows. In the next section, we highlight how the proximity effect modulates hybrid S/F structures (the most interesting of the applications discussed), present the model and methods used in the theoretical research, and discuss the obtained results. In the “Experimental results” section, we analyze the transport measurements of the manufactured samples. At the end, we discuss possible applications of the results for the implementation of superconducting synapses and give a conclusion.

Results

Model and theoretical results

Contrary to traditional semiconductor basic elements (transistors), tunable kinetic inductors (TKIs), as well as nonlinear elements (Josephson junctions), are not fabricated in a substrate. This allows for 3D topology benefits, which are especially important for deep ANNs. The F1/s/F2/s superlattice, in which the thick S-bank acts as the source of induced superconductivity, is the simplest model of the 3D structure. Let us consider the applications that are possible due to the control over the order parameter in thin superconductor layers (s-layers) in such a structure.

The simplest cell for the current flow control using the TKI is a splitter. The input current, i_{in}, induced in the input inductance, l_{in}, splits between the two TKI elements. Figure 1b presents the principal scheme of a synaptic element in a superconducting ANN (with TKI elements instead of Josephson junctions, which were used previously [20]).

The synapse modulates the “weight” of an arriving signal, which corresponds to the input current. The transfer function of this current transformer can be described as follows:

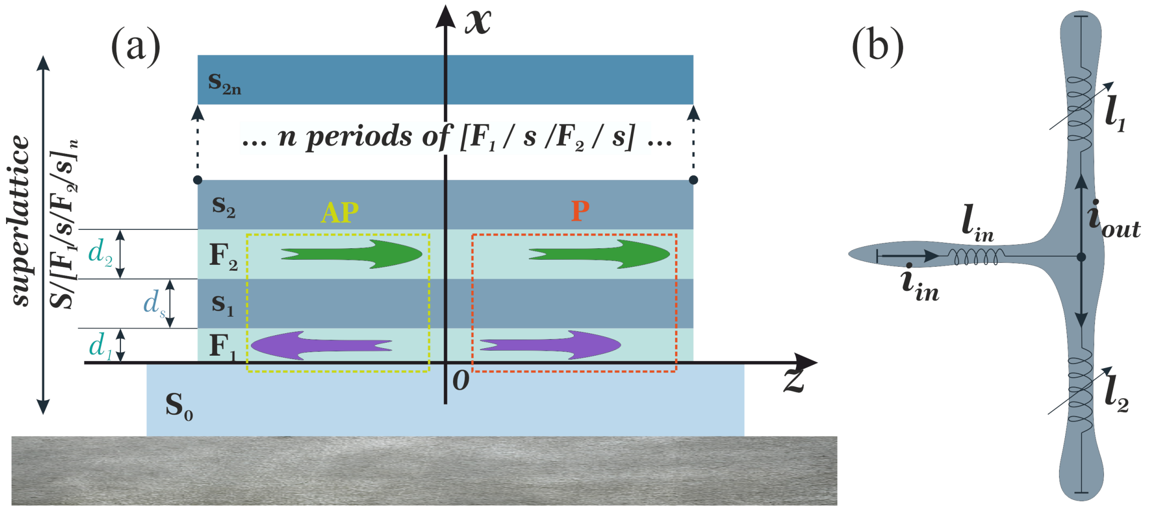

Figure 1: (a) Sketch of the investigated multilayer Co(1.5 nm)/Nb(6 nm)/Co(2.5 nm)/Nb(6 nm) structure. (b) The simplest splitter model based on this TKI.

$$i_{\text{out}} = i_{\text{in}} \cdot \frac{\Delta l}{\Sigma l + 2l_p}, \tag{1}$$

where i_{in} and i_{out} stand for the normalized input/output current, respectively, $\Delta l = l_1 - l_2$ and $\Sigma l = l_1 + l_2$; l_1, l_2 are the normalized inductance values of two TKIs, and l_p is the stray geometric inductance of a splitter branch. For this device to function properly, it is critically important to find conditions in which the kinetic inductance changes significantly due to the controlled proximity effect in the S/F structure.

To test the concept of the magnetically tunable kinetic inductor, we calculated the superconducting order parameter in S/[F1/s/F2/s]_n superlattices, as presented in Figure 1.

We studied the proximity effect and electronic transport in the multilayer hybrid structures in the frame of Usadel equations [22],

$$\begin{gathered}\frac{\pi T_C \xi_p^2}{\tilde{\omega}_p G_m}\frac{\mathrm{d}}{\mathrm{d}x}\left(G_p^2\frac{\mathrm{d}\Phi_p}{\mathrm{d}x}\right) - \Phi_p = -\Delta_p, G_\omega = \frac{\tilde{\omega}}{\sqrt{\tilde{\omega}^2 + \Phi_\omega \Phi_{-\omega}^*}} \\ \Delta_p \ln\frac{T}{T_C} + \frac{T}{T_C}\sum_{\omega=-\infty}^{\infty}\left(\frac{\Delta_p}{|\omega|} - \frac{\Phi_p G_p}{\omega}\right) = 0,\end{gathered} \tag{2}$$

using the Kupriyanov–Lukichev boundary conditions [23,24],

$$\pm\gamma_{Bpq}\xi_p G_p \frac{\mathrm{d}}{\mathrm{d}x}\Phi_p = G_q\left(\frac{\tilde{\omega}_p}{\tilde{\omega}_q}\Phi_q - \Phi_p\right), \tag{3}$$

at the S/F interfaces. Here, $G_{p,q}$ and $\Phi_{p,q}$ are normal and anomalous Green's functions, respectively, and $\omega = \pi T(2n + 1)$ is the Matsubara frequency. In addition, $\tilde{\omega} = \omega + iH$, where H is the exchange energy in the F-layer, p and q are indexes that denote the materials, ξp is the coherence length, $\gamma_{Bpq} = R_{BA}/\rho_p\xi_p$ is the interface parameter, in which R_{BA} is the resistance per square of the interface, and ρ_p is the resistivity of the material at the p-side of the boundary. Note that the boundary conditions at the S/F interface are written from both sides, leading to two independent parameters, γ_{BSF} and γ_{BFS}. The ratio between these parameters, $\gamma = \rho_S\xi_S/\rho_F\xi_F$, is a suitable parameter to understand the physics of the system, since it depends only on the material properties.

In our calculations we put the origin of the x axis at the free interface of the bulk semiconductor electrode, with thickness $L_S = 10\xi_S$. In addition, we considered the proximity effect of an artificial ferromagnetic material (AFM), consisting of alternating thin superconducting ($L_S = 1\xi_S$) and ferromagnetic layers, with an exchange energy of $H = 10T_C$. In an AFM, every odd-numbered ferromagnetic layer has a thickness of $L_{F1} = 0.15\xi_S$, while every even-numbered ferromagnetic layer has a thickness of $L_{F2} = 0.1\xi_S$. We assume that the diffusive coherence length of the superconducting and ferromagnetic materials are the same; however, the relative resistivity values can differ. The numerical solution of the boundary problem (Equation 2, Equation 3) provides the required spatial distribution of the pair potential, $\Delta(x)$, as well as the anomalous, $\Phi(x)$, and normal, $G(x)$, Green's functions at a given temperature.

We found that the behavior of the system significantly depends on the relative resistivity values and coherence lengths of a chosen material. When the ferromagnetic metal and the superconductor have the same resistivity and diffusion coefficients (i.e., for $\gamma = 1$), the pair potential in the whole structure grows evenly with the temperature decrease (Figure 2a). The main source of the superconductivity is the bulk semiconductor layer, while the thin s-layers only slightly support the pairing amplitude coming from the source. Figure 2b shows the spatial distributions of the anomalous Green's function

$$F_\omega = \frac{\Phi_\omega}{\sqrt{\tilde{\omega}^2 + \Phi_\omega \Phi_{-\omega}^*}}$$

at the first ($n = 0$) Matsubara frequency, $F_1(x)$, for parallel (solid lines) and antiparallel (dashed lines) magnetization orientations at low, $T = 0.25T_C$ (panel b), and high, $T = 0.6T_C$ (panel c), temperature values. The real part of $F_1(x)$ decreases inside the AFM almost exponentially, with a small step-like modulation in thin superconducting layers. In the antiparallel case, the real part of the functions decreases slowly with an increase in x. At the same time, the imaginary part behaves differently for parallel (P) and antiparallel (AP) configurations. In the AP case, the imaginary part oscillates, returning to almost zero after every second layer. In the P case, the imaginary part decreases almost exponentially. However, this decrease is slower than the decrease observed for the real part of the function, increasing the possibility of a 0–π transition.

However, the proximity effect properties are completely different if the resistivity of the superconductor is significantly smaller than that of the ferromagnetic material ($\gamma = 0.1$). In this case, thin s-layers are protected from the superconductivity suppression due to the inverse proximity effect. Moreover, the s/F-multilayer structure acts as an additional source of superconductivity. However, the effective critical temperature of the magnetic superconductor is significantly smaller than of the bulk semiconductor material. This property of the system is demonstrated in Figure 3. Figure 3a presents the temperature

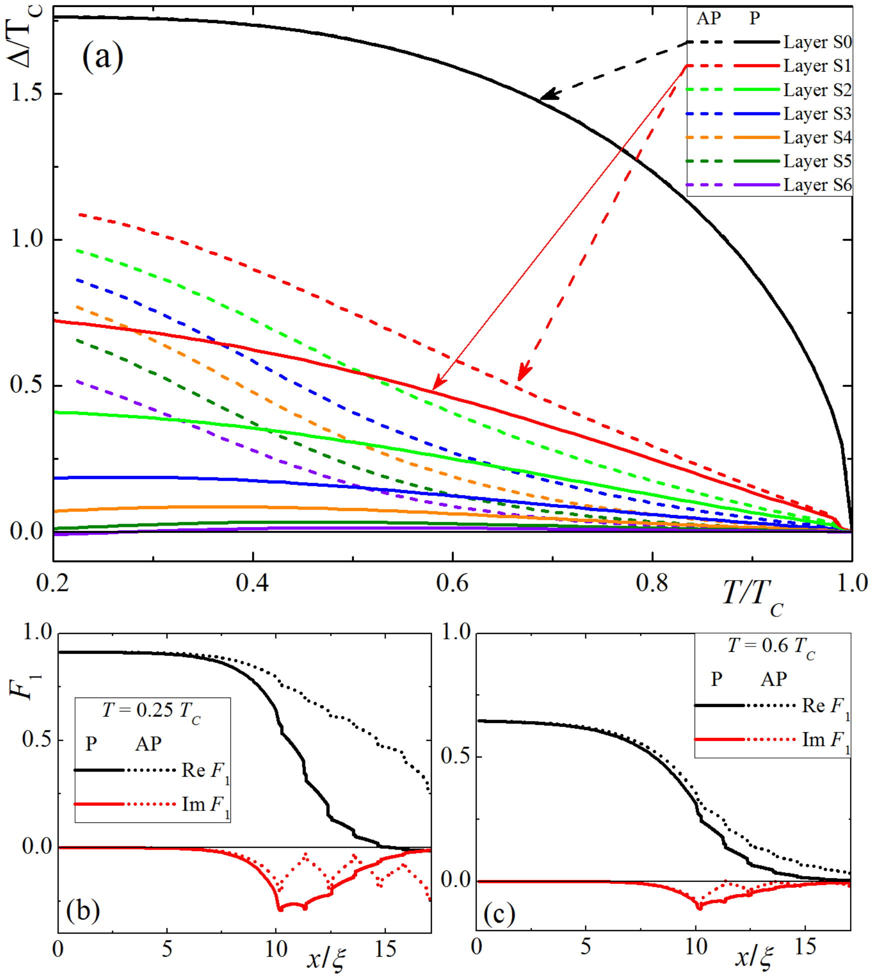

Figure 2: (a) Pair amplitude, Δ, in a S(F1sF2s)$_{x3}$F1 structure in different superconducting layers as a function of temperature, *T*, for parallel (solid lines) and antiparallel (dashed lines) magnetization orientations, considering γ = 1. (b,c) Spatial distributions of the anomalous Green's function, $F_1(x)$, for parallel (solid lines) and antiparallel (dashed lines) magnetization orientations at different temperature values: $T = 0.25T_C$ (b) and $T = 0.6T_C$ (c).

dependence of the pair potential in different superconducting layers for P (solid lines) and AP (dashed) magnetization configurations in F-layers. In the large semiconductor electrode, the temperature dependence of the pair potential coincides with the prediction of the pure Bardeen–Cooper–Schrieffer (BCS) model. At the same time, the pair potential in thin s-layers rapidly increases near the effective critical temperature, $T_C^* \approx 0.5T_C$. It should be noticed that the superconductivity support from the bulk semiconductor source provides a nontrivial shape for Δ(T) in the closest s-layer, with a sharp increase in the pair potential to a constant value in the vicinity of T_C^*. The farther the layer, the weaker the support effect. Deep s-layers that are far from the bulk source are barely influenced by the bulk source and their properties are similar to independent (s/F)$_x$ multilayer structures with sloping Δ(T) dependencies. The spatial distributions of the Green's functions (Figure 3b and Figure 3c) also have step-like shapes. Since the pair potential inside the multilayer structure has a superconducting source independent of the bulk semiconductor layer, the value of the pairing amplitude $F_1(x)$ is almost constant inside every s-layer. However, this value inside each layer is strongly dependent on the distance from the bulk electrode. At temperature values above T_C^*, the spatial distribution has a similar shape, although a significant pairing amplitude appears only in the s-layers closest to the bulk semiconductor electrode. An additional possible consequence of such spatial distribution appears in the screening of F-layers in multilayer structures from an outer magnetic field due to the Meissner effect. The inner F-layers are strongly screened while the opposite is observed for the outer layers. This means that the remagnetization of the layers in an increasing homogeneous external magnetic field do not occur simultaneously, but instead gradually from the outer to the inner layers of the structure.

The calculated distribution of the anomalous Green's function, F, allows for the estimation of the screening properties of the

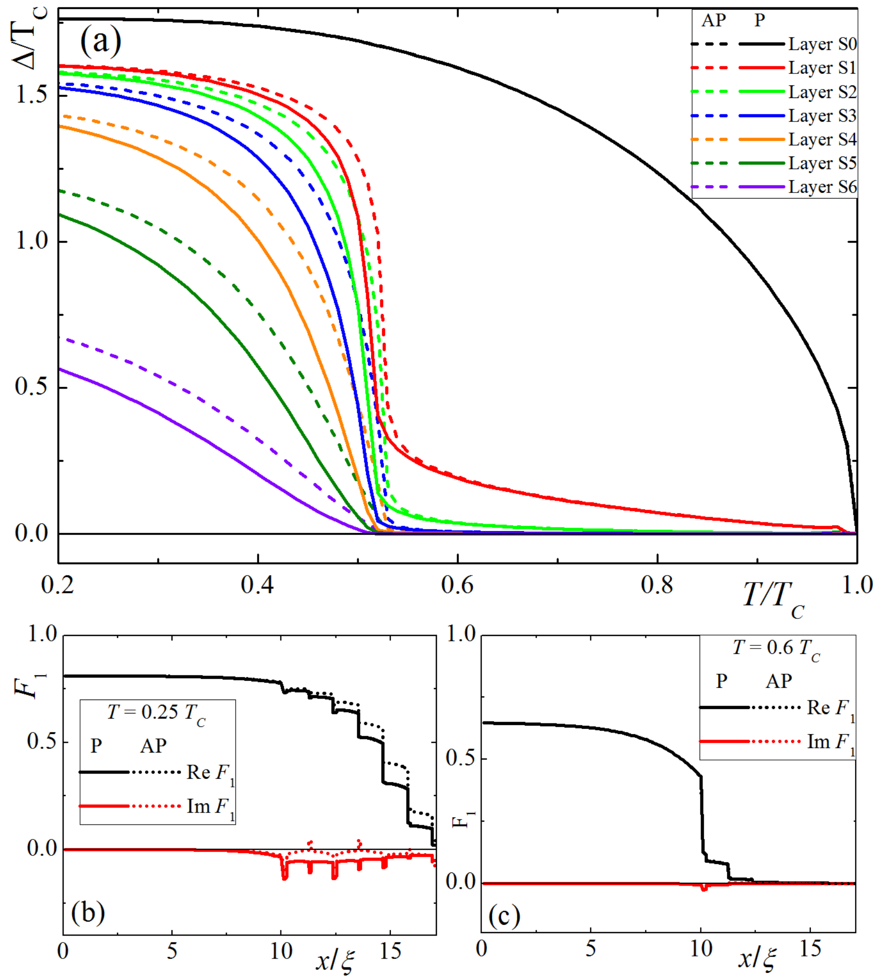

Figure 3: (a) Pair amplitude, Δ, in a S(F1sF2s)$_{x3}$F1 structure in different superconducting layers as a function of temperature, *T*, for parallel (solid lines) and antiparallel (dashed lines) magnetization orientations, considering $\gamma = 0.1$. (b,c) Spatial distributions of the anomalous Green's function, *F*, for parallel (solid lines) and antiparallel (dashed lines) magnetization orientations at different temperature values: $T = 0.4T_C$ (b) and $T = 0.6T_C$ (c).

hybrid structure. The spatial distribution of the screening length directly depends on the proximity of the superconducting order parameter in the system [25], given by

$$\lambda(x)^{-2} = \frac{16\pi T^2}{\rho} \sum_{\omega>0} \mathrm{Re}\left(F(x)^2\right).$$

Hence, the screening length and the kinetic inductance of the considered s-layers are significantly higher in the P case compared to the AP case. This leads to a redistribution of the current flowing along the multilayer structure which increases the total kinetic inductance of the structure [26], according to the following relation

$$L_K \approx \mu_0 \frac{l}{W}\left[\int_0^d \lambda(x)^2 \, \mathrm{d}x\right]^{-1},$$

where *l* is the length of the strip, *W* and *d* are the width and the thickness of the multilayer structure, respectively. It can be concluded that small changes in the temperature or in the applied magnetic field [9] can significantly change (from zero to relatively large values) the kinetic inductance of thin s-layers in the hybrid structures studied in this work.

Experimental results

The next step was to experimentally verify the significant changes, predicted in the model, for the pair potential in thin s-layers of a [Co(1.5 nm)/Nb(8 nm)/Co(2.5 nm)/Nb(8 nm)]$_3$ AFM. For these superlattices, the possibility of switching between the P and AP cases, using a magnetic field with an intensity of ≈30 oersteds, has already been demonstrated [9]. The samples were prepared by using the magnetron sputtering system Leybold Heraeus Z-400 during a single deposition cycle without depressurization of the chamber. Only three targets were used for the structure preparation: niobium (99.95%

purity) was used as a superconducting Cooper pair generator and interlayer separator between two neighboring films of ferromagnetic layers grown using cobalt (99.95% purity). Pure silicon (99.999%) was the third target used to create a passivating layer to prevent structure oxidation. The details regarding the deposition technology were previously described [27].

The structure for the transport measurements was etched under pure argon atmosphere (Ar^+ milling) in a CRYO RIE Alba Nova machine (Stockholm University). The patterned design allowed for a four-point type measurement of six segments of the sample in one cooling cycle (Figure 4). The pair of contacts was applied for setting the current and the pair of microwires was used to test an induced potential difference. Each contact was marked with a letter. Therefore, each measurement was denoted by a pair of letters ("RT","TV", etc.). All the low-temperature measurements performed in this work were done using a cryogen-free magnet system with an insert for the flowing gas.

Figure 4 represents the principle scheme of the measurements performed in this work. This “centipede-like” sample design facilitates the measurements of the electrical resistance values in different synapse-like segments simply by alternating the arms. Before the measurements, the sample was cooled down to 10 K in a zero-field cooling mode and no current was applied. The critical temperature measurements started at 10 K and afterwards a temperature sweeping was performed (R(T) measurements). In addition, and external 1 μA current (AC mode with frequency of 127 Hz) was applied. The temperature change rate was chosen such that a minimal temperature gradient was generated in both downward and upward sweeping directions. Therefore, the resulting shapes of the curves resembled one another but with a slight 0.05 K shift.

In this article, only the measurements performed in three segments were presented since the rest of the measurements showed a similar behavior. In the beginning of the experiment, the resistivity as a function of the temperature was measured without any applied external magnetic field for all the synapse-like segments, immediately after the sample was cooled down. In Figure 5a, the curves of the resistance, R, as a function of the temperature, T, are shown for the case in which there is no magnetic field applied. The results show a similarity to common homogeneous superconductors subjected to the same conditions: a slight change in the resistance is noticed above critical temperature and after that there is a quick decrease to zero in the critical temperature region at 7.3 K. Niobium enters a superconducting state within the entire volume of sample. The uppercase letters indicate a voltmeter contact connection in the principal scheme of the sample (Figure 4b). The current was applied to the opposite arm of the “centipede”. Note that, in the initial state, in which small domains in the Co layers were randomly distributed, resistive transitions (R(T)) at different segments (e.g., “RT” (black circles), “TV” (blue dashed line)), etc.) were similar in shape. The difference in the resistance values can be explained by geometrical factors, such as the shape and width of the segments.

The next series of measurements were carried out under the same conditions. However, for these experiments, the samples were previously submitted to a training protocol, in which they were exposed to an alternating magnetization in the field applied parallel to the layers of the sample at 10 K. The magnetic field ranged from −200 Oe to +200 Oe and, during this process, the electric current was not applied to the sample. After remagnetization, the R(T) behavior significantly changed. For all the segments the superconducting transition started at a lower temperature, T = 7.2 K, and the resistance gradually decreased until T = 6.7 K where it went to zero. Moreover, several

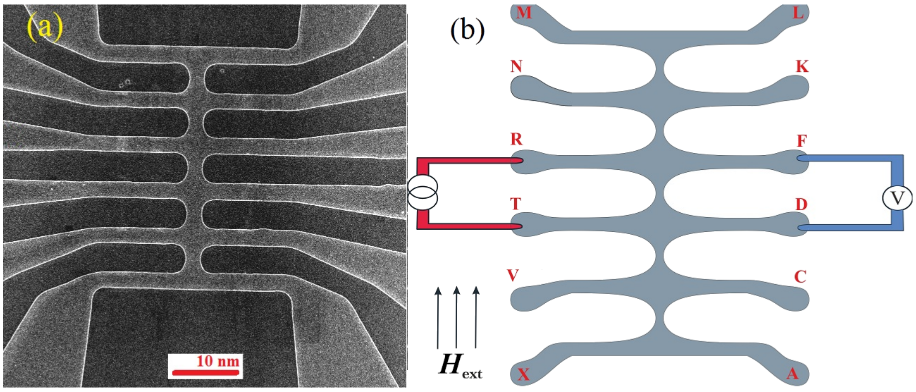

Figure 4: A micrograph (a) and a principal scheme (b) of the structure used for the critical temperature measurements (each contact was marked with a letter).

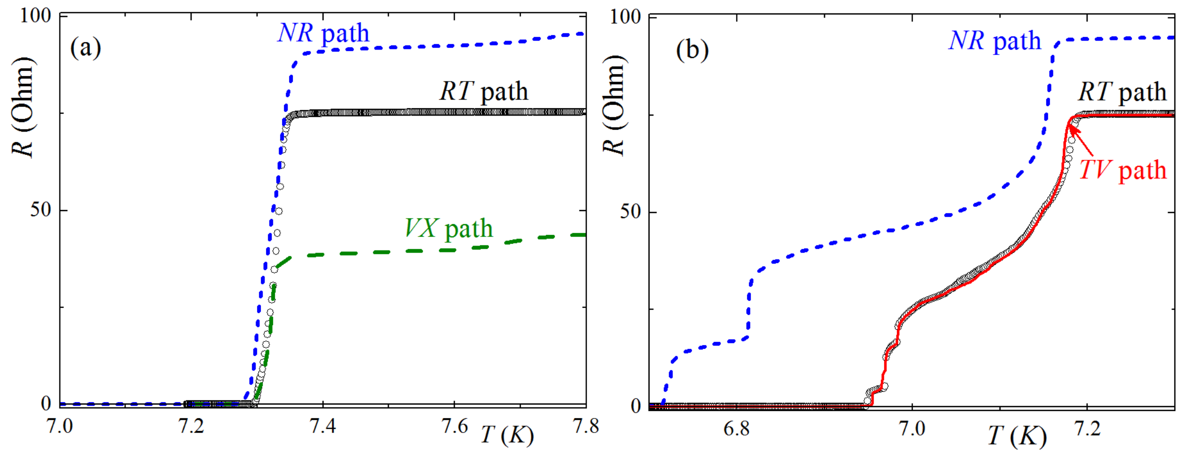

Figure 5: Resistance as a function of the temperature (a) without an initial magnetization of the sample, at a current I = 20 μA, and (b) after remagnetization in the longitudinal direction, at a current I = 1 mkA. Each contact in the “centipede-like” structure was marked with a letter. Therefore, each measurement was denoted by a pair of letters ("RT", "TV", etc.).

distinct steps appeared in the $R(T)$ curves, which we attribute to resistive transitions of individual superconducting layers (or groups of layers) in the multilayer structure. As explained previously in the simulations (Figure 2 and Figure 3), the effective critical temperature of the s-layers within the multilayer structure (i.e., the temperature in which the superconducting order parameter exceeds the value sufficient for carrying the applied transport current) depends on the magnetization orientation in the neighboring F-layers. It is at a maximum for the AP and at a minimum for the P orientation. From Figure 5b one can see that different segments may have a different sequence of steps. For example, the “RT” (black circles) and “TV” (red line) segments have a very similar $R(T)$ curve, with three steps in the temperature range of 6.95 K < T < 7.05 K. Conversely, for the “NR” segment (blue dashed line) the steps have a different shape and expand down to T = 6.7 K. This variation indicates that, although the state of the multilayer structure is not homogeneous across the whole sample, it is homogeneous enough within each segment to cause a significant variation in the effective T_c values of individual layers with minimal values, corresponding to the P state.

Such behavior of $R(T)$ in the vicinity of T = 7.3 K is similar to the behavior of $R(T)$ in the S/N and S/F contacts upon the conversion of the current from normal to a supercurrent. Furthermore, there are several resistance jumps in the temperature region around T = 6.7 K. The actual number of jumps changes for different electrodes (Figure 5b).

The observed variation in the $R(T)$ step-like behavior may also be due to the specific sample geometry (i.e., electrodes with horizontal and vertical orientations, Figure 4a). Due to the shape anisotropy, the “body” of the “centipede” is magnetized along the longitudinal direction, while the arms are perpendicular to the field. This geometry provides different magnetic structures and effective exchange fields for different parts of the structure. Probably the critical temperature of the arms is lower than in the body, providing the injection of a normal current into the body. The conversion process from normal to supercurrent provides the finite voltage, measured in the middle segments. Such measurement also gives some additional information about the properties of the arms. For instance, the dependence between $R(T)$ and the current transport along the “RT” and “TV” (Figure 5b) segments are almost the same. This means that the source of the voltage is in the “T”-electrode, which is the source of the normal quasiparticles, while the “R”- and “V”-arms are in the superconductive state. At the same time, due to the connection between the “N”- and “R”-electrodes, the jumps occur at significantly smaller temperature values, which probably correspond to the resistive state of the “N”-electrode.

The results in Figure 5b reveal the presence of a series of jumps in the $R(T)$ curves. The explanation for why the number of jumps exceeds two in the $R(T)$ curve is beyond the trivial transition of electrodes to the superconducting state. There are two possible reasons for such behavior in this system. The first one is associated with the sequential transition of the thin s-layers in the middle part of the “centipede” that was measured. This mechanism is shown in Figure 3a. In that case, thin s-layers of the middle part of the structure transition, one by one, from a normal to a superconducting state, leading to a step-like change in the conversion rate of the current and to the appearance of steps in the $R(T)$ curve. The steps in the “RT”- and “TV”-segments are suitable for that model, since they are close to each other. At the same time, the middle part of the "centipede", between the connection of the electrodes "R"- and "V"-, stays in the single-domain state of the multilayer structure, while the part between the "N"- and "R"- electrodes stays in the other one.

The second possible explanation is based on the magnetic structure of the connected electrodes. If we assume that the "N"- (or "T"-) electrode consists of two (or three) domains with significantly different mutual magnetization orientation in the F-layers, this can provide different critical temperature values for each domain. Then, the transition of each domain to the superconducting state leads to the decrease in the resistance to the final value at the end of the experiment. This model can explain every jump distribution and how the $R(T)$ curve behavior depends on the "RT"- and "TV"-segments. At the same time, the same model contradicts the presence of a thick S-bank at the bottom part of the electrode, which probably should determine its critical temperature, with a weak dependence on the magnetic state of the multilayer structure. Maybe, due to technical reasons, the S-bank becomes thinner in some arms, providing a stronger dependence of the critical temperature on a mutual magnetization. In the latter, both mechanisms can generate the steps on the $R(T)$ curve.

Discussion

We continued with the theoretical and experimental research on the Co/Nb multilayer structure since the polarized neutron reflectometry and superconducting quantum interference device (SQUID)-magnetometry results have proven that the effective exchange energy can be controlled by applying relatively weak magnetic fields. This time we focused on the "life" of superconductivity (pair potential) in thin s-layers in a changing magnetic environment.

The theoretical studies in the present article showed that it is possible to magnetically change the kinetic inductance of superconducting layers, and even transfer thin layers to a normal state at a fixed temperature.

The experimental results showed that the transition of thin s-layers to the normal state in the multilayer structure is possible. In addition, the temperature of this transition depends on the magnetic environment.

Given the aforementioned results, one can conclude that the electronic transport properties in the multilayer structure $S/[F1/s/F2/s]_n$ can be used to create different switching electronic elements, including synapses. This new type of application will be discussed in more detail.

The creation of artificial neural networks is one of the current trends in the development of superconductor electronics [10-15]. Such an artificial neural network contains layers of elements that nonlinearly transform the incoming signal (neurons), which is connected by linear tunable connections (synapses). There are more than 10^6 synapses in the neural networks that are used in these applications. The energy dissipation at these interconnects is a serious problem, which motivates the search for energy-efficient superconducting solutions in this research field.

In the early 1990s, two-contact interferometers and their modifications, operating in a resistive mode, were used as basic elements (artificial neurons) in a superconducting ANN. In these neurons, the signal level usually corresponded to the average voltage level in the cell. As a result, these ANN schemes were neither fast nor energy efficient. New studies in this area appeared again at the end of the 2000s. This revival was associated with the spike in neural networks, in which the information is presented as a sequence of identical (single-quantum) voltage pulses, and the signal corresponds to a time delay between pulses [10,21]. From a circuitry point of view, such neural networks resemble the rapid single flux quantum (RSFQ) logic devices. Therefore, the development of energy-efficient RSFQ logic devices motivated us to investigate neural networks (and primarily synapses) with an ultra-small energy dissipation. That was done based on adiabatic superconducting logic cells with the presentation of information in the form of magnitudes and directions of currents in the superconducting circuits [17-19].

The main problem in these approaches is the complexity of the practical implementation of an effective synaptic connection: they should be tunable but, at the same time, retain a memory effect. In order to create a synapse, a Josephson contact with a ferromagnetic component in the weak coupling region was recently proposed to adjust the critical current during the functioning of a neural network [20].

In this paper, we propose a way to eliminate completely the Josephson nonlinearity from the synapse circuit. The processes of switching on and off the superconductivity in the thin s-layers, surrounded by magnetic materials, can be used to vary the transmission coefficient of the simplest synapse, shown in Figure 1a. The dependence of the output current of the inductive synapse, i_{out}, with the parasitic inductance, l_p, and the sum of the controlled kinetic inductors of the arms, Σl, is presented below. The configurable dynamic range of the element increases with the difference between the kinetic inductances of the arms and decreases with the rise of the geometric inductance.

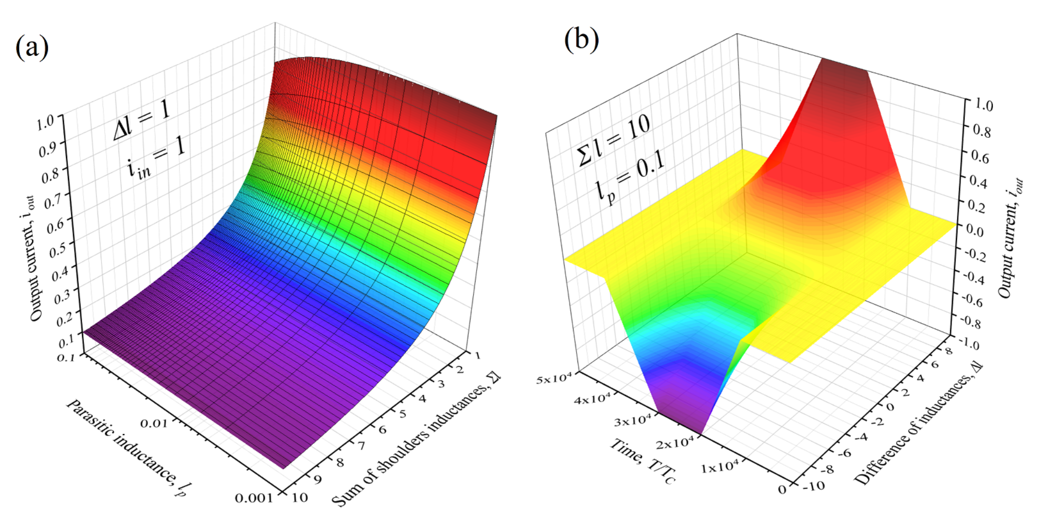

Figure 6: (a) The output current, i_{out}, of the inductive synapse versus the geometric inductance, l_p, and the sum of the controlled kinetic inductors of the arms, Σ*l*. (b) The output current under the action of a single input pulse for different values of the difference between the inductors of the arms, Δ*l*.

Taking into account more complex physical phenomena in the S/F multilayer structure, the future studies aim to increase the functionality of the proposed synapse. With a noncollinear magnetization in the neighboring Co layers, the formation of a long triplet component in a supercurrent is possible in the considered AFM [28-31]. This allows for a significant influence on the magnitude of the order parameter in superconducting layers, controlling the misorientation in the magnetization angles. The triplet superconducting correlations of electrons are formed from singlet correlations. Hence, this effect reduces the kinetic inductance of the s-layers in a quasi-monotonic manner with the magnitude of the controlling magnetic field. This effect enables the construction of a magnetically tunable kinetic inductor for artificial neural networks.

Acknowledgements

We are grateful to Vladimir Krasnov, Olena Kapran, Taras Golod, Vladimir Boian for the sample fabrication and stimulating discussions. A. Schegolev appreciates the support from the Foundation for the Advancement of Theoretical Physics and Mathematics, “BASIS”. The samples were made in IEEN with the analytical support of the group from the Orel State University. The neutron reflectometry technique was performed at the Max-Planck-Institute in Stuttgart. The lithography was made in the Stockholm University.

Funding

We acknowledge the partial financial support from Grant No. 20-69-47013 of the Russian Science Foundation (theoretical approach and calculations). R. Morari is grateful for the support from the Russian Ministry of Education and Science within the program 5top100. A. Sidorenko would like to thank the support from the European Union H2020-WIDESPREAD-05-2017-Twinning program (“SPINTECH” project under the grant agreement Nr. 810144).

ORCID® iDs

Mikhail Kupriyanov - https://orcid.org/0000-0003-1204-9664
Nikolay V. Klenov - https://orcid.org/0000-0001-6265-3670
Andrey Schegolev - https://orcid.org/0000-0002-5381-3297
Anatoli S. Sidorenko - https://orcid.org/0000-0001-7433-4140

Preprint

A non-peer-reviewed version of this article has been previously published as a preprint: https://doi.org/10.3762/bxiv.2020.69.v1

References

1. Baek, B.; Rippard, W. H.; Benz, S. P.; Russek, S. E.; Dresselhaus, P. D. *Nat. Commun.* **2014,** *5,* 3888. doi:10.1038/ncomms4888
2. Alidoust, M.; Halterman, K. *Phys. Rev. B* **2014,** *89,* 195111. doi:10.1103/physrevb.89.195111
3. Gingrich, E. C.; Niedzielski, B. M.; Glick, J. A.; Wang, Y.; Miller, D. L.; Loloee, R.; Pratt, W. P., Jr.; Birge, N. O. *Nat. Phys.* **2016,** *12,* 564–567. doi:10.1038/nphys3681
4. Shafranjuk, S.; Nevirkovets, I. P.; Mukhanov, O. A.; Ketterson, J. B. *Phys. Rev. Appl.* **2016,** *6,* 024018. doi:10.1103/physrevapplied.6.024018
5. Soloviev, I. I.; Klenov, N. V.; Bakurskiy, S. V.; Kupriyanov, M. Y.; Gudkov, A. L.; Sidorenko, A. S. *Beilstein J. Nanotechnol.* **2017,** *8,* 2689–2710. doi:10.3762/bjnano.8.269
6. Shafraniuk, S. E.; Nevirkovets, I. P.; Mukhanov, O. A. *Phys. Rev. Appl.* **2019,** *11,* 064018. doi:10.1103/physrevapplied.11.064018
7. Golod, T.; Kapran, O. M.; Krasnov, V. M. *Phys. Rev. Appl.* **2019,** *11,* 014062. doi:10.1103/physrevapplied.11.014062

8. Satchell, N.; Shepley, P. M.; Algarni, M.; Vaughan, M.; Darwin, E.; Ali, M.; Rosamond, M. C.; Chen, L.; Linfield, E. H.; Hickey, B. J.; Burnell, G. *Appl. Phys. Lett.* **2020,** *116,* 022601. doi:10.1063/1.5140095
9. Klenov, N.; Khaydukov, Y.; Bakurskiy, S.; Morari, R.; Soloviev, I.; Boian, V.; Keller, T.; Kupriyanov, M.; Sidorenko, A.; Keimer, B. *Beilstein J. Nanotechnol.* **2019,** *10,* 833–839. doi:10.3762/bjnano.10.83
10. Schneider, M. L.; Donnelly, C. A.; Russek, S. E. *J. Appl. Phys.* **2018,** *124,* 161102. doi:10.1063/1.5042425
11. Harada, Y.; Goto, E. *IEEE Trans. Magn.* **1991,** *27,* 2863–2866. doi:10.1109/20.133806
12. Hidaka, M.; Akers, L. A. *Supercond. Sci. Technol.* **1991,** *4,* 654–657. doi:10.1088/0953-2048/4/11/027
13. Mizugaki, Y.; Nakajima, K.; Sawada, Y.; Yamashita, T. *Appl. Phys. Lett.* **1993,** *62,* 762–764. doi:10.1063/1.108571
14. Mizugaki, Y.; Nakajima, K.; Sawada, Y.; Yamashita, T. *IEEE Trans. Appl. Supercond.* **1994,** *4,* 1–8. doi:10.1109/77.273058
15. Crotty, P.; Schult, D.; Segall, K. *Phys. Rev. E* **2010,** *82,* 011914. doi:10.1103/physreve.82.011914
16. Chiarello, F.; Carelli, P.; Castellano, M. G.; Torrioli, G. *Supercond. Sci. Technol.* **2013,** *26,* 125009. doi:10.1088/0953-2048/26/12/125009
17. Yamanashi, Y.; Umeda, K.; Yoshikawa, N. *IEEE Trans. Appl. Supercond.* **2013,** *23,* 1701004. doi:10.1109/tasc.2012.2228531
18. Schegolev, A. E.; Klenov, N. V.; Soloviev, I. I.; Tereshonok, M. V. *Beilstein J. Nanotechnol.* **2016,** *7,* 1397–1403. doi:10.3762/bjnano.7.130
19. Klenov, N. V.; Schegolev, A. E.; Soloviev, I. I.; Bakurskiy, S. V.; Tereshonok, M. V. *IEEE Trans. Appl. Supercond.* **2018,** *28,* 1301006. doi:10.1109/tasc.2018.2836903
20. Soloviev, I. I.; Schegolev, A. E.; Klenov, N. V.; Bakurskiy, S. V.; Kupriyanov, M. Y.; Tereshonok, M. V.; Shadrin, A. V.; Stolyarov, V. S.; Golubov, A. A. *J. Appl. Phys.* **2018,** *124,* 152113. doi:10.1063/1.5042147
21. Schneider, M. L.; Donnelly, C. A.; Russek, S. E.; Baek, B.; Pufall, M. R.; Hopkins, P. F.; Dresselhaus, P. D.; Benz, S. P.; Rippard, W. H. *Sci. Adv.* **2018,** *4,* e1701329. doi:10.1126/sciadv.1701329
22. Usadel, K. D. *Phys. Rev. Lett.* **1970,** *25,* 507–509. doi:10.1103/physrevlett.25.507
23. Kuprianov, M. Y.; Lukichev, V. F. *Sov. Phys. - JETP* **1988,** *67,* 1163–1168.
24. Bakurskiy, S. V.; Kupriyanov, M. Y.; Baranov, A. A.; Golubov, A. A.; Klenov, N. V.; Soloviev, I. I. *JETP Lett.* **2015,** *102,* 586–593. doi:10.1134/s0021364015210043
25. Mironov, S.; Mel'nikov, A. S.; Buzdin, A. *Appl. Phys. Lett.* **2018,** *113,* 022601. doi:10.1063/1.5037074
26. Annunziata, A. J. *Single-photon detection, kinetic inductance, and non-equilibrium dynamics in niobium and niobium nitride superconducting nanowires*. Ph.D. Thesis, Yale University, 2010.
27. Morari, R.; Zdravkov, V.; Antropov, E.; Sidorenko, A. *J. Nanoelectron. Optoelectron.* **2012,** *7,* 678–680. doi:10.1166/jno.2012.1417
28. Bergeret, F. S.; Volkov, A. F.; Efetov, K. B. *Phys. Rev. Lett.* **2001,** *86,* 3140–3143. doi:10.1103/physrevlett.86.3140
29. Houzet, M.; Buzdin, A. I. *Phys. Rev. B* **2007,** *76,* 060504. doi:10.1103/physrevb.76.060504
30. Niedzielski, B. M.; Diesch, S. G.; Gingrich, E. C.; Wang, Y.; Loloee, R.; Pratt, W. P., Jr.; Birge, N. O. *IEEE Trans. Appl. Supercond.* **2014,** *24,* 1800307. doi:10.1109/tasc.2014.2311442
31. Zdravkov, V. I.; Lenk, D.; Morari, R.; Ullrich, A.; Obermeier, G.; Müller, C.; Krug von Nidda, H.-A.; Sidorenko, A. S.; Horn, S.; Tidecks, R.; Tagirov, L. R. *Appl. Phys. Lett.* **2013,** *103,* 062604. doi:10.1063/1.4818266

License and Terms

The definitive version of this article is the electronic one which can be found at:
https://doi.org/10.3762/bjnano.11.118

BEILSTEIN JOURNAL OF NANOTECHNOLOGY

Superconductor–insulator transition in capacitively coupled superconducting nanowires

Alex Latyshev[1,2], Andrew G. Semenov[1,3] and Andrei D. Zaikin[*2,4]

Full Research Paper

Open Access

Address:
[1]I.E. Tamm Department of Theoretical Physics, P.N. Lebedev Physical Institute, 119991 Moscow, Russia, [2]National Research University Higher School of Economics, 101000 Moscow, Russia, [3]Department of Physics, Moscow Pedagogical State University, 119435 Moscow, Russia and [4]Institute for Quantum Materials and Technologies, Karlsruhe Institute of Technology (KIT), 76021 Karlsruhe, Germany

Email:
Andrei D. Zaikin* - andrei.zaikin@kit.edu

* Corresponding author

Keywords:
quantum phase slips; quantum phase transitions; RG equations

Beilstein J. Nanotechnol. **2020,** *11,* 1402–1408.
https://doi.org/10.3762/bjnano.11.124

Received: 31 May 2020
Accepted: 27 August 2020
Published: 14 September 2020

This article is part of the thematic issue "Functional nanostructures for electronics, spintronics and sensors".

Guest Editor: A. S. Sidorenko

Abstract

We investigate superconductor–insulator quantum phase transitions in ultrathin capacitively coupled superconducting nanowires with proliferating quantum phase slips. We derive a set of coupled Berezinskii–Kosterlitz–Thouless-like renormalization group equations demonstrating that interaction between quantum phase slips in one of the wires gets modified due to the effect of plasma modes propagating in another wire. As a result, the superconductor–insulator phase transition in each of the wires is controlled not only by its own parameters but also by those of the neighboring wire as well as by mutual capacitance. We argue that superconducting nanowires with properly chosen parameters may turn insulating once they are brought sufficiently close to each other.

Introduction

Quantum fluctuations dominate the physics of superconducting nanowires at sufficiently low temperatures making their behavior markedly different from that of bulk superconductors [1-4]. Many interesting properties of such nanowires are attributed to the effect of quantum phase slips (QPSs) which correspond to fluctuation-induced local temporal suppression of the superconducting order parameter inside the wire accompanied by the phase slippage process and quantum fluctuations of the voltage in the form of pulses. By applying a bias current the symmetry between positive and negative voltage pulses is broken and, as a result, a superconducting nanowire acquires a non-vanishing electrical resistance down to the lowest temperatures [5,6]. This effect was directly observed in a number of experiments [7-10].

Likewise, quantum phase slips in superconducting nanowires yield shot noise of the voltage [11] which originates from the process of quantum tunneling of magnetic flux quanta across the wire. One can also proceed beyond the voltage–voltage correlator and evaluate all cumulants of the voltage operator, thus deriving full counting statistics of quantum phase slips [12]. This theory enables one to obtain a complete description of superconducting fluctuations in such nanowires. Interesting QPS-related effects also occur in superconducting nanorings which can be employed, for example, for possible realization of superconducting qubits [13]. Such effects were investigated theoretically [14] and observed experimentally [15,16].

Each quantum phase slip generates sound-like plasma modes [17] which propagate along the wire and interact with other QPSs. The exchange of such Mooij–Schön plasmons produces a logarithmic interaction in space–time between different QPSs where the magnitude is controlled by the wire diameter (cross section) [5]. For sufficiently thick wires this interaction is strong and the QPSs are bound in close pairs. Accordingly, the (linear) resistance of such wires tends to zero at $T \to 0$, thus demonstrating a superconducting-like behavior in this limit. On the other hand, inter-QPS interaction in ultrathin wires is weak, quantum phase slips are unbound and the superconducting phase fluctuates strongly along the wire. In this case the wire looses long-scale superconducting properties, its total resistance remains non-zero and even tends to increase with decreasing temperature thus indicating an insulating behavior at $T \to 0$. At zero temperature the transition between these two types of behavior comes as a quantum phase transition (QPT) driven by the wire diameter [5]. Below we will also refer to this QPT as a superconductor–insulator transition (SIT).

In this work we will show that this SIT can be substantially modified in a system of capacitively coupled superconducting nanowires even without any direct electrical contact between them. In our previous work [18] we already elucidated some non-local QPS-related effects in such nanowires which yield non-equilibrium voltage fluctuations in the system which exhibit a non-trivial dependence on frequency and bias current. Here we will demonstrate that quantum fluctuations in one of the two wires effectively ”add up” to those of another one, thereby shifting the QPT in each of the wires in a way to increase the parameter range for the insulating phase. Qualitatively the same effect is expected to occur in a single superconducting nanowire that has the form of a meander frequently used in experiments.

Results and Discussion

The model

We first consider the system of two long superconducting nanowires parallel to each other, as schematically shown in Figure 1a.

The wires are described by geometric capacitances C_1 and C_2 (per unit wire length) and kinetic inductances $\mathcal{L}_1$ and $\mathcal{L}_2$ (times length) effectively representing the two transmission lines. Capacitive coupling between these two nanowires is accounted for by the mutual capacitance C_m. The corresponding contribution to the system Hamiltonian that keeps track of both electric and magnetic energies in these coupled transmission lines reads

$$\begin{aligned}\hat{H}_{TL} = \frac{1}{2}\sum_{i,j=1,2}\int \mathrm{d}x \Big(&\mathcal{L}_{ij}^{-1}\hat{\Phi}_i(x)\hat{\Phi}_j(x)\\ &+\left(1/\hat{\Phi}_0^2\right)C_{ij}^{-1}\left(\nabla\hat{\chi}_i(x)\nabla\hat{\chi}_j(x)\right)\Big),\end{aligned} \tag{1}$$

where x is the coordinate along the wires, $\mathcal{L}_{ij}$ and C_{ij} denote the matrix elements of the inductance and capacitance matrices

$$\check{\mathcal{L}} = \begin{bmatrix}\mathcal{L}_1 & 0\\ 0 & \mathcal{L}_2\end{bmatrix},\ \check{C} = \begin{bmatrix}C_1 & C_m\\ C_m & C_2\end{bmatrix} \tag{2}$$

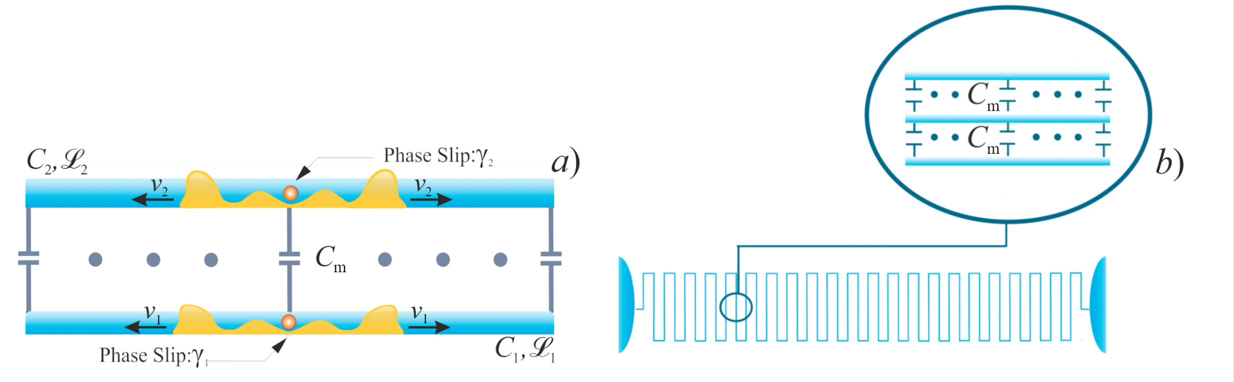

Figure 1: The systems under consideration: a) Two capacitively coupled superconducting nanowires and b) a superconducting nanowire in the form of a meander.

and $\Phi_0 = \pi/e$ is the superconducting flux quantum. Note that for the sake of simplicity here and below we set Planck constant $\hbar$, speed of light, c, and Boltzmann constant, k_B, equal to unity.

The Hamiltonian (Equation 1) is expressed in terms of the dual operators $\hat{\chi}(x)$ and $\hat{\Phi}(x)$[14] which obey the canonical commutation relation

$$\left[\hat{\Phi}(x),\hat{\chi}(x')\right] = -i\Phi_0\delta(x-x') \tag{3}$$

and are related to the charge density and the local phase operators, $\hat{Q}(x)$ and $\hat{\varphi}(x)$, respectively, by means of the following equations

$$\hat{Q}(x) = \frac{1}{\Phi_0}\nabla\hat{\chi}(x), \quad \hat{\varphi} = 2e\int_0^x dx'\hat{\Phi}(x'). \tag{4}$$

Physically, $\hat{\Phi}_i(x)$ represents the magnetic flux operator, while the operator $\hat{\chi}_i(x)$ is proportional to that of the total charge $\hat{q}_i(x)$ that has passed through the point x of the ith wire up to the time moment t, i.e., $\hat{q}_i(x) = -\hat{\chi}_i(x)/\Phi_0$.

Provided that the wires are thick enough, the low energy Hamiltonian in Equation 1 is sufficient. However, for thinner wires, one should also account for the effect of quantum phase slips. The corresponding contribution to the total Hamiltonian for our system can be expressed in the form [14]

$$\hat{H}_{\text{QPS}} = -\sum_{j=1,2}\gamma_j\int dx\cos\left(\hat{\chi}_j(x)\right), \tag{5}$$

where

$$\gamma_j \sim \left(g_{j\xi}\Lambda/\xi\right)\exp\left(-ag_{j\xi}\right), \quad j=1,2 \tag{6}$$

denotes the QPS amplitudes per unit wire length [6], $g_{j\xi} = R_q/R_{j\xi}$ is the dimensionless conductance of the jth wire segment of length equal to the superconducting coherence length ξ (here and below $R_q = 2\pi/e^2 \simeq 25.8$ kΩ is the quantum resistance unit and $R_{j\xi}$ is the normal state resistance of the corresponding wire segment), Δ is the superconducting order parameter and $a \approx 1$ is a numerical prefactor. We also note that the Hamiltonian (Equation 5) describes tunneling of the magnetic flux quantum, Φ_0, across the wire and can be viewed as a linear combination of creation ($e^{i\hat{\chi}_i}$) and annihilation ($e^{-i\hat{\chi}_i}$) operators for the flux quantum Φ_0.

It is obvious from Equation 4 that QPS events cause redistribution of charges inside the wire and generate pairs of voltage pulses moving simultaneously in the opposite direction (cf., Figure 1a)

$$\hat{V}_i(t) = 1/\Phi_0\sum_{j=1,2}C_{ij}^{-1}\left(\nabla\hat{\chi}_j(x_1,t) - \nabla\hat{\chi}_j(x_2,t)\right). \tag{7}$$

Clearly, in the presence of capacitive coupling quantum phase slips in one of the wires also generate voltage pulses in another one.

To summarize the above considerations, the total Hamiltonian for our system is defined as a sum of the two terms in Equation 1 and Equation 5,

$$\hat{H} = \hat{H}_{\text{TL}} + \hat{H}_{\text{QPS}}, \tag{8}$$

representing an effective sine-Gordon model that will be treated below.

Quantum phase transitions: renormalization group analysis

In order to quantitatively describe QPT in coupled superconducting wires we will employ the renormalization group (RG) analysis. This approach is well developed and was successfully applied to a variety of problems in condensed matter theory, such as, the problem of weak Coulomb blockade in tunnel [19-22] and non-tunnel [23-25] barriers between normal metals or that of a dissipative phase transition in resistively shunted Josephson junctions [19,26-28]. In the case of superconducting nanowires QPT was described [5] with the aid of RG equations equivalent to those initially developed for two-dimensional superconducting films [29] which exhibit classical Berezinskii–Kosterlitz–Thouless (BKT) phase transition driven by temperature. In contrast, quantum SIT in quasi-one-dimensional superconducting wires [5] with geometric capacitance C and kinetic inductance $\mathcal{L}$ is controlled by the parameter [5]

$$\lambda = \frac{R_q}{8}\sqrt{\frac{C}{\mathcal{L}}} \tag{9}$$

which is proportional to the square root of the wire cross section, s.

It follows immediately from the analysis of [5] that, provided the two superconducting wires depicted in Figure 1a are decoupled from each other (i.e., for $C_m \to 0$), one should expect two independent QPTs to occur in these two wires respectively at

$\lambda_1 = 2$ and at $\lambda_2 = 2$ where, according to Equation 9, we define $\lambda_{1,2} = \left(R_\mathrm{q}/8\right)\sqrt{C_{1,2}/\mathcal{L}_{1,2}}$. The task at hand is to investigate the effect of capacitive coupling between the wires on these two QPTs.

For this purpose let us express the grand partition function of our system $\mathcal{Z} = \mathrm{Tr}\exp\left(-\hat{H}/T\right)$ in terms of the path integral

$$\mathcal{Z} = \int D\chi_1 \int D\chi_2 \exp\left(-S\left[\chi_1, \chi_2\right]\right), \tag{10}$$

where

$$\begin{aligned} S = {} & \frac{1}{2\Phi_0^2} \sum_{i,j=1,2} \int \mathrm{d}x\mathrm{d}\tau \left(\xi\Delta \mathcal{L}_{ij} \partial_\tau \chi_i \partial_\tau \chi_j + \frac{1}{\xi\Delta} C_{ij}^{-1} \partial_x \chi_i \partial_x \chi_j \right) \\ & - \sum_{i=1,2} y_i \int \mathrm{d}x\mathrm{d}\tau \cos\chi_i \end{aligned} \tag{11}$$

is the effective action corresponding to the Hamiltonian (Equation 8) and

$$y_i = \gamma_i \xi/\Delta \sim g_{j\xi} \exp\left(-a g_{j\xi}\right) \ll 1 \tag{12}$$

denotes the effective fugacity for the gas of quantum phase slips in the ith wire. Note that, having in mind that the QPS core size in x- and τ-directions is respectively $x_0 \sim \xi$ and $\tau_0 \sim \Delta^{-1}$, in Equation 11 for the sake of convenience we rescaled the spatial coordinate in units of x_0, i.e. $x \to x\xi$ and the time coordinate in units of τ_0, i.e. $\tau \to \tau/\Delta$.

In the spirit of Wilson's RG approach we routinely divide the χ-variables into fast and slow components, $\chi_i = \chi_i^f + \chi_i^s$, where

$$\begin{aligned} \chi_i^f(x,\tau) &= \int\limits_{\Lambda < \omega^2 + q^2 < \Lambda + \delta\Lambda} \frac{\mathrm{d}\omega\mathrm{d}q}{2\pi} \chi_{\omega,q} e^{i\omega\tau + iqx}, \\ \chi_i^s(x,\tau) &= \int\limits_{\omega^2 + q^2 < \Lambda} \frac{\mathrm{d}\omega\mathrm{d}q}{2\pi} \chi_{\omega,q} e^{i\omega\tau + iqx}. \end{aligned} \tag{13}$$

Setting $\delta\Lambda/\Lambda \ll 1$, expanding in the fast field components χ_i^f and integrating them out we proceed perturbatively in $y_{1,2}$ and observe that in order to account for the leading order corrections it is necessary to evaluate the matrix Green function at coincident points which reads

$$\begin{aligned} \check{G}^f(0,0) &= \Phi_0^2 \int \frac{\mathrm{d}\omega\mathrm{d}q}{(2\pi)^2} \left(\xi\Delta\check{\mathcal{L}}\omega^2 + \frac{1}{\xi\Delta}\check{C}^{-1}q^2 \right)^{-1} \\ &= 2\left(\delta\Lambda/\Lambda\right)\check{\lambda}, \end{aligned} \tag{14}$$

where $\check{\lambda} = \left(R_\mathrm{q}/8\right)\check{\mathcal{V}}\check{C}$ and $\check{\mathcal{V}} = \left(\check{C}\check{\mathcal{L}}\right)^{-1/2}$ is the velocity matrix for plasmon modes propagating along the wires. The matrix $\check{\lambda}$ has the form

$$\check{\lambda} = \frac{1}{\sqrt{\dfrac{1}{v_1^2} + \dfrac{1}{v_2^2} + \dfrac{2\sqrt{1 - \dfrac{C_\mathrm{m}^2}{C_1 C_2}}}{v_1 v_2}}} \cdot \begin{bmatrix} \lambda_1 \left(\dfrac{1}{v_1} + \dfrac{\sqrt{1 - \dfrac{C_\mathrm{m}^2}{C_1 C_2}}}{v_2} \right) & R_\mathrm{q} C_\mathrm{m}/8 \\ R_\mathrm{q} C_\mathrm{m}/8 & \lambda_2 \left(\dfrac{1}{v_2} + \dfrac{\sqrt{1 - \dfrac{C_\mathrm{m}^2}{C_1 C_2}}}{v_1} \right) \end{bmatrix}, \tag{15}$$

where $v_i = 1/\sqrt{C_i \mathcal{L}_i}$ is the velocity of the Mooij–Schön modes in the ith wire in the absence of capacitive coupling between the wires, i.e. for $C_\mathrm{m} \to 0$.

Following the standard procedure [29] and proceeding to bigger and bigger scales Λ, we eventually arrive at the following RG equations for the QPS fugacities y_1 and y_2:

$$\frac{\mathrm{d}y_i}{\mathrm{d}\log\Lambda} = \left(2 - \lambda_{ii}\right) y_i, \quad i = 1,2, \tag{16}$$

where λ_{11} and λ_{22} are diagonal elements of the matrix $\check{\lambda}$ (Equation 15). Note that here we restrict our RG analysis to the lowest order in $y_{1,2}$ which is sufficient for our purposes. As long as one keeps only the linear $y_{1,2}$ terms in the RG equations, all other parameters of our problem, e.g., λ_{ii}, remain un-renormalized.

As it can be observed from Equation 16, our system exhibits two BKT-like QPTs at $\lambda_{11} = 2$ and $\lambda_{22} = 2$. In the limit $C_\mathrm{m} \to 0$ the wires are independent from each other, $\lambda_{11(22)} \to \lambda_{1(2)}$ and these QPTs obviously reduce to that predicted in [5]. However, for non-zero capacitive coupling between the wires, the two

QPTs occur at the values of $\lambda_{1,2}$ exceeding 2. For the first wire the corresponding phase transition point is fixed by the condition

$$\lambda_1 = 2\frac{\sqrt{1+\frac{v_1^2}{v_2^2}+2\frac{v_1}{v_2}\sqrt{1-\frac{C_\mathrm{m}^2}{C_1C_2}}}}{1+\frac{v_1}{v_2}\sqrt{1-\frac{C_\mathrm{m}^2}{C_1C_2}}}. \qquad (17)$$

The same condition for the second wire is obtained from (Equation 17) by interchanging the indices 1 ↔ 2.

The above results allow us to conclude that in the presence of capacitive coupling SIT in both wires occurs at larger values of $\lambda_{1,2}$ than in the absence of such coupling. In other words, quantum fluctuations in one of these wires effectively decrease the superconducting properties of the other one.

It follows from Equation 17 that the magnitude of such mutual influence depends on the ratio of the plasmon velocities in the two wires v_1/v_2 and on the strength of the capacitive coupling controlled by C_m. Provided the wire cross sections s_1 and s_2 differ strongly the plasmon velocities $v_i \propto \sqrt{s_i}$ also differ considerably. Assume, for instance, that the first wire is much thinner than the second one. In this limit we have $v_1 \ll v_2$ and, hence, the QPT condition (Equation 17) in the first wire remains almost unaffected for any capacitive coupling strength. If, on the contrary, the first wire is much thicker than the second one, then one has $v_1 \gg v_2$ and the condition (Equation 17) reduces to $\lambda_1 \simeq 2/\sqrt{1-C_\mathrm{m}^2/(C_1C_2)}$ demonstrating that the critical value λ_1 can exceed 2 considerably for sufficiently large C_m values.

It is obvious that the strength of capacitive coupling depends on the distance between the wires. At large distances this coupling is negligible $C_\mathrm{m} \to 0$. However, as the wires get closer to each other the value C_m increases and, hence, their mutual influence increases as well. Let us choose the wire parameters in such a way that for $C_\mathrm{m} = 0$ both these wires remain in the superconducting phase being relatively close to SIT. In this case the parameters λ_1 and λ_2 should be just slightly larger than 2. Moving the wires closer to each other we "turn on" the capacitive coupling between them, thus, decreasing both values λ_1 and λ_2 to less than 2. As a result, two superconducting wires become insulating as soon as they are brought sufficiently close to each other. This remarkable physical phenomenon is illustrated by the phase diagram in Figure 2b.

In order to complete this part of our analysis, we point out that transport properties can be investigated in exactly the same manner as was done in [5] in the case of a single nanowire. Generalization of the technique [5] to the case of two capacitively coupled superconducting nanowires is straightforward. For a linear resistance of the ith wire $R_i(T)$ and for $\lambda_{ii} > 2$ (or for any λ_{ii} at sufficiently high temperatures) we obtain

$$R_i(T) \propto \gamma_i^2 T^{2\lambda_{ii}-3}, \quad i = 1,2. \qquad (18)$$

Extension to other geometries

The effects discussed here can be observed in a variety of structures involving superconducting nanowires. For instance, superconducting nanowires in the form of a meander (see Figure 1b) are frequently employed in experiments [30]. In this case different segments of the wire are parallel to each other being close enough to develop electromagnetic coupling. Having in mind the above analysis, one expects that the wire of such a geome-

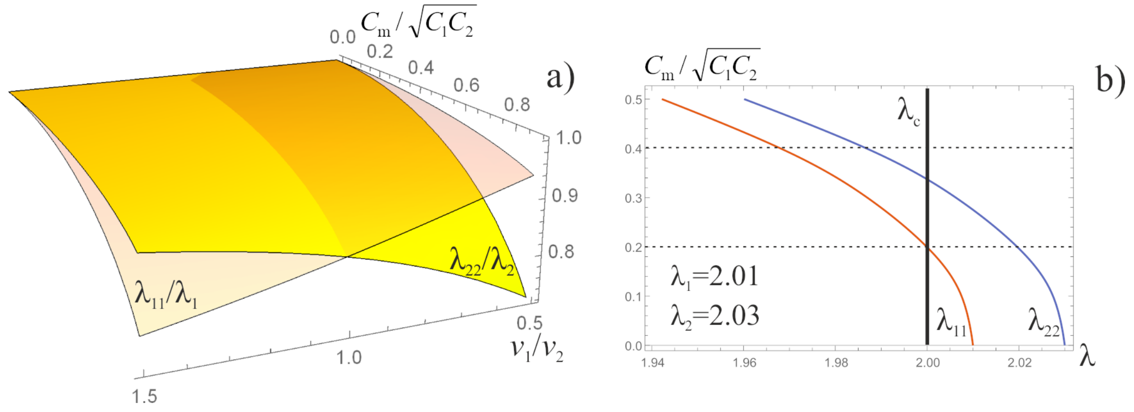

Figure 2: a) Critical surfaces corresponding to SIT at $\lambda_{11} = 2$ and $\lambda_{22} = 2$. b) Phase diagram for two capacitively coupled superconducting nanowires with $\lambda_1 = 2.01$ and $\lambda_2 = 2.03$. Both curves $\lambda_{11}(C_\mathrm{m})$ and $\lambda_{22}(C_\mathrm{m})$ decrease and cross the critical line $\lambda_\mathrm{c} = 2$ with increasing mutual capacitance, C_m.

try would be ”less superconducting” than the same wire that has the form of a straight line.

For illustration, let us mimic the behavior of the wire depicted in Figure 1b by considering three identical capacitively coupled superconducting nanowires parallel to each other. For simplicity we will assume the nearest neighbor interaction, that is, the second (central) nanowire is coupled to both the first and the third nanowires via the mutual capacitance, C_{m}, whereas the latter two are decoupled from each other. We again assume that the wires are thin enough and quantum phase slips may proliferate in each of these wires.

The quantum properties of this system are described by the same effective action (Equation 11) where the inductance and capacitance matrices now take the form

$$\check{\mathcal{L}}=\begin{bmatrix}\mathcal{L} & 0 & 0\\ 0 & \mathcal{L} & 0\\ 0 & 0 & \mathcal{L}\end{bmatrix},\ \check{C}=\begin{bmatrix}C & C_{\mathrm{m}} & 0\\ C_{\mathrm{m}} & C & C_{\mathrm{m}}\\ 0 & C_{\mathrm{m}} & C\end{bmatrix}, \qquad (19)$$

and the summation runs over the indices $i,j = 1,2,3$. Proceeding along the same lines as in the previous section we again arrive at Equation 14, where the diagonal elements of the matrix $\check{\lambda}$ now read

$$\lambda_{22}=\frac{\lambda}{2}\left(\sqrt{1-\sqrt{2}\frac{C_{\mathrm{m}}}{C}}+\sqrt{1+\sqrt{2}\frac{C_{\mathrm{m}}}{C}}\right), \qquad (20)$$

$$\lambda_{11}=\lambda_{33}=\frac{\lambda}{2}\left(1+\frac{1}{2}\left(\sqrt{1-\sqrt{2}\frac{C_{\mathrm{m}}}{C}}+\sqrt{1+\sqrt{2}\frac{C_{\mathrm{m}}}{C}}\right)\right) \qquad (21)$$

and the QPS interaction parameter λ is defined in Equation 9. We again arrive at the RG equations of the form (Equation 16) (now with $i = 1,2,3$). Being combined with Equation 20 and Equation 21 these RG equations demonstrate that in the presence of capacitive coupling SETs occur at $\lambda_{ii} = 2$ implying $\lambda > 2$ for each of the three wires. This observation is fully consistent with our previous results derived for two coupled nanowires.

Furthermore, the RG equation (Equation 16) with $i = 2$ combined with Equation 20 also describes the effect of interacting quantum phase slips and QPTs in the wire having the form of a meander (Figure 1b). In this case, within the approximation of the nearest neighbor, capacitive interaction between the wire segments QPT occurs at

$$\lambda=\frac{4}{\sqrt{1-\sqrt{2}\frac{C_{\mathrm{m}}}{C}}+\sqrt{1+\sqrt{2}\frac{C_{\mathrm{m}}}{C}}}, \qquad (22)$$

that is, the critical value of the parameter λ exceeds 2 as soon as the mutual capacitance C_{m} differs from zero. As it is clear from Equation 20 and Equation 21, the approximation of the nearest neighbor interaction appears to be well justified in the limit $C_{\mathrm{m}} \ll C$. For stronger interactions with $C_{\mathrm{m}} \approx C$ this approximation most likely becomes insufficient for a quantitative analysis. However, on a qualitative level our key observations should hold also in this case: A nanowire in the form of a straight line with λ slightly exceeding the critical value 2 should demonstrate superconducting-like behavior with $R(T) \propto T^{2\lambda-3}$ [5] whereas a wire with exactly the same parameters may turn insulating provided it has the form of a meander with capacitive coupling between its segments.

Conclusion

We have analyzed the effect of quantum fluctuations in capacitively coupled superconducting nanowires. We have demonstrated that plasma modes propagating in one such nanowire play the role of an effective quantum environment for another one, modifying the logarithmic interaction between quantum phase slips in this wire. As a result, the superconductor–insulator quantum phase transition gets shifted in a way to increase the parameter range for the insulating phase. Hence, superconducting nanowires may turn insulating provided they are brought close enough to each other. It would be interesting to observe this effect in forthcoming experiments with superconducting nanowires.

Funding

We acknowledge partial support by RFBR Grant No. 18-02-00586. AGS acknowledges support by the Russian Science Foundation (project No. 19-72-10101).

ORCID® iDs

Alex Latyshev - https://orcid.org/0000-0001-6717-7044
Andrew G. Semenov - https://orcid.org/0000-0002-6992-7862
Andrei D. Zaikin - https://orcid.org/0000-0001-8744-3792

Preprint

A non-peer-reviewed version of this article has been previously published as a preprint: https://doi.org/10.3762/bxiv.2020.65.v1

References

1. Zaikin, A. D.; Golubev, D. S. *Dissipative Quantum Mechanics of Nanostructures: Electron Transport, Fluctuations and Interactions;* Jenny Stanford Publishing: New York, NY, USA, 2019. doi:10.1201/9780429298233

2. Arutyunov, K. Y.; Golubev, D. S.; Zaikin, A. D. *Phys. Rep.* **2008,** *464,* 1–70. doi:10.1016/j.physrep.2008.04.009
3. Larkin, A. I.; Varlamov, A. A. *Theory of fluctuations in superconductors;* Clarendon: Oxford, U.K., 2005.
4. Bezryadin, A. *Superconductivity in Nanowires;* Wiley-VCH: Weinheim, Germany, 2013. doi:10.1002/9783527651931
5. Zaikin, A. D.; Golubev, D. S.; van Otterlo, A.; Zimányi, G. T. *Phys. Rev. Lett.* **1997,** *78,* 1552–1555. doi:10.1103/physrevlett.78.1552
6. Golubev, D. S.; Zaikin, A. D. *Phys. Rev. B* **2001,** *64,* 014504. doi:10.1103/physrevb.64.014504
7. Bezryadin, A.; Lau, C. N.; Tinkham, M. *Nature* **2000,** *404,* 971–974. doi:10.1038/35010060
8. Lau, C. N.; Markovic, N.; Bockrath, M.; Bezryadin, A.; Tinkham, M. *Phys. Rev. Lett.* **2001,** *87,* 217003. doi:10.1103/physrevlett.87.217003
9. Zgirski, M.; Riikonen, K.-P.; Touboltsev, V.; Arutyunov, K. Y. *Phys. Rev. B* **2008,** *77,* 054508. doi:10.1103/physrevb.77.054508
10. Baumans, X. D. A.; Cerbu, D.; Adami, O.-A.; Zharinov, V. S.; Verellen, N.; Papari, G.; Scheerder, J. E.; Zhang, G.; Moshchalkov, V. V.; Silhanek, A. V.; Van de Vondel, J. *Nat. Commun.* **2016,** *7,* 10560. doi:10.1038/ncomms10560
11. Semenov, A. G.; Zaikin, A. D. *Phys. Rev. B* **2016,** *94,* 014512. doi:10.1103/physrevb.94.014512
12. Semenov, A. G.; Zaikin, A. D. *Phys. Rev. B* **2019,** *99,* 094516. doi:10.1103/physrevb.99.094516
13. Mooij, J. E.; Harmans, C. J. P. M. *New J. Phys.* **2005,** *7,* 219. doi:10.1088/1367-2630/7/1/219
14. Semenov, A. G.; Zaikin, A. D. *Phys. Rev. B* **2013,** *88,* 054505. doi:10.1103/physrevb.88.054505
15. Astafiev, O. V.; Ioffe, L. B.; Kafanov, S.; Pashkin, Y. A.; Arutyunov, K. Y.; Shahar, D.; Cohen, O.; Tsai, J. S. *Nature* **2012,** *484,* 355–358. doi:10.1038/nature10930
16. de Graaf, S. E.; Skacel, S. T.; Hönigl-Decrinis, T.; Shaikhaidarov, R.; Rotzinger, H.; Linzen, S.; Ziegler, M.; Hübner, U.; Meyer, H.-G.; Antonov, V.; Il'ichev, E.; Ustinov, A. V.; Tzalenchuk, A. Y.; Astafiev, O. V. *Nat. Phys.* **2018,** *14,* 590–594. doi:10.1038/s41567-018-0097-9
17. Mooij, J. E.; Schön, G. *Phys. Rev. Lett.* **1985,** *55,* 114–117. doi:10.1103/physrevlett.55.114
18. Latyshev, A.; Semenov, A. G.; Zaikin, A. D. *J. Supercond. Novel Magn.* **2020,** *33,* 2329–2334. doi:10.1007/s10948-019-05402-3
19. Schön, G.; Zaikin, A. D. *Phys. Rep.* **1990,** *198,* 237–412. doi:10.1016/0370-1573(90)90156-v
20. Guinea, F.; Schön, G. *Europhys. Lett.* **1986,** *1,* 585–593. doi:10.1209/0295-5075/1/11/007
21. Panyukov, S. V.; Zaikin, A. D. *Phys. Rev. Lett.* **1991,** *67,* 3168–3171. doi:10.1103/physrevlett.67.3168
22. Hofstetter, W.; Zwerger, W. *Phys. Rev. Lett.* **1997,** *78,* 3737–3740. doi:10.1103/physrevlett.78.3737
23. Kindermann, M.; Nazarov, Y. V. *Phys. Rev. Lett.* **2003,** *91,* 136802. doi:10.1103/physrevlett.91.136802
24. Golubev, D. S.; Zaikin, A. D. *Phys. Rev. B* **2004,** *69,* 075318. doi:10.1103/physrevb.69.075318
25. Bagrets, D. A.; Nazarov, Y. V. *Phys. Rev. Lett.* **2005,** *94,* 056801. doi:10.1103/physrevlett.94.056801
26. Schmid, A. *Phys. Rev. Lett.* **1983,** *51,* 1506–1509. doi:10.1103/physrevlett.51.1506
27. Bulgadaev, S. A. *JETP Lett.* **1984,** *39,* 315–319.
28. Guinea, F.; Hakim, V.; Muramatsu, A. *Phys. Rev. Lett.* **1985,** *54,* 263–266. doi:10.1103/physrevlett.54.263
29. Kosterlitz, J. M. *J. Phys. C* **1974,** *7,* 1046–1060. doi:10.1088/0022-3719/7/6/005
30. Delacour, C.; Pannetier, B.; Villegier, J.-C.; Bouchiat, V. *Nano Lett.* **2012,** *12,* 3501–3506. doi:10.1021/nl3010397

License and Terms

BEILSTEIN JOURNAL OF NANOTECHNOLOGY

A wideband cryogenic microwave low-noise amplifier

Boris I. Ivanov[*1], Dmitri I. Volkhin[1], Ilya L. Novikov[1], Dmitri K. Pitsun[1],
Dmitri O. Moskalev[2,3], Ilya A. Rodionov[2,3], Evgeni Il'ichev[1,4] and Aleksey G. Vostretsov[1]

Full Research Paper

Address:
[1]Novosibirsk State Technical University, K.Marx-Av.20, Novosibirsk, 630073, Russia, [2]FMN Laboratory, Bauman Moscow State Technical University, 2-nd Baumanskaya str. 5, Moscow, 105005, Russia, [3]Dukhov Automatics Research Institute, (VNIIA), 22 ul. Sushchevskaya, Moscow, Russia, 127055 and [4]Leibniz Institute of Photonic Technology, PO Box 100239, D-07702 Jena, Germany

Email:
Boris I. Ivanov* - to_ivanov_boris@yahoo.com

* Corresponding author

Keywords:
cryogenic low-noise amplifier; high-electron-mobility transistor (HEMT); HEMT amplifier; microwave cryogenic amplifier; microwave superconducting circuit readout; superconducting qubit readout

Beilstein J. Nanotechnol. **2020,** *11,* 1484–1491.
https://doi.org/10.3762/bjnano.11.131

Received: 30 May 2020
Accepted: 31 August 2020
Published: 30 September 2020

This article is part of the thematic issue "Functional nanostructures for electronics, spintronics and sensors".

Guest Editor: A. S. Sidorenko

Abstract

A broadband low-noise four-stage high-electron-mobility transistor amplifier was designed and characterized in a cryogen-free dilution refrigerator at the 3.8 K temperature stage. The obtained power dissipation of the amplifier is below 20 mW. In the frequency range from 6 to 12 GHz its gain exceeds 30 dB. The equivalent noise temperature of the amplifier is below 6 K for the presented frequency range. The amplifier is applicable for any type of cryogenic microwave measurements. As an example we demonstrate here the characterization of the superconducting X-mon qubit coupled to an on-chip coplanar waveguide resonator.

Introduction

Quantum microwave devices are widely used for different applications ranging from radio astronomy [1-3] to quantum information processing circuits [4]. The latter include the most challenging and attractive topics such as quantum bits (qubits) [5], quantum dots [6], microwave single-photon detectors [7], high-quality resonators [8], superconducting microwave beam splitters [9], and other circuit quantum electrodynamics structures aimed to be used as elements for quantum processors. The experimental study of the abovementioned quantum devices requires precise low-noise readout electronics including low-noise amplifiers [10].

Two main low-noise amplifiers parameters are small equivalent noise temperature (T_n) and relatively high gain (G). The superconducting qubit measurement setup requires particular low-noise amplifiers applicable for cryogenic temperatures. An important point is that cryogenic low-noise amplifiers (cLNAs) are wideband noise sources itself. In the superconducting qubit experimental setup the noise generated from a cLNA is introduced to the sample, which might be crucial for the main qubit parameters, especially for the relaxation time T_1 and coherence time T_2. Therefore, cryogenic microwave isolators are used between the sample and the cLNA.

Most of the modern cryogenic amplifiers operate at temperatures of liquid helium [11-16] and are, usually, placed at the 4 K stage of dilution refrigerators. These amplifiers can be implemented using two modern semiconductor transistor technologies, that is, high-electron-mobility transistor (HEMT) technology, including GaAs and InP, and SiGe heterojunction bipolar technology (HBT). Recently, it has been shown that cryogenic amplifiers based on SiGe HBT [16-18] can provide low noise levels and high gain at 4 K. They are suitable for superconducting qubit readout [25,26] and radio astronomy systems [12,14].

In order to obtain high gain values for *C* (ranging from 4 to 8 GHz) and *X* (ranging from 8 to 12 GHz) frequency bands the number of amplification stages of the HBT cLNA should be increased. This leads to an increase of the total power dissipation in the dilution refrigerator, which makes its operation unstable. In contrast, using modern HEMT technology allows one to implement cryogenic amplifiers with high gain values for a wide frequency range up to tens of gigahertz [11,13,19]. Most of them are based on monolithic microwave integrated circuit (MMIC) technology, which yields outstanding noise parameters in the *C* and *X* frequency bands. However, for some applications a flexible amplifier design is needed. Indeed, there are known schematic realizations of cLNAs based on discrete components [11,17,20-24]. The experimental characteristics of the presented amplifiers show that they do not provide gain values of more than 30 dB in the frequency range from 8 to 12 GHz. The evolving semiconductor technology provides the modern market with state-of-art commercially available transistors to substitute old types. A new type of commercially available transistors was used for the cLNA presented in this paper. A realization of a microwave frequency cLNA design, based on commercially available HEMT transistors, requires accurate and precise matching and an appropriate selection of passive components for liquid-helium temperatures.

In this paper we show that an accurate microwave matching circuit design based on commercially available transistors yields low-cost stable cryogenic low-noise amplifiers with a frequency range up to 12 GHz. The implemented cLNA has the following parameters: a gain value of more than 30 dB for a frequency range from 6 to 12 GHz and an equivalent noise temperature below 6 K. The cLNA has 50 Ω input and output terminations and can be installed in a microwave measurement setup at the 4 K stage of modern dilution refrigerators. The implemented amplifier was tested by superconducting X-mon qubit measurements. In order to measure the X-mon qubit parameters the standard low signal power one microwave tone [25,26] and two microwave tone [27] spectroscopy experiments were performed.

Results and Discussion

Cryogenic four-stage low-noise amplifier design

The amplifier design was optimized for low noise, adequate gain, and appropriate output matching at cryogenic temperatures. The latter is important for better matching with room-temperature amplifiers. CE3512K2 GaAs pseudomorphic HEMT transistors made by CEL were used. The transistors were selected with regard to the two following parameters: minimum noise figure (NF) of 0.3 dB and minimum required value of associated gain of 12 dB at a frequency of 12 GHz. The design was optimized for the frequency range from 6 to 12 GHz, which fits to most of modern qubit measurement setups. We used the available S-parameters of the transistor for the matching circuit design. From a circuit simulation with ideal components a minimal gain value of more than 36 dB at 300 K in the frequency range from 6 to 12 GHz was obtained. For the next step we used the real S-parameters of passive circuit components placed on a dielectric substrate. High-frequency edged trimmed block resistors with a 0402 package size from Vishay company were used in drain and gate biasing lines. The appropriate selection of the resistors in cryogenics is a crucial point in amplifier implementation. We should mention that the first stage of the amplifier does not have a gate resistor in its circuit. One of the reasons is a noise reduction, which is introduced to the input circuit of the amplifier. For increasing the circuit stability around 10 GHz and better matching, 10 Ω gate resistors were used for the second and the fourth stage. Multilayer ceramic capacitors with C0G dielectric material in a 0402 package were used. Murata ceramic core coils with 0201 SMD package size and a self-resonance frequency of about 20 GHz were used for gate and drain power supply circuits. All passive components, for example, microwave capacitors, coils, and precision resistors were measured before at liquid helium temperature for obtaining the spread of nominal parameters. The amplifier was assembled on a Rogers RO 4350 substrate and the matching circuits were carried out as microstrip lines.

The amplifier was mounted inside a brass box separated into two chambers. Each chamber contains two stages of the amplifier. The separation was made in order to avoid standing waves

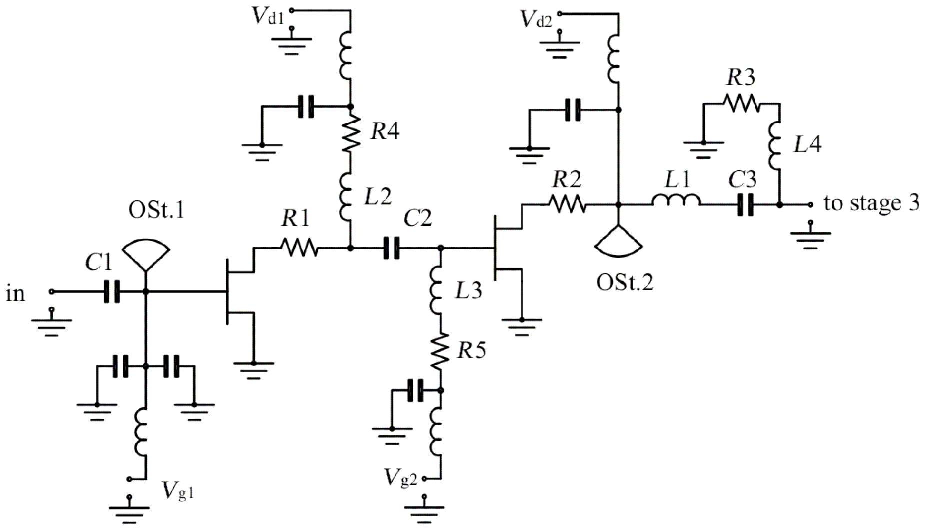

Figure 1: Schematic of the 6–12 GHz cryogenic LNA. The important component values are: C_1 = 0.6 pF, C_2 = 0.3 pF, C_3 = 0.2 pF, L_1 = 0.8 nH, L_2 = 0.8 nH, L_3 = 0.6 nH, L_4 = 3 nH, R_1 = 10 Ω, R_2 = 18 Ω, R_3 = 25 Ω, R_4 = 25 Ω, R_5 = 10 Ω. The capacitors and resistors are realized in 0402 packages and the inductances are realized in a 0201 package (OSt.: open stub lines). The other passive components do not affect to the signal matching and are used for filtering of the bias lines.

and self-resonances in the box in the operation frequency range. We did an electromagnetic simulation of the box and it showed us the absence of self-resonances in a frequency range from 1 to 12 GHz. The substrate was soldered directly to the brass box and SubMiniature version A (SMA) connectors with a specified frequency range up to 12 GHz were soldered directly to the microwave laminate. The feedthrough filters were used as the input biasing electrodes and the power supply cables from a micro-D cryostat connector were soldered directly to them. The first two stages of the amplifier circuit are presented in Figure 1. The third and the fourth stage are identical. One of the key elements in the matching circuits is an open stub line (marked as OSt. in Figure 1) in the gate circuit of the input stage and in the drain circuit of the second and the fourth stage (Figure 2).

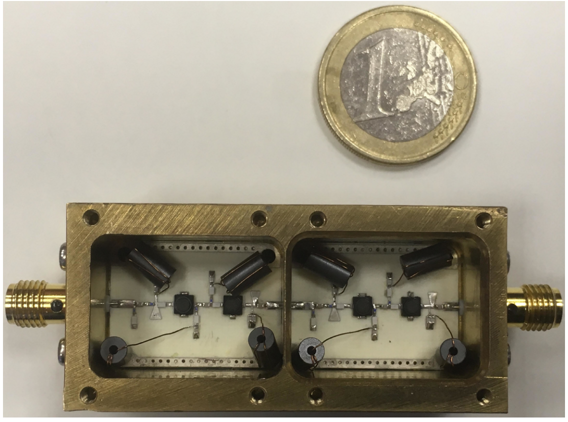

Figure 2: Realization of the cryogenic LNA.

Cryogenic LNA characterization

The measurement system of the amplifier was based on a 10 mK closed-cycle dilution refrigerator where the amplifier was installed and fixed with screws to the copper holder at the 4 K plate. We used standard 2.2 mm CuBe 50 Ω coaxial microwave lines between 4 K stage and room-temperature SMA flange as input and output signal lines installed into the dilution refrigerator for the S-parameter and noise temperature measurements of the amplifier. The simplified measurement scheme is presented in Figure 3. In order to reduce the input signal level, to perform thermal anchoring at each stage, and to prepare the noise measurement setup, cryogenic broadband 10 dB and 20 dB attenuators were installed at the 50 K flange and the 4 K flange, respectively. Moreover, with the described setup we were able to perform gain and noise measurements during one cooldown without rebuilding the measurement scheme and warming up the cryostat. An additional channel with identical microwave coaxial cables and cryogenic attenuators was used for compensating the losses and calibrating the noise temperature. It is marked as satellite line in Figure 3. A short 2.2 mm 50 Ω coaxial cable with SMA termination was used to connect the satellite lines. Gain and noise properties of the amplifier were characterized at the exact temperature of 3.8 K.

We designed and implemented an independent eight-channel power supply unit based on Pb batteries, which allowed us to bias drain and gate circuits of each stage independently. The S-parameters of the designed cLNA and the satellite lines were measured using a vector network analyzer (VNA) in a frequency range from 4 to 13 GHz and with an output signal power

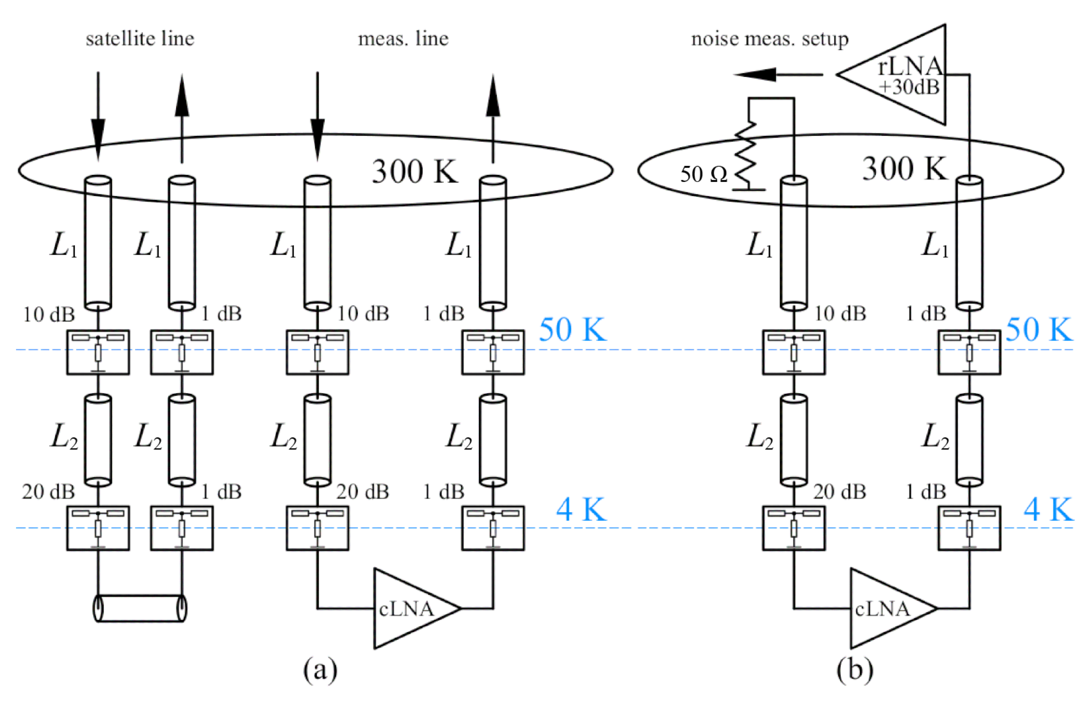

Figure 3: Noise and gain measurement setup. (a) Calibration lines (left-hand side sketch) and gain measurement setup (right-hand side sketch). (b) Noise measurement setup for the cryogenic LNA.

level of −20 dBm. The total power applied to the input of the cLNA was lower than −50 dBm. We performed transmission measurements of the satellite lines and calibrated our measurement setup according to the loss rate. The gain curve is presented in Figure 4. We were not able to measure the reflection coefficients during the cooldown because of the setup features. The output reflection of the cLNA $|S_{22}|$ was measured separately and the reflection level did not exceed −10 dBm for the presented frequency range.

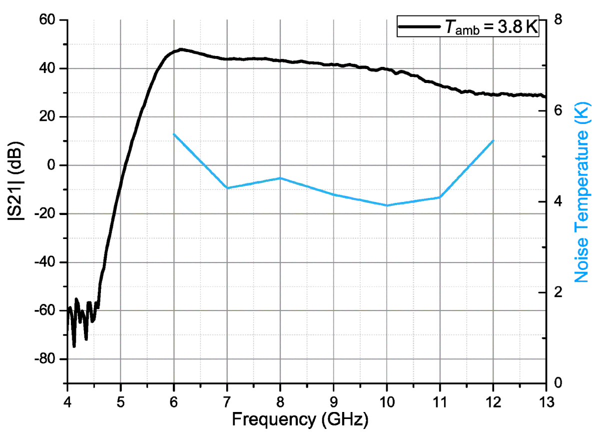

Figure 4: Gain and noise temperature of the cryogenic LNA at the experimental temperature of 3.8 K.

The noise measurement procedure required an approach with higher precision. In this work we estimated the highest equivalent noise temperature level. We used the VNA in the spectrum analyzer mode and measured the power noise density at the output of the setup. In order to increase the sensitivity we applied an additional low-noise broadband room-temperature microwave amplifier (see rLNA in Figure 3a) directly to the 300 K cryostat SMA output flange. The gain G_2 and noise P_2 properties of the rLNA were characterized before by means of a calibrated noise source and the Y-factor procedure [28]. In order to terminate the input line we placed a broadband 50 Ω load at the cryostat microwave input at the 300 K flange SMA connector, see Figure 3b. Using the setup shown in Figure 3b we measured the total noise power density P_{total} in the frequency range from 6 to 12 GHz. It is defined as

$$P_{\text{total}} = P_1 t + P_2 G_2 + P_{\text{VNA}}, \qquad (1)$$

where P_1 is the cLNA input power noise density, $P_2 G_2$ is the output power noise density of the room-temperature low-noise amplifier, P_{VNA} is the spectrum analyzer self-noise, and t is the transmission coefficient from the input of the cLNA to the output of the rLNA. It is defined as

$$t = \frac{G_1 G_2}{L_{\text{out}}}, \qquad (2)$$

where L_{out} is the loss rate of the output line calibrated previously. All variables are in the linear scale. The output line loss coefficient depends linearly on the frequency. First, we obtained the power noise density of the cryogenic LNA with an exception of rLNA noise and VNA noise, $P_1t = P_{total} - P_2G_2 - P_{VNA}$. Then the power noise density related to the input, P_1, was obtained and the equivalent noise temperature was calculated according to the formula

$$T_{Na} = \frac{P_1}{k_B}. \quad (3)$$

The noise curve is presented in Figure 4 and the equivalent noise temperature does not exceed 6 K for the frequency range from 6 to 12 GHz. The minimum noise temperature of 4 K was obtained at 10 GHz. This can be explained by better noise matching at 4 K where the parameters of the passive components are slightly different. The amplifier parameters measured at 3.8 K are summarized in Table 1. The amplifier exhibits low equivalent noise temperature and high gain. Therefore, it is suitable for the superconducting qubit readout.

Table 1: The main parameters of the cryogenic LNA.

G_{min} [dB]	BW [GHz]	max T_{noise} [K]	P_{cons} [mW]	T_{amb} [K]
30	6–12	6	20	3.8

The main parameters in Table 1 were obtained for the optimum working points for each amplifier stage with the following operating drain currents: $I_{d1} = I_{d2} = 3.3$ mA, $I_{d3} = 5.8$ mA, $I_{d4} = 6$ mA. Increasing the drain working currents to 10 mA does not lead to an increase of gain but significantly increases the noise temperature to 15 K with a total power consumption of 73 mW. It is important to note that during the cLNA and qubit measurement experiments the dilution refrigerator was working stable with a constant He_3/He_4 mixture flow rate and with stable temperature values at each cooling stage.

X-mon qubit characterization

The implemented cryogenic LNA is dedicated for measurements in a frequency range from 6 to 12 GHz and it was installed at the 4 K stage of the dilution refrigerator. The sensitivity and measurement speed of the full measurement setup is obviously defined by the signal-to-noise ratio and, thus, by the gain and the noise temperature of the cLNA.

The sample under study contained superconducting X-mon qubits coupled to coplanar quarter wavelength resonators. Each resonator was coupled to a single qubit. The sample was made at the BMSTU Nanofabrication Facility (FMN Laboratory, FMNS REC, ID 74300) using Al technology [29,30]. The X-mon qubit was made of two Al/Al_xO_y/Al parallel Josephson junctions forming a SQUID-type structure coupled to the main ground plane. The standard spectroscopy experiments were carried out using low input signal powers.

The qubit measurement setup is presented in Figure 5 where the designed and implemented amplifier is marked as cLNA. In order to decouple the sample from external noise sources we used two cryogenic circulators (marked as CC1 and CC2 in Figure 3) installed in series at the output of the sample and wideband cryogenic attenuators installed in a microwave input line, see Figure 5. The two circulators placed in series at the 10 mK stage had a direct loss rate of about 4 dB and a return loss rate of about 40 dB in our measurement frequency range. Their main function was to isolate the sample from cLNA noise.

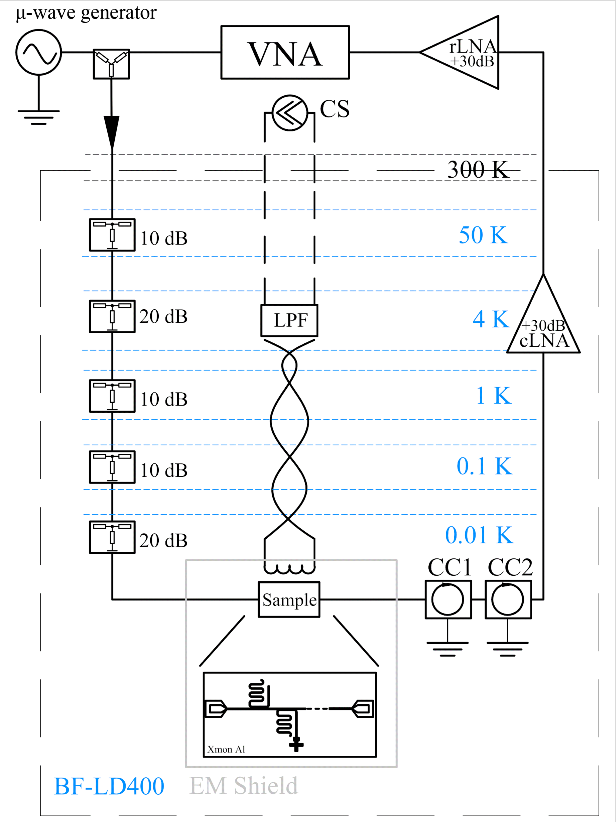

Figure 5: The X-mon qubit measurement setup. The implemented amplifier is marked as cLNA and the room-temperature amplifier is marked as rLNA. CC1 and CC2 are cryogenic circulators with 50 Ω termination (LPF: low-pass filter for the superconducting coil line, CS: high-precision current source). The following setup was installed in a BlueFors BF-LD400 dilution refrigerator.

Wideband cryogenic attenuators (marked as 10 dB and 20 dB) for room-temperature noise suppression and noise suppression of each next following temperature stage were placed according to the scheme in Figure 5. The VNA and a wideband stable microwave sweeping signal generator (marked as “μ-wave” generator in Figure 5) were used for spectroscopy measurements. The standard heterodyne measurement method was used. A superconducting Nb coil was used for tuning the qubit eigenfrequency for each experiment. The coil was biased by means of a highly stable current source (marked as CS in Figure 5). The sample was placed in the copper sample holder with Pb and Mu-metal electromagnetic shields at the 10 mK temperature stage. A two-stage differential low-pass filter (marked as LPF) with 10 kHz bandwidth and wide stopband frequency range was implemented characterized and installed into the measurement system at the 4 K temperature stage of the diluton refrigerator. Since the power level of the measured signal applied to the sample was approximately −120 dBm and the gain of the cryogenic LNA was 30 dB, an additional room-temperature low-noise microwave amplifier (marked as rLNA in Figure 5) was used. It was dedicated to increasing the signal level at the output of cLNA before data acquisition. The rLNA did not influence the signal-to-noise ratio of the measurement system since this parameter is mainly defined by the cLNA output noise. The rLNA noise figure corresponded to 2.1 dB with a gain value of about 40 dB for the frequency range from 6 to 13 GHz.

The transmission $|S_{21}|$ of the sample was measured and the resonance frequencies of resonators were defined in the frequency spectrum from 6 to 9 GHz. We defined a resonator fundamental frequency of f_0 = 7.0554 GHz and experimentally characterized the qubit responce. First, one-tone spectroscopy was carried out. The transmission of a sweeping microwave signal through the sample in a frequency range of 7.05–7.06 GHz for different DC bias currents, producing an external magnetic field, was measured. The obtained curve is shown in Figure 6.

Here, the horizontal axis is a sweeping DC magnetic field in current values, the vertical axis is the sweeping frequency of a probing microwave signal and the color intensity graph shows the normalized transmission amplitude $|S_{21}|$ in units of dB, where 0 corresponds to a normalized maximum transmission. Due to the magnetic flux quantization the qubit characteristic has periodic behavior. The maximum shift of the resonance frequency corresponds to a so called “sweet spot” and the distance between two sweet spots corresponds to the magnetic flux quantum Φ_0. We would like to mention that the current graph was obtained with 100 Hz of the intermediate frequency VNA filter bandwidth and for our experimental setup only four averages were required. In this sense, the cLNA reduces the measurement time of the experiment, which is especially important for preliminary qubit experiments.

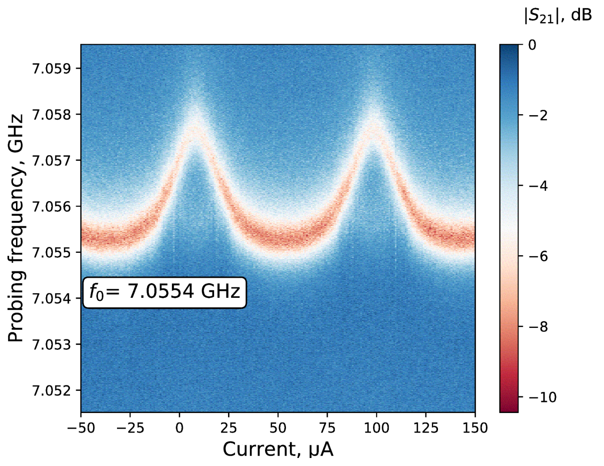

Figure 6: The qubit “sweet spot”. The transmission (color intensity graph with the blue color corresponding to the maximum and the red color corresponding to the minimum) at the resonator resonance frequency depending on the external flux bias for the frequency range from 7.0515 to 7.0595 GHz (vertical axis) and a constant probing power of −120 dBm.

We have performed also a standard two-tone spectroscopy measurement using an additional stable wideband microwave generator, marked as “μ-wave generator” in in Figure 5 and a resistive power combiner. We applied two microwave tones, that is, first a probing signal tone and then sweeping driving signal tones in a frequency range of 6.4–7.1 GHz. The powers applied to the sample after the input line attenuation were −120 dBm for the probing signal tone and −80 dBm for the driving signal tone, respectively. We defined the qubit spectrum depending on the external flux bias and found a minimum qubit energy gap of Δ = 6.625 GHz. The qubit spectrum as a function of the current is shown in Figure 7. Here, the transition $|g\rangle$–$|e\rangle$ is shown.

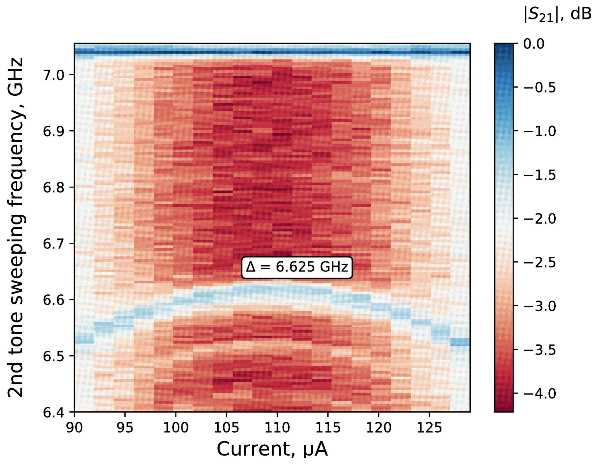

Figure 7: The qubit spectroscopy. The transmission dependence of the probing signal (color intensity graph) on the bias current (horizontal axes) for different values of driving signal frequency in a range from 6.4 to 7.1 GHz (vertical axes).

Conclusion

The characteristics of a low-noise cryogenic microwave amplifier and the measurement of a superconducting X-mon qubit are shown. The amplifier has a gain of more than 30 dB and a noise temperature lower than 6 K and is suitable for any high-sensitivity experiments in the presented frequency range. It is also necessary to mention that, during the qubit measurements with the implemented cLNA, the cryostat operating parameters, that is, the temperature of the stages and the cryostat He_3/He_4 mixture flow rate, were stable. The two-tone qubit spectroscopy experiment shown in this paper required about 48 h of continued measurements with the operating amplifier. The spectrum does not have any artifacts and shows a defined dependence on the external flux. Therefore, we conclude that the main parameters of the amplifier were stable during this time. From the noise curve it is seen that it is possible to achieve a noise temperature of 4 K. This fact can be explained by a better noise matching for this particular cryogenic temperature.

Acknowledgements

The authors thank Ya. S. Greenberg and A. N. Sultanov for valuable discussions.

Funding

The research leading to these results has received funding from the Ministry of Science and Higher Education of the Russian Federation through the project number FSUN-2020-0007.

ORCID® iDs

Boris I. Ivanov - https://orcid.org/0000-0003-3410-349X
Ilya L. Novikov - https://orcid.org/0000-0001-6328-9911
Ilya A. Rodionov - https://orcid.org/0000-0002-8931-5142
Aleksey G. Vostretsov - https://orcid.org/0000-0002-4753-4304

References

1. Hagmann, C.; Kinion, D.; Stoeffl, W.; van Bibber, K.; Daw, E.; Peng, H.; Rosenberg, L. J.; LaVeigne, J.; Sikivie, P.; Sullivan, N. S.; Tanner, D. B.; Nezrick, F.; Turner, M. S.; Moltz, D. M.; Powell, J.; Golubev, N. A. *Phys. Rev. Lett.* **1998,** *80,* 2043–2046. doi:10.1103/physrevlett.80.2043
2. Hoskins, J.; Crisosto, N.; Gleason, J.; Sikivie, P.; Stern, I.; Sullivan, N. S.; Tanner, D. B.; Boutan, C.; Hotz, M.; Khatiwada, R.; Lyapustin, D.; Malagon, A.; Ottens, R.; Rosenberg, L. J.; Rybka, G.; Sloan, J.; Wagner, A.; Will, D.; Carosi, G.; Carter, D.; Duffy, L. D.; Bradley, R.; Clarke, J.; O'Kelley, S.; van Bibber, K.; Daw, E. J. *Phys. Rev. D* **2016,** *94,* 082001. doi:10.1103/physrevd.94.082001
3. Brubaker, B. M.; Zhong, L.; Gurevich, Y. V.; Cahn, S. B.; Lamoreaux, S. K.; Simanovskaia, M.; Root, J. R.; Lewis, S. M.; Al Kenany, S.; Backes, K. M.; Urdinaran, I.; Rapidis, N. M.; Shokair, T. M.; van Bibber, K. A.; Palken, D. A.; Malnou, M.; Kindel, W. F.; Anil, M. A.; Lehnert, K. W.; Carosi, G. *Phys. Rev. Lett.* **2017,** *118,* 061302. doi:10.1103/physrevlett.118.061302
4. Wendin, G. *Rep. Prog. Phys.* **2017,** *80,* 106001. doi:10.1088/1361-6633/aa7e1a
5. Clarke, J.; Wilhelm, F. K. *Nature* **2008,** *453,* 1031–1042. doi:10.1038/nature07128
6. Martin, E. W.; Cundiff, S. T. *Phys. Rev. B* **2018,** *97,* 081301. doi:10.1103/physrevb.97.081301
7. Oelsner, G.; Andersen, C. K.; Rehák, M.; Schmelz, M.; Anders, S.; Grajcar, M.; Hübner, U.; Mølmer, K.; Il'ichev, E. *Phys. Rev. Appl.* **2017,** *7,* 014012. doi:10.1103/physrevapplied.7.014012
8. Macha, P.; van der Ploeg, S. H. W.; Oelsner, G.; Il'ichev, E.; Meyer, H.-G.; Wünsch, S.; Siegel, M. *Appl. Phys. Lett.* **2010,** *96,* 062503. doi:10.1063/1.3309754
9. Neilinger, P.; Oelsner, G.; Grajcar, M.; Ivanov, B. I.; Novikov, I. L.; Il'ichev, E. V. *Tech. Phys. Lett.* **2015,** *41,* 314–316. doi:10.1134/s1063785015040136
10. Il'ichev, E.; Oukhanski, N.; Wagner, T.; Meyer, H.-G.; Smirnov, A. Y.; Grajcar, M.; Izmalkov, A.; Born, D.; Krech, W.; Zagoskin, A. *Low Temp. Phys.* **2004,** *30,* 620–628. doi:10.1063/1.1789933
11. Wadefalk, N.; Mellberg, A.; Angelov, I.; Barsky, M. E.; Bui, S.; Choumas, E.; Grundbacher, R. W.; Kollberg, E. L.; Lai, R.; Rorsman, N.; Starski, P.; Stenarson, J.; Streit, D. C.; Zirath, H. *IEEE Trans. Microwave Theory Tech.* **2003,** *51,* 1705–1711. doi:10.1109/tmtt.2003.812570
12. Weinreb, S.; Bardin, J.; Mani, H.; Jones, G. *Rev. Sci. Instrum.* **2009,** *80,* 044702. doi:10.1063/1.3103939
13. Aja, B.; Schuster, K.; Schafer, F.; Gallego, J. D.; Chartier, S.; Seelmann-Eggebert, M.; Kallfass, I.; Leuther, A.; Massler, H.; Schlechtweg, M.; Diez, C.; Lopez-Fernandez, I.; Lenz, S.; Turk, S. *IEEE Microwave Wireless Compon. Lett.* **2011,** *21,* 613–615. doi:10.1109/lmwc.2011.2167502
14. Montazeri, S.; Grimes, P. K.; Tong, C.-Y. E.; Bardin, J. C. *IEEE Trans. Appl. Supercond.* **2017,** *27,* 1500605. doi:10.1109/tasc.2016.2631441
15. Ivanov, B. I.; Trgala, M.; Grajcar, M.; Il'ichev, E.; Meyer, H.-G. *Rev. Sci. Instrum.* **2011,** *82,* 104705. doi:10.1063/1.3655448
16. Ivanov, B. I.; Grajcar, M.; Novikov, I. L.; Vostretsov, A. G.; Il'ichev, E. *Tech. Phys. Lett.* **2016,** *42,* 380–383. doi:10.1134/s1063785016040076
17. Risacher, C.; Vassilev, V.; Pavolotsky, A.; Belitsky, V. *IEEE Microwave Wireless Compon. Lett.* **2003,** *13,* 262–264. doi:10.1109/lmwc.2003.815182
18. Bardin, J. C.; Weinreb, S. *IEEE Microwave Wireless Compon. Lett.* **2009,** *19,* 407–409. doi:10.1109/lmwc.2009.2020041
19. Cha, E.; Wadefalk, N.; Nilsson, P.-A.; Schleeh, J.; Moschetti, G.; Pourkabirian, A.; Tuzi, S.; Grahn, J. *IEEE Trans. Microwave Theory Tech.* **2018,** *66,* 4860–4869. doi:10.1109/tmtt.2018.2872566
20. Korolev, A. M.; Shnyrkov, V. I.; Shulga, V. M. *Rev. Sci. Instrum.* **2011,** *82,* 016101. doi:10.1063/1.3518974
21. Neilinger, P.; Trgala, M.; Grajcar, M. *Cryogenics* **2012,** *52,* 362–365. doi:10.1016/j.cryogenics.2012.02.006
22. Arakawa, T.; Nishihara, Y.; Maeda, M.; Norimoto, S.; Kobayashi, K. *Appl. Phys. Lett.* **2013,** *103,* 172104. doi:10.1063/1.4826681
23. Tracy, L. A.; Luhman, D. R.; Carr, S. M.; Bishop, N. C.; Ten Eyck, G. A.; Pluym, T.; Wendt, J. R.; Lilly, M. P.; Carroll, M. S. *Appl. Phys. Lett.* **2016,** *108,* 063101. doi:10.1063/1.4941421
24. Oukhanski, N.; Grajcar, M.; Il'ichev, E.; Meyer, H.-G. *Rev. Sci. Instrum.* **2003,** *74,* 1145. doi:10.1063/1.1532539
25. Ivanov, B. I.; Novikov, I. L.; Sultanov, A. N.; Greenberg, Y. S.; Krivetskii, A. V.; Vostretsov, A. G.; Il'ichev, E. *JETP Lett.* **2016,** *103,* 425–430. doi:10.1134/s0021364016060047

26. Novikov, I. L.; Ivanov, B. I.; Sultanov, A. N.; Greenberg, Y. S.; Il'ichev, E. V. *Phys. Solid State* **2016,** *58,* 2155–2159. doi:10.1134/s1063783416110287
27. Oelsner, G.; van der Ploeg, S. H. W.; Macha, P.; Hübner, U.; Born, D.; Anders, S.; Il'ichev, E.; Meyer, H.-G.; Grajcar, M.; Wünsch, S.; Siegel, M.; Omelyanchouk, A. N.; Astafiev, O. *Phys. Rev. B* **2010,** *81,* 172505. doi:10.1103/physrevb.81.172505
28. Y-Factor Method for Noise Figure Measurement Accuracy; Keysight Application Note 57-2. https://www.keysight.com/ru/ru/assets/7018-06829/application-notes/5952-3706.pdf (accessed Aug 28, 2020).
29. Moskalenko, I. N.; Besedin, I. S.; Tsitsilin, I. A.; Mazhorin, G. S.; Abramov, N. N.; Grigor'ev, A.; Rodionov, I. A.; Dobronosova, A. A.; Moskalev, D. O.; Pishchimova, A. A.; Ustinov, A. V. *JETP Lett.* **2019,** *110,* 574–579. doi:10.1134/s0021364019200074
30. Rodionov, I. A.; Baburin, A. S.; Gabidullin, A. R.; Maklakov, S. S.; Peters, S.; Ryzhikov, I. A.; Andriyash, A. V. *Sci. Rep.* **2019,** *9,* 12232. doi:10.1038/s41598-019-48508-3

License and Terms

The definitive version of this article is the electronic one which can be found at:
https://doi.org/10.3762/bjnano.11.131

BEILSTEIN JOURNAL OF NANOTECHNOLOGY

Selective detection of complex gas mixtures using point contacts: concept, method and tools

Alexander P. Pospelov[1], Victor I. Belan[2], Dmytro O. Harbuz[1,2], Volodymyr L. Vakula[2], Lyudmila V. Kamarchuk[3,4], Yuliya V. Volkova[5] and Gennadii V. Kamarchuk[*2]

Full Research Paper

Open Access

Address:
[1]Department of Physical Chemistry, National Technical University "Kharkiv Polytechnic Institute", 2 Kyrpychov Str., Kharkiv, 61002, Ukraine, [2]Department of Spectroscopy of Molecular Systems and Nanostructured Materials, B. Verkin Institute for Low Temperature Physics and Engineering, 47 Nauky Ave., Kharkiv, 61103, Ukraine, [3]Department of Pediatrics and Rehabilitation, SI "Institute for Children and Adolescents Health Care" of NAMS of Ukraine, 52-A Yuvileinyi Ave., Kharkiv, 61153, Ukraine, [4]Department of Pediatrics, V. Karazin Kharkiv National University, 4 Svobody Sq., Kharkiv, 61077, Ukraine and [5]Laboratory of Age Endocrinology and Metabolism, SI "Institute for Children and Adolescents Health Care" of NAMS of Ukraine, 52-A Yuvileinyi Ave., Kharkiv, 61153, Ukraine

Email:
Gennadii V. Kamarchuk[*] - kamarchuk@ilt.kharkov.ua

* Corresponding author

Keywords:
breath profile; cortisol; hormone detection; point contact; quantum sensor; selective detection; serotonin; Yanson point contacts

Beilstein J. Nanotechnol. **2020,** *11,* 1631–1643.
https://doi.org/10.3762/bjnano.11.146

Received: 24 July 2020
Accepted: 09 October 2020
Published: 28 October 2020

This article is part of the thematic issue "Functional nanostructures for electronics, spintronics and sensors".

Guest Editor: A. S. Sidorenko

Abstract

Of all modern nanosensors using the principle of measuring variations in electric conductance, point-contact sensors stand out in having a number of original sensor properties not manifested by their analogues. The nontrivial nature of point-contact sensors is based on the unique properties of Yanson point contacts used as the sensing elements. The quantum properties of Yanson point contacts enable the solution of some of the problems that could not be solved using conventional sensors measuring conductance. In the present paper, we demonstrate this by showing the potential of quantum point-contact sensors to selectively detect components of a gas mixture in real time. To demonstrate the high efficiency of the proposed approach, we analyze the human breath, which is the most complex of the currently known natural gas mixtures with extremely low concentrations of its components. Point-contact sensors allow us to obtain a spectroscopic profile of the mixture. This profile contains information about the complete set of energy interactions occurring in the point contact/breath system when the breath constituents adsorb to and desorb from the surface of the point-contact conduction channel. With this information we can unambiguously characterize the analyzed system, since knowing the energy parameters is key to successfully identifying and modeling the physicochemical properties of various quantum objects. Using the point-contact spectroscopic profile of a complex gas mixture it is possible to get a functional dependence of the concentration of particular breath components on the amplitude of the sensor output signal. To demonstrate the feasibility of the proposed approach, we analyze the point-contact profiles from the breath of several patients and compare them with the concentrations of serotonin and cortisol in the body of each patient. The obtained results demonstrate that the proposed methodology allows one to get an effective calibration function for a non-invasive analysis of the level of serotonin and cortisol in the human body using the point-contact breath test. The present study indicates some necessary prerequisites for the design of fast detection methods using differential sensor analysis in real time, which can be implemented in various areas of science and technology, among which medicine is one of the most important.

Introduction

The functioning of devices comprising low-dimensional structures as basic elements depends on quantum effects, which play a crucial role in the unique properties of nanomaterials [1,2]. In order to achieve the maximum efficiency in using nanostructures, a comprehensive use of the fundamental scientific basis is necessary to open up opportunities for the creation of new devices and technologies. This approach to enlarging the variety of analytical tools includes using Yanson point contacts as the basic element of quantum sensor devices [3,4].

Of all modern nanosensors measuring a variation in electrical conductance, point-contact sensors have a number of unique properties. The nontrivial nature of point-contact sensors is based on the distinctive properties of the Yanson point contacts [4], used as the sensing elements. Spectral studies clearly demonstrate the fundamental difference between Yanson point contacts and traditional electrical contacts. The latter normally behave as bulk conductors of electric current without spectral properties. In contrast, Yanson point contacts display quantum properties that enable the direct measurement of the interaction between electrons and various quasiparticles, such as phonons or magnons [5,6], the observation of the spectral aspects of processes occurring in the superconducting state [7,8], and the extraction of spectral information from the electric noise [9]. Similar advantages arise in sensor studies. In this case, Yanson point contacts are responsible for the unique properties of point-contact sensors, which make them different from the existing analogues. In sensor studies, the quantum properties of Yanson point contacts solve the problems that could not be solved when analogues were used to measure the variation in electrical conductance. This can be exemplified by the new quantum mechanism of selective detection in gaseous and liquid media [10] and by the possibility of real-time detection of carcinogenic strains of *Helicobacter pylori* [11].

The original properties of point-contact sensors significantly contribute to their functionality and lay the foundation for a wide spectrum of new applications and solutions to new complex problems. In the present paper, we demonstrate the unique property of a quantum point-contact sensor to selectively detect components of a gas mixture in real time. The importance of using point-contact sensor devices to solve complex problems is highlighted by, at least, two facts. First, our analyzed medium, the human breath, is the most complex of the currently known natural gas mixtures. Second, the concentrations of the components that are quantitatively related to the detected substances are extremely low in the mixture.

The human breath is a complex biological medium, which contains more than 2000 components [12]. It has been widely studied by using a broad spectrum of techniques [13]. The main goal of these studies is to find peculiarities of the human metabolism that are typical of various diseases and to develop new noninvasive medical diagnostic methods. The functioning of the human body is accompanied by the biosynthesis of specific chemical substances. These substances become part of the exhaled breath and, as such, can be used as markers for breath characterization. Hence, it is important to detect single components of the exhaled breath for medical purposes.

Mass spectrometry, gas chromatography–mass spectrometry, as well as various optical spectroscopy techniques are successfully used to detect substances in the breath [14-20]. Yet, the high costs of the equipment and the need for highly skilled staff to operate and maintain it impede the large-scale implementation of these techniques in daily medical practice. From this point of view, it seems promising to use sensor devices to analyze the breath [21-23]. The main advantage of using sensors is that they are portable, inexpensive, and easy to use [24,25]. Gas sensors can detect breath components in extremely low concentrations and, thereby, they enable the development of medical diagnostic methods based on the concept of marker identification. However, this approach has a significant drawback since the processes happening in complex gaseous media are highly dynamic. Therefore, it negatively impacts the efficacy of medical diagnosis.

In the breath, there is a high possibility of interactions between the components, similarly to any multicomponent medium that contains substances of different chemical nature [26]. These interactions may eventually result in significant changes not only in the concentrations of the original components, but also in the chemical composition of the gas mixture. The breath contains oxidizing agents (e.g., nitrogen oxides, carbon oxide, and sulfur oxides), reducing agents (e.g., hydrogen sulfide, ammonia, mercaptans, and organic molecules), and other chemically active components that can participate in various chemical transformations. It is known, for example, that hydrochloric acid interacts almost instantaneously with ammonia to form NH_4Cl. Therefore, there is a high probability that the composition of the human breath medium is transformed after it is formed in the human body and before it is released in the atmosphere. It should also be noted that the new compounds formed as a result of these interactions can be catalysts for new chemical reactions. This leads to a change in the original state of the breath, which may cause false-positive or false-negative results in medical diagnosis [27,28]. This problem has motivated the development of an alternative approach to analyze the breath, which is based on the inherent characteristics of the gas mixture. This new approach aims to obtain an integral portrait of the analyzed complex gas mixture, which is called the “breath profile” or the “breath fingerprint” [13]. Generally, the breath profile can be obtained by finding the complete composition of the breath, the concentration of its components, and the temporal dynamics of the changes in breath composition. In the case of a medium with more than 2000 components, this is a difficult task even for the most modern sensor devices. This problem is solved by using sensor devices known as “electronic noses” [29]. These modern systems can obtain up to a few dozens of points for the breath profile. But this is not enough to get a comprehensive portrait of the analyzed breath medium, which contains hundreds or thousands of components. As a consequence, there is a high probability of low reproducibility of the results obtained under different experimental conditions or in a series of independent experiments performed in different locations and over different periods of time.

It is clear that the process to obtain a complete dataset of a real breath profile at a specific time interval is extensive and time-consuming. In addition, it does not guarantee reliable results. To avoid these risks, new approaches must be developed. Quantum detection offers several possibilities to find and implement new mechanisms to selectively detect various substances. Therefore, it has the potential to become a breakthrough approach [4,10].

To implement the new quantum approach in sensor technology, new tools with unusual quantum properties need to be developed and applied. These new sensor devices can be based on Yanson point contacts [3,4]. Yanson point contacts are well known as the main instrument of Yanson point-contact spectroscopy [5,6]. They are quantum objects that are easy to produce and use. In addition, they are a source of unique information that is hard or even impossible to obtain with other methods. Yanson point contacts have a number of unique electrophysical properties, one of them being the nonequilibrium electron distribution function, which is formed in the current state of the point contact [30]. This function reflects the presence, in the area of a point contact, of a group of electrons in nonequilibrium states, which is formed as the electrons get accelerated by the electric field of the contact. The electric field is concentrated in the Yanson point contact area due to a specific electric drop in the potential in that area as the current flows through the electrode/point contact/electrode system. Upon crossing the area of the Yanson point contact, electrons are excited and transition to a nonequilibrium state. Then, the electrons gradually relax as they interact with quantum quasiparticle excitations and other objects. This process is fundamental for Yanson spectroscopy of electron–phonon interactions [30] and is responsible for the unique properties of point-contact sensors [4].

Point-contact sensors can detect single substances [31,32] and also obtain an integrated profile of a complex gas mixture [4,11]. This profile contains information about the complete set of energy interactions that take place in the point contact/ breath system. As a result, the obtained function can unambiguously characterize the analyzed system, since the knowledge of the energy parameters is the key to successfully identifying and modeling the physical–chemical properties of various quantum objects. In the present paper, by using the quantum properties of Yanson point contacts, we propose a new method that selectively detects the breath components based on the point-contact energy profile of this complex gas mixture.

Experimental

In the present paper, we studied the breath of patients treated at the State Institution "Institute for Children and Adolescents Health Care at the National Academy of Medical Sciences of Ukraine", within the framework of the program that studies the fundamental mechanisms of disease development in the upper gastrointestinal tract. The development and testing of the method to detect the breath components involved patients in the age range between 12 and 18 years who had functional dyspepsia. The average age of the participants was 15.5 years. The study involved a total of 40 participants, among which 22 were male and 18 were female patients. Patients younger than 12 and older than 18 years old, or who had at least one of the following symptoms, such as acute diseases, fever, unintentional weight loss, blood vomiting, melena, anemia, leukocytosis, or destructive changes in the mucosa of the upper digestive tract were excluded from the studies.

The clinical diagnosis was made based on the medical history of the patients, complaints of the patients, and results obtained from physical examination. Special attention was paid to the identification and detailing of clinical symptoms based on the medical history, the presence of a family history of digestive system lesions, and disease duration, in accordance with the Rome IV criteria [33]. All patients received a full medical examination identical to the previously described procedures [11].

The breath profile was registered using point-contact sensor matrices based on tetracyanoquinodimethane (TCNQ) compounds [34] in accordance with the method we developed and verified in our earlier medical studies [11,35]. A point-contact sensor matrix is a structure consisting of a large number of mechanically stable Yanson point contacts. These contacts correspond to point contacts produced using the Chubov technique [36], which is the most efficient technique used in Yanson point-contact spectroscopy [4,5]. The density of the primary nanostructured sensing elements in the sensor matrix was between 5×10^4 and 6×10^4 Yanson point contacts per square millimeter of the observable surface.

The mesoscopic point-contact sensor matrix has a small integrated source of energy, which is manufactured with a special technique during the synthesis of this nanostructure. The production of the energy source and the matrix as a whole is based on electrochemical processes described previously [34,37,38]. The applied technology guaranteed high reliability and longevity to the sensor elements. Point-contact sensor matrices can function autonomously without an external energy source for more than a year even under field conditions [11].

The portable sensor system used for this study was developed by us earlier and consists of the following main elements [39]: a holder with an electrical connector for the sensor, which also has all the necessary elements for communication and transmission of the sensor signal to the recorder; a programmed recorder, which can not only register the sensor signal and transmit it to a computer, but also function as a signal amplifier if necessary; a computer with an original software (developed at the B. Verkin Institute for Low Temperature Physics and Engineering of the National Academy of Sciences of Ukraine) used for storing information and performing real-time data analysis.

The process of obtaining the breath profile starts when the sensor is mounted on the electrical connector at the upper end of the holder, before the measurements are taken. Then, a disposable hood, in the form of a removable cone-shaped tube, used for the formation of a cell containing the sensor, is attached to the upper end of the holder. During the measurement, this cell is kept inside the mouth of the patient for 1 min. Thus, the sensor is directly exposed to the breath of the patient. Any influence from the external environment can be excluded. The optimal exposure time was experimentally selected based on previous studies [11,35,40]. It corresponds to the period of time required to have all breath components interact with the sensing elements of the point-contact sensor matrix. When the exposure is over, the sensor cell is removed from the mouth and the relaxation of the sensor in the ambient atmospheric environment begins. The relaxation time depends on the composition of the breath and usually is in the range of 1–3 min. Thus, the whole process of registering the breath profile occurs in real time. After the relaxation, the sensor is ready for the next measurement. To increase the reproducibility and reliability of the obtained results, we made three consecutive measurements for each patient. According to the methodology we developed earlier for obtaining breath profiles [11,35], the measurements must be taken after the patient fasted overnight. On the day of the experiment, the patients did not take any medication. The fulfilment of these requirements guarantees the maximum exclusion of any side factors and effects that could alter the characteristic breath profile of a patient.

A heating of the sensor in order to prevent condensation of the exhaled breath inside the sensor holder was not performed in our studies since it is the condensate from the exhaled gas that activates the sensing element. A condensate film formed on the gas-sensing surface switches on the autonomous power supply of the sensing element, enabling the observation and measurement of the dynamics of resistance variation during the exposure and relaxation periods. This is due to the fact that, in the process of exposure, components of the exhaled breath diffuse through the condensate film to the surfaces of the conduction channels of the point-contact matrix. This impacts the resistance characteristics of each one of the point-contact nanostructures and, as a result, the resistance of the whole matrix.

The metabolic profile of a patient is registered by measuring the dependence of the electrical conductance of the point-contact sensor matrix with time. This dependence is called the response curve. The complete metabolic profile of the patient is obtained through the response curves measured during the exposure and relaxation of the sensor.

A set of 49 sensors was manufactured for the study. To avoid the influence of any variation in some of the electrical parameters of the sensor on the experimental results, we selected samples with the most similar parameters. All manufactured samples were tested using the breath media from healthy participants as a control. Cluster analysis of the testing results using the criteria we developed earlier [41] was performed to select sensors with the most similar parameters. As a result of these procedures, a set of 25 sensors was selected in which any pair of sensing elements had a very similar response to the analyzed gas mixture [34,41].

To test the proposed new method in which single components of a complex gas mixture are selectively detected using point-contact sensors, serotonin and cortisol were chosen as the substances to be detected. The concentration of these substances was obtained from the breath of the patients during the medical studies. These substances were selected because of the important role they play in the metabolic processes of the human body.

Serotonin (5-hydroxytryptamine, $C_{10}H_{12}N_2O$) has several biological functions [42,43]. It plays an important role in regulating human psycho-emotional states [44,45]. The serotonin concentration increases during euphoria and decreases during depression and this is why serotonin is often called the “hormone of happiness”. Serotonin participates in the physiological regulation of various functions of the digestive organs, including gastric secretion and motility [46-48]. Between 60% and 90% of all serotonin generated in the human body is produced in the digestive tract [49], which is where this amine becomes part of the exhaled breath.

Cortisol (11β,17α,21-trihydroxypregn-4-ene-3,20-dione, $C_{21}H_{30}O_5$) is a biologically active hormone produced by the adrenal cortex. It belongs to the class of glucocorticoid hormones [50] and it controls several functions in the human organism [51]. For example, it participates in the carbohydrate, lipid, and protein metabolism, is responsible for the energy conservation in the organism, and affects the synthesis of cellular enzymes. Cortisol generates the defense reactions of the organism against external threats and stressful situations [52]; therefore, it is called the “stress hormone”. In the case of heavy stress, cortisol changes the muscle activity by decreasing their glucose consumption and stimulating its arrival to other organs. Cortisol prevents the secretion of substances in the organism that can cause inflammation [53]. At the same time, a high level of cortisol inhibits the immune system and worsens the ability of the organism to resist against infections and other harmful factors [54].

A comprehensive study of how the concentrations of serotonin and cortisol vary in the human body can promote a better understanding of various disease mechanisms and help to find new approaches for improving medical treatment. Overall, this contributes to the development of new noninvasive tests for the detection of these hormones.

The concentration of serotonin in the blood was determined by the fluorometric method [55,56] whereas the concentration of cortisol in the blood serum was determined via the enzyme-linked immunoassay using the reagents produced by the NPL Granum company (Kharkiv, Ukraine).

Statistical calculations were made using the WEKA data mining software [57]. Additional control and verification of the results were performed with the SPSS statistical package [58]. The data were processed statistically using the standard parametric and nonparametric methods [59].

Ethics

The research protocol was approved by the Institutional Review Board and the Ethical Committee of the State Institution "Institute for Children and Adolescents Health Care at the National Academy of Medical Sciences of Ukraine". All the patients gave their written consent to participate in the study.

Results and Discussion

The idea of the method proposed here is based on the fact that any spectrum contains the energy information about the components of a system and their interactions. This paradigm is actively used as the basis of many research methods and techniques (e.g., optical spectroscopy). The application of the energy approach to solve practical problems is often limited by the complexity of the systems under study and the lack of simple and reliable tools to measure and analyze processes. The implementation of innovative mechanisms based on the quantum properties of objects and the usage of quantum tools and methods provide new unlimited opportunities for the development of technologies based on the principles of data collection and analysis of energy.

Earlier, we proposed to use the information about energy processes occurring in the breath for its detection and analysis [11]. The idea was feasible and could be implemented using appropriate tools that met the basic requirements for modern sensor technology, including simplicity, high efficiency, portability, low cost, and real-time detection. All of these criteria are met by modern nanosensors created on the basis of Yanson point contacts. A Yanson point contact is a unique quantum object and the main instrument for Yanson point-contact spectroscopy. The operating principle of Yanson point-contact spectroscopy is based on measuring the interaction between electrons and other quantum quasiparticle excitations using point contacts. This was clearly demonstrated for the first time by Yanson while studying electron–phonon interactions in metals [60]. When a current flows through Yanson point contacts, a unique condition for the manifestation of the quantum properties of these objects arises. These properties are essential for Yanson point-contact spectroscopy [6] and are used to create a new generation of advanced nanosensors [4].

The Yanson point contact itself is the simplest electrophysical structure and it can be represented as an electrode/point contact/electrode system. In the electric current mode, in which this system is usually studied, the decrease in the voltage applied to the system occurs exclusively in the area of the point contact [30]. This allows for the concentration of the electric field in a small region, which serves as an additional energy source for the electrons passing through the contact, leading to acceleration and subsequent transition to a nonequilibrium state. As a result, a nonequilibrium electron distribution function is formed in the contact area [30]. The electron relaxation upon interaction with other groups of quasiparticles leads to the manifestation of the energy parameters of this interaction in the electrical characteristics of the point contacts. Due to this phenomenon, the spectrum of the electron–phonon interaction in metals [5], superconductors [8,61], and even in more complex compounds such as organic conductors [62] can be easily obtained. The point-contact spectrum of the electron–phonon interaction contains the information about the characteristic parameters of the phonon system of a material, which is difficult or even impossible to obtain using other methods.

In order to understand our proposed approach to analyze the human breath, one should first consider the point-contact spectrum of the electron–phonon interaction in indium [63] (Figure 1a). The abscissa directly characterizes the energy of the phonons that interact with the electrons, which in turn obtain an excess energy of the order of eV_{pc} when accelerated by the electric field in the Yanson point contact. Here e is the electron charge and V_{pc} is the voltage applied to the contact. Thus, each section of the curve reflects the energy parameters of a certain group of phonons. This fact allows, for example, the determination of phonon groups with energy values that are characteristic of various types of atomic vibrations in a solid. The ordinate of the point contact-spectrum characterizes the phonon concentration in a certain section of the spectrum and reflects the amplitude of the density function of the phonon states.

The operation of point-contact sensors is in line with the principles of Yanson point-contact spectroscopy [3,6]. Point-contact sensors exhibit quantum properties during the detection of various objects and enable new detection mechanisms [4,10]. The quantum properties of the point-contact sensors enable the measurement of the breath spectral profiles, which contain comprehensive information about this complex gas medium [11]. One representative point-contact breath spectral profile obtained in the present study is shown in Figure 1b. As already mentioned, the full point-contact sensor profile of the breath consists of two parts obtained during exposure and relaxation. In this profile, the exposure curve encompasses the time range between 0 and 60 s whereas the range above 60 s corresponds to the relaxation curve. The point-contact sensor breath profile has a nonmonotonic spectral character with a number of nonlinearities, maxima, and minima. Unlike other nanosensors and conventional sensors based on the principle of changing electrical conductance, point-contact sensors are able to explicitly display energy interactions and their features in the breath profile. This is possible because, in Yanson point contacts, heat

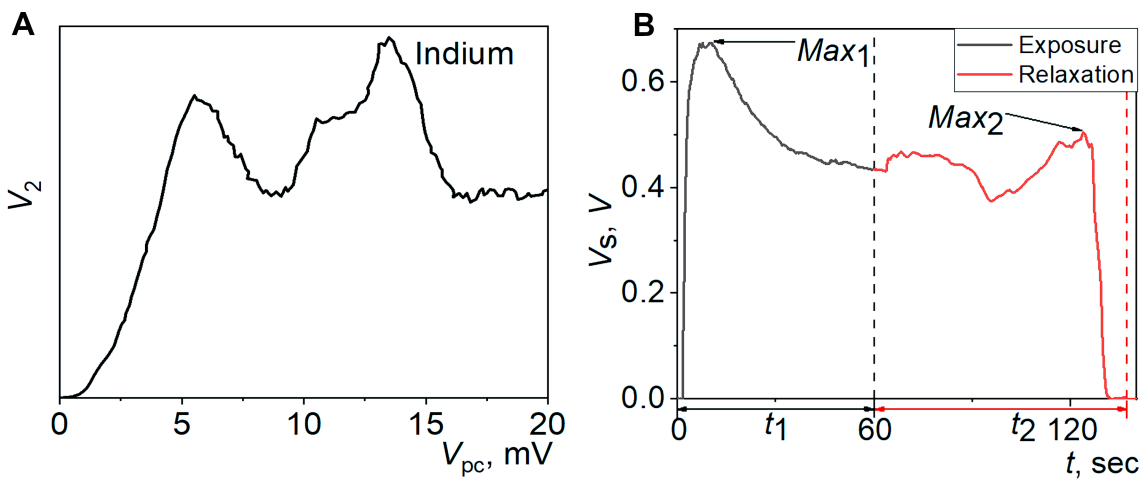

Figure 1: (a) Spectrum of the electron–phonon interaction in indium obtained using Yanson point contacts. V_2 is the second derivative of the current–voltage characteristic of the point contact and V_{pc} is the decrease in contact voltage. (b) A typical time dependence of the point-contact sensor conductance based on TCNQ compounds as a result of its interaction with the human breath (i.e., the breath point-contact sensor profile). V_s is the voltage decrease that occurs in the sensor, t is the time, t_1 is the exposure time, and t_2 is the relaxation time.

generation and nonlinear electric current processes in the contact caused by scattering of electrons in a nonequilibrium state are spatially separated [30]. The separation of nonlinear electric current phenomena from other interactions allows us to directly observe their energy component as a result of the interactions in the point contact/breath system. This property of the Yanson point contact arises from the large mean free path of the electrons in the contact, which allows for the manifestation of all thermal effects outside the contact. Thus, the interaction-related nonlinear changes in the point-contact conductance result only from scattering processes of electrons in a nonequilibrium state [30]. In addition, the voltage sweep in the contact ranges widely and so does the excess energy of nonequilibrium electrons, which they can transfer as a result of the interaction. This allows us to effectively influence the processes of adsorption and desorption and directly measure their energy parameters.

Thus, the operation mechanism of the point-contact sensor and the measurement of the energy parameters of the components of the analyzed system can be understood as follows. Depending on the nature of a given molecule, the molecule can be characterized by a certain energy of interaction with the gas-sensing matrix material (i.e., the adsorption energy). Any adsorption event in the Yanson point contact entails a redistribution of the electron density in the conduction channel of the point contact, the scattering of the conduction electrons in a nonequilibrium state on adsorbed atoms, the transfer of the excess energy of electrons to the adsorbed atoms followed by their desorption, and the relaxation of the nonequilibrium distribution function of electrons in the contact, which results in a change in the point-contact resistance. These changes are displayed in the dependencies of the Yanson point contact parameters. In the case of classical Yanson point-contact spectroscopy studies of electron–phonon interaction in metals, the energy-related processes are described by the current–voltage characteristic of the Yanson point contacts and its derivatives. In our study of the exhaled breath, the energy-related processes can be seen as the temporal variations of the electric conductance of the point contact and plotted as a spectral profile of the exhaled breath. The fundamental properties of Yanson point contacts enable the measurement of the electric conductance variations when they are equivalent to at least one conductance quantum. This guarantees an extremely high sensitivity of the point-contact sensors and the measurement of minute energy perturbations occurring during the interaction of the breath components with the point-contact conduction channel. Therefore, the nature of the molecule is revealed through the energy parameters of the molecule.

In the initial state, the gas-sensitive surface of the sensor is in equilibrium with the surrounding atmosphere. Experiments show that the nature of the gas-sensitive material provides a reversible physical adsorption under the action of substances that prevail in the environment. When there are gaseous analyte substances near to the gas-sensitive surface, they occupy a certain portion of the active centers as a result of a competing adsorption. This process changes the resistance of the point-contact array. Therefore, there is no need to provide special storage conditions for the sensor before the measurements. The nature of the active centers is such that, between measurements, the atmospheric nitrogen is able to completely block them and preserve the gas-sensitive layer, neutralizing the influence even of active oxidizing agents such as oxygen.

When the sensor is placed in the oral cavity, the nature and thermodynamic parameters of the gas-sensitive surface/gaseous-environment system change dramatically. The temperature and humidity rises and the chemical composition of the gaseous medium changes. With an increase in humidity and temperature, the galvanic element, which is integrated in the point-contact gas-sensitive array and generates the electric field, is activated. The field initiates quantum-energy effects in the bulk and on the surface of the conduction channels of Yanson point contacts. At the active centers, molecules of metabolic products and their derivatives replace the nitrogen molecules. Under these conditions, the system transitions to a new quasi-equilibrium state. The events occurring in this case correspond to the quantum dissipation of energy, which is measured as a voltage change in the sensor element by a special device. Since the relaxation process lasts for about a minute, it can easily be recorded as an equidistant time series. We consider this series as a sensor response to the breath medium during the exposure period in the oral cavity (or simply during the exposure period). The next phase of the measurements consists of recording the voltage in the sensor when it comes into contact with the original atmosphere after the exposure in the oral cavity is over. This process is opposite to the previous one and it is caused by the desorption of the breath components and the return of atmospheric nitrogen molecules to the active centers. It is also initiated by the electric field of the galvanic cell integrated into the point-contact array. Yet, in this case, due to a decrease in humidity and temperature, the field also decreases. The reverse process, which is essentially the relaxation step, usually lasts between 1 and 3 min. The exposure and relaxation processes are measured as an equidistant time series which represents the sensor metabolic profile of the patient (Figure 1b).

The adsorption–desorption processes on the active surface of the sensor are eventually reversible and are characterized by a significant hysteresis. This complex nature of the response unfolds broad prospects for identifying the specific metabolism of each patient. Therefore, using the sensor in medical diagnostics is an efficient tool to analyze the breath medium. Some progress has already been made in this area. In the complex response configuration, the so-called “characteristic parameters” have been already distinguished in a few published studies [3,35,40]. Regular individual differences measured in the breath of some of the patients may be caused by metabolic peculiarities and may indicate the presence of a certain pathology. The characteristic parameters were analyzed considering the history and clinical parameters of the examined patients (i.e., results of clinical, laboratorial, and instrumental examinations). Next, a search for relevant correlations between the analyzed parameters of the patient and the characteristics of their breath was made. The obtained correlations were used as criteria for determining the deviation of the sensor curve response in patients with a pathology in comparison with patients with a normal metabolism. The detected deviation of the response curve of the sensor made it possible to identify one or more pathologies or to assign patients to certain risk groups. This approach was quite fruitful and enabled the development of the scientific basis for breath tests in early non-invasive diagnosis of erosive-ulcerative lesions of the gastrointestinal tract based on the detection in the breath of ill patients of waste products from the bacterium *Helicobacter pylori*, including cytotoxic strains of this microorganism.

However, it should be noted that further improvement of analytical procedures involves lowering the sensitivity threshold of the sensor in relation to a wider list of controlled substances and their derivatives. This, in turn, requires a finer and more detailed analysis of the features of the response curve configuration. A reliable tool for the precise differentiation of a complex response curve can be a systematic approach to the synthesis of its characteristic elements and the search for singularities associated with the target object.

One of the directions of the systematic approach can be related to the analysis of the level of correlation of the sensor output parameter (voltage) with the target detection parameter (marker concentration in the breath) during the time of the analysis (exposure period plus relaxation period). This analysis is convenient since a complex response curve reflects the totality of interactions of a complex gaseous medium including the target substance with the gas-sensitive array. The higher the correlation level in a certain period, the higher the probability of the marker (or derivatives of its interaction with certain components of the breath) to give a signal in the response curve. These marked sections have a physical meaning: Gas atoms adsorbed on the conduction channel of the Yanson point contact create areas with distortions in the crystal structure of the contact material. This leads to a shortening of the mean free path of electrons in the contact area and increases the probability of scattering of nonequilibrium electrons at the sites of the adsorbed atoms. As a result of the scattering, the excess energy of the electron is transferred to the adsorbed atoms, which subsequently desorb. Upon transferring the excess energy to the gas atoms the electrons return to their equilibrium state. In turn, the gas atoms, upon receiving enough energy, desorb from the surface of the Yanson point contact. The process proceeds in a real-time regime enabling the measurement of the energy profile of a complex gaseous medium (e.g., the human breath). The result of the interaction is displayed on the time axis of the sensor response curve, since the duration of the interaction actually reflects the amount of energy transferred. Thus, by analogy with the point-contact spectra of the electron–phonon interaction, the point-contact profile of the breath contains information about the energy parameters of the atoms and molecules adsorbed on the surface of the Yanson point-contact conduction channel.

The target substance or the derivatives formed during its interaction with the components of a complex gaseous medium can change the resistance of the point-contact array when the galvanic cell creating the electric field is in a certain energy state. This, in turn, happens due to the peculiarities of the electron transfer through the conduction channel of the point contact viewed as the elementary unit of the gas-sensitive array. This allows us to propose a method for detecting individual components of a complex gaseous medium by determining the section of the curve of the spectral sensor profile that corresponds to the energy of interaction between the conduction electrons and these components.

The starting point of the proposed strategy for the analysis of the metabolic profile of the patients was to obtain the dependence of the correlation coefficient of the studied component of the breath with the level of the sensor output signal during the measurement. It was assumed that all points with a deviation of less than 2% from the maximum value can be used as the data in parallel experiments for obtaining the dependence of the response voltage on the concentration of a specific target substance. The dependence of the response voltage, for a period of maximum correlation with the analyte concentration, in a studied patient group allows us to obtain a linear regression equation. This equation can serve as a characteristic calibration curve for determining the concentration of the target component of a complex gaseous medium using a sensor.

By applying the above strategy to determine the concentration of hormones in the human body with the help of a sensor, we experimentally show the possibility of detecting singular characteristic sections of a complex response curve of a point-contact nanosensor upon breath exposure. To demonstrate the operability of the proposed approach, we analyze the point-contact breath profiles of the patients (the so-called metabolic profiles in the form of response curves of the point-contact nanosensor) and compare them with the values of serotonin and cortisol in the body of each patient.

To get the primary data, we obtained respiratory tests results from 16 patients with a known level of serotonin concentration in their blood (group 1) and from 16 patients with a known level of cortisol concentration in their blood serum (group 2). To be able to employ the spectral approach we proposed to detect the components of complex gas mixtures using point-contact sensors. For this we needed to identify the sections of the sensor response curves that were related to the metabolic profiles of the patients and were most informative regarding the concentration of the targeted hormone. To do this, we presented the sensor response in a time series form with a step of 0.5 s. Next, the temporal dependences of the correlation coefficient between the response voltage and the hormone concentration for groups 1 and 2 were determined. The linear correlation coefficient (i.e., the Pearson correlation coefficient) r between the response voltage V at a given time and the hormone concentration C was calculated using the following relation:

$$r = \frac{\mathrm{cov}_{VC}}{\sigma_V \sigma_C} = \frac{\sum_{j=1}^{n}\left(V_j - \overline{V}\right)\left(C_j - \overline{C}\right)}{\sqrt{\sum_{j=1}^{n}\left(V_j - \overline{V}\right)^2 \sum_{j=1}^{n}\left(C_j - \overline{C}\right)^2}}, \quad (1)$$

where cov_{VC} is the covariance of the values V and C, σ_V is the root-mean-square deviation of V, σ_C is the root-mean-square deviation of C, V_j is the response voltage at a given time for the j-th patient (out of n patients), and C_j is the hormone concentration of the j-th patient. $\overline{V}$ and $\overline{C}$ (see Equation 2) are the mean values of the respective samplings:

$$\overline{V} = \frac{1}{n}\sum_{j=1}^{n} V_j, \overline{C} = \frac{1}{n}\sum_{j=1}^{n} C_j. \quad (2)$$

The obtained correlation coefficients r were used for plotting the temporal dependencies of the absolute values $|r|$ for the groups 1 and 2 (Figure 2).

The highest negative correlation for serotonin is observed in the range of 70–85 s and for cortisol in the range of 89–92 s. These time intervals of the measurements represent the period in which the hormones and the products of their interactions with other components of the breath are able to significantly affect the physicochemical state of the point-contact array and change the resistive characteristics of the gas-sensitive elements. The time range in which the dependence shown in Figure 2 was calculated is limited by the maximum time of the breath test. However, the total exposure time and relaxation time of the majority of the breath tests did not reach 180 s and the missing points of the response curves were assigned zero values.

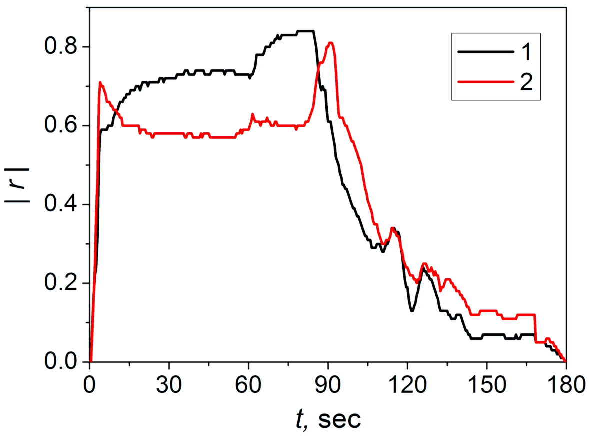

Figure 2: Temporal dependence of the absolute values of the correlation coefficient |*r*|. Here, *r* describes the correlation between the response voltage values of the breath tests of the patients and the concentration of serotonin (1, black curve) and cortisol (2, red curve) according to the medical tests.

Thus, the characteristic time interval to estimate the level of serotonin in the blood of a patient via a breath test is in the range of 70–85 s. The values of the average voltage $\overline{V}_\mathrm{s}$ of the metabolic profile of a particular patient during this interval (Figure 2) and the concentration of serotonin C_ser in the blood uniquely determine the position of the points in the graph of response voltage as a function of the concentration (Figure 3). Since there is no information a priori about the nature of the relationship between the concentration of serotonin and the voltage of the sensor, it is reasonable to use a linear approximation and draw a straight line through the obtained points using the least-squares method:

$$C_\mathrm{ser}[\mu\mathrm{mol}\cdot\mathrm{L}^{-1}] = 1.17 - 2.41 \times \overline{V}_\mathrm{s}. \quad (3)$$

This is a characteristic calibration line for estimating the serotonin concentration using the sensor method based on the breath test. Statistical analysis showed that the standard deviation of the medical analysis data from the approximation line does not exceed 0.115 μmol·L^{-1}. Thus, with a 95% probability, the confidence interval is 0.230 μmol·L^{-1}.

The model for determining the serotonin concentration (Equation 3) was verified by adding relevant results of the breath tests

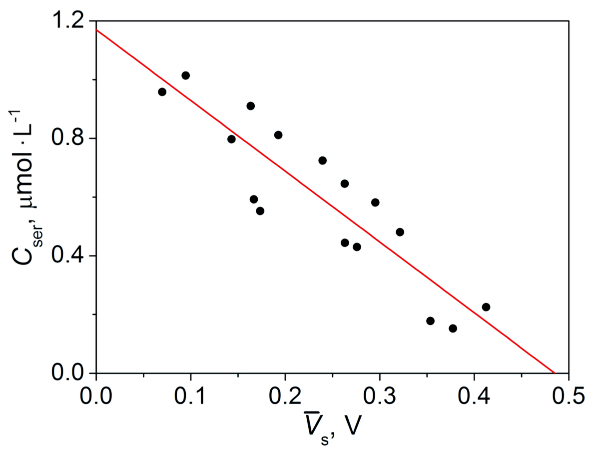

Figure 3: Dependence of the analytical concentration of serotonin C_{ser} on the average response voltage $\overline{V}_{\mathrm{s}}$ in the area of the maximum correlation. Black dots correspond to the data from the medical tests and the red line is the result of the linear approximation, given by Equation 3.

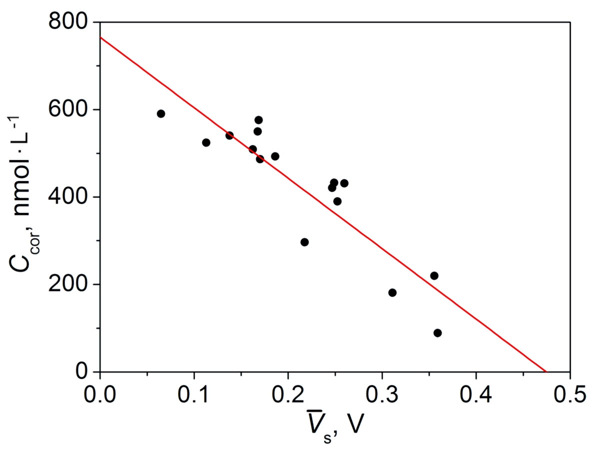

Figure 4: Dependence of the analytical concentration of cortisol C_{cor} on the average response voltage $\overline{V}_{\mathrm{s}}$ in the area of the maximum correlation. Black dots correspond to the data from the medical tests and the red line is the result of the linear approximation, given by Equation 4.

of four new patients from whom the serotonin content in the blood was known (Table 1).

For group 2 (comprising of 16 people), in addition to the results of the breath tests, the cortisol content in the blood serum of the patients was also known. The correlation analysis of the cortisol metabolic profile showed that, in this case, the section of the maximum correlation is in the range of 89–92 s (Figure 2).

The dependence of the concentration of cortisol C_{cor} on the average voltage $\overline{V}_{\mathrm{s}}$ in the area of maximum correlation can be approximated by the linear equation:

$$C_{\mathrm{cor}}[\mathrm{nmol}\cdot\mathrm{L}^{-1}] = 765.54 - 1612.32 \times \overline{V}_{\mathrm{s}}. \qquad (4)$$

The results of this approximation are presented in Figure 4.

Statistical analysis showed that the standard deviation of the medical analysis data from the approximation line does not exceed 61.8 nmol·L^{-1}. Thus, with a 95% probability, the confidence interval is 123.6 nmol·L^{-1}. The verification of the model (Equation 4) for the determination of the cortisol concentration was carried out similarly to the verification of the model (Equation 3) for the determination of the serotonin concentration. Again, for four new patients with a known cortisol concentration in the blood serum were used to test the model (Table 2).

The verification of the linear mathematical models, given by Equation 3 and Equation 4, showed that all the sensor analysis results are within the corresponding confidence intervals. This evidenced that the statistical calculation was appropriately done and the models can be used to estimate the concentration of hormones using breath tests. The obtained results demonstrate that the proposed mathematical models for obtaining the dependence of the concentration of the target substance on the output signal parameters of a quantum sensor yields an effective calibration function for a noninvasive analysis of the serotonin and cortisol levels in the human body using the breath test.

Table 1: Verification of the sensor model for the determination of serotonin concentration.

Patient number	Average response voltage $\overline{V}_{\mathrm{s}}$ in the area of maximum correlation (V)	Serotonin concentration, C_{ser} (μmol·L^{-1})		
		Analysis data	Estimation from model (Equation 3)	Model error
1	0.253397	0.394	0.559	−0.165
2	0.263031	0.451	0.536	−0.085
3	0.281277	0.585	0.492	0.093
4	0.170466	0.733	0.759	−0.026

Table 2: Verification of the sensor model for the determination of cortisol concentration.

Patient number	Average response voltage $\bar{V}_s$ in the area of maximum correlation (V)	Cortisol concentration C_{cor} (nmol·L^{-1})		
		Analysis data	Estimation from model (Equation 4)	Model error
1	0.365943	166.6	175.5	−8.9
2	0.256083	300.0	352.7	−52.7
3	0.156115	498.8	513.8	−15.0
4	0.165320	570.3	499.0	71.3

The results of the study clearly demonstrate the indisputable advantages of using nanotechnology in the field of sensor technology to develop and improve environmental-monitoring tools. The level at which the components of the analyzed complex gaseous medium were identified and the sensitivity of this detection, previously unattainable by conventional sensors, have become possible due to the in-depth differentiation of the gas-sensitive surface at the atomic level, under laboratory conditions. For the first time it became possible to analyze the human hormonal background using the breath, which is the most convenient biological material. With the hormones serotonin and cortisol used as examples, it was shown that concentrations of these substances can be monitored in real time, whereas in the case of conventional medical analysis it might take hours or even days.

Special attention should be paid to the unprecedented sensitivity of the developed point-contact nanosensor element. It should be reinforced that the studied analytes are not gaseous substances that can be directly found in the breath. Not exceeding a fraction of micromoles per liter in the blood, these molecules “transmit” the information about their quantity through a chain of mediators (transmitters), the last of which is recognized by the surfaces of the atomic structures of the gas-sensitive array (i.e., the Yanson point contacts). As a result, we can quantitatively estimate, with a probability of 95%, the stress level in the body. Wide prospects are opening for more detailed studies regarding the dynamics of the emotional states when various factors simultaneously affect the state of the organism, and our preliminary investigation confirms that. Due to the instability of the hormonal molecules, the validity of the conclusions and medical reports made based on the analysis from data sets taken during a long measurement period are being contested. Therefore, performing express tests using point-contact nanosensors for the observation of hormone concentration profiles in a dynamic manner is of undeniable importance.

The present study proposes a sequence of procedures to unravel the correlation between the concentration of a particular hormone and the level of the output signal. This dependence can be used to estimate the hormonal background of the patient using the data from the sensor analysis of the breath medium. The establishment of this correlation was possible due to the unique point-contact nanosensor with an ultrahigh surface density of information recognition elements in the form of Yanson point contacts. As a result, the characteristic output of this sensor is a time series of the complex profile. A systematic approach to decode the information coming from the internal organs of a human body allowed us to develop a universal approach to analyze a wide spectrum of breath components.

The presented study shows that a combination of advanced techniques based on Yanson point contacts, accessible material base, and modern analysis tools creates a robust and fast detection method in which the real-time differential sensor analysis can be widely applied in various areas of science and technology, especially medicine.

ORCID® iDs

Victor I. Belan - https://orcid.org/0000-0002-8356-9985
Volodymyr L. Vakula - https://orcid.org/0000-0002-3423-9779
Gennadii V. Kamarchuk - https://orcid.org/0000-0002-1105-8019

References

1. Obermair, C.; Kuhn, H.; Schimmel, T. *Beilstein J. Nanotechnol.* **2011,** *2,* 740–745. doi:10.3762/bjnano.2.81
2. Jeevanandam, J.; Barhoum, A.; Chan, Y. S.; Dufresne, A.; Danquah, M. K. *Beilstein J. Nanotechnol.* **2018,** *9,* 1050–1074. doi:10.3762/bjnano.9.98
3. Kamarchuk, G. V.; Pospelov, A. P.; Kamarchuk, L. V.; Kushch, I. G. Point-Contact Sensors and Their Medical Applications for Breath Analysis: A Review. In *Nanobiophysics: Fundamentals and Applications;* Karachevtsev, V. A., Ed.; Pan Stanford Publishing Pte. Ltd.: Singapore, 2016; pp 327–379. doi:10.1201/b20480
4. Kamarchuk, G. V.; Pospelov, A. P.; Kamarchuk, L. V.; Savytskyi, A. V.; Harbuz, D. A.; Vakula, V. L. Point-Contact Sensors as an Innovative Tool in Defense Against Chemical Agents, Environment and Health Risks: A Review. In *Functional Nanostructures and Sensors for CBRN Defence and Environmental Safety and Security;* Sidorenko, A.; Hahn, H., Eds.; NATO Science for Peace and Security Series C: Environmental Security; Springer: Dordrecht, Netherlands, 2020; pp 245–270. doi:10.1007/978-94-024-1909-2_18

5. Khotkevich, A. V.; Yanson, I. K. *Atlas of Point Contact Spectra of Electron-Phonon Interactions in Metals;* Kluwer Acacemic Publishers, 1995. doi:10.1007/978-1-4615-2265-2
6. Naidyuk, Yu. G.; Yanson, I. K. *Point-Contact Spectroscopy;* Springer: New York, NY, USA, 2005.
7. Yanson, I. K.; Kamarchuk, G. V.; Khotkevich, A. V. *Sov. J. Low Temp. Phys.* **1984,** *10,* 220–222.
8. Bobrov, N. L.; Khotkevich, A. V.; Kamarchuk, G. V.; Chubov, P. N. *Low Temp. Phys.* **2014,** *40,* 215–222. doi:10.1063/1.4869565
9. Akimenko, A. I.; Gudimenko, V. A.; Verkin, A. B. *Sov. J. Low Temp. Phys.* **1988,** *14,* 133–135.
10. Kamarchuk, G. V.; Pospelov, A. P.; Savytskyi, A. V.; Herus, A. O.; Doronin, Y. S.; Vakula, V. L.; Faulques, E. *SN Appl. Sci.* **2019,** *1,* 244. doi:10.1007/s42452-019-0241-x
11. Kushch, I.; Korenev, N.; Kamarchuk, L.; Pospelov, A.; Kravchenko, A.; Bajenov, L.; Kabulov, M.; Amann, A.; Kamarchuk, G. *J. Breath Res.* **2015,** *9,* 047111. doi:10.1088/1752-7155/9/4/047111
12. de Lacy Costello, B.; Amann, A.; Al-Kateb, H.; Flynn, C.; Filipiak, W.; Khalid, T.; Osborne, D.; Ratcliffe, N. M. *J. Breath Res.* **2014,** *8,* 014001. doi:10.1088/1752-7155/8/1/014001
13. Amann, A.; Smith, D., Eds. *Volatile Biomarkers: Non-Invasive Diagnosis in Physiology and Medicine;* Elsevier: Amsterdam, Netherlands, 2013. doi:10.1016/c2012-0-01274-4
14. Smith, D.; Španěl, P.; Herbig, J.; Beauchamp, J. *J. Breath Res.* **2014,** *8,* 027101. doi:10.1088/1752-7155/8/2/027101
15. Lamote, K.; Brinkman, P.; Vandermeersch, L.; Vynck, M.; Sterk, P. J.; Van Langenhove, H.; Thas, O.; Van Cleemput, J.; Nackaerts, K.; van Meerbeeck, J. P. *Oncotarget* **2017,** *8,* 91593–91602. doi:10.18632/oncotarget.21335
16. Henderson, B.; Khodabakhsh, A.; Metsälä, M.; Ventrillard, I.; Schmidt, F. M.; Romanini, D.; Ritchie, G. A. D.; te Lintel Hekkert, S.; Briot, R.; Risby, T.; Marczin, N.; Harren, F. J. M.; Cristescu, S. M. *Appl. Phys. B: Lasers Opt.* **2018,** *124,* 161. doi:10.1007/s00340-018-7030-x
17. Vaks, V. *J. Infrared, Millimeter, Terahertz Waves* **2012,** *33,* 43–53. doi:10.1007/s10762-011-9846-x
18. Pereira, M. F.; Zubelli, J. P.; Winge, D.; Wacker, A.; Rodrigues, A. S.; Anfertev, V.; Vaks, V. *Phys. Rev. B* **2017,** *96,* 045306. doi:10.1103/physrevb.96.045306
19. Apostolakis, A.; Pereira, M. F. *AIP Adv.* **2019,** *9,* 015022. doi:10.1063/1.5050917
20. Apostolakis, A.; Pereira, M. F. *Nanophotonics* **2020,** *9,* 3941–3952. doi:10.1515/nanoph-2020-0155
21. Kamarchuk, G.; Pospelov, A.; Kushch, I. Sensors for Exhaled Gas Analysis: an Analytical Review. In *Volatile Biomarkers: Non-Invasive Diagnosis in Physiology and Medicine;* Amann, A.; Smith, D., Eds.; Elsevier: Amsterdam, Netherlands, 2013; pp 264–300. doi:10.1016/b978-0-44-462613-4.00015-5
22. Bohli, N.; Belkilani, M.; Casanova-Chafer, J.; Llobet, E.; Abdelghani, A. *Beilstein J. Nanotechnol.* **2019,** *10,* 2364–2373. doi:10.3762/bjnano.10.227
23. Wu, K.; Luo, Y.; Li, Y.; Zhang, C. *Beilstein J. Nanotechnol.* **2019,** *10,* 2516–2526. doi:10.3762/bjnano.10.242
24. Proença, C. A.; Freitas, T. A.; Baldo, T. A.; Materón, E. M.; Shimizu, F. M.; Ferreira, G. R.; Soares, F. L. F.; Faria, R. C.; Oliveira, O. N., Jr. *Beilstein J. Nanotechnol.* **2019,** *10,* 2171–2181. doi:10.3762/bjnano.10.210
25. Platonov, V. B.; Rumyantseva, M. N.; Frolov, A. S.; Yapryntsev, A. D.; Gaskov, A. M. *Beilstein J. Nanotechnol.* **2019,** *10,* 1537–1547. doi:10.3762/bjnano.10.151
26. Liao, D.; Li, E.; Li, J.; Zeng, P.; Feng, R.; Xu, M.; Sun, G. *PLoS One* **2018,** *13,* e0189927. doi:10.1371/journal.pone.0189927
27. Michaud, L.; Gottrand, F.; Ganga-Zandzou, P. S.; Wizla-Derambure, N.; Turck, D.; Vincent, P. *Gut* **1998,** *42,* 594–595.
28. Lin, E. C.; Massey, B. T. *Clin. Gastroenterol. Hepatol.* **2016,** *14,* 203–208. doi:10.1016/j.cgh.2015.07.032
29. Montuschi, P.; Mores, N.; Trové, A.; Mondino, C.; Barnes, P. J. *Respiration* **2013,** *85,* 72–84. doi:10.1159/000340044
30. Kulik, I. O.; Omelyanchuk, A. N.; Shekhter, R. I. *Sov. J. Low Temp. Phys.* **1977,** *3,* 1543–1558.
31. Kamarchuk, G. V.; Pospelov, A. P.; Yeremenko, A. V.; Faulques, E. C.; Yanson, I. K. *Europhys. Lett.* **2006,** *76,* 575–581. doi:10.1209/epl/i2006-10303-6
32. Kamarchuk, G. V.; Kolobov, I. G.; Khotkevich, A. V.; Yanson, I. K.; Pospelov, A. P.; Levitsky, I. A.; Euler, W. B. *Sens. Actuators, B* **2008,** *134,* 1022–1026. doi:10.1016/j.snb.2008.07.012
33. Drossman, D. A.; Hasler, W. L. *Gastroenterology* **2016,** *150,* 1257–1261. doi:10.1053/j.gastro.2016.03.035
34. Kamarchuk, G. V.; Pospelov, A. P.; Harbuz, D. A.; Gudimenko, V. A.; Kamarchuk, L. V.; Zaika, A. S.; Pletnev, A. M.; Kravchenko, A. V. *Biophys. Bull.* **2017,** *2,* 66–78. doi:10.26565/2075-3810-2017-38-07
35. Kushch, I. G.; Korenev, N. M.; Kamarchuk, L. V.; Pospelov, A. P.; Alexandrov, Y. L.; Kamarchuk, G. V. Sensors for breath analysis: an advanced approach to express diagnostics and monitoring of human diseases. In *Biodefence. NATO Science for Peace and Security Series A: Chemistry and Biology;* Mikhalovsky, S.; Khajibaev, A., Eds.; Springer Science & Business Media: Luxembourg, 2011; pp 63–75. doi:10.1007/978-94-007-0217-2_7
36. Chubov, P. N.; Yanson, I. K.; Akimenko, A. I. *Sov. J. Low Temp. Phys.* **1982,** *8,* 32–39.
37. Pospelov, A. P.; Kushch, I. G.; Alexandrov, Y. L.; Pletnev, A. M.; Kamarchuk, G. V. *Sens. Electron. Microsyst. Technol.* **2007,** *4,* 49–54. doi:10.18524/1815-7459.2007.2.113793
38. Pyshkin, O.; Kamarchuk, G.; Yeremenko, A.; Kravchenko, A.; Pospelov, A.; Alexandrov, Yu.; Faulques, E. *J. Breath Res.* **2011,** *5,* 016005. doi:10.1088/1752-7155/5/1/016005
39. Golovko, S. A.; Gudimenko, V. A.; Pospelov, A. P.; Kamarchuk, G. V. *Sci. Herald Uzhhorod Univ., Ser. Phys.* **2014,** *35,* 95–102. doi:10.24144/2415-8038.2014.35.95-102
40. Kushch, I.; Korenev, N.; Kamarchuk, L.; Pospelov, A.; Alexandrov, Yu.; Kamarchuk, G. New Possibilities in Diagnosing Helicobacter Pylori Infection by the Non-Urease Products of Its Activity. In *Selected Papers from 8th World Congress of the World Society for Pediatric Infectious Diseases WSPID,* Cape Town, South Africa, Nov 19–22, 2013; MEDIMOND International Proceedings: Bologna, Italy; pp 89–92.
41. Golovko, S. A.; Gudimenko, V. A.; Klimkin, A. S.; Pletnev, A. M.; Vakula, V. L.; Zaika, A. S.; Kamarchuk, L. V.; Kushch, I. G.; Pospelov, A. P.; Kravchenko, A. V.; Kamarchuk, G. V. *Univers. J. Mater. Sci.* **2016,** *4,* 32–39. doi:10.13189/ujms.2016.040203
42. Young, S. N. *J. Psychiatry Neurosci.* **2007,** *32,* 394–399.
43. Pilowsky, P. M., Ed. *Serotonin: the Mediator That Spans Evolution;* Academic Press, 2019.
44. Blier, P.; El Mansari, M. *Philos. Trans. R. Soc., B* **2013,** *368,* 20120536. doi:10.1098/rstb.2012.0536
45. Jenkins, T. A.; Nguyen, J. C. D.; Polglaze, K. E.; Bertrand, P. P. *Nutrients* **2016,** *8,* 56. doi:10.3390/nu8010056
46. Crowell, M. D. *Br. J. Pharmacol.* **2004,** *141,* 1285–1293. doi:10.1038/sj.bjp.0705762
47. Berger, M.; Gray, J. A.; Roth, B. L. *Annu. Rev. Med.* **2009,** *60,* 355–366. doi:10.1146/annurev.med.60.042307.110802

48. Barinov, E. F.; Sulayeva, O. N. *Russ. J. Gastroenterol., Hepatol., Coloproctol.* **2012,** *21,* 4–13.
49. Yano, J. M.; Yu, K.; Donaldson, G. P.; Shastri, G. G.; Ann, P.; Ma, L.; Nagler, C. R.; Ismagilov, R. F.; Mazmanian, S. K.; Hsiao, E. Y. *Cell* **2015,** *161,* 264–276. doi:10.1016/j.cell.2015.02.047
50. Katsu, Y.; Iguchi, T. Cortisol. In *Handbook of Hormones. Comparative Endocrinology for Basic and Clinical Research;* Takei, Y.; Ando, H.; Tsutsui, K., Eds.; Academic Press, 2016; pp 533–534. doi:10.1016/b978-0-12-801028-0.00231-2
51. Thau, L.; Gandhi, J.; Sharma, S. *Physiology, Cortisol;* [Updated 2020 May 29]. https://www.ncbi.nlm.nih.gov/books/NBK538239/ (accessed Oct 5, 2020).
52. Lee, D. Y.; Kim, E.; Choi, M. H. *BMB Rep.* **2015,** *48,* 209–216. doi:10.5483/bmbrep.2015.48.4.275
53. Jefferies, W. M. *Med. Hypotheses* **1991,** *34,* 198–208. doi:10.1016/0306-9877(91)90212-h
54. Straub, R. H.; Cutolo, M. *Rheumatology (Oxford, U. K.)* **2016,** *55* (Suppl. 2), ii6–ii14. doi:10.1093/rheumatology/kew348
55. Kulinskiy, V. I.; Kostjukovskaya, L. S. *Lab. Sci.* **1969,** *14,* 390–394.
56. Zubkov, G. V.; Petrushin, V. D.; Chipizhenko, V. A.; Aniskina, A. A. *Collect. Proc. Kharkov Med. Inst.* **1974,** *109,* 77–81.
57. Hall, M.; Frank, E.; Holmes, G.; Pfahringer, B.; Reutemann, P.; Witten, I. H. *ACM SIGKDD Expl. Newsl.* **2009,** *11,* 10–18. doi:10.1145/1656274.1656278
58. Norušis, M. J. *SPSS 16.0 Advanced Statistical Procedures Companion;* Prentice Hall Press: Upper Saddle River, NJ, USA, 2008.
59. Tyurin, N. I. *Introduction to Metrology;* Standards Publishing: Moscow, Russia, 1985.
60. Yanson, I. K. *Sov. Phys. - JETP* **1974,** *66,* 1035–1050.
61. Yanson, I. K.; Kamarchuk, G. V.; Khotkevich, A. V. *Sov. J. Low Temp. Phys.* **1984,** *10,* 423–426.
62. Kamarchuk, G. V.; Khotkevich, A. B.; Kozlov, M. E.; Pokhodnya, K. I. *Sov. J. Low Temp. Phys.* **1992,** *18,* 679–683.
63. Kamarchuk, G. V.; Khotkevich, A. V. *Sov. J. Low Temp. Phys.* **1987,** *13,* 717–722.

License and Terms

The definitive version of this article is the electronic one which can be found at:
https://doi.org/10.3762/bjnano.11.146

BEILSTEIN JOURNAL OF NANOTECHNOLOGY

Absorption and photoconductivity spectra of amorphous multilayer structures

Oxana Iaseniuc* and Mihail Iovu

Full Research Paper

Open Access

Address:
Institute of Applied Physics, No. 5 Academiei Str., Chisinau, MD-2028, R. Moldova

Email:
Oxana Iaseniuc* - oxana.iaseniuc@gmail.com

* Corresponding author

Keywords:
amorphous multilayer structures; photocurrent; transmission spectra

Beilstein J. Nanotechnol. **2020,** *11,* 1757–1763.
https://doi.org/10.3762/bjnano.11.158

Received: 08 June 2020
Accepted: 17 October 2020
Published: 20 November 2020

This article is part of the thematic issue "Functional nanostructures for electronics, spintronics and sensors".

Associate Editor: P. Leiderer

Abstract

The experimental results regarding optical absorption and steady-state photoconductivity of amorphous single-layer structures (Al–$As_{0.40}S_{0.30}Se_{0.30}$–Al, Al–$Ge_{0.09}As_{0.09}Se_{0.82}$–Al, and Al–$Ge_{0.30}As_{0.04}S_{0.66}$–Al) and of an amorphous heterostructure (Al–$As_{0.40}S_{0.30}Se_{0.30}$/$Ge_{0.09}As_{0.09}Se_{0.82}$/$Ge_{0.30}As_{0.04}S_{0.66}$–Al) at different values of the voltage, with positive or negative polarity, applied to the illuminated top Al electrode are presented and discussed. The complex structure of the photocurrent spectra is attributed to the different values of the optical bandgap of the involved amorphous layers ($E_g \approx 2.0$ eV for $As_{0.40}S_{0.30}Se_{0.30}$ and $Ge_{0.09}As_{0.09}Se_{0.82}$ and $E_g \approx 3.0$ eV for $Ge_{0.30}As_{0.04}S_{0.66}$). The obtained experimental results are discussed taking into account the light absorption depending on the nature and the thickness of each amorphous layer, on the wavelength, and on contact phenomena at the interfaces between different layers and between the amorphous layers and the metal electrodes with different work functions.

Introduction

The As–S–Se, Ge–As–Se, and Ge–As–S ternary glass systems currently attract a lot of attention because of their wide application in IR optics, non-linear optics, photonics, optoelectronics, and as recording media for holography and e-beam lithography [1-3]. The physical properties of covalently bonded glasses are determined by the mean coordination number Z (average number of covalent bonds per atom) [4]. It is well known that the functionality of many photonic and optoelectronic devices is based on the intrinsic photoelectric effect. The photocurrent spectra and the kinetics of the photocurrent can provide information regarding the mechanisms of generation, recombination, and drift processes of non-equilibrium carriers in amorphous materials. Thus, investigations of stationary and transient characteristics of the photoconductivity of ternary amorphous thin films are of special interest. For thermally deposited amorphous films, the structure of which exhibits a higher level of disorder than that of the bulk glasses, the incorporation of impurity atoms is easier, and in many cases the metal additives could become electrically active. The influence of Sn impurities on stationary and transient photoconductivity was demonstrated for amorphous $As_2Se_3Sn_x$ thin films [5]. The introduction of Sn in the host material increases the drift mobility and the photosensitivity of the amorphous material. According to ^{119}Sn Mössbauer spectroscopy studies of the As_2Se_3:Sn_x glassy system [6] and X-ray photoelectron spectroscopy studies of $As_xGe_xSe_{1-2x}$ glasses [4], the introduction of elements such as Sn or Ge in glasses based on arsenic selenides, leads to the formation of new tetrahedral $Sn(Se_{1/2})_4$ and quasi-octahedral SnSe structural units or of $GeSe_4$, respectively. Recently, experimental results of steady-state and transient photocurrents of amorphous $Ge_xAs_xSe_{1-2x}$ and $(As_4S_3Se_3)_{1-x}Sn_x$ thin films were presented [7,8]. It was established that the predominant mechanisms of recombination of the photo-excited carriers in the investigated amorphous materials are mono- and bimolecular and that the transport is controlled through multiple trapping processes with exponential distribution of the localized states in the bandgap. Regarding the physics and applications of chalcogenide materials, multilayered amorphous thin-film structures are especially interesting because they offer advantages over single-layer structures [9,10].

Experimental

The bulk chalcogenide glasses $As_{0.40}S_{0.30}Se_{0.30}$, $Ge_{0.09}As_{0.09}Se_{0.82}$, and $Ge_{0.30}As_{0.04}S_{0.66}$ were prepared from the elements (Ge, As, S, and Se; 99.9999% purity) by conventional melt quenching. The initial materials were weighed and filled into quartz ampoules, which were sealed under vacuum ($P = 10^{-5}$ Torr). After sealing, the ampoules were heated for 48 h at a temperature of $T = 1000$ °C. The ampoules were then let to cool in air to room temperature. Some of the glass samples were then cut and polished for optical measurements; other samples were prepared as granules of small dimensions for vacuum evaporation. For optical and photoelectric measurements, thin film samples of each amorphous material, with thickness values of $d = 1000$ nm for $As_{0.40}S_{0.30}Se_{0.30}$, $d = 500$ nm for $Ge_{0.09}As_{0.09}Se_{0.82}$, and $d = 200$ nm for $Ge_{0.30}As_{0.04}S_{0.66}$, without and with Al electrodes, were prepared by thermal evaporation in vacuum ($P = 10^{-5}$ Torr) of the synthesized initial glasses onto glass substrates. Longitudinal, instead of lateral, conductivity measurements were carried out. The thickness of each layer was chosen such that the distribution of the applied electrical field was as uniformly as possible in each layer. The transparence of the top Al electrode was 60–70%, and the sample area was $S = 0.5$ cm^2.

In the same technological cycle, the multilayer heterostructure (HS) Al–$As_{0.40}S_{0.30}Se_{0.30}$/$Ge_{0.09}As_{0.09}Se_{0.82}$/$Ge_{0.30}As_{0.04}S_{0.66}$–Al was prepared. The experimental samples had a sandwich configuration with two Al electrodes, of which the top electrode was transparent to the incident light. The dark conductivity σ_d and the spectral distribution of the stationary photocurrent $I_{ph} = f(\lambda)$ have been measured under constant-current conditions using a spectrophotometer SPM-2 and an electrometrical amplifier U1-7, with a measurement error below ±1.0%. All experiments were performed at room temperature ($T \approx 20$ °C).

Results and Discussion

Figure 1 shows the transmission spectra $T = f(\lambda)$ of the separate amorphous thin films $Ge_{0.30}As_{0.04}S_{0.66}$ (1), $Ge_{0.09}As_{0.09}Se_{0.82}$ (2), $As_{0.40}S_{0.30}Se_{0.30}$ (3), and the HS $As_{0.40}S_{0.30}Se_{0.30}$/$Ge_{0.09}As_{0.09}Se_{0.82}$/$Ge_{0.30}As_{0.04}S_{0.66}$ (4). The thin film layer $Ge_{0.30}As_{0.04}S_{0.66}$ with the largest bandgap energy, $E_g \approx 3.0$ eV [11], which was placed on the top of the multilayer structure, has a thickness of $d \approx 200$ nm and was transparent to the incident visible light to reach the other layers with a bandgap energy of $E_g \approx 2.0$ eV [12,13] and with a thicknesses of $d \approx 500$ nm for $Ge_{0.09}As_{0.09}Se_{0.82}$ and $d \approx 1000$ nm for $As_{0.40}S_{0.30}Se_{0.30}$. Figure 2 shows that the amorphous film $Ge_{0.30}As_{0.04}S_{0.66}$ is highly transparent to incident light in the visible region, in contrast to the other thin-film structures (curve 4).

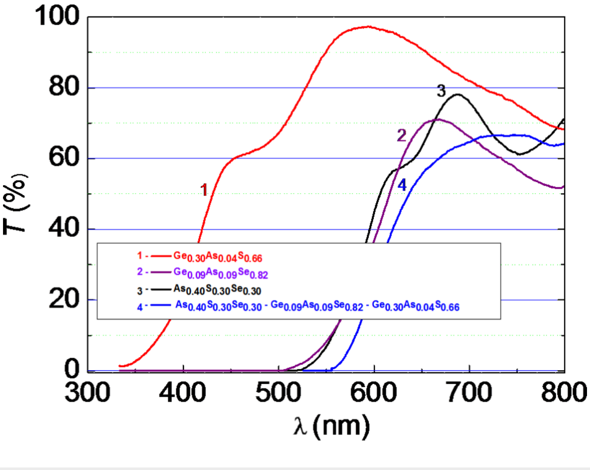

Figure 1: Transmission spectra $T = f(\lambda)$ of separate amorphous thin films and multilayer HS (1: $Ge_{0.30}As_{0.04}S_{0.66}$, 2: $Ge_{0.09}As_{0.09}Se_{0.82}$, 3: $As_{0.40}S_{0.30}Se_{0.30}$, 4: $As_{0.40}S_{0.30}Se_{0.30}$/$Ge_{0.09}As_{0.09}Se_{0.82}$/$Ge_{0.30}As_{0.04}S_{0.66}$).

Figure 2 shows the function log $\alpha = f(h\nu)$ of the absorption coefficient for single amorphous layers and for the amorphous HS. The absorption coefficient α for each layer can be calculated using the expression:

$$\alpha = \frac{1}{d}\ln\frac{(1-R)^2}{T}. \tag{1}$$

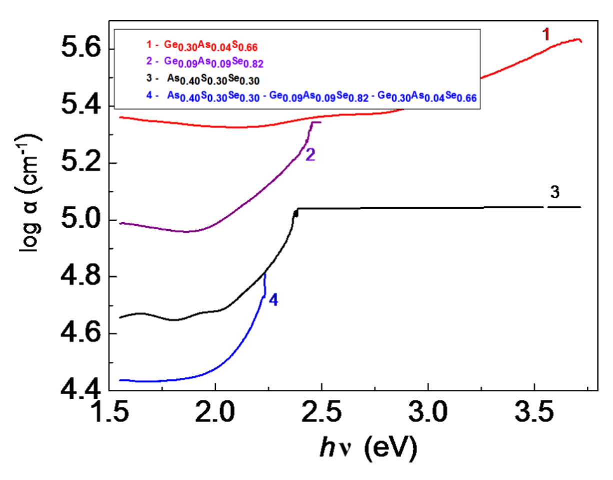

Figure 2: Absorption spectra α = *f*(*h*ν) of separate amorphous thin films and multilayer HS (1: $Ge_{0.30}As_{0.04}S_{0.66}$, 2: $Ge_{0.09}As_{0.09}Se_{0.82}$, 3: $As_{0.40}S_{0.30}Se_{0.30}$, 4: $As_{0.40}S_{0.30}Se_{0.30}/Ge_{0.09}As_{0.09}Se_{0.82}/Ge_{0.30}As_{0.04}S_{0.66}$).

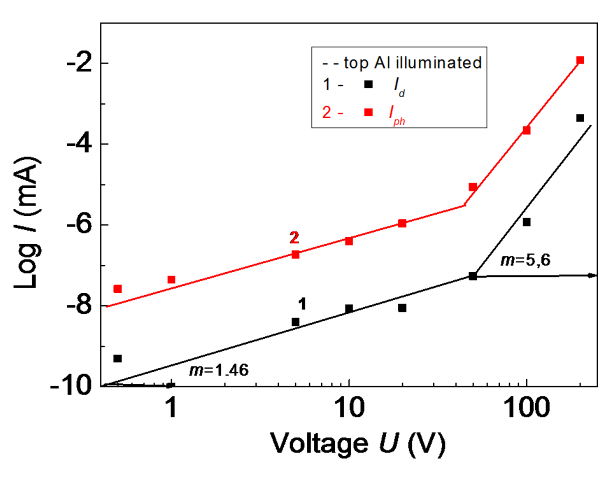

Figure 4: Current–voltage characteristics of the amorphous thin-film HS with a negative voltage applied to the top Al electrode, in the dark (1) and under illumination (2).

The absorption coefficient α of each separate component layer is higher than that of the HS. The highest value of the absorption coefficient α was obtained for the amorphous film of $Ge_{0.30}As_{0.04}S_{0.66}$ with the smallest thickness of $d \approx 200$ nm. The amorphous structures described above with two Al electrodes, of which the upper one was transparent to the incident light, have been used for electrical and photoelectrical measurements.

Figure 3 and Figure 4 show the current–voltage (*I*–*V*) characteristics of the amorphous thin-film HS Al–$As_{0.40}S_{0.30}Se_{0.30}$/$Ge_{0.09}As_{0.09}Se_{0.82}$/$Ge_{.0.30}As_{0.04}S_{0.66}$–Al with positive or negative voltage applied to the top Al electrode in the dark (curve 1) and under illumination with the wavelength of the maximum value of the photoconductivity (curve 2).

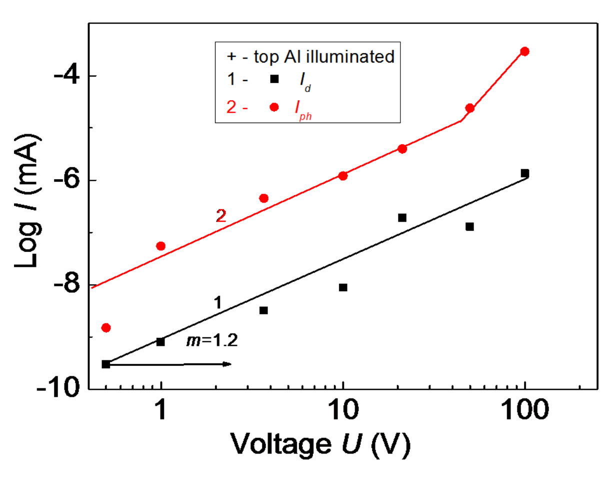

Figure 3: Current–voltage characteristics of the amorphous thin-film HS with a positive voltage applied to the top Al electrode, in the dark (1) and under illumination (2).

When a positive voltage is applied to the top Al electrode, a sharp increase of the current occurs, only under illumination, when the applied external electric field reaches high values. When a negative voltage is applied, this sharp increase of the current occurs in dark and under illumination. This effect was observed for amorphous thin-film structures with different electrodes (As_2S_3, $As_2S_3Ge_x$) and amorphous HS (As_2S_3/Sb_2S_3, Si/As_2S_3) [14]. *I*–*V* characteristics are described by the expression $I = A \cdot V^m$, where A is a constant coefficient, and m is the exponent. When carriers are injected from an amorphous or crystalline layer (or electrode) into another amorphous layer, m cannot take values larger than 1. The part of the *I*–*V* characteristics with $m = 2$ is explained by the existence of an exponential distribution of the localized sates in the bandgap of the amorphous material. In this case the *I*–*V* characteristics are described by the expression [15]:

$$j = N_V \mu e \left(\varepsilon / N_t e\right)^t \left(V^{t+1} \big/ d^{2^{t+1}} \right), \qquad (2)$$

where j is the current density, N_v is the effective density of states in the valence band, N_t is the concentration of traps, e is the electron charge, μ is the drift mobility, ε is the dielectric constant, $t = \Delta/(k_BT)$ (Δ is the parameter of the trap distribution, k_B is the Boltzmann constant, T is the absolute temperature), V is the applied voltage, and d is the sample thickness.

The explanation of our experimental data, as in the case for CIS-based solar cells with $1 < m < 2$ (the transition part to

$m > 2$) [16], is more complicated than that of the data of single-layer structures, because according to [16] the origin of the non-linear behavior may be the interface between the absorber and the buffer layer, and can thus not be attributed to space-charge-limited current (SCLC). We thank for fruitful discussion and we suggest that for more detailed information regarding the origin of SCLC in our investigated structures, additional investigations of the I–V characteristics at different temperatures are needed for the estimation of the parameters of localized states.

The steady-state photoconductivity spectra of all amorphous thin-film structures were measured with an applied external electric field of $E = 5 \times 10^4$ V/cm, that is, in the region were the I–V characteristics exhibit linear behavior. In our previous papers [7,8], we have presented the experimental results of steady-state and transient photocurrents of amorphous $\mathrm{Ge}_x\mathrm{As}_x\mathrm{Se}_{1-2x}$ and $(\mathrm{As}_4\mathrm{S}_3\mathrm{Se}_3)_{1-x}\mathrm{Sn}_x$ thin films. It was demonstrated that the dependence of the steady-state photocurrent on the light intensity for all investigated amorphous thin films is non-linear, and can be described by the expression $I_{\mathrm{ph}} \sim F^{\alpha}$ with the parameter $1.0 \leq \alpha \leq 0.5$, which indicates the existence of mono- and bimolecular recombination mechanisms in these materials.

Figure 5 and Figure 6 show the steady-state photocurrent spectra of separate amorphous thin films and HS Al–$\mathrm{As}_{0.40}\mathrm{S}_{0.30}\mathrm{Se}_{0.30}$/$\mathrm{Ge}_{0.09}\mathrm{As}_{0.09}\mathrm{Se}_{0.82}$/$\mathrm{Ge}_{.0.30}\mathrm{As}_{0.04}\mathrm{S}_{0.66}$–Al with positive or negative voltage applied to the illuminated top Al electrode. The steady-state photocurrent spectra show that the maximum of photosensitivity of the component layers of the multilayer HS is in a good agreement with the absorption spectra. The spectral distribution of the photocurrent for the HS is situated between the distributions of the separate layers and depends on the polarity of the illuminated electrode. The positions of the maximum of Al–$\mathrm{Ge}_{0.09}\mathrm{As}_{0.09}\mathrm{Se}_{0.82}$–Al ($h\nu = 2.47$ eV) and the maxima of Al–$\mathrm{Ge}_{0.30}\mathrm{As}_{0.04}\mathrm{S}_{0.66}$–Al ($h\nu = 2.95$ eV and $h\nu = 2.42$ eV) do not depend on the polarity of the applied voltage.

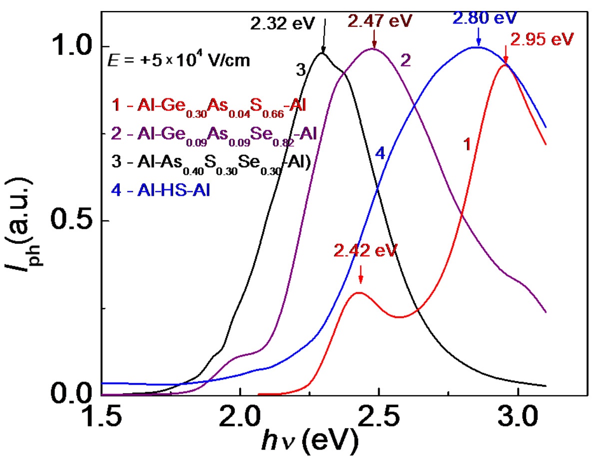

Figure 5: Photocurrent spectra of separate amorphous thin films and the multilayer HS with a positive voltage applied to the illuminated top Al electrode.

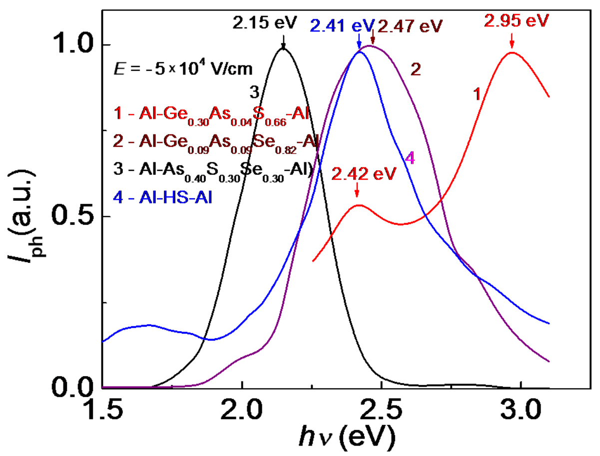

Figure 6: Photocurrent spectra of separate amorphous thin films and the HS with a negative voltage applied to the illuminated top Al electrode.

The presence of two maxima in the photoconductivity spectra of Al–$\mathrm{Ge}_{0.30}\mathrm{As}_{0.04}\mathrm{S}_{0.66}$–Al, located at $h\nu = 2.95$ eV and $h\nu = 2.42$ eV, indicates a probable separation of this sample into multiple phases that contain trigonal ($\mathrm{AsS}_{3/2}$) and tetrahedral (GeS_4) structural units, respectively. Figure 5 and Figure 6 also show that for the thin-film structure Al–$\mathrm{As}_{0.40}\mathrm{S}_{0.40}\mathrm{Se}_{0.30}$–Al and for the multilayer HS the position of the maximum in the spectral distribution of the photocurrent depends on the polarity of the applied voltage. When a positive voltage is applied to the illuminated Al electrode, the maximum is shifted toward the region of higher energies of the spectrum. As was mentioned in [8], this behavior can be associated with contact phenomena at the interfaces between metallic electrode and amorphous layers, as well as with the drift and surface recombination of the non-equilibrium carriers [14].

The normalized photocurrent spectra of the multilayer thin-film HS at different, positive and negative, values of the voltage applied to the illuminated top Al electrode ($U = 1.0$–10.0 V) are presented in Figure 7 and Figure 8. It is evident that increasing the positive applied voltage leads to a shift of the photocurrent maximum toward higher energies (Figure 7). An increase of the negative applied voltage leads to a shift of the photocurrent maximum toward lower energies (Figure 8). This shift can be attributed to the different resistance values and the different I–V characteristics of the component layers of the HS. The distribution of the applied voltage among the layers depends on the

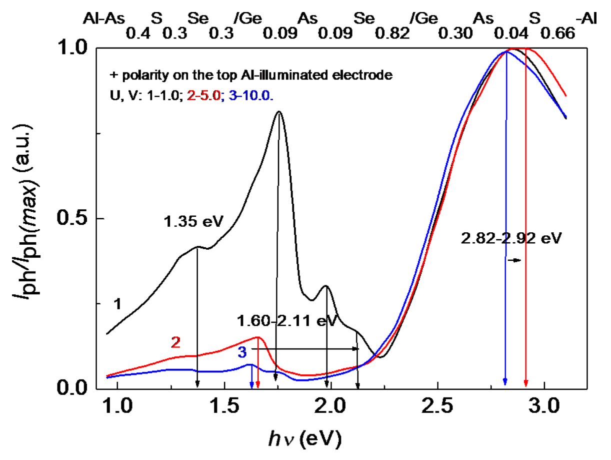

Figure 7: Normalized photocurrent spectra of the multilayer HS with different positive values of the voltage applied to the illuminated top Al electrode.

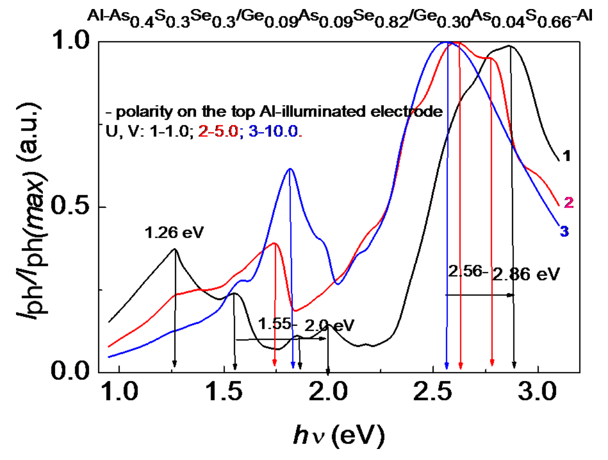

Figure 8: Normalized photocurrent spectra of the multilayer HS with different negative values of the voltage applied to the illuminated top Al electrode.

photocurrent. Therefore, the contribution of each layer to the total photocurrent is different. When the applied voltage has a positive polarity (0.1–200 V), the structure of the photocurrent spectra is more complicated. It was observed that at low applied voltages (0.1–0.5 V) the photocurrent is negative, and at U = 1.0 V the photocurrent changes to positive values. This phenomenon can occur when the external applied field becomes higher than the internal electrical field. For amorphous semiconductors the barrier height of an Al–semiconductor contact, with a work function of φ_m = 4.18 eV, is φ_b = 0.40–0.75 eV [14,17]. This is very important from a practical point of view, because there is the possibility to build photodetectors with different signs of the photocurrent. This phenomenon of photocurrent sign inversion through polarization was also observed for photodetectors based on $ZnAs_2$ anisotropic crystals [18].

Figure 8 shows that, besides the main peaks in the spectral distribution of the photocurrent at 2.56–2.92 eV, there are also significant peaks in the region of 1.26–2.11 eV. When the voltage applied to the top Al electrode has a positive polarity, the maximum at 2.82–2.92 eV is attributed to the absorption of light in the wide bandgap of $Ge_{0.30}As_{0.04}S_{0.66}$ ($E_g \approx 3.0$ eV). It weakly depends on the applied voltage, $\Delta(h\nu)$ = 0.1 eV. When the voltage applied to the top Al electrode has a negative polarity, the maximum at 2.56–2.86 eV is also attributed to the absorption of light in the wide bandgap of $Ge_{0.30}As_{0.04}S_{0.66}$ ($E_g \approx 3.0$ eV). However, it depends more strongly on the applied voltage, $\Delta(h\nu)$ = 0.3 eV. The other maxima at 1.26–2.11 eV correspond to the narrow-bandgap materials $Ge_{0.30}As_{0.04}S_{0.66}$ and $Ge_{0.09}As_{0.09}Se_{0.82}$. Some of them are also present in the spectral distribution of the single-layer structures (Figure 5 and Figure 6). Spectral position and amplitude of these maxima depend, among others, on the value and polarity of the applied voltage.

Figure 9 shows the position of the photocurrent maximum of the different components of the HS and of the HS itself at positive (curve 1) and at negative (curve 2) polarity of the voltage applied to the illuminated top Al electrode. The spectral position of the maximum of the photocurrent of the HS has an intermediate value with respect to the component layers.

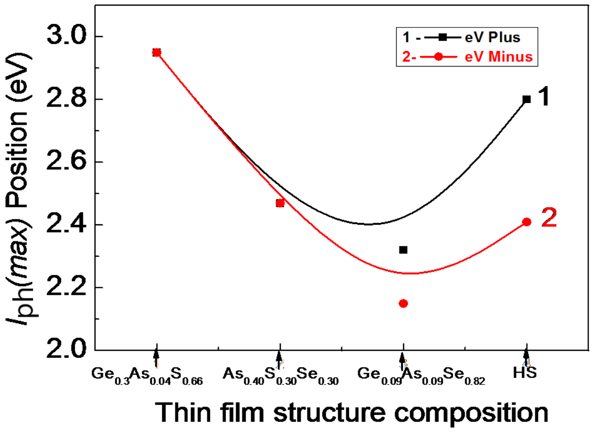

Figure 9: Peak position in the spectral distribution of the photocurrent for the different thin-film structures at positive (curve 1) and at negative (curve 2) polarity of the voltage applied to the illuminated top Al electrode. The lines are a guide to the eye.

Figure 10 shows the peak position in the spectral distribution of the photocurrent of the amorphous thin-film HS as a function of the applied voltage with positive (1) and with negative (2) polarity. At low applied voltages with positive polarity ($U \leq 10$ V), a shift of the maximum of the photocurrent to higher photon energies (from 2.3 eV to 2.9 eV) is observed. When the applied voltage is increased further up to U = 100 V,

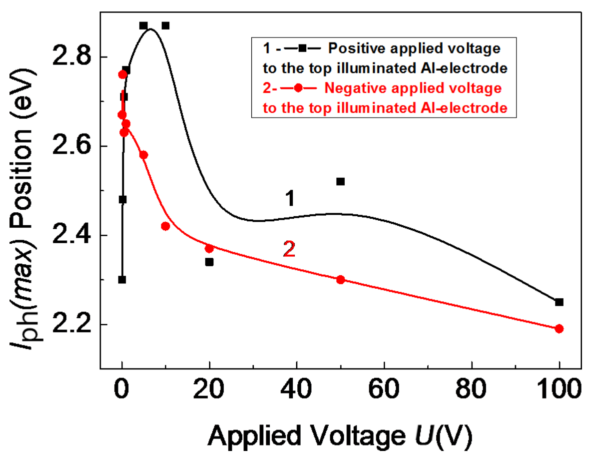

Figure 10: Peak position in the spectral distribution of the photocurrent of amorphous thin-film HS as a function of the applied voltage with positive (1) and negative (2) polarity (applied field $E = 5 \times 10^4$ V/cm). The lines are a guide to the eye.

the maximum returns to its initial position ($h\nu = 2.3$ eV, curve 1). At negative polarity, the maximum of the photocurrent is shifted only to lower photon energies (from 2.75 to 2.2 eV).

Figure 11 shows the magnifying power K (i.e., the ratio between photocurrent and dark current, $K = I_{ph}/I_{dark}$) of the thin-film structures and the HS both at positive (curve 1) and at negative (curve 2) polarity of the applied voltage. The value of K is higher at positive polarity than at negative polarity. Also, the amorphous Al–$As_{0.40}S_{0.30}Se_{0.30}$–Al thin-film structure shows the highest values of K.

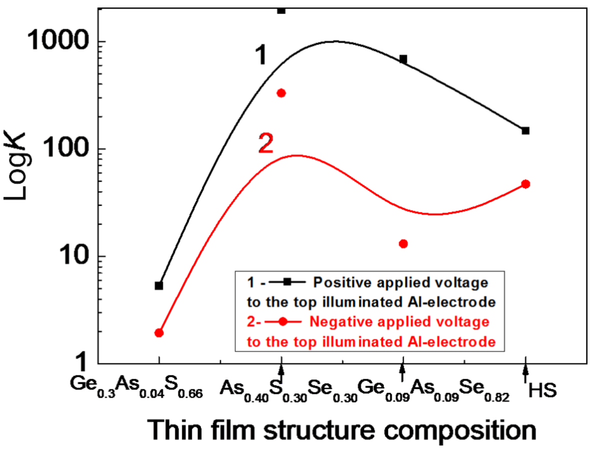

Figure 11: The magnifying power K of the different thin-film structures at positive (1) and at negative (2) polarity of the applied voltage (applied field $E = 5 \times 10^4$ V/cm). The lines are a guide to the eye.

Figure 12 shows the dependence of the magnifying power K of the amorphous thin-film HS as a function of the applied voltage with positive (1) and with negative (2) polarity. The photosensitivity is higher when the voltage applied at the illuminated top Al electrode has a positive polarity, which was also demonstrated for structures of single thin films [7].

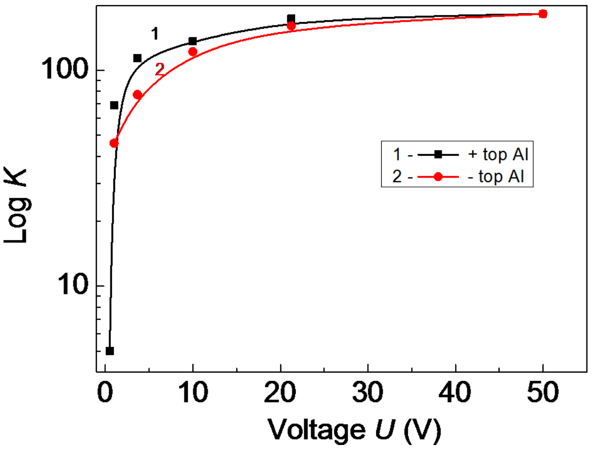

Figure 12: The magnifying power K of the amorphous thin-film HS as a function of the applied voltage with positive (1) and negative (2) polarity. The lines are a guide to the eye.

Conclusion

The experimental results regarding optical absorption and steady-state photoconductivity of both amorphous single-layer structures, Al–$As_{0.40}S_{0.30}Se_{0.30}$–Al, Al–$Ge_{0.09}As_{0.09}Se_{0.82}$–Al, and Al–$Ge_{0.30}As_{0.04}S_{0.66}$–Al and the heterostructure Al–$As_{0.40}S_{0.30}Se_{0.30}$/$Ge_{0.09}As_{0.09}Se_{0.82}$/$Ge_{0.30}As_{0.04}S_{0.66}$–Al have been discussed. The spectral distribution of the photocurrent depends on the value and on the polarity of the voltage applied to the illuminated top Al electrode. It was found, that at low applied voltages with positive polarity ($U \le 10$ V) the maximum of the photocurrent is shifted to higher photon energies (from 2.3 to 2.9 eV) with increasing voltage. When the applied voltage is further increased up to $U = 100$ V, the maximum returns to its initial position.

The shift of the photocurrent maximum may be related to the component layers of the HS. Because the resistance of the wide-bandgap material ($Ge_{0.30}As_{0.04}S_{0.66}$) is higher, at low voltages the electrical field mainly is distributed in this material, which leads to a photoconductivity maximum in the high-energy region. When the voltage is further increased, the electrical field is also distributed in the narrow-bandgap materials and the position of the photocurrent maximum is shifted in to the low-energy region. For GeTe and GeSe films, an analogous shift was explained by bulk phenomena in the material, not by contact phenomena [19]. In contrast, when the applied voltage has a negative polarity, the maximum of the photocurrent is shifted only to lower photon energies (from 2.75 to 2.2 eV).

Besides that, the magnifying power, $K = I_{\text{ph}}/I_{\text{dark}}$, depends on the composition of the thin-film structures and of the HS and on the polarity of the applied voltage as well. Moreover, it was demonstrated that higher values of the magnifying power K were reached at positive polarity for all investigated amorphous thin-film structures. This result can be explained by drift processes of non-equilibrium carriers in amorphous semiconductors as well as by the contact phenomena between interfaces of different amorphous materials and the metallic electrodes.

Funding

This work was supported by the project ANCD 20.80009.5007.14.

References

1. Blonskyi, I.; Kadan, V.; Shpotyuk, O.; Iovu, M.; Korenyuk, P.; Dmitruk, I. *Appl. Phys. B: Lasers Opt.* **2011,** *104,* 951–956. doi:10.1007/s00340-011-4390-x
2. Reinfelde, M.; Teteris, J. *J. Optoelectron. Adv. Mater.* **2011,** *13,* 1531–1533.
3. Sergeev, S. A.; Iovu, M. S.; Meshalkin, A. Y. *Chalcogenide Lett.* **2020,** *17,* 25–31.
4. Golovchak, R.; Shpotyuk, O.; Iovu, M.; Kovalskiy, A.; Jain, H. *J. Non-Cryst. Solids* **2011,** *357,* 3454–3460. doi:10.1016/j.jnoncrysol.2011.06.019
5. Iovu, M. S.; Shutov, S. D.; Arkhipov, V. I.; Adriaenssens, G. J. *J. Non-Cryst. Solids* **2002,** *299–302,* 1008–1012. doi:10.1016/s0022-3093(01)01067-5
6. Boolchand, P.; Georgiev, P.; Iovu, M. *Chalcogenide Lett.* **2005,** *2,* 27–34.
7. Iaseniuc, O.; Iovu, M. *Rom. Rep. Phys.* **2017,** *69,* No. 505.
8. Iovu, M.; Iaseniuc, O. *Optoelectron. Adv. Mater., Rapid Commun.* **2018,** *12,* 563–567.
9. Kikineshi, A.; Palyok, V.; Szabó, I. A.; Shipljak, M.; Ivan, I.; Beke, D. L. *J. Non-Cryst. Solids* **2003,** *326–327,* 484–488. doi:10.1016/s0022-3093(03)00457-5
10. Trunov, M. L.; Nagy, P. M.; Takats, V.; Lytvyn, P. M.; Kokenyesi, S.; Kalman, E. *J. Non-Cryst. Solids* **2009,** *355,* 1993–1997. doi:10.1016/j.jnoncrysol.2009.04.055
11. Blonskyi, I.; Kadan, V.; Shpotyuk, O.; Iovu, M.; Pavlov, I. *Opt. Mater.* **2010,** *32,* 1553–1557. doi:10.1016/j.optmat.2010.07.006
12. Iovu, M. S.; Iaseniuc, O.; Colomeico, E. P.; Cojocaru, I. A.; Shepel, D. F.; Meshalkin, A. In *Proceedings of ARA 36th International Congress,* University LUM, School of Management Gioia del Colle, Bari, Italy; 2012.
13. Iovu, M. S.; Benea, V. G.; Colomeico, E. P.; Iovu, M. A.; Cojocaru, I. A.; Shpotyuk, O.; Golovchak, R. Y. *J. Optoelectron. Adv. Mater.* **2011,** *13,* 1417–1422.
14. Popescu, M.; Andrieș, A.; Ciumaș, V.; Iovu, M.; Șutov, S.; Țiuleanu, D. *Physics of chalcogenide glasses;* Stiința Publishing house: Chisinau, 1996.
15. Lampert, M.; Mark, P. *Injection currents in solids;* Mir Publishing house: Moscow, Russia, 1973.
16. Zelenina, A.; Werner, F.; Elanzeery, H.; Melchiorre, M.; Siebentritt, S. *Appl. Phys. Lett.* **2017,** *111,* 213903. doi:10.1063/1.5006040
17. Ciobanu, M. *Mold. J. Phys. Sci.* **2017,** *16,* 234–241.
18. Stamov, I. G.; Syrbu, N. N.; Dorogan, A. V.; Nemerenco, L. L. *Opt. Commun.* **2008,** *281,* 2459–2466. doi:10.1016/j.optcom.2007.12.053
19. Stiles, P. J.; Chang, L. L.; Esaki, L.; Tsu, R. *Appl. Phys. Lett.* **1970,** *16,* 380–382. doi:10.1063/1.1653033

License and Terms

BEILSTEIN JOURNAL OF NANOTECHNOLOGY

Molecular dynamics modeling of the influence forming process parameters on the structure and morphology of a superconducting spin valve

Alexander Vakhrushev*[1,2,3], Aleksey Fedotov[1,2,3], Vladimir Boian[3,4], Roman Morari[4,5] and Anatolie Sidorenko[3,4,6]

Full Research Paper

Open Access

Address:
[1]Modeling and Synthesis of Technological Structures Department, Institute of Mechanics, Udmurt Federal Research Center, Ural Division, Russian Academy of Sciences, Baramzinoy 34, Izhevsk 426067, Russia, [2]Nanotechnology and Microsystems Department, Kalashnikov Izhevsk State Technical University, Studencheskaya 7, Izhevsk 426069, Russia, [3]Orel State University named after I.S. Turgenev, Komsomolskaya Str. 95, 302026, Orel, Russia, [4]Ghitu Institute of Electronic Engineering and Nanotechnologies, Academiei Str. 3/3, MD-2028, Chisinau, Republic of Moldova, [5]Laboratory of Topological Quantum Phenomena in Superconducting Systems (TQPSS), MIPT, Institutskiy Per. 9, 141701, Dolgoprudny, Russia and [6]Technical University of Moldova, 168 Stefan cel Mare Avenue, MD-2004, Chisinau, Republic of Moldova

Email:
Alexander Vakhrushev* - Vakhrushev-a@yandex.ru

* Corresponding author

Keywords:
hybrid nanostructure; mathematical modeling; modified embedded-atom method; molecular dynamics; spintronics; spin valve; vacuum deposition

Beilstein J. Nanotechnol. **2020,** *11,* 1776–1788.
https://doi.org/10.3762/bjnano.11.160

Received: 01 June 2020
Accepted: 30 October 2020
Published: 24 November 2020

This article is part of the thematic issue "Functional nanostructures for electronics, spintronics and sensors".

Associate Editor: P. Leiderer

Abstract

This work is a study of the formation processes and the effect of related process parameters of multilayer nanosystems and devices for spintronics. The model system is a superconducting spin valve, which is a multilayer structure consisting of ferromagnetic cobalt nanolayers separated by niobium superconductor nanolayers. The aim was to study the influence of the main technological parameters including temperature, concentration and spatial distribution of deposited atoms over the nanosystem surface on the atomic structure and morphology of the nanosystem. The studies were carried out using the molecular dynamics method using the many-particle potential of the modified embedded-atom method. In the calculation process the temperature was controlled using the Nose–Hoover thermostat. The simulation of the atomic nanolayer formation was performed by alternating the directional deposition of different composition layers under high vacuum and stationary temperature conditions. The structure and thickness of the formed nanolayers and the distribution of elements at their interfaces were studied. The alternating layers of the formed nanosystem and their interfaces are shown to have significantly different atomic structures depending on the main parameters of the deposition process.

Introduction

Multilayer superconductor/ferromagnetic (S/F) hybrid nanostructures are a new type of quantum electronics elements based on electron spin transport. Unlike conventional electronics, spintronics uses not only charge transfer, but also the electron spin in solids, solving the problem of transport and recording of information [1-7]. Based on the basic nondissipative elements of spintronics, it is possible to create new superconducting nanoelectronics devices that consume minimum energy and have a high operation speed [8-13].

One type of magnetic nanostructure with wide potential use is the spin valve [14,15], consisting of several magnetic films separated by a magneto-resistive layer. Due to the exchange interaction with the adjacent antiferromagnetic nanofilm, one of the layers has constant magnetization. For the adjacent nanofilm, the direction of magnetization can be controlled by an external magnetic field. The weak link of the ferromagnetic layers causes a restructuring of the magnetic moment configuration under low-power magnetic fields and switches the spin valve from a high to a low resistance state. When a superconducting film is used as a magneto-resistive interlayer, a superconducting spin valve is obtained. Furthermore, these structures are highly sensitivity to magnetic field switching and energy consumption is significantly reduced due to the absence of dissipation in such a valve in the ground (superconducting) state.

Practice shows that the creation of multilayer S/F nanostructures with the required properties is an extraordinarily complex process. Figure 1 and Figure 2 show actual spin-valve multilayer nanosystems formed from various materials [9]. As demonstrated in the figures, the structure of real nanosystems is far from ideal. In particular, it can be noted that the surface separating the various nanolayers of the system is not perfectly flat. The surface has noticeable irregularities that penetrate into adjacent layers. The figures also show that there is a mutual penetration of one contact layer into another. Therefore, the layer interface has a certain quantifiable thickness. It should be noted that the atomic structure of each layer does not form an

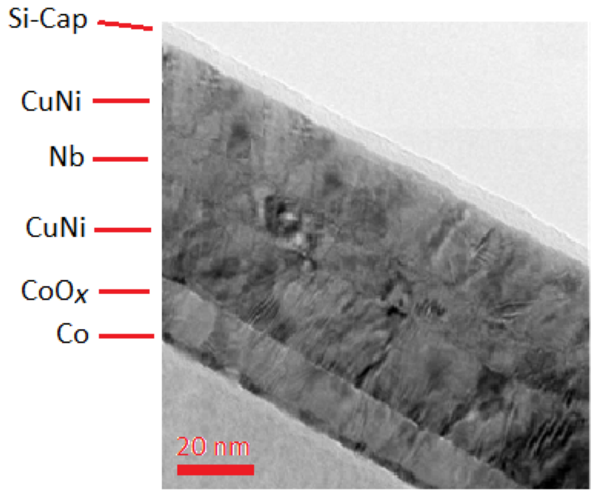

Figure 1: Transmission electron microscopy (TEM) image of a layered nanostructure consisting of Nb, CuNi, CoO_x and Co layers, prepared by magnetron sputtering.

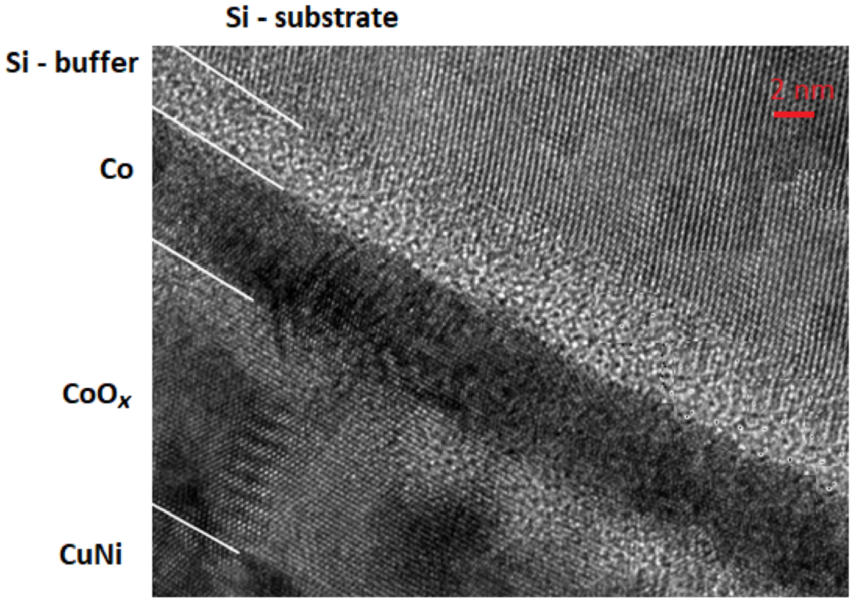

Figure 2: High-resolution transmission electron microscopy (HR-TEM) image of a layered Co, CoO_x and CuNi nanostructure prepared by magnetron sputtering.

ideal single crystal, but rather a polycrystalline system is formed.

The influence of the interface quality on the spin valve functionality is an especially important issue, which has been experimentally investigated in previous works [16-19] where the quantum-mechanical transparency of the interface, T_F, was assigned. Here, they considered the effect of the mutual solubility of the metals (of a superconductor and a ferromagnet) on the quantum-mechanical transparency. The transparency parameter of the interface for completely non-wetting metals, such as lead–iron, is small: $T_\text{F} \approx 0.4$. This reduces the probability of penetration of Cooper pairs from the superconductor into the ferromagnetic material and requires smaller thicknesses of superconducting layers in order to obtain a significant effect of ferromagnetism on superconductivity. In turn, the structural quality of superconducting niobium layers, for example, with a thickness comparable to the coherence length of approximately <10 nm, is worse than that of thicker films, and the destructive effect of the interface roughness also suppresses the manifestation of interference effects in ultrathin films.

For highly mutually soluble metals, such as vanadium and iron (solubility of about 30% at room temperature), the quantum-mechanical transparency parameter is many times higher, $T_\text{F} \approx 1.6$. However, if the structural quality of the films requires deposition on a substrate heated to 100–300 °C, there is a high risk of mutual diffusion and the formation of a thick "dead" layer, which also suppresses the transparency of the S/F interface [20].

In the case of materials wetting and limited mutual solubility (as in niobium–nickel and niobium–cobalt, with solubility of about 5% at room temperature), the transparency parameter is $T_\text{F} \approx 2$ and is the highest of all possible metal pairs. It is possible that high transparency is facilitated not only in the mixing layer at the interface between extremely thin film materials, but also by a good matching of the band structures of two metals (see the study in [21,22]). A detailed discussion of the boundary resistance issue of two metals in contact and experimental data analysis for a number of magnetic and nonmagnetic metals pairs is given in [23].

A number of previous studies suggest that a significant increase in the interdiffusion of niobium and cobalt with an increase in the substrate temperature will decrease the transparency parameter T_F and worsen the functional parameters of the layered S/F heterostructure.

The implementation of optimal technological processes is required to minimize these defects and imperfections of layered nanosystems. This would require basic research for a deep understanding of the physical and chemical processes taking place at different structural levels of the used materials. In addition, the development of manufacturing technology for a fundamentally new device for superconducting spintronics requires a long period of equipment time and highly specialized knowledge, together with a large number of experiments aimed at optimizing the process.

Thus, due to the laborious nature of vacuum technologies, the high cost and long duration of experimental methods for investigation of the physics and chemical properties of S/F nanosystem formation, it would be very useful to develop new integrated methods that combine theoretical modeling and experimental methods for analyzing the formation processes and properties of this class of functional nanomaterials and nanostructures. Here, computer simulation can significantly reduce the number of technological steps and adjustments required to obtain the desired multilayer nanostructure.

It should be noted that mathematical modeling is widely used in the design and analysis of various nanosystems properties [24,25]; however, in relation to the considered class of multilayer nanosystems for spintronics, the number of works is extremely limited.

This work presents the advancements in our previous studies on the modeling of various nanosystems [26-29], including spintronic studies [30-32], where the aim was to investigate the influence of selected technological parameters (substrate temperature, concentration and spatial distribution of the deposited atoms over the interface) on the structure and morphology of the layered nanosystem.

Mathematical Model and Theoretical Foundations

The formation processes and the structure of multilayer systems for spintronics applications were studied by the molecular dynamics method [33,34]. Molecular dynamics describes the motion of each nanosystem atom at a certain point in time, therefore, it is possible to reproduce the detailed evolution of nanoelements and their properties. The basis of the method is the equations of motion of all atoms supplemented by the initial conditions in the form of atom coordinates and velocities:

$$m_i \frac{\mathrm{d}^2\mathbf{r}}{\mathrm{d}t^2} = -\frac{\partial U(\mathbf{r})}{\partial \mathbf{r}_i} + \mathbf{F}_\text{ex},\ \mathbf{r}_i(t_0) = \mathbf{r}_{i0},\ \frac{\mathrm{d}\mathbf{r}_i(t_0)}{\mathrm{d}t} = \mathbf{V}_{i0}, \tag{1}$$

$$i = 1,\ldots N,$$

where N is the number of atoms that form the nanosystem. In this equation, m_i is the mass of the ith atom; $\mathbf{r}_{i0}$, $\mathbf{r}_i(t)$ are the initial and current radius vector of the ith atom, respectively; $U(\mathbf{r})$ is the system potential, which depends on the relative position of all atoms; $\mathbf{V}_{i0}$, $\mathbf{V}_i(t)$ are the initial and current speed of the ith atom, respectively; $\mathbf{r}(t) = \{\mathbf{r}_1(t), \mathbf{r}_2(t), \ldots, \mathbf{r}_N(t)\}$ shows the dependence of the location of all the atoms in the system; $\mathbf{F}_{\mathrm{ex}}$ is the external force, which reflects the interaction of the nanosystem with the external environment, including adjustments to the energy to maintain a constant temperature.

The molecular dynamics method is based on the concept of potential $U(\mathbf{r})$, which is responsible for the nature and magnitude of the interactions of the atoms in the nanosystem.

There are many possible choices for the type of potential, but recently, due to its accuracy and adequacy, many-particle force fields have gained great popularity. In this work, we used the potential of the modified embedded-atom method (MEAM) which is based on density functional theory (DFT). In this method, the resulting potential of the nanosystem is represented as the sum of the energy contributions of the individual atoms, and the contributions of pair and multielement interactions are considered separately. Thus,

$$U(r) = \sum_i U_i(r) = \sum_i \left(F_i(\bar{\rho}_i) + \frac{1}{2} \sum_{j \neq i} \phi_{ij}(r_{ij}) \right), i = 1, 2, \ldots N, \quad (2)$$

where $U_i(r)$ is the potential of an individual atom, affecting the type and degree of interaction in the equations of motion (Equation 1); F_i is the atom immersion function, which is dependent on electron background density $\bar{\rho}_i$; $\phi_{ij}(r_{ij})$ is a contribution of the pair potential to the total energy, which varies with distance r_{ij}.

The immersion function is corrected by the force field created through pair interactions and refines this value. This value is due to the presence of electron gas in the material and, in accordance with [33,34], can be calculated by the formula

$$F_i(\bar{\rho}_i) = \begin{cases} A_i E_i^0 \bar{\rho}_i \ln(\bar{\rho}_i), & \bar{\rho}_i \geq 0 \\ -A_i E_i^0 \bar{\rho}_i, & \bar{\rho}_i < 0 \end{cases}, \quad (3)$$

where A_i is an empirical force field parameter; E_i^0 is the value of sublimation energy; and $\bar{\rho}_i$ is the value of the background electron density.

To calculate the background electron density at the immersion point, the following equation is used in which all electronic orbitals of atoms of various configurations contribute their terms as

$$\bar{\rho}_i = \frac{\rho_i^{(0)}}{\rho_i^0} G(\Gamma_i), \ \Gamma_i = \sum_{k=1}^{3} t_i^{(k)} \left(\frac{\rho_i^{(k)}}{\rho_i^{(0)}} \right)^2, \quad (4)$$

where the parameters $t_i^{(k)}$ are the weight coefficients of the model; ρ_i^0 is the magnitude of the background electron density of the initial structure; and $\rho_i^{(k)}$ characterizes the change in electron density under real conditions. The indices $k = 1,2,3$ represent the different types of electronic orbitals of an atom. In this sense, there are spherically symmetric one-electron s-orbitals and angular-electron p-, d-, and f-clouds. The electronic distribution density of each orbital is calculated according to its own formula:

$$s \text{ orbital: } \rho_i^{(0)} = \sum_{i \neq j} \rho_j^{A(0)}(r_{ij}) S_{ij}, \quad (5)$$

$$p \text{ orbital: } \left(\rho_i^{(1)}\right)^2 = \sum_{\alpha} \left[\sum_{i \neq j} \frac{r_{ij\alpha}}{r_{ij}} \rho_j^{A(1)}(r_{ij}) S_{ij} \right]^2, \quad (6)$$

$$\begin{aligned} d \text{ orbital: } \left(\rho_i^{(2)}\right)^2 &= \sum_{\alpha,\beta} \left[\sum_{i \neq j} \frac{r_{ij\alpha} r_{ij\beta}}{r_{ij}^2} \rho_j^{A(2)}(r_{ij}) S_{ij} \right]^2 \\ &- \frac{1}{3} \left[\sum_{i \neq j} \rho_j^{A(2)}(r_{ij}) S_{ij} \right]^2, \end{aligned} \quad (7)$$

$$\begin{aligned} f \text{ orbital: } \left(\rho_i^{(3)}\right)^2 &= \sum_{\alpha,\beta,\gamma} \left[\sum_{i \neq j} \frac{r_{ij\alpha} r_{ij\beta} r_{ij\gamma}}{r_{ij}^3} \rho_j^{A(3)}(r_{ij}) S_{ij} \right]^2 \\ &- \frac{5}{3} \sum_{\alpha} \left[\sum_{i \neq j} \frac{r_{ij\alpha}}{r_{ij}} \rho_j^{A(3)}(r_{ij}) S_{ij} \right]^2, \end{aligned} \quad (8)$$

where $\rho^{A(k)}$ are radial functions; S_{ij} is the potential shielding function; and $r_{ij\alpha}$ is component α from the distance vector between atoms $\alpha,\beta,\gamma = x,y,z$.

The functional $G(\Gamma)$ in Equation 4 can be defined in various ways. One of the most popular formulations is used here and is given as follows:

$$G(\Gamma)=\begin{cases}\sqrt{1+\Gamma},\ \Gamma\geq -1\\ -\sqrt{|1+\Gamma|},\ \Gamma<-1\end{cases}. \tag{9}$$

The weight coefficients of the MEAM from Equation 4 also have an additive relationship with single-electron radial functions given as

$$t_i^{(k)}=\frac{\sum_{i\neq j}t_{0,j}^{(k)}\rho_j^{A(0)}S_{ij}}{\sum_{i\neq j}\left(t_{0,j}^{(k)}\right)^2\rho_j^{A(0)}S_{ij}}, \tag{10}$$

where $t_{0,j}^{(k)}$ are empirical parameters that depend on the chemical type of the element.

Distance energy smoothing in MEAM is achieved by introducing a shielding function. Using the screening function, the attenuation of the potential occurs gradually, which allows one to provide a more physically accurate nanomaterial properties description and reduces computational costs during simulation:

$$\begin{gathered}S_{ij}=f_{\mathrm{c}}\left(\frac{r_{\mathrm{c}}-r_{ij}}{\Delta r}\right)\prod_{k\neq i,j}f_{\mathrm{c}}\left(\frac{C_{ikj}-C_{\min,ikj}}{C_{\max,ikj}-C_{\min,ikj}}\right),\\ C_{ikj}=1+2\frac{r_{ij}^2r_{ik}^2+r_{ij}^2r_{jk}^2-r_{ij}^4}{r_{ij}^4-\left(r_{ik}^2-r_{jk}^2\right)^2},\end{gathered} \tag{11}$$

$$f_{\mathrm{c}}(x)=\begin{cases}1,\ x\geq 1\\ \left[1-(1-x)^4\right]^2,\ 0<x<1,\\ 0, x\leq 0\end{cases} \tag{12}$$

where $C_{\min}$, $C_{\max}$ are the parameters of the mutual influence of atoms, depending on their chemical types, and are set for each triple of atoms with numbers i, j, k. In Equation 11, r_{c} is the distance at which the force field is cut off and $f_{\mathrm{c}}(x)$ is a function that smooths the potential after x exceeds the cutoff distance r_{c}.

Problem Statement and Software

The influence of the process parameters on the formation of spin system S/F hybrid structures is studied for a multilayer nanosystem based on cobalt and niobium. This system is a functional material that has demonstrated a giant spin-valve effect, which was theoretically and experimentally investigated in previous works [13,19,35]. In these works, the authors proposed a new design and performed the calculation of a spin valve consisting of superconducting plates and an artificial magnetic metamaterial placed between them, formed by periodically alternating thin and thick nanolayers of a ferromagnetic metal. The thickness of the layers affects the magnetic exchange interaction between ferromagnetic layers, which allows for the possibility of artificial magnetic metamaterials designed with tunable properties.

The choice of niobium and cobalt as the metals forming the nanolayers is made because of the wide potential of using these elements in spintronics. At the moment, not only has research been carried out on spintronic devices involving these metals [36,37], but also new patents are being issued [38-40].

The general scheme of the investigated nanosystem is presented in Figure 3.

The numbers in Figure 3 next to the elements in the layers represent their thickness in nanometers. The sample production is carried out by the magnetron deposition method in vacuum. In general, a nanosystem contains about 20 layers. In this work,

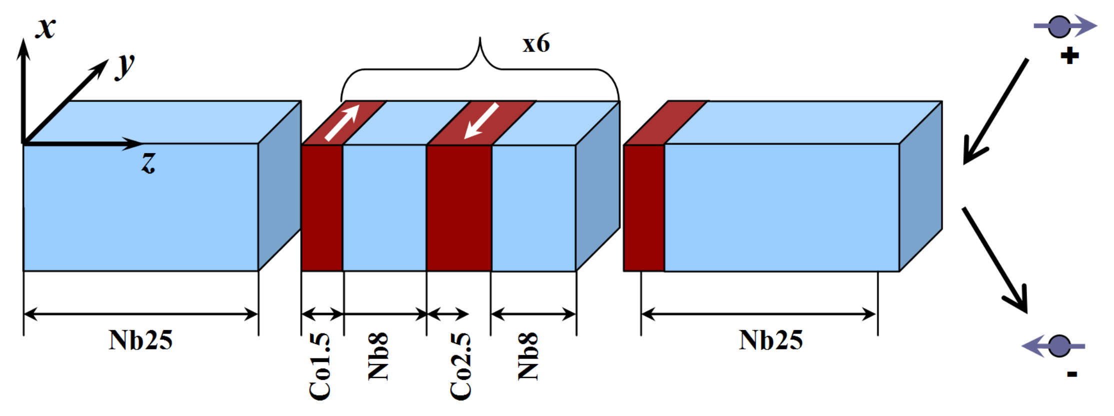

Figure 3: Sketch of a Nb/Co spin-valve nanosystem. The numbers next to the elements in the layers represent the layer thickness in nanometers.

we consider the deposition of only the first four layers of cobalt and niobium.

The general problem statement for the multilayer nanosystem formation process modeling is presented in Figure 4. The first material layer formed by atoms of single-crystal niobium (in the real deposited structures niobium layers have crystalline structure [18]) serves as the substrate and the basis for the vacuum deposition of subsequent nanofilms.

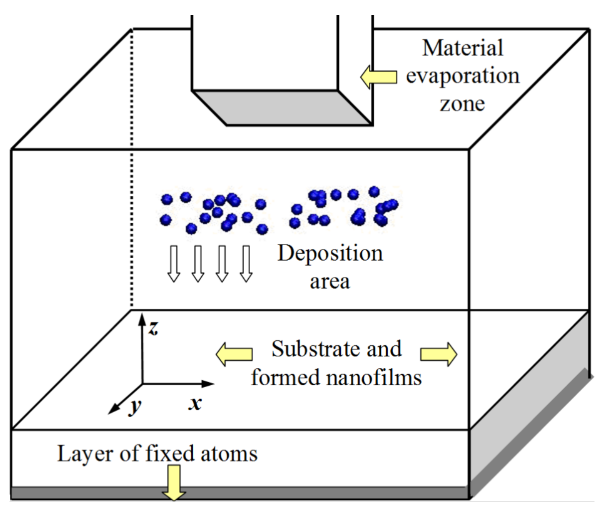

Figure 4: Scheme of the multilayer nanosystem formation modeling processes. The nanosystem contains a material evaporation zone, atom deposition area, and a substrate with a fixed lower layer of atoms. During the first nanofilm formation, the deposition is carried out directly on the substrate; subsequent depositions are made on the substrate with previously formed nanofilms.

The substrate is placed in the lower region of the computational cell; its extreme layer is fixed to prevent chaotic movement of the sample during the simulation. In the horizontal direction, periodic boundary conditions are imposed on the computational cell, which reduces the computational cost. In the upper region, boundary reflection conditions are present so that the deposited atoms do not leave the modeling system. The deposition process is simulated by the appearance of atoms in the evaporation zone above the substrate. In this case, the deposited atoms gained speed towards the substrate. The layers are sprayed in stages. During the formation of all layers, the magnetic field was absent in the nanosystem.

The temperature and pressure for the deposited atoms was not regulated. The deposited atoms are given an initial velocity of approximately 0.1 Å/ps (or 10 m/s) towards the substrate surface. Subsequently, the speed of these atoms gradually decreases due to the energy exchange with the substrate surface atoms and the upper atom's layers of the formed nanolayers. The substrate temperature in each calculation is held constant. The concentration of the deposited atoms was about five atoms per cubic nanometer.

The upper boundary of the computational cell was shifted during the transition to the deposition of the next nanolayer by the value of its thickness. Thus, the deposition region above the substrate turned out to be approximately the same for each nanosystem layer. The process parameters that affect the resulting nanomaterial properties were the following: the deposition rate, controlled through the number of deposited atoms per unit time; substrate temperature; and spraying flux density, which was determined by the area of the evaporation zone.

As the computational module of the program for theoretical research, the large-scale atomic/molecular massively parallel simulator (LAMMPS) computing complex was used [41]. This software and tool package is freely distributed, contains the ability to perform parallel computing and supports multilevel mathematical models, including molecular dynamics. The results analysis algorithms were described in TCL and C++. Based on LAMMPS, scripts and algorithms were developed and implemented for a detailed study of the structure and spatial profile of a S/F material. The results were visualized using the Visual Molecular Dynamics (VMD) [42] and Open Visualization Tool (OVITO) [43] software packages, which not only provide images of nano-objects atomic and molecular structures, but also construct spatial profiles and distributions by the target parameter, e.g. height or coordination number.

Results and Discussion

A series of numerical experiments on modeling the multilayer hybrid structure formation processes based on cobalt and niobium were performed. The variable elements in the studies were the material fabrication technological parameters, including the substrate temperature, the intensity and area of the deposition flow. The influence of technological modes was evaluated in comparison with the basic version of the nanosystem.

As a basic variant, the growth processes were considered at 300 K (substrate temperature) and deposition was carried out by a uniform flow over the entire surface of the substrate. The term temperature in this work is synonymous with substrate temperature.

The temperature of the nanosystem was controlled using a Nose–Hoover thermostat. The deposited atoms had a directed velocity; therefore, they were not involved in the direct correction of the thermostat. The formation of a multilayer system was carried out in several stages. Each layer was deposited by the sequential deposition of niobium or cobalt.

At the first stage, cobalt was deposited on a substrate formed by niobium atoms. The substrate had a crystalline structure with a height of 3.7 nm and a width of 13.2 nm in the horizontal direction. For the mark of zero height, from which the layers of the deposited material began to form, the substrate surface was chosen. The number of niobium atoms in the substrate was 33,600.

To match the simulation results and experimental data, in addition to the required nanolayer thickness, 18,000 cobalt atoms were deposited on the substrate in the first stage, 70,000 niobium atoms were deposited in the second, and 30,000 cobalt atoms were deposited in the third stage. As a result, three nanofilms with a thickness of 1.5 nm, 8.0 nm and 2.5 nm were formed. The duration of the layer deposition process under normal conditions was chosen according to the desired thickness and was 0.2 ns, 0.6 ns, and 0.4 ns, respectively. An image of a multilayer nanosystem resulting from the mathematical modeling is presented in Figure 5.

Figure 5 clearly demonstrates the niobium and cobalt layered nanosystem formation: the layers formed by niobium and cobalt atoms have a polycrystalline structure. In this case, groups of atoms are combined into domains with different spatial orientations. The blurring of the contact area between the layers and a less even surface profile compared to niobium are noticeable.

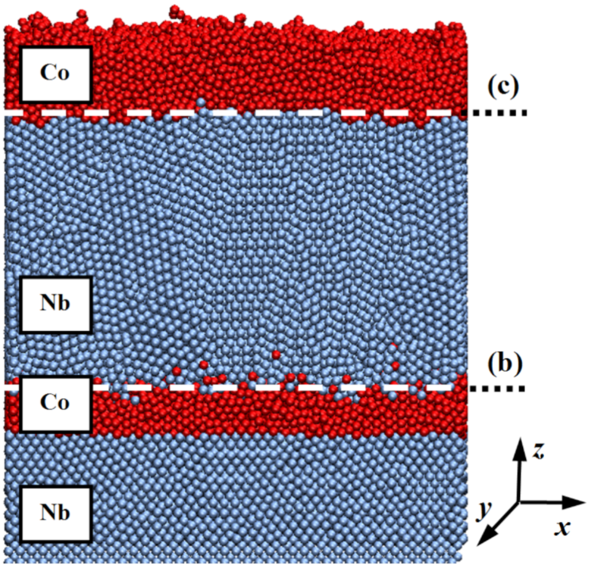

Figure 5: Multilayer nanosystem of niobium and cobalt. The contact points of the nanofilms are indicated by (b) and (c). At the indicated contact points, the distribution of coordination numbers is given in Figure 6. The substrate temperature was fixed at 300 K.

A quantitative characteristic of the material spatial structure can be obtained by calculating the coordination number. The coordination number in crystallography reflects the number of nearby equally distant atoms of the same type in the crystal lattice. The number of nearest neighbors determines the material packing density. For different types of crystal lattices, the coordination number will be different. The cubic volume-centered lattice (characteristic of niobium) has a coordination number equal to 8, whereas the hexagonal close-packed lattice (corresponding to cobalt) is 12. For the formed nanosystem, the change in the average value of the coordination number in the layers was calculated and shown in Figure 6.

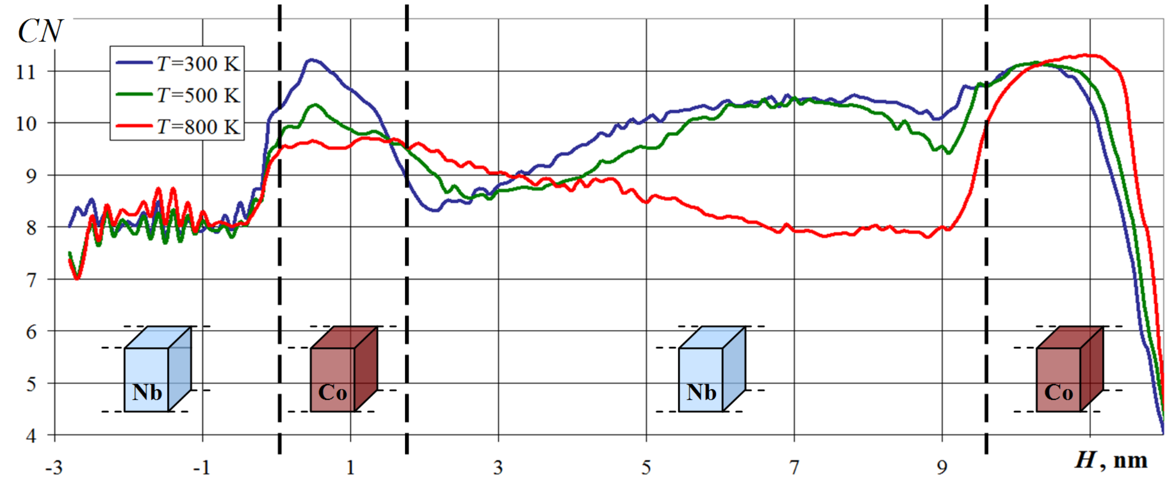

Figure 6: Change in coordination (CN) number along the *z*-axis (shown in Figure 5) in Nb and Co layers of the nanostructure. The contact points of the nanofilms are shown by the dashed vertical lines. The distribution is plotted for substrate deposition at 300, 500, and 800 K.

The change in the coordination number in Figure 6 correlates with the structure of the nanomaterial shown in Figure 5. The niobium substrate has a parameter value close to 8, which indicates its crystalline structure. The cobalt nanofilms are characterized by a higher coordination number in the range of 10–11. This value does not reach 12, which corresponds to the ideal crystalline state of a hexagonal close-packed lattice, indicating an amorphous-like structure of cobalt nanofilms. Variations in the coordination number within the intermediate niobium layer are more significant. When approaching the contact regions with cobalt, an increase in this parameter is observed.

Thus, it was shown that the structure of the nanomaterial depends not only on the current layer characteristics, but also on the structural features of the regions adjacent to it. In addition, the temperature has a definite effect on the number of nearest neighbors in a nanosystem, and therefore on its structure and properties. A significant decrease in the coordination number in the outer layers of the last nanofilm is associated with the surface effects and boundary phenomena appearance in that region. The spatial distribution of this parameter is shown in Figure 7.

The spatial distribution of the coordination number in the formed multilayer nanocomposite, illustrated in Figure 7, characterizes its structure in more detail. The dashed lines in Figure 7 indicate the locations of the parallel sections shown in Figure 7b and Figure 7c. The sections correspond to the contact zones of the nanolayers and are also marked in Figure 5. The color profile of the coordination number corresponds to an increased value for cobalt layers. The value of the parameter in these layers is variable with a spread over a certain range of values. The niobium substrate has a lower coordination number. The structure of this region was initially crystalline and changed insignificantly during modeling and deposition. An interesting effect is observed in the intermediate niobium nanolayer, where distinct crystallization zones appeared. Crystallization zones have a higher coordination number and are characterized by a denser packing of atoms. The described regions arise in sufficiently thick films mainly near cobalt layers. The initial metal crystal lattice mismatch causes mutual rearrangements of atoms and structure transformation inside the material.

The next series of computational experiments was aimed at understanding the deposition flux area influence and the modeling region size on the structure and morphology of the simulated layered nanosystem. Figure 8 shows these parameters of the nanosystem.

The change in the area of the deposition flow, illustrated in Figure 8a, was carried out by reducing the evaporation zone of the starting materials shown in the upper region of this figure. The spray flow area was reduced four times from the original value.

Also, nanocomposite formation modeling was performed on a scale reduced by four times. In this case, the number of deposited atoms in each layer was proportionally reduced so that the thickness of the formed nanofilms did not change.

The deposition flow area influence and the modeling region size on the relative layer-by-layer nanosystem composition are shown in Figure 9. The dependencies without an index in parentheses correspond to the nanosystem formation in its basic mode. The analysis of this result reveals a decrease in the evaporated metal content and a decrease in the calculated region, which does not lead to the rearrangement of the active atoms or a change of the nanolayer composition. A decrease in the area of the deposition flux led only to the increase in the atomic

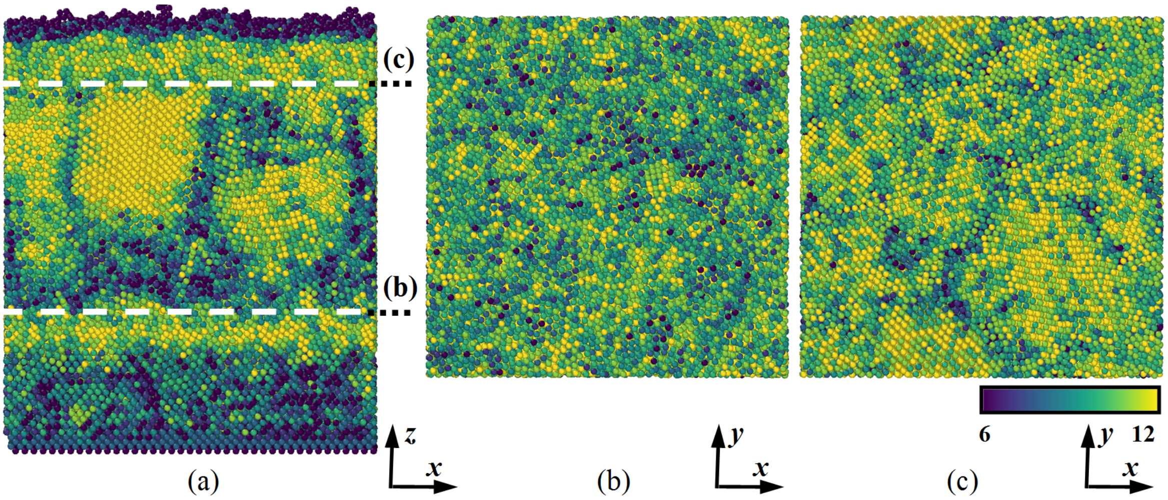

Figure 7: Spatial distribution of the coordination number in the formed multilayer Nb–Co (a) system and in its parallel sections (b) and (c). Substrate temperature is 300 K.

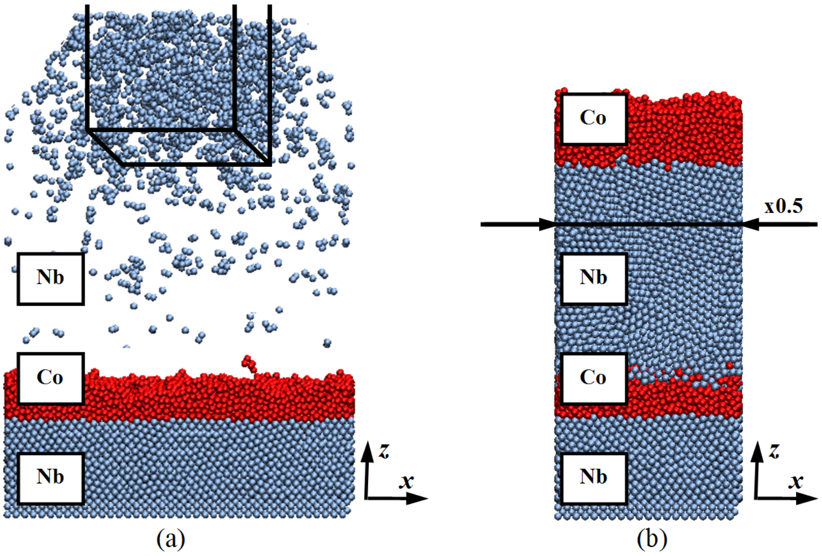

Figure 8: The area of deposition flow (a) and the size of the simulation area (b). The deposition flow area is shown at the top of (a) with solid black lines. The narrowing of the computational domain in (b) is illustrated by the factor ×0.5 in the horizontal direction.

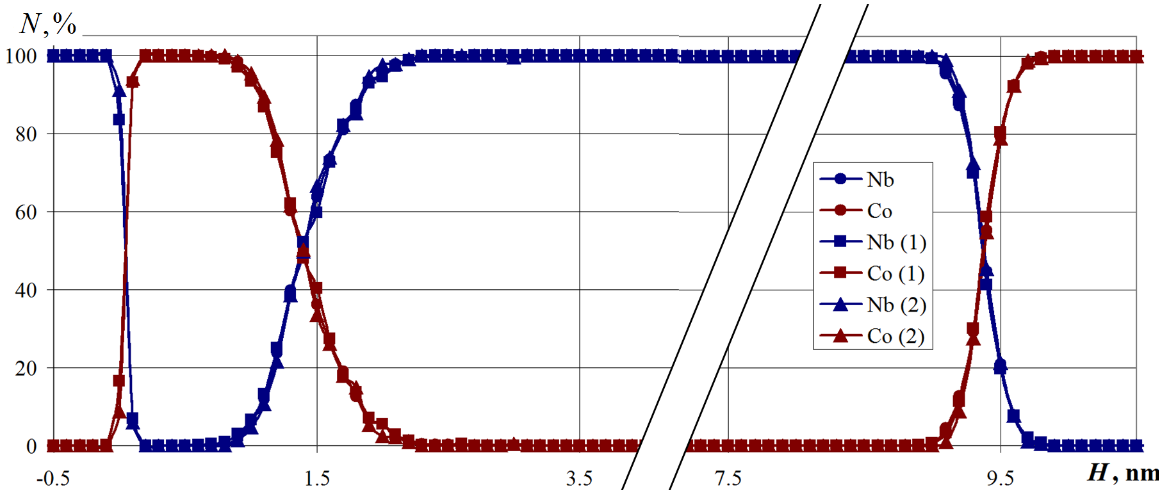

Figure 9: Relative layer-by-layer composition of the Nb–Co nanosystem when the deposition flux is reduced by four times (1) and the modeling area is reduced by four times (2). The parameter *N* is the cobalt or niobium percentage in the horizontal nanofilm layers. The substrate temperature is 300 K.

density zone in the upper region above the substrate. Leaving the evaporation zone, the deposited atoms tend to occupy a more energetically favorable state and are scattered in an evenly distributed layer throughout the entire free volume. When the deposited atoms reach the substrate surface, the effect of reducing the flux is leveled.

A decrease in the nanosystem transverse size by a factor of four also did not affect the nanosystem layer composition, which can be seen in Figure 9. The dependence of the niobium and cobalt fractions slightly differ from the basic version of the nanosystem.

Changing the size of the simulation area allows us to analyze how well the computational cell is represented. Small computational domains can lead to incorrect simulation results due to the appearance of boundary effects. As follows from the calculations, a four-fold decrease in the volume of the nanosystem did not affect the nanocomposite layer composition. The layers are connected at the same places, and the proportion of niobium and cobalt differ slightly from the main part of the sample. The obtained data indicate that the initially selected modeling area is fully representative, and the results properly reproduce the properties of the modeled nanosystem.

The next series of computational experiments was aimed at elucidating the dependence of the multilayer nanosystem structure on the flux density of deposited atoms. This value is controlled by an increase or decrease in the number of deposited atoms per unit time introduced into the system from the evaporation zone. Here, numerical calculations for the nanofilm variations with a 2-fold increase and a 1.5-fold decrease of the deposited atom flux density are performed.

The relative layered composition of the nanocomposite for the calculations is shown in Figure 10. Here, the fraction of elements in the composition during the nanolayer formation when the deposition rate was reduced by 1.5-fold is shown by the solid lines without markers, the increased intensity is represented by dashed lines without markers and the base atom deposition intensity is represented by solid lines with markers. The analysis of Figure 10 reveals that a decrease in the deposition rate of the metals did not significantly affect the composition distribution within the layers of the multilayer nanosystem.

An increase in speed led to a deviation of the composition from the data obtained in the basic version of the calculation. A significant increase in the flux intensity leads to higher agglomeration of the metal atoms above the surface of the substrate. The structure of the resulting nanofilms directly depends on the size of the deposited clusters and does not always have time to rebuild upon direct contact with the surface. Due to the effects that arise, inhomogeneity, dislocations, and voids can occur in the material. The deviations in the constructed composition in the upper layers of the nanocomposite were due to a more rarefied structure, and additional mixing of the nanofilm contact regions is especially noticed. The conducted studies indicate that there is a critical deposition rate, whereby a higher rate leads to the formation of a nanomaterial with a different structure. Since in real technological processes the deposition is carried out using a sufficiently low intensity (about 1000 nm per hour), in order to obtain physically adequate results, the deposition process must be simulated at a speed not exceeding this critical value. On the other hand, there is no need to increase the duration of the nanofilm growth stage. The maximum should approximate the true experimental value, and as given in Figure 10, the structure and composition in this case are similar.

A series of computational experiments was carried out in which the multilayer Nb–Co nanosystem formation was studied in the temperature range of 300–800 K for substrate temperatures of 300, 500, and 800 K, respectively. The simulation results are presented in Figure 11 in the form of a percentage composition of the nanosystem.

The calculations showed that the temperature of the substrate significantly affects the nanosystem structure formation. An increase in temperature leads to an increase in the total thickness of the nanosystem (at 800 K, this value is increased by 0.3 nm compared with a temperature of 300 K). The region of mutual penetration of Nb atoms into the Co layers (and vice versa) also increases, which is clearly seen in Figure 11.

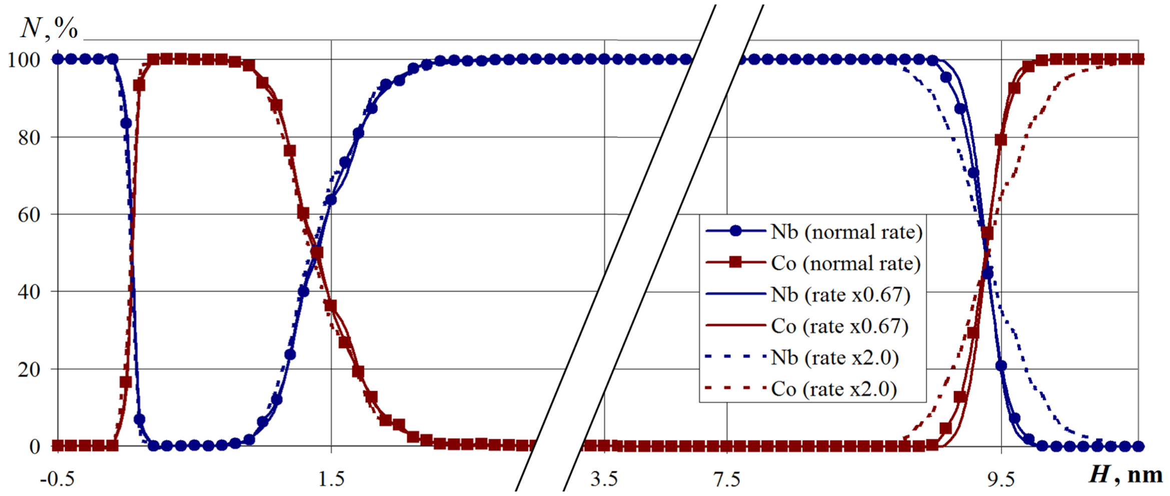

Figure 10: The relative layered composition of the Nb–Co nanosystem for different deposition rates. The parameter *N* is the cobalt or niobium percentage in the horizontal nanofilm layers. The substrate temperature is 300 K.

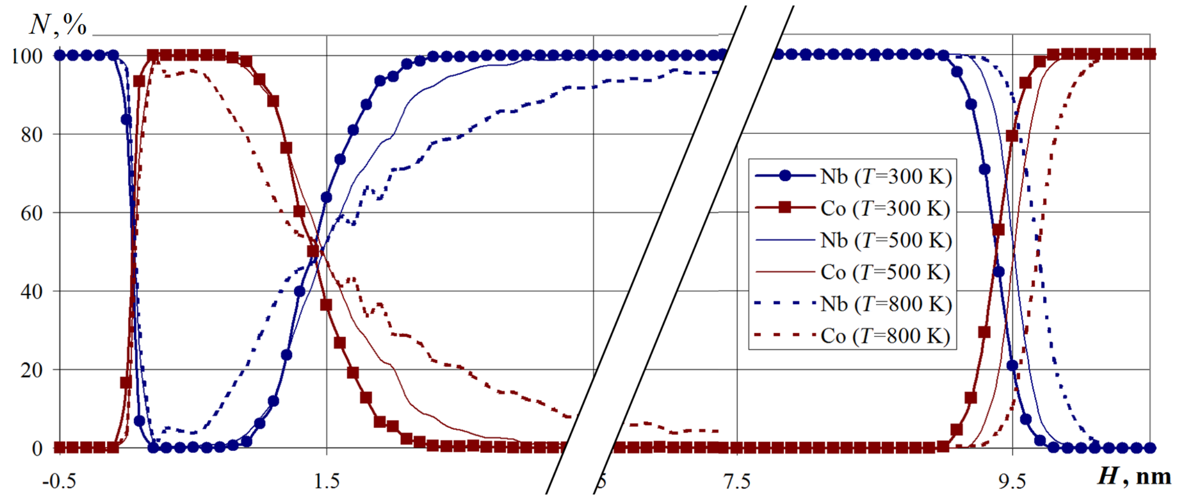

Figure 11: The percentage composition of the Nb–Co multilayer nanosystem formed at a substrate temperature of 300, 500, and 800 K. The parameter *N* is the cobalt and niobium percentage in the horizontal nanofilm layers.

Noticeable variations in the nanosystem layer composition at the interface regions of all nanolayers are visible. The obtained results indicate the multilayer nanosystem formation processes vary significantly including the atomic structure of the interface contact areas, as well as the multilayer nanosystem composition and structure due to the increase in the thermal diffusion processes.

Conclusion

The paper proposes a technique and describes a mathematical model for studying technological modes and parameters in the manufacture of multilayer nanosystems. The model was tested in the study of the formation of a nanosystem based on a hybrid niobium and cobalt structure for a superconducting spin valve design. The influence of various technological parameters was investigated including substrate temperature, deposition flow rate and density, and the nanosystem dimensions.

An analysis of the coordination number distribution in the material showed that the layers have a different structure when multilayer nanofilms are formed under normal conditions. The niobium substrate structure is close to crystalline; cobalt nanofilms are characterized by an amorphous-like structure. In the thickened niobium layer, crystallization zones are observed where direct contact with the cobalt nanolayer occurs. The crystal lattice mismatch of the starting metals causes mutual rearrangements of atoms and the structure transformation inside the nanosystem.

It was also found that a decrease in the area of the deposition flux and the simulation region by 75% of the initial value does not lead to atomic rearrangement or to a change in the nanofilm composition. A decrease in the deposition flux area caused an increase in the atomic density zone in the upper region above the substrate.

The adjustment in the number of vaporized atoms per unit time and the duration of the nanofilm deposition stages revealed the layer and contact area compositional dependence on the intensity of the starting element deposition. A significant increase in the deposition flux intensity led to the appearance of inhomogeneities, dislocations and voids inside the formed nanosystem due to the preliminary clustering of free atoms.

In order to obtain representative results that correspond to real technological processes, it was found to be critical to model the growth mechanisms of nanoscale films and layers using a deposition rate not exceeding the critical value of clustering.

It was also found that the substrate temperature is a leading factor affecting the multilayer nanosystem formation, the atomic structure of the interface contact areas, as well as the composition and structure of the multilayer nanosystem as a whole.

The results presented in this work can be used as a tool to support future experimental investigations and for adjusting and optimizing technological processes related to the production of multilayer nanosystems and devices for spintronics.

Acknowledgements

The authors are thankful to Prof. Lenar Tagirov and Prof. Alexander Golubov for useful discussions.

Funding

This study was financially supported by the project 0427-2019-0029 Ural Branch of the Russian Academy of Sciences "Study of the laws of formation and calculation of macroparameters of nanostructures and metamaterials based on them using multilevel mathematical modeling" (Section 2 of this article). This work was partially supported by the European Union H2020-project "SPINTECH" under grant agreement Nr. 810144 (high-resolution TEM images in Figure 1 and 2) and by the Russian Science Foundation Grant (RSF) Nr. 20-62-47009 "Physical and engineering basis of computers non-von Neumann architecture based on superconducting spintronics" (the remainder of the article).

ORCID® iDs

Alexander Vakhrushev - https://orcid.org/0000-0001-7901-8745
Aleksey Fedotov - https://orcid.org/0000-0002-0463-3089
Vladimir Boian - https://orcid.org/0000-0001-5708-4098
Anatolie Sidorenko - https://orcid.org/0000-0001-7433-4140

Preprint

A non-peer-reviewed version of this article has been previously published as a preprint: https://doi.org/10.3762/bxiv.2020.67.v1

References

1. Chang, C. S.; Kostylev, M.; Ivanov, E. *Appl. Phys. Lett.* **2013,** *102,* 142405. doi:10.1063/1.4800923
2. Endoh, T.; Honjo, H. *J. Low Power Electron. Appl.* **2018,** *8,* 44. doi:10.3390/jlpea8040044
3. Bell, C.; Burnell, G.; Leung, C. W.; Tarte, E. J.; Kang, D.-J.; Blamire, M. G. *Appl. Phys. Lett.* **2004,** *84,* 1153–1155. doi:10.1063/1.1646217
4. Deminov, R. G.; Useinov, N. K.; Tagirov, L. R. *Magn. Reson. Solids* **2014,** *16,* 14209.
5. Wang, Z.; Zhang, L.; Wang, M.; Wang, Z.; Zhu, D.; Zhang, Y.; Zhao, W. *IEEE Electron Device Lett.* **2018,** *39,* 343–346. doi:10.1109/led.2018.2795039
6. Akerman, J. *Science* **2005,** *308,* 508–510. doi:10.1126/science.1110549
7. Bai, Y.; Yang, B.; Zhang, H.; Wu, X.; Jiang, N.; Zhao, S. *Acta Mater.* **2018,** *155,* 166–174. doi:10.1016/j.actamat.2018.05.069
8. Maciel, N.; Marques, E. C.; Naviner, L. A. B.; Cai, H.; Yang, J. *Microelectron. Reliab.* **2019,** *100–101,* 113332. doi:10.1016/j.microrel.2019.06.024
9. Lenk, D.; Morari, R.; Zdravkov, V. I.; Ullrich, A.; Khaydukov, Y.; Obermeier, G.; Mueller, C.; Sidorenko, A. S.; Krug von Nidda, H.-A.; Horn, S.; Tagirov, L. R.; Tidecks, R. *Phys. Rev. B* **2017,** *96,* 184521. doi:10.1103/physrevb.96.184521
10. Gobbi, M.; Novak, M. A.; Del Barco, E. *J. Appl. Phys.* **2019,** *125,* 240401. doi:10.1063/1.5113900
11. Sidorenko, A., Ed. *Functional Nanostructures and Metamaterials for Superconducting Spintronics;* NanoScience and Technology; Springer International Publishing: Cham, Switzerland, 2018. doi:10.1007/978-3-319-90481-8
12. Klenov, N.; Khaydukov, Y.; Bakurskiy, S.; Morari, R.; Soloviev, I.; Boian, V.; Keller, T.; Kupriyanov, M.; Sidorenko, A.; Keimer, B. *Beilstein J. Nanotechnol.* **2019,** *10,* 833–839. doi:10.3762/bjnano.10.83
13. Soloviev, I. I.; Klenov, N. V.; Bakurskiy, S. V.; Kupriyanov, M. Y.; Gudkov, A. L.; Sidorenko, A. S. *Beilstein J. Nanotechnol.* **2017,** *8,* 2689–2710. doi:10.3762/bjnano.8.269
14. Sidorenko, A. S. *Low Temp. Phys.* **2017,** *43,* 766–771. doi:10.1063/1.4995623
15. Zdravkov, V. I.; Kehrle, J.; Obermeier, G.; Lenk, D.; Krug von Nidda, H.-A.; Müller, C.; Kupriyanov, M. Y.; Sidorenko, A. S.; Horn, S.; Tidecks, R.; Tagirov, L. R. *Phys. Rev. B* **2013,** *87,* 144507. doi:10.1103/physrevb.87.144507
16. Aarts, J.; Geers, J. M. E.; Bruck, E.; Golubov, A. A.; Coehoorn, R. *Phys. Rev. B* **1997,** *56,* 2779–2787. doi:10.1103/physrevb.56.2779
17. Lazar, L.; Westerholt, K.; Zabel, H.; Tagirov, L. R.; Goryunov, Y. V.; Garif'yanov, N. N.; Garifullin, I. A. *Phys. Rev. B* **2000,** *61,* 3711–3722. doi:10.1103/physrevb.61.3711
18. Sidorenko, A. S.; Zdravkov, V. I.; Prepelitsa, A. A.; Helbig, C.; Luo, Y.; Gsell, S.; Schreck, M.; Klimm, S.; Horn, S.; Tagirov, L. R.; Tidecks, R. *Ann. Phys. (Berlin, Ger.)* **2003,** *12,* 37–50. doi:10.1002/andp.200310005
19. Kushnir, V. N.; Prischepa, S. L.; Mancusi, D.; Ilyina, E. A.; Cirillo, C.; Attanasio, C. *J. Supercond. Novel Magn.* **2013,** *26,* 2861–2862. doi:10.1007/s10948-013-2219-z
20. Vodopyanov, B. P.; Tagirov, L. R.; Durusoy, H. Z.; Berezhnov, A. V. *Phys. C (Amsterdam, Neth.)* **2001,** *366,* 31–42. doi:10.1016/s0921-4534(01)00904-2
21. Cirillo, C.; Prischepa, S. L.; Salvato, M.; Attanasio, C. *Eur. Phys. J. B* **2004,** *38,* 59–64. doi:10.1140/epjb/e2004-00099-7
22. Kushnir, V. N.; Prischepa, S. L.; Cirillo, C.; Attanasio, C. *Eur. Phys. J. B* **2006,** *52,* 9–14. doi:10.1140/epjb/e2006-00264-0
23. Tagirov, L. R.; García, N. *Superlattices Microstruct.* **2007,** *41,* 152–162. doi:10.1016/j.spmi.2006.08.002
24. Steinhauser, O. M. *Computational Multiscale Modelling of Fluids and Solids. Theory and Application;* Springer-Verlag: Berlin – Heidelberg, 2008. doi:10.1007/978-3-662-53224-9
25. Vakhrushev, A. V. *Computational Multiscale Modeling of Multiphase Nanosystems;* Apple Academic Press: Toronto ; New Jersey : Apple Academic Press, 2017. | Series: Innovations in chemical physics and mesoscopy, 2017. doi:10.1201/9781315207445
26. Vakhrouchev, A. V.; Lipanov, A. M. *Comput. Math. Math. Phys.* **2007,** *47,* 1702–1711. doi:10.1134/s0965542507100107
27. Vakhrushev, A. V.; Severyukhina, O. Y.; Severyukhin, A. V.; Vakhrushev, A. A.; Galkin, N. G. *Nanosci. Technol.: Int. J.* **2012,** *3,* 51–75. doi:10.1615/nanomechanicsscitechnolintj.v3.i1.30
28. Vakhrushev, A. V.; Fedotov, A. Y. *Frattura ed Integrità Strutturale* **2019,** *13,* 370–382. doi:10.3221/igf-esis.49.37
29. Vakhrushev, A. V.; Fedotov, A. Y. *Eur. Phys. J.: Spec. Top.* **2020,** *229,* 305–314. doi:10.1140/epjst/e2019-900105-0
30. Vakhrushev, A. V.; Fedotov, A. Y.; Savva, Y. B.; Sidorenko, A. S. *Himičeskaâ fizika i mezoskopiâ* **2019,** *21,* 362–374. doi:10.15350/17270529.2019.3.38
31. Sidorenko, A. S.; Boian, V.; Savva, Y. B.; Fedotov, A. Y.; Vakhrushev, A. V. Functional nanostructures superconductor-ferromagnet for spintronics. In *Proceedings of the International Symposium Nanophysics and Nanoelectronics,* 2020; pp 114–115.
32. Vakhrushev, A. V.; Fedotov, A. Y.; Savva, Y. B.; Sidorenko, A. S. *PNRPU Mech. Bull.* **2020,** *2,* 16–27. doi:10.15593/perm.mech/2020.2.02

33. Baskes, M. I. *Phys. Rev. B* **1992,** *46,* 2727–2742. doi:10.1103/physrevb.46.2727
34. Baskes, M. I.; Srinivasan, S. G.; Valone, S. M.; Hoagland, R. G. *Phys. Rev. B* **2007,** *75,* 094113. doi:10.1103/physrevb.75.094113
35. Khaydukov, Y.; Morari, R.; Zdravkov, V.; Mustafa, L.; Keller, T.; Keimer, B.; Sidorenko, A. *Low Temp. Phys.* **2017,** *43,* 837–840. doi:10.1063/1.4995633
36. Jamet, M.; Dupuis, V.; Mélinon, P.; Guiraud, G.; Pérez, A.; Wernsdorfer, W.; Traverse, A.; Baguenard, B. *Phys. Rev. B* **2000,** *62,* 493–499. doi:10.1103/physrevb.62.493
37. Chen, G.; Wang, Y.; Sunarso, J.; Liang, F.; Wang, H. *Energy* **2016,** *95,* 137–143. doi:10.1016/j.energy.2015.11.061
38. Gill, H. S. Spin valve sensor with free layer structure having a cobalt niobium (CoNb) or cobalt niobium hafnium (CoNbHf) layer. U.S. Patent No. 6665155, Dec 16, 2003.
39. Pinarbasi, M. Spin valve sensor having antiparallel (AP) pinned layer structure with low coercivity and high resistance. U.S. Patent No. 6353518, March 5, 2002.
40. Ju, K.; Horng, C.; Zheng, Y.; Liao, S.; Chang, J.-W. Integrated spin valve head. U.S. Patent No. 6995959, Feb 7, 2006.
41. Plimpton, S. *J. Comput. Phys.* **1995,** *117,* 1–19. doi:10.1006/jcph.1995.1039
42. Humphrey, W.; Dalke, A.; Schulten, K. *J. Mol. Graphics* **1996,** *14,* 33–38. doi:10.1016/0263-7855(96)00018-5
43. Stukowski, A. *Modell. Simul. Mater. Sci. Eng.* **2009,** *18,* 015012. doi:10.1088/0965-0393/18/1/015012

License and Terms

The definitive version of this article is the electronic one which can be found at:
https://doi.org/10.3762/bjnano.11.160